Comparative Evolution of the Shyok and Yarlung Suture Zones:

Implications for the Collision Between India and Eurasia

by

Nathaniel Borneman

A Dissertation Presented in Partial Fulfillment
of the Requirements for the Degree
Doctor of Philosophy

Approved February 2016 by the
Graduate Supervisory Committee:

Kip Hodges, Chair
Stephen Reynolds
Kelin Whipple
Thomas Sharp
James Tyburczy

ARIZONA STATE UNIVERSITY

May 2016

ABSTRACT

The collision between the Indian and Eurasian tectonic plates marked the onset of the rise of the Himalayan-Tibetan orogen, but also brought about profound changes to the Earth's oceans and climate. The exact sequence of events that occurred during this collision is poorly understood, leading to a wide range of estimates of its age. The Indus and Yarlung sutures are generally considered to represent the final collision between India and Eurasia, and together form a mostly continuous belt that can be traced over 2000 km along strike. In the western portions of the orogen the Karakoram Fault introduces a key complexity to the study of timing of collision by offsetting the Indus and Yarlung sutures. Recent work has used the complexities introduced by the Karakoram Fault to suggest that the more northerly Shyok suture, not the Indus suture, represents the India-Eurasia collision zone. Estimates for timing of the India-Eurasia collision fall into one of three groups: 40-34 Ma, 55-50 Ma, and 66-60 Ma. Attempts to reconcile these models have thus far been unsuccessful. In order to provide additional data that might further clarify the timing and location of collision, studies have been performed along the Shyok suture in India and along the Yarlung suture in Tibet at Sangsang. A study along the Shyok suture argues that the suture formed between 92-85 Ma. This timing precludes an interpretation that the Shyok suture marks the location of the India-Eurasia collision. A second study demonstrates the utility of two new geochronometers, (U-Th)/Pb joaquinite and 40Ar/39Ar neptunite, that play an important role in unraveling the tectonic history of the Yarlung suture. A third study is an investigation of the structure and geochronology of the Sangsang ophiolite complex. Here, multiple (U-Th)/Pb and 40Ar/39Ar systems record magmatism and metamorphism spanning ca. 125-52 Ma. By

tying these chronometers to tectonic process, a history is reconstructed of the southern margin of Tibet that includes Early Cretaceous to Late Cretaceous forearc rifting associated with mid ocean ridge subduction, Paleocene accretionary wedge uplift and erosion, and finally Eocene metasomatism and collision.

DEDICATION

To Greg King, William Vanca, Jane Burton, and Yolanda Vanca

ACKNOWLEDGMENTS

It seems appropriate to start by thanking my advisor, Kip Hodges, for his countless hours of advising. I would also like to thank my other committee members: Stephen Reynolds, Thomas Sharp, James Tyburczy, and Kelin Whipple, all of whom helped shape my thinking throughout this project.

Matthijs van Soest and Jo-Ann Wartho have taught me what I know about analytical lab work, and without them the data that follows would not exist.

Hodges group members past and present have greatly helped me along the way: Michele Aigner, Wendy Bohon, Frances Cooper, Sarah Cronk, Alex Horne, Cameron Mercer, Brian Monteleone, Mary Schultz, Alka Tripathy-Lang, and Kelsey Young.

I owe gratitude to all of the coauthors of my papers, but special thanks go those who partnered with me directly in the field and endured my antics.

Members of the SESE community I owe gratitude to are numerous, and I thank you all.

My family has earned recognition for supporting me when I needed it, and for putting up with my long bouts of absence otherwise.

Special thanks to Katherine Sheppard for reading and commenting on this entire dissertation.

I have been funded throughout my time as a graduate student by the NSF (awards EAR 1007929 (Tectonics) and EAR 0642731 (Sedimentary Geology and Paleobiology)) and by the School of Earth and Space Exploration at ASU.

TABLE OF CONTENTS

Page

CHAPTER Page

CHAPTER Page

CHAPTER Page

CHAPTER Page

LIST OF TABLES

TABLE Page

LIST OF FIGURES

FIGURE Page

CHAPTER 1

INTRODUCTION

MOTIVATION

The collision between the Indian and Eurasian tectonic plates was an event of global significance. It not only marked the onset of the rise of the Himalayas, but also brought about profound changes to the Earth's oceans and climate (Broeker, 2015). The exact sequence of events that occurred during the collision is poorly understood, leading to a wide range of estimates of its age. Some of the lack of consensus likely results from different definitions of what geologic events actually correspond to the onset of collision. Regardless, the spread in estimates has proved unsettling enough to geoscientists to promote more or less constant investigation into the timing of collision since the late-1980's (e.g. Treloar et al., 1989, Rowley, 1996; Searle et al., 1999; Hodges et al., 2000; Yin and Harrison, 2000; Ding et al., 2005; Aitcheson et al., 2007; Henderson et al., 2011; van Hinsbergen et al., 2012; Boilhol et al., 2013; Wu et al., 2014; Jagoutz et al., 2015).

These investigations have focused primarily on the Indus and Yarlung sutures of southern Tibet and adjacent India and Pakistan (Figure 1.1). Broadly defined, a suture is a heavily deformed zone, typically marked by ophiolitic remnants of a former oceanic plate, that separates merged island arcs and/or continental plates. The Indus and Yarlung sutures are the southernmost sutures in the Himalayan-Tibetan orogen for which there is direct geologic evidence, and together form a mostly continuous belt that can be traced over 2000 km along strike.

The Yarlung suture is the longer of the two, stretching from the eastern portions of the orogen to the Karakoram Fault (Figure 1.1). This suture separates Eurasia to the

north from India to the south. Eurasian-affinity rocks to the north are typically ascribed to the Lhasa tectonic block, the southernmost portions of which are mostly comprised of the Gangdese batholith (Jiang et al., 2014). This batholith represents a Jurassic-Tertiary continental arc formed by northward subduction of the oceanic lithosphere separating India and Eurasia (Yin and Harrison, 2000). South of the suture are heavily deformed portions of the Tibetan Sedimentary sequence, which is generally interpreted as the northern-most Indian plate passive margin (Hodges, 2000). The suture itself consists of tectonically interleaved slices of syncollisional basin sediments, forearc, ophiolitic, high pressure, and accretionary wedge rocks. Farther to the west, the Indus suture has by and large the same structural characteristics, but separates Indian-affinity rocks to the south from the Early Cretaceous to Miocene Kohistan and Ladakh batholiths (Bouilhol et al., 2013) to the north, which have an unclear relationship to the Gangdese Batholith. While it is easy to correlate these batholiths to each other based on their similar ages, the oceanic arc nature of the Kohistan batholith and the continental arc nature of the Gangdese batholith make it harder to link them tectonically (Hodges, 2000). One explanation for this discrepancy proposes that the Ladakh batholith is it was a transitional oceanic to continental arc that served to link the Kohistan and Gangdese arcs (Raz and Honegger, 1989).

In the western portions of the orogen, the Karakoram Fault introduces a key complexity to the study of timing of collision. Namely, the Karakoram Fault offsets the Indus and Yarlung sutures. In addition, many contested international boundaries fall along the Karakoram Fault. For these reasons, the Indus and Yarlung sutures are sometimes regarded as separate structures, and the names of geologic features associated

with them change based on what side of the Karakoram Fault is being considered. Furthermore, recent work has used the complexities introduced by the Karakoram Fault to suggest that a more northerly structure occurring on the southern flank of the Jurassic to Tertiary (Karakoram batholith (the Shyok: Figure 1.1) – not the Indus suture – represents the India-Eurasia collision zone (Bouilhol et al., 2013). This suggestion runs counter to the more conventional notion that says the Shyok suture is correlative to the Bangong suture farther east, which forms the northern boundary of the Lhasa block.

For many years, estimates for timing of the India-Eurasia collision fell into one of two groups: 55-50 Ma and 66-60 Ma. Estimates favoring 55-50 Ma (as reviewed by Hodges, 2000) are based on paleomagnetic plate reconstructions that place India near Eurasia at the time of a decrease in convergence rate (Klootwijk et al., 1992; Huang et al., 2015), the timing of ultra-high pressure metamorphism in Indian-plate continental crust (St. Onge et al., 2013), and the switch from marine to non-marine sedimentation as preserved by rocks primarily within the Indus suture (Rowley, 1996). Estimates favoring collision at 66-60 Ma (as reviewed by Yin and Harrison, 2000) have been based primarily on the timing of obduction of ocean affinity rocks onto the Indian margin (Beck, 1995; Ding et al., 2005; Decelles et al., 2014), and proponents of an older age for collision remind me that sedimentary records can, at best, only place a minimum bound on the age of collision (Yin and Harrison, 2000).

Much more recently, a new hypothesis has arisen (initially proposed in Aitcheson et al., 2007) that correlates the timing of collision to the initiation of major deformation in the Himalaya at ca. 40-34 Ma. Further support for this model comes in the form of a potential intra-oceanic accretion event providing a false signal of the final collision

(Aitcheson et al., 2011), and the first appearance of continentally derived inherited zircons in batholiths bordering the collision zone at ca. 40 Ma (Bouilhol et al., 2014).

Attempts to reconcile these models have thus far been unsuccessful, and each model has its drawbacks. Collision at 66-50 Ma requires ca. 1000-2000 km of convergence within India that has left no evidence in the geologic record. This discrepancy has led to the proposal the northern margin of India had been rifted from the rest of the plate prior to collision, thus accounting for "missing" portions of India while permitting a 55-50 Ma age for (van Hinsbergen et al., 2012). Collision at 65-50 Ma also raises the question as to why the major Himalaya-Tibetan deformational features did not initiate until millions of years after collision (Aitcheson et al., 2007). Paleomagnetic estimates place India too far from Eurasia at 65-60 Ma and too close at 40-35 Ma (Huang et al., 2015). Collision during 40-35 Ma leads to what can be considered an unreasonable convergence rate (Rehman et al., 2011), though the presence of two subduction zones between India and Eurasia could account for this rapid convergence (Jagoutz et al., 2015).

In order to provide additional data that might further clarify the timing of collision, I have undertaken studies in the western part of the Himalayan-Tibetan orogen along the Shyok suture at Nubra in NW India and in the southern part of the orogen along the Yarlung suture in southern Tibet at Sangsang (Figure 1.1). These studies combined (U-Th)/Pb and $^{40}Ar/^{39}Ar$ geochronology and thermochronology, geochemistry, geologic mapping, and remote sensing. This combination of techniques has led to the development of several important constraints on the timing of the India-Eurasia collision.

A summary of chapters is below. Chapter 2-5 have been prepared for publication, and therefore overlap in background material. Chapter 2 has been published in *Tectonics* (Borneman et al., 2015). Chapter 3 has been submitted to *Geology*. Chapter 4 will be submitted to *Contributions to Mineralogy and Petrology*. Chapter 5 will be submitted to *GSA Bulletin*.

CHAPTER OUTLINE

Chapter 2 contains the bulk of my work on the Shyok suture zone in the Nubra region of northernmost India. The results argue that the suture formed between 92-85 Ma, bracketed by the appearance of mixed provenance strata with a maximum depositional age of ca. 92 Ma deposited on Ladakh affinity rocks, all of which are crosscut by a ca. 85 Ma dike. This timing precludes an interpretation that the Shyok suture marks the location of the India-Eurasia collision and supports its correlation with the Bangong suture to the east. Given that correlation, the offset of the Shyok and Bangong sutures across the Karakoram Fault limits total right-lateral separation on that section of the fault to 130-190 km.

Chapter 3 deviates from a discussion of Himalayan-Tibetan tectonics to demonstrate the utility of two new geochronometers – (U-Th)/Pb joaquinite and $^{40}Ar/^{39}Ar$ neptunite – that play an important role in unraveling the tectonic history of the Yarlung suture at Sangsang (Chapter 5). Chapter 3 shows how the new chronometers could be used to date the uplift of the New Idria serpentinite diapir of the southern Coast Ranges, in California. This diapir was triggered by the passage of the Mendocino Triple Junction and activation of the San Andreas Fault in the region. Therefore, my data also indicates a

precise age of 12.375 ± 0.082 Ma for the timing of initiation of the San Andreas Fault in the region.

Chapter 4 discusses the implications of a new find of the rare minerals winchite ($\square$(NaCa) $(Mg,Fe)_4(Al,Fe^{3+})Si_8O_{22}(OH)_2$, an amphibole), katophorite ($((K,Na)(NaCa)((Mg,Fe)_4Al)(Si_7Al)O_{22}(OH)_2$, an amphibole), benitoite ($BaTiSi_3O_9$, a cyclosilicate), joaquinite ($NaBa_2REE_2FeTi_2Si_8O_{26}$ $(OH, F)\cdot H_2O$, a cyclosilicate), and neptunite ($KNa_2Li(Fe, Mn, Mg)_2Ti_2Si_8O_{24}$, a transitional phyllo-inosilicate) in meta-trondhjemites found within the Yarlung suture at Sangsang. These minerals all likely formed under high-pressure conditions, and the current structural position of their host rocks requires tectonically significant extensional faulting in the suture zone.

Chapter 5 is a detailed study of the structure and geochronology of the Sangsang ophiolite complex. Here, the U/Pb zircon, $^{40}Ar/^{39}Ar$ hornblende, $^{40}Ar/^{39}Ar$ Na/NaCa-amphibole, $^{40}Ar/^{39}Ar$ neptunite, and (U-Th)/Pb joaquinite systems record magmatism and metamorphism spanning ca. 125-52 Ma. By tying these chronometers to tectonic process, I reconstruct a history of the southern margin of Tibet that includes Early Cretaceous to Late Cretaceous forearc rifting associated with mid ocean ridge subduction, Paleocene accretionary wedge uplift ad erosion, and finally Eocene metasomatism and collision.

Chapter 6 is a synthesis of the previous chapters and also contains a discussion of potential avenues for further research.

FIGURE CAPTIONS

Figure 1.1. Tectonic overview of the Himalayan-Tibetan orogen, showing the locations of the study areas, blocks, batholiths, faults, and sutures. Batholiths are highlighted in grey.

REFERENCES

Aitcheson, J.C.; Ali, J.R.; Davis, A.M., 2007, When and where did India and Asia collide?, Journal of Geophysical Research, 112, B05423, 10.1029/2006JB004706.

Aitcheson, J.C.; Xia, X.; Baxter, A.T.; Ali, J.R., 2011, Detrital zircon U-Pb ages along the Yarlung-Tsangpo suture zone, Tibet: Implications for oblique convergence and collision between India and Asia, Gondwana Research, 20, 691-709, 10.1016/j.gr.2011.04.002.

Beck, R. A., 1995, Stratigraphic evidence for an early collision between northwest India and Asia, Nature, 373, 55–58.

Borneman, N.L.; Hodges, K.V.; van Soest, M.C.; Bohon, W.; Wartho, J.-A.; Cronk, S.S.; Ahmad, T., 2015, Age and Structure of the Shyok Suture in the Ladakh Region of Northwestern India: Implications for Slip on the Karakoram Fault System, Tectonics, 34, 2011-2033.

Bouilhol, P.; Jagoutz, O.; Hanchar, J.M.; Dudas, F.O., 2013, Dating the India-Eurasia collision through arc magmatic records, Earth and Planetary Science Letters, 366, 163-175, 10.1016/j.epsl.2013.01.023.

Broecker, W., 2015, The collision that changed the world, Elementa Science of the Anthropocene, 3, 000061, 10.12952/journal.elementa.

DeCelles, P. G.; Kapp, P.; Gehrels, G. E.; Ding, L., 2014, Paleocene-Eocene foreland basin evolution in the Himalaya of southern Tibet and Nepal: Implications for the age of initial India-Asia collision, Tectonics, 33, 5, 824-849.

Ding, L; Kapp, P; Wan, X.Q., 2005, Paleocene-Eocene record of ophiolite obduction and initial India-Asia collision, south central Tibet, Tectonics, 24, 3, TC3001, 10.1029/2004TC001729.

Henderson, A.L.; Najman, Y.; Parrish, R.; Mark, D.F.; Foster, G.L., 2011, Constraints to the timing of India-Eurasia collision: a re-evaluation of evidence from the Indus Basin

sedimentary rocks of the Indus-Tsangpo Suture Zone, Ladakh, India, Earth-Science Reviews, 106, 265-292.

Hodges, K.V., 2000, Tectonics of the Himalaya and southern Tibet from two perspectives, Geological Society of America Bulletin, 112, 324-350, 10.1130/0016-7606(2000)112<0324:TOTHAS>2.3.CO;2.

Huang, W.; van Hinsbergen, D.J.J.; Lippert, P.C.; Guo, Z.; Dupont-Nivet, G., 2015, Paleomagnetic tests of tectonic reconstructions of the India-Asia collision zone, Geophysical Research Letters, 42, 8, 2642-2649, 10.1002/2015GL063749.

Jagoutz, O.; Royden, L.; Holt, A. F.; Becker, T. W., 2015, Anomalously fast convergence of India and Eurasia caused by double subduction, Nature Geoscience, accepted but not yet published.

Jiang, Z.Q.; Wang, Q.; Wyman, D.A.; Li, Z.X.; Yang, J.H.; Shi, X.B.; Ma, L.; Tang, G.J.; Gou, G.N.; Jia, X.H.; Guo, H.F., 2014, Transition from oceanic to continental lithosphere subduction in southern Tibet: Evidence from the Late Cretaceous-Early Oligocene (similar to 91-30 Ma) intrusive rocks in the Chanang-Zedong area, southern Gangdese, Lithos, 196, 213-231, 10.1016/j.lithos.2014.03.001.

Klootwijk, C.; Gee, J.; Peirce, J.; Smith, G; McFadden, P., 1992, An early India-Asia contact: Paleomagnetic constraints from the Ninetyeast Ridge, ODP Leg 121, Geology, 20, 395–398.

Raz, U.; Honegger, K., 1989, Magmatic and tectonic evolution of the Ladakh block from field studies, Tectonophysics, 161, 107, 118, 10.1016/0040-1951(89)90306-5.
Rehman, H.U.; Seno, T.; Yamamoto, H.; Khan, T., 2011, Timing of collision of the Kohistan-Ladakh Arc with India and Asia: Debate, Island Arc, 20, 308-328, 10.1111/j.1440-1738.2011.00774.x.

Rowley, D.B., 1996, Age of initiation of collision between India and Asia: A review of stratigraphic data, Earth and Planetary Science Letters, DEC, 145, 1-4, 1-13, 10.1016/S0012-821X(96)00201-4.

Searle, M.P.; Khan, M.A.; Fraser, J.E.; Gough, S.J.; Jan, M.Q., 1999, The tectonic evolution of the Kohistan-Karakoram collision belt along the Karakoram Highway transect, north Pakistan, Tectonics, 18, 929-949, 10.1029/1999TC900042.

St-Onge, M. R.; Rayner, N.; Palin, R. M.; Searle, M. P.; and Waters, D. J., 2013, Integrated pressure-temperature-time constraints for the Tso Morari dome (Northwest India): implications for the burial and exhumation path of UHP units in the western Himalaya, Journal of Metamorphic Geology, 31, 5, 469-504.

Treloar, P.J.; Rex, D.C.; Guise, P.G.; Coward, M.P.; Searle, M.P.; Windley, B.F.; Petterson, M.G.; Jan, M.Q.; Luff, I.W., 1989, K-Ar and Ar-Ar geochronology of the Himalayan collision in NW Pakistan - constraints on the timing of suturing, deformation, metamorphism and uplift, Tectonics, 8, 881-909, 10.1029/TC008i004p00881.

van Hinsbergen, D.J.J.; Lippert, P.C.; Dupont-Nivet, G.; McQuarrie, N.; Doubrovine, P.V.; Spakman, W.; Torsvik, T.H., 2012, Greater India Basin hypothesis and a two-stage Cenozoic collision between India and Asia, Proceedings of The National Academy Of Sciences Of The United States of America, 109, 20, 7659-7664, 10.1073/pnas.1117262109.

Wu, F.Y.; Ji, W.Q.; Wang, J.G.; Liu, C.Z.; Chung, S.L.; Clift, P.D., 2014, Zircon U-Pb and Hf isotopic constraints on the onset time of India-Asia collision, American Journal of Science, 314, 548 -579, 10.2475/02.2014.04.

Yin, A.; Harrison, T.M., 2000, Geologic evolution of the Himalayan-Tibetan orogen, Annual Review of Earth and Planetary Sciences, 28, 211-280, 10.1146/annurev.earth.28.1.211.

FIGURE 1.1

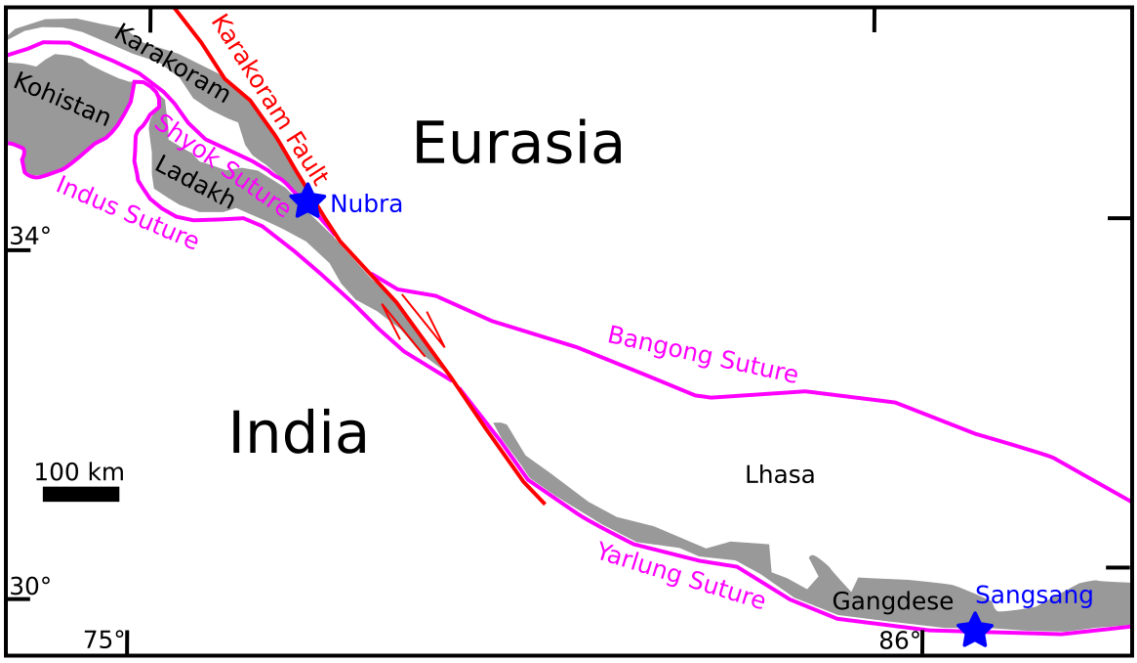
Karakoram
Kohistan
Karakoram Fault
Shyok Suture
Ladakh
Indus Suture
Nubra
Eurasia
34°
Bangong Suture
India
100 km
Lhasa
Yarlung Suture
Gangdese
Sangsang
30°
75°
86°

CHAPTER 2

AGE AND STRUCTURE OF THE SHYOK SUTURE IN THE LADAKH REGION OF NORTHWESTERN INDIA: IMPLICATIONS FOR SLIP ON THE KARAKORAM FAULT SYSTEM

ABSTRACT

A precise age for the collision of the Kohistan-Ladakh block with Eurasia along the Shyok suture zone (SSZ) is one key to understanding the accretionary history of Tibet and the tectonics of Eurasia during the India-Eurasia collision. Knowing the age of the SSZ also allows the suture to be used as a piercing line for calculating total offset along the Karakoram Fault, which effectively represents the SE border of the Tibetan Plateau and has played a major role in plateau evolution. I present a combined structural, geochemical, and geochronologic study of the SSZ as it is exposed in the Nubra region of India to test two competing hypotheses: that the SSZ is of Late Cretaceous or, alternatively, of Eocene age. Coarse-continental strata of the Saltoro Molasse, mapped in this area, contain detrital zircon populations suggestive of derivation from Eurasia despite the fact that the molasse itself is deposited unconformably on Kohistan-Ladakh, indicating that the molasse is post-collisional. The youngest population of detrital zircons in these rocks (ca. 92 Ma) and a U/Pb zircon date for a dike that cuts basal molasse outcrops (ca. 85 Ma) imply that deposition of the succession began in the Late Cretaceous. This establishes a minimum age for the SSZ and rules out the possibility of an Eocene collision between Kohistan-Ladakh and Eurasia. My results support

correlation of the SSZ with the Bangong suture zone in Tibet, which implies total offset across the Karakoram Fault of ca. 130-190 km.

INTRODUCTION

Major late Cenozoic transcurrent fault systems offset preexisting suture zones of varied ages, which form the boundaries between tectonic elements of the Tibetan Plateau (Yin, 2010). These suture zones can provide important constraints on the nature and magnitude of transcurrent tectonics on the plateau provided that they can be correlated with confidence. Unfortunately, suture zone correlations are not always straightforward, as many sutures contain similar rock associations and geochemical characteristics regardless of their ages. The most robust approach to correlating suture zones involves a comparison of the ages of oceanic rock assemblages (which provide a maximum age for a given suture zone), the ages of subduction zone metamorphic assemblages (which similarly provide a maximum age for a given suture zone), and the ages of overlapping sedimentary packages, which provide a minimum age for a given suture zone. If these three classes of ages for two apparently offset suture zones are found to be compatible, I can reasonably interpret the sutures to be offset equivalents and use that offset to constrain transcurrent slip magnitudes and long-term average slip rates. Here I apply this approach to one of the most important late Cenozoic transcurrent structures on the Tibetan Plateau - the Karakoram Fault system (KFS, Figure 2.1).

The KFS is a dextral transpressive structural system which strikes NW-SE and effectively marks the southwestern boundary of the Tibetan Plateau. It links four suture zones of Cretaceous-early Cenozoic age. To the east of the KFS are the roughly E-W–striking Bangong suture zone– regarded as having formed between ca. 101 and 83 Ma (Liu et al., 2014), and the Yarlung suture zone. Most Himalayan researchers are persuaded by the preponderance of available evidence that the Indus and Yarlung suture

zones are Eocene structures (e.g., Najman et al., 2010; St-Onge et al., 2010; Rowley, 1996; van Hinsbergen et al., 2012), but some researchers have concluded that the Yarlung suture formed later (e.g., Oligocene; Aitcheson et al. (2011)) or earlier (e.g., Late Cretaceous; Yin and Harrison (2000)). To the west of the KFS are two comparable suture zones: the NW-SE Shyok suture zone (SSZ), which can be traced westward into Pakistan and north of the Nanga Parbat syntaxis as the 'northern suture', and the more southern E-W Indus suture zone (ISZ) or 'southern suture'. Exactly how these structures might correlate across the KFS is a fundamental problem in Himalayan-Tibetan tectonics because it has important implications for the measurement of the total offset of the central sector of the Karakoram Fault system: ca. 120 km vs. 200 km (e.g. Phillips et al., 2004; Valli et al., 2008). A central issue in this debate is the age of the SSZ, which has been alternatively interpreted as a Cretaceous structure (Rehman et al., 2011; Robertson and Collins, 2002; Weinberg et al., 2000) – implying correlation with the Bangong suture zone – or an Eocene structure (Bouilhol et al., 2013), instead implying correlation with the Indus suture zone. In this study, I present new structural, geochronological, and geochemical data from the Shyok suture zone as exposed in the Saltoro Range of Ladakh region of northern India (Figure 2.2a). My results not only have implications for the total offset of the Karakoram Fault system, but also for the significance of the Shyok suture in the Mesozoic to Cenozoic India-Eurasia collision process.

REGIONAL SETTING

The region of interest for my study (indicated by a rectangle in Figure 2.1 and shown in detail in Figures 2.2 and 2.3) includes three major lithotectonic elements: the Kohistan-Ladakh block, the Karakoram block, and the intervening SSZ.

The Kohistan-Ladakh Block

The Ladakh block (Figures 2.1 and 2.3) makes up the bulk of the Ladakh Range (Figure 2.2a) and is comprised predominantly of calc-alkaline batholithic rocks and their extrusive equivalents (typically referred to as the Khardung Volcanic sequence), with rare pendants of pre-intrusive country rock (Weinberg and Dunlap, 2000; Thanh et al., 2010). Intrusive compositions range from gabbro to granite, while the Khardung Volcanics are dominantly felsic (Dunlap and Wysoczanski, 2002). Two possible eastward extensions of the Ladakh block have been proposed. The most commonly made correlation is to the Mesozoic-Cenozoic Gangdese arc to the east in southern Tibet (Ji et al, 2009). The Gangdese arc is widely regarded as a continental arc developed on the southern margin of Eurasia prior to final closure of the Tethys ocean basin (Hodges, 2000). Along with its previously deformed Mesoproterozoic(?)-Mesozoic country rocks, the Gangdese arc was built on the Lhasa tectonic block of southern Tibet (Yin and Harrison, 2000). Thus, the Lhasa block country rock would correlate tectonostratigraphically with Ladakh country rock in this scenario, although exposures of the host rocks for the Ladakh batholith are rare and mostly restricted to small screens making this interpretation difficult to test. A second possibility is that the eastern equivalent of the Ladakh arc is not the Gangdese arc, but instead an oceanic arc that has been eroded away, over-thrust, buried, or some

combination of the three. In this scenario (Bouilhol et al., 2013; Aitchison et al., 2011), the only record of the oceanic arc in southern Tibet would be the Zedong block described by McDermid et al. (2002), a Jurassic igneous and volcaniclastic package distributed along the Yarlung suture zone. However, Zhang et al. (2014) have correlated the Zedong block to the Lhasa block, calling into question the need to invoke the existence of an oceanic arc in south-central Tibet.

Most researchers also regard the Ladakh batholith to be, at least in part, the eastward continuation of the Kohistan arc in Pakistan to the west (Hodges, 2000). Since the Kohistan arc appears to have been intraoceanic prior to collision, the possible correlation with Ladakh implies that the later may have been transitional in nature, beginning as an intra-oceanic arc that collided with either India or Eurasia and became continental thereafter (Clift et al., 2002; Raz and Honeggar, 1989). Calc-alkaline plutons of the Kohistan batholith are separated from the Ladakh intrusions by convergence of the ISZ and the SSZ around the Nanga Parbat syntaxis. The Kohistan portion of the arc formed as early as the Early Cretaceous (Robertson and Collins, 2002), while the majority of the Ladakh batholith intruded in Paleocene-Eocene time (St-Onge et al., 2010; Weinberg and Dunlap, 2000; White et al., 2011), with some components even as young as Miocene (Bouilhol et al., 2013). Existing geochronologic data suggest that the Khardung Volcanics were erupted between 67.4 ± 1.1 and 60.5 ± 1.3 Ma (2σ) (Dunlap and Wysoczanski, 2002).

The Karakoram Block

The Karakoram block (Figures 2.1 and 2.3) includes granitoid rocks of the Jurassic to Cenozoic Karakoram batholith that intruded and metamorphosed host rocks that are referred to collectively as the Karakoram metamorphic complex (Searle and Tirrul, 1991; Crawford and Searle, 1992; Fraser et al., 2001; Heuberger et al., 2007; Searle et al., 2010; Horton and Leech, 2013). Protoliths of metamorphic rocks in the Karakoram encompass most major rock types and sedimentary protoliths within the Karakoram block range in age from Carboniferous to Upper Cretaceous. Four main metamorphic events have been identified in the Karakoram block: a high-temperature (T), low-pressure (P) event from 63 to 50 Ma that peaked at ca. 50 Ma; a kyanite-sillimanite grade event from 40 to 22 Ma that peaked at ca. 28 Ma; a high-T low-P from 25 to 13 Ma that peaked at ca. 21 Ma; and migmatite generation to retrograde metamorphism associated with thrusting in the Neogene (e.g. Searle et al., 2010). The youngest metamorphic event formed in conjunction with slip on the Main Karakoram Thrust (MKT), a Cenozoic structure that thrusts the Karakoram block units southward over the SSZ (Allen et al., 1991; Fraser et al., 2001). All metamorphic events are associated with igneous rock emplacement and broadly correlate with the major magmatic episodes.

The Shyok Suture and Plausible Correlatives

The SSZ has been mapped in a narrow region of NW India and contiguous NE Pakistan between the Karakoram and Ladakh blocks. Previous work documented that the dominant rock types in the zone are basaltic ophiolitic fragments of the ocean basin that

separated the Kohistan-Ladakh arc from Eurasia, as well as associated oceanic sediments of pelagic to continental shelf affinity (Robertson and Collins, 2002; Rolland 2000 et al.; Upadhyay, 2014). Published geochronology of rocks from the ophiolitic fragments range from ca. 134 to 104 Ma (Khan et al., 2009; Thanh et al., 2012) and place a maximum age constraint on the SSZ development. Additional constraints are provided by cross-cutting igneous rocks from exposures of the SSZ in Pakistan. Treloar et al. (1989) inferred that SSZ formation in Kohistan is younger than the ca. 102 ± 12 Ma (2σ) Rb-Sr age of the pre-suturing Matum Das pluton. They considered the SSZ to be older than the ca. 75 Ma $^{40}Ar/^{39}Ar$ hornblende age of the Jutal dikes, which crosscut the SSZ and the aforementioned pluton. They further suggested that the SSZ is younger than the ca. 85 Ma metamorphism of the Kohistan-Ladakh arc. Searle et al. (1999) argued that the SSZ in Kohistan must be younger than the 95 Ma U-Pb zircon age of the pre-suturing Hunza pluton unit, but older than the ca. 75 Ma Jutal dikes. A Cretaceous age for the SSZ was also inferred by Weinberg et al. (2000) and Rehman et al. (2011).

More recently, the interpretation of a Cretaceous age of the SSZ has been challenged. Khan et al., (2009) proposed a ca. 50 Ma age, although Rehman et al. (2011) dismissed their arguments on the basis that an Eocene age would require a geologically unreasonable convergence rate. Subsequently, Bouilhol et al. (2013) built on Khan et al.'s methodology, using Hf isotopes in zircon to detect continental input into magmas. They inferred an even younger collision between Kohistan-Ladakh and Eurasia at 40 Ma. This interpretation also figures prominently in a recent model of India-Eurasia geodynamics that features double subduction within the Tethys ocean basin over the Cretaceous-early Tertiary interval (Jagoutz et al., 2015).

There is also a lack of complete consensus on the timing of final suturing between Eurasia and India. The various interpretations focus on permissible correlations among the Indus suture zone separating the Kohistan-Ladakh block from India, the Bangong suture zone separating the Lhasa block from the Qiangtang block to the north, the Yarlung suture zone separating the Lhasa block from India, and the Shyok suture zone separating the Kohistan-Ladakh block from the Karakoram block (Schwab et al., 2004; Yin and Harrison, 2000). Of special importance in evaluating these interpretations are the ages of these sutures. Consensus has been reached only on the ca. 50-55 Ma age of the Indus suture (e.g., Tripathy-Lang et al., 2013; Bouilhol et al., 2013). Work thus far on the Bangong suture suggests some diachroneity of activity along its strike, but – in general – it appears to be Cretaceous in age, with final closure in the 101-83 Ma range toward its western terminus against the Karakoram Fault (Kapp et al., 2007; Liu et al., 2014). Considerable disagreement exists in the literature regarding the ages of the others.

Conventional wisdom (as reviewed by Hodges (2000)) holds that collision along the Yarlung suture zone occurred at approximately the same time as that along the Indus suture zone at ca. 55-50 Ma (Najman et al., 2010; Rowley, 1996; van Hinsbergen et al., 2012). However, some recent papers have called that age into question. For example, Aitchison et al. (2011) argued for an age of collision possibly as young as ca. 35 Ma, while DeCelles et al. (2014) and Wu et al., (2014) argued for a 58-60 Ma age based on what they interpreted as a change from Indian to Asian detritus in sedimentary basins within the Yarlung suture.

Proposed Total Displacements for the Central Karakoram Fault System

As is apparent form the above background, the correct correlation of the SSZ with other sutures in Tibet would provide an important constraint on the total displacement along the central sector of the Karakoram Fault system. Correlating it to the Bangong suture zone proper leads to a total offset of 120 km, consistent with proposed offsets of Karakoram block granites and the antecedent Indus river, respectively to the north and south along strike of the Karakoram Fault (Phillips et al., 2004). Correlating the SSZ with a thrust sheet of the Bangong suture zone referred to as the Shequanhe suture zone (Kapp et al., 2003) leads to a total offset estimate of 200 km (Valli et al 2008). Bouilhol et al.'s (2013) correlation of the SSZ with the Yarlung suture zone implies an offset of ca. 450 km, more or less consistent with the 480 km total offset implied by correlating the Bangong suture zone with the Rushan-Pshart suture zone to the north of the Karakoram block (Figure 2.1) (Valli et al., 2008).

Our research was motivated by a belief that better constraints on the timing of the formation of the SSZ would improve my level of confidence in how best to correlate the SSZ to the Bangong suture zone or the Yarlung suture zone and thus improve my understanding of the broader accretionary history of southern Tibet.

GEOLOGY OF THE SALTORO RANGE AND RESULTS

Much of the trace of the SSZ lies in a politically sensitive international border region, but the best and most accessible exposures are found in the Saltoro Range of NW India. The geologic basis for my work was developed by field mapping and sample collection over three months in 2010 and 2012 (Figures 2.2 and 2.3). The study area is,

for the most part, extremely rugged and some important outcrops are difficult to access. As a consequence, I augmented field observations with remote sensing data analysis. NASA's *Reverb ECHO* service was used to select a Landsat 7 scene (LE71470362000241SGS00) with minimal snow and cloud cover in the region of interest. All processing was done using the *ENVI* software suite. The scene was clipped to the vicinity of the Saltoro Range to in order to focus any processing on the region of interest. My image processing methods follow those of Cooper et al. (2012) adapted for Landsat imagery which has similar visible and infrared spectral coverage to the ASTER imagery used in that study. Heavily vegetated regions were masked out. All spectral bands were then processed using Principal Components Analysis (Cooper et al., 2012; Jolliffe, 2002), and three bands showing the least influence of topography and shadow and the best opportunity for distinguishing different lithologies were combined into a single image. This image was then combined with the higher resolution band 8 from the original un-stretched image to produce a higher resolution final image. Google Earth imagery (Figure 2.2a) and the final decorrelation-stretched Landsat image (DSI; Figure 2.2b) were used as base maps for field mapping, which permitted me to correlate colors on the DSI with observed lithologies. These correlations then permitted me to extend the mapping to regions of the Saltoro Range that were otherwise inaccessible. Throughout the area, heavy dust cover and desert varnish masks the characteristic spectral data of various rock types to varying degrees, making it difficult to robustly interpret the spectral data. However, sharp color changes in the remote sensing image were found to be highly indicative of lithologic change. Based on a combination of field observation and remote sensing data interpretation, I classified five mapping units within the SSZ; their

distributions and relationships are shown on the geologic map and illustrative cross section in Figure 2.3 and simplified tectonostratigraphic columns in Figure 2.4.

Ladakh Block Lithologies

The Ladakh block forms the southernmost portion of the study area, where it is thrust over the SSZ along a south dipping fault (Figure 2.3). The Ladakh block primarily consists of coarse to fine grained granites to diorites with K-Ar biotite ages of ca. 66-49 Ma with abundant associated hornfels of coincident age (Thanh et al. 2010). Included in this tectonostratigraphic block is the ca. 67.4-60.5 Ma Khardung Volcanics unit, which overlies and is interpreted to be the volcanic equivalent of the Ladakh-affinity granitoids within the block (Dunlap and Wysoczanski, 2002).

Shyok Suture Zone Volcanic and Sedimentary Units

Historically, names for extrusive igneous and low-grade meta-igneous rocks, as well as associated sedimentary and low-grade meta-sedimentary rocks in the SSZ, have been inconsistently applied (e.g., Rai, 1982; Rolland et al., 2000; Weinberg et al, 2000; Juyal, 2006; Ehiro et al.; 2007; Thanh et al., 2012; Upadhyay, 2014). For example, a volcanic or volcaniclastic unit that may or may not include serpentinite-bearing mélanges may variably be mapped as the Shyok Volcanics, Shyok Formation, Nubra Formation, Saltoro Andesite, Tsoltalk-Shyok Formation, and Mélange Unit. With the exception of a relatively consistently recognized molassic conglomerate, sedimentary rocks in Nubra are variably referred to as Flysch, Tsoltak Formation, Saltoro Flysch Formation, Hundiri Formation, Sedimentary Unit, Tsoltalk-Shyok Formation, and Saltoro Formation. Much

of the confusion of units in the region likely results from limited access within the Saltoro Range itself, forcing prior workers to attempt correlation of rocks from the bank of the Nubra River to rocks from the south bank of the Shyok River (Figure 2.2a) without knowledge of the intervening geology. For the purpose of this discussion, I choose to divide units based on geologic/tectonic environment. At the same time, I do not wish to introduce further nomenclature to an already confusing situation. Therefore, for the most part, I choose to denote units based on the nomenclature of Upadhyay (2014).

Shyok Volcanics of the Saltoro Range

The structurally lowest exposed units in the study area are lower greenschist facies meta-volcanic and meta-volcaniclastic rocks (shown in green in Figure 2.3). These are typically green in outcrop but altered exposures can be bright to dull earthy-orange. The bottom of the Shyok Volcanics unit is not observed, placing its minimum thickness at 2 km. Protolith lithologies include intermediate to mafic volcanic rocks and less common interlayered volcanogenic sedimentary rocks (Weinberg et al., 2000). Most exposures contain massive porphyritic rocks of intermediate composition that locally display relict brecciated texture indicative of emplacement as block and ash flows. Common metamorphic assemblages are plagioclase + epidote + chlorite + actinolite + quartz + calcite + opaques ± sphene with relict pyroxenes, biotite and hornblende. Alteration is common, with veins consisting of quartz, calcite, and oxides with occasional sulfides and Cu mineralization. Towards the northwestern portion of the study area along the Shyok River, the Shyok Volcanics unit is intruded by gabbroic rock and hornblendite

dikes oriented perpendicular to bedding. These dikes are interpreted to be hypabyssal equivalents to the Shyok Volcanics.

Evidence of both metamorphism and localized alteration suggest that robust classification and tectonic setting discrimination of these rocks must be based on relatively immobile trace elements. I performed such analyses on representative samples (see Appendix A for details and Table A1 for data). Figure 2.5 illustrates salient features of the results using Zr/Ti vs. Nb/Y, Th vs. Co, and Th/Nb vs. La/Yb diagrams (Winchester and Floyd, 1977; Hastie et al., 2007, and Hollacher et al., 2012). For the most part, the analyzed samples are best described as sub-alkaline basalts or andesites following a primarily calc-alkaline trend (Figure 2.5a-b). All but one sample fall within the continental arc or alkaline arc fields of the Th/Nb vs. La/Yb discrimination diagram proposed by Hollocher et al. (2012) (Figure 2.5c), consistent with a pre-India-Eurasia collision, arc-magmatic origin for the Shyok Volcanics.

Due to similar grade and composition, volcanic rocks north of the Khalsar thrust that underlie the Saltoro Molasse are here grouped together as the Shyok Volcanics unit. The Shyok Volcanics unit does not include any sort of mélange, such as the Metavolcanics of Thanh et al. (2012). The Shyok Volcanics unit includes all volcanic outcrops in the Ladakh Range west of Skuru and similar greenschist outcrops in the Saltoro Range. A major source of confusion in the region is the structural juxtaposition of the Shyok Volcanics unit, Khardung Volcanics unit, and an ophiolite-bearing mélange within a few kilometers of the confluence of the Shyok and Nubra Rivers (Rolland et al., 2000; Upadhyay, 2014; Weinberg et al., 2000). I approached this problem by mapping into this area of structural complexity from areas that are less complicated but not well

studied. I therefore feel that out mapping provides a better representation of the distribution of rock units.

Saltoro Formation

An unconformity (Figure 2.4a) separates the Shyok Volcanics unit from the overlying Saltoro Formation (Upadhyay, 2014). The Saltoro Formation (shown in lavender in Figure 2.3) consists of interstratified carbonate rocks, sandstones, and mudstones. In the Saltoro Range, carbonate rocks dominate basal portions of the formation, but decrease in abundance upwards before becoming totally absent in the topmost exposures. In outcrop, the carbonate rocks are black to light gray, sandstones are buff, and mudstones are light gray. Bedding is on the centimeter to meter scale. Outcrops are largely transposed by subsequent deformation (see below) but, in places, possess preserved sedimentary structures showing normal graded bedding, dewatering features, and fossils. Fossils in limestone layers such as *Horiopleura haydeni*, *Eoradiolites gilgitensis, Cyclamina* sp. and *Numulites* sp. suggest a middle Cretaceous or older age (Rai, 1982; Upadhyay, 2014). The maximum observed thickness of the Saltoro Formation is 3 km, however the extent of thickening or thinning within the Saltoro Formation as a consequence of deformation is unconstrained.

We group all marine sedimentary rocks within the Saltoro Range as the Saltoro Formation due to their similar depositional environment. Some workers further group the Shyok Volcanics unit and Saltoro Formation together as the Tsoltalk-Shyok Formation (e.g., Thanh et al., 2012) or simply the Shyok Formation (e.g., Weinberg et al., 2000). This grouping is defensible based on the likely similar age and depositional contact

between the two rock types. I choose to split the rocks into two units because the sharp transition from volcanic rocks to marine sedimentary rocks, even on the remote sensing images, makes doing so straightforward. The combination of volcanic rocks and shallow marine sediments suggests an island arc environment for the eruption of the Shyok Volcanics and deposition of the Saltoro Formation (Upadhyay, 2008; Upadhyay 2014).

Saltoro Molasse

The Saltoro Molasse (shown in red in Figure 2.3) is separated from the underlying Shyok Volcanics unit and Saltoro Formation by a buttress unconformity (Figure 2.4a). This contact is exposed along the Nubra River and interior of the Saltoro Range, however along much of the southern side of the Saltoro Range along the Shyok River a presumably small offset thrust separates the Saltoro Molasse from the Saltoro Formation. The Saltoro Molasse (Rai, 1982), presenting as ca. 10 m-thick layers of conglomerates and coarse sandstones, is typically pink to red, with local alteration to light green. The primarily clast-supported conglomerates have clast sizes ranging from 1 cm to 1 m, averaging ~10 cm. The majority of clasts are volcanic, resembling the Shyok Volcanics sequence and other local greenschist facies volcanic rocks, with subordinant granite, phyllites, and schist clasts. The sandstone beds are usually massive, but occasionally show centimeter-scale bedding. The unit as a whole is oxidized, giving it a characteristic red color. Based on the preceding observations, the Saltoro Molasse is interpreted to have been deposited in a proximal alluvial fan system. This is in stark contrast to the underlying yet similarly named marine Saltoro Formation. The minimum thickness of the molasse is 3.2 km.

Mélange

Highest within the Shyok suture zone, a ca. 1 km-thick, low-grade structural Mélange unit (shown in purple in Figure 2.3) with a metaphyllitic matrix has been emplaced over the Saltoro Molasse on a late, post-SSZ thrust fault described below as the Murgi thrust. Within the matrix are decimeter- to kilometer-scale blocks of phyllite, limestone, red chert, basalt, gabbro, and peridotite. Greenschist facies assemblages are common throughout the matrix but are only developed in the blocks when bulk compositions are appropriate. I have no direct constraints on the relative ages of this unit and other SSZ units, nor do I have direct constraints on its structural relationship with other SSZ units prior to development of the Murgi thrust.

Late Intrusive Igneous Rocks Cutting the SSZ

All SSZ units except the Mélange unit are intruded by numerous decimeter- to meter-scale, fine-grained, felsic to mafic dikes. Some individual dikes can be traced over 1 km in the field. The felsic to intermediate composition dikes typically have an aplitic texture, and are often heavily altered and crumbly in hand sample.

Several larger granitic bodies (shown in blue in Figure 2.3) intrude the Saltoro Formation and Shyok Volcanics. The best studied of these bodies is the Tirit Granite, found at the confluence of the Shyok and Nubra Rivers, which has an exposed outcrop area of ca. 20 km^2. Within the Saltoro Range, the Tirit 'granite' is predominantly medium-grained biotite granite to granodiorite with lesser amounts of aegerine diorite. The Tirit Granite has been described geochemically as showing an arc igneous trend (Rao and Rai, 2009).

Two more granitic bodies within the SSZ of comparable size to the Tirit Granite were identified in this study. A hypabyssal, homogenous, fine-grained granite containing dendritic muscovite and miarolitic cavities (sample BCUM12-135) intrudes the Saltoro Formation. The age of a sample from this granite (BCUM12-135) was determined as part of this study (see Section 5.3.3). In addition, a composite pluton with a wide variety of lithologies including calcite-bearing hornblende gabbros, cumulate hornblende gabbros, and diorites intrudes the Shyok Volcanics. A sample from this unit (BCUM12-97) was also dated and the results are also reported in Section 5.3.3.

Karakoram Block Lithologies

The structurally highest rock exposures in the study area are of Karakoram block units (Figure 2.4a), which are thrust over all of the SSZ units. Many of the highest exposures have proven difficult to access, but the rocks exposed there can be identified from observations of rockfalls from known locations when direct access was not possible. The majority of the Karakoram block in the Saltoro Range is composed of high-grade metasedimentary quartzites, schists, gneisses, migmatites and granitoid rocks which are not differentiated on Figure 2.3. The typical metamorphic assemblage I observed in metapelitic and metapsammitic schists, gneisses and migmatites is quartz + muscovite ± biotite ± plagioclase ± K-feldspar. Granitic rocks ranged from tourmaline-garnet pegmatitic leucogranites to biotite-hornblende-sphene granodiorites. Similar intrusive igneous rocks are observed near Panamik along the more accessible east bank of the Nubra River, adjacent to the Karakoram Fault zone (Ravikant et al., 2009; Thanh et al., 2010).

Correlations within the Shyok Suture Zone

The nominally calc-alkaline Shyok Volcanics unit has a distinct geochemistry from the boninite-bearing ophiolitic greenschist metavolcanic units described by Thanh et al. (2012) as part of the SSZ, here mapped as part of the Mélange unit. Those rocks, which are exposed to the east of the study area, have geochemical characteristics more consistent with eruption in a forearc basin environment instead of the likely arc environment of the Shyok Volcanics unit. With respect to trace elements, for example (Figure 2.6), the Shyok Volcanics unit is generally more enriched and lacks the distinct Pb enrichment found in the ophiolitic meta-volcanics. While Thanh et al. (2012) regarded some rocks within my map area as having an ophiolitic character, I mapped them instead as part of the Shyok Volcanics unit. The Shyok Volcanics unit is chemically much more similar to the alkaline Khardung Formation (Clift et al., 2002; Rolland et al., 2000). However, the two units have radically different ages: Cretaceous or older for the Shyok Volcanics (as constrained by the fossil age from the depositionally overlying Saltoro Formation (Upadhyay, 2014)) versus ca. 67.4-60.5 for the Khardung Formation (Dunlap and Wysoczanski, 2002).

Along the Shyok Suture Zone in the Baltistan region of Pakistan, the Pakora Formation's lower volcanogenic member (Robertson and Collins, 2002) is broadly similar to the Shyok Volcanics. For example, their described basaltic to andesitic composition, lack of pillow lavas, and massive to volcaniclastic morphology are similar to those I have documented in the Shyok Volcanics succession, therefore I tentatively correlate these two units.

Likewise, the Pakora Formation limestone member, along with the base of the Pakora Formation's upper volcanogenic member, is likely correlative to the Saltoro Formation. Both contain similar limestones, sandstones, and shales and have similar ages, as Robertson and Collins (2002) reported rudist-bearing fauna in the limestone layers of the Pakora Formation indicative of a Cretaceous (post-Valanginian) age.

Robertson and Collins (2002) also reported the existence of molasse and mélange units in the Baltistan region, providing lithologic descriptions that suggest correlation to the Saltoro Molasse and Mélange unit in my study area. However, if this correlation is correct, the relative structural position of the units is reversed: in Baltistan, the mélange sits below the molasse unit, and is separated from it by N-dipping reverse faults. This reversal of tectonostratigraphic positions of the two units seems plausible given the documented activity of younger thrust faults in the region, including those related to the late Cenozoic Main Karakoram thrust system (Searle, 1991).

Structural Geology

Major thrusts separate the study area into four blocks with differing histories: the Ladakh block, stratified and volcanic rocks of the SSZ (Shyok Volcanics, Saltoro Formation, and Saltoro Molasse), the SSZ Mélange unit, and the Karakoram block. Below I describe structures both internal to and separating these blocks.

Deformational Features of the Ladakh Block

Relatively little of the Ladakh block is exposed in my study area, but the rocks I observed were largely granitic and displayed predominately igneous textures. Locally

developed planar fabrics within the block are likely magmatic in origin. Some exposures of genetically associated, low-grade metavolcanic rocks (Khardung Volcanics) were mapped just to the southeast of the study area by Weinberg et al. (2000), and these displayed a weak, 50˚-60˚ N-dipping cleavage.

Khalsar Thrust

The contact between the Ladakh block and stratified rocks of the SSZ is mapped as the Khalsar thrust (Weinberg et al., 2000) (Figures 2.3 and 2.4b). At the classic exposure of the thrust, near the town of Khalsar and southeast of the study area, the structure was mapped as striking northwest and dipping northeast, placing Shyok suture zone rocks over Khardung Volcanics of the Ladakh block. This exposure of the Khalsar thrust is of very limited extent (only a few km along strike) and it becomes covered to the northwest by modern sediments along the Shyok River. Farther northwest, near Diskit, the structure is exposed and has been mapped by Rolland et al. (2000) as a fault zone with two principal, SW-dipping strands separated by a 300-3000 m thick slice of deformed sedimentary rock. Upadhyay (2014) correlated these sediments to the Saltoro Formation. The fault once again strikes beneath modern sediments before re-emerging in my study area. Here, the fault strikes NW, dips ~ 70˚SW, and places the Ladakh block granitic rocks over deformed phyllites that I correlate to the Saltoro Formation. It is marked by a highly deformed zone roughly 200 m-thick, and hanging wall rocks in this zone, especially near the contact with the footwall, display cataclastic textures. Footwall rocks of the Saltoro Formation contain a strong phyllitic fabric subparallel to the contact. S-C planar fabrics in these rocks (Lister and Snoke, 1984), defined by chlorite and

sericite, along with a prominent SW-plunging stretching lineation, confirm that this structure is a reverse fault. The hanging-wall-to-the-NE shear sense and the observation that the hanging wall here contains Ladakh block lithologies argue against the correlation of this structure with the Main Karakoram thrust, as proposed by Weinberg et al. (2000). As noted below, I regard the structurally higher Waris thrust (described in Section 4.6) to be a more likely candidate for correlation with the Main Karakoram thrust.

Deformational Features of Stratified and Volcanic Rocks of the Shyok Suture Zone

Both the Shyok Volcanics unit and the Saltoro Formation were subjected to greenschist-facies metamorphism subsequent to deposition. Synmetamorphic deformational fabrics (predominately a moderately northwest dipping cleavage) can be found in most outcrops of the Saltoro Formation, but are not well developed in the more massive Shyok Volcanics. Outcrop and thin section examination suggests that the Saltoro Molasse displays no obvious deformational fabrics and does not appear to be metamorphosed. I infer that the metamorphic fabrics found in the lower units of this structural block predate molasse deposition.

The well-defined thick bedding of the Saltoro Molasse makes that unit especially useful for characterizing the internal deformation of the rocks between the Khalsar thrust and the Murgi thrust, the next higher major thrust at the base of the Mélange unit (described below). A large, overturned anticline-syncline pair was observed near the confluence of the Nubra and Shyok Rivers that affects both the molasse and the underlying Saltoro Formation. The axial planes of both folds strike roughly E-W and dip to the south. Neither structure could be traced eastward across the Shyok Valley and into

the Shyok Volcanics or the structurally higher Ladakh block, and they are presumed to be internal to the suture zone sedimentary successions. The folds are cut locally by younger, steep, brittle faults that can be traced in the remote sensing imagery for several kilometers along their N-S to NW-SE strikes but appear to have minor offsets. These structures appear to be truncated by a family of thrust faults that strike WNW-ESE, locally subparallel to bedding, and dip moderately (ca. 35˚) to the northeast. In most instances, these thrusts appear to duplicate parts of the Saltoro Molasse sequence, but the basal structure, near its easternmost exposure, thrusts Shyok Volcanics over Saltoro Molasse and thus has appreciable offset. This family of structures is truncated to the northwest by the thrust at the base of the SSZ Mélange unit. A similarly oriented thrust is found along one exposure of the base of the Saltoro Molasse, as noted previously by Upadhyay (2014). I mapped this disrupted segment of the unconformity over a distance of roughly 20 km along strike, but its displacement appears to be minor and it dies out to the NW into the unconformity that characterizes the base of the molasse elsewhere.

Murgi Thrust

The newly named Murgi thrust places structurally chaotic rocks of the Mélange unit over the Saltoro Molasse (Figure 2.3). The Murgi thrust is interpreted as being responsible for carrying the SSZ Mélange unit from a structurally deeper position within the SSZ to its current structural position above the Saltoro Molasse. The Murgi thrust strikes WNW-ESE and dips 35° northward. Older deformational fabrics within the hanging wall are transposed into near-parallelism near the Murgi thrust, but I was unable to definitively recognize primary thrust-related fabrics in the basal parts of the hanging

wall. However, the typically weakly to unfoliated molasse lithologies of the footwall pick up a moderate to strong cleavage near the thrust. Clasts in the molasse near the contact become rotated in a way consistent with thrust-sense (hanging wall to the southeast). In the northwestern part of the study area, the Murgi thrust appears to be cut by the Waris thrust, or plausibly merges with it.

Deformational Features of the SSZ Mélange Unit

Although some of the larger blocks of appropriate mineralogy contain older foliations, other (more massive) blocks do not. The predominant planar fabric of the SSZ Mélange unit is a strongly developed schistosity in its matrix. This schistosity, defined by chlorite and sericite, typically strikes WNW-ESE and dips moderately (~ 45˚) to the NE. Lineations trending ~ N35˚E but variably plunging are found in some outcrops. The ages of these fabrics are unclear, but the fact that they cannot be traced beyond outcrops of the SSZ Mélange unit and into surrounding units implies that they formed during mélange development or, plausibly, earlier and within the pre-collisional subduction complex along the southern margin of the Karakoram arc.

The Waris Thrust

The structurally highest major thrust in the Saltoro Range (Figure 2.3) – referred to informally here as the Waris thrust – places rocks of the Karakoram block over various units of the SSZ. This WNW-ESE-striking fault dips shallowly (5-30˚) northward. The thrust appears to maintain a more-or-less uniform structural position within its hanging wall, but cuts downward into the footwall from east to west; in the eastern Saltoro Range,

the Mélange unit forms the immediate footwall, but the Saltoro Molasse and, eventually, the Shyok Volcanics appear beneath the thrust toward the west, indicating tilting of the footwall prior to hanging wall emplacement. The structure strikes and dips similarly to the Murgi thrust and minor thrusts within the stratified and volcanic rocks of the SSZ. The intersection between the Waris and Murgi thrusts was not observed in the field, but remote sensing imagery is consistent with a merger of the two – perhaps suggesting that they are coeval – or that the Waris thrust cuts the Murgi thrust at a very low angle, which would indicate that the latter structure is at least slightly older. A roughly 10 m-thick fault zone characterizes the trace of the Waris thrust. Within this zone is a localized S-C composite fabric – defined by chlorite and sericite – that strikes parallel to the fault zone, as well as a mineral lineation that is presumed to have developed synchronously. These fabrics indicate hanging wall-to-the-southeast shear sense. They are deformed, at least locally, by a second crenulation cleavage not observed in other Saltoro Range lithologies.

Hanging wall and footwall lithologies and the eastward vergence of the Waris thrust are similar to those characterizing the classic Main Karakoram thrust (MKT, Figure 2.1) mapped to the west in northern Pakistan (Rex et al., 1988; Searle, 1991; Searle et al., 2010), and I propose that the Waris thrust represents the eastward continuation of the MKT.

Deformational Features of the Karakoram Block

Rocks in the hanging wall of the Waris thrust (MKT) were observed only in a limited number of places. Most exposures are in the higher elevations of the Saltoro Range to which access was not possible but I was able to sample and date rockfall from

the hanging wall. Unfortunately, I know little about the outcrop orientation of these samples and I can only describe the fabrics. Metasedimentary rocks display typical gneissosities and schistosities defined by muscovite and biotite, whereas the intrusive igneous rocks do not typically show penetrative fabrics. The igneous textures of granitic rockfall samples are similar to the 'Nubra-Siachen leucogranite' described by Phillips and Searle (2007), which are exposed immediately east of the Karakoram Fault zone in the Saser Muztagh subrange (Figure 2.2) of the Eastern Karakoram. Many of the fabrics within the metasedimentary rockfall samples are similar to rocks described from the Saser Muztagh for rocks described by Van Buer et al. (2015) as characteristic of the footwall of their Angmong fault.

Deformational Features of the Karakoram Fault System

The NW-SE-striking, dextral-oblique slip, Karakoram Fault system generally occupies the valley of the Shyok River east of the Saltoro Range, and separates Karakoram block units from the Karakoram Range proper. Numerous papers have been published describing the Karakoram Fault system and its evolutionary history based on studies undertaken east and southeast of my study area (e.g., Searle et al., 1998; Brown et al., 2002; Phillips et al., 2004; Rolland et al., 2009), and the reader is referred to them for details. Although the earliest deformational fabrics associated with this fault are of Miocene age, it remains active today.

On the extreme eastern edge of the Saltoro Range, along the west bank of the Shyok River, I observed highly strained rocks recognizable as representative of the Karakoram block and SSZ units that contain greenschist-facies tectonite fabrics with

appropriate orientation to have been produced during Karakoram Fault slip. I map these as a distinctive Karakoram Fault zone unit. Rocks in this unit display a strong, subvertical shear fabric striking NW-SW, parallel to the Shyok Valley and inferred general strike of the Karakoram Fault system. Especially in fine-grained, metasedimentary lithologies, the planar fabrics are composite and S-C relationships indicate a component of NE-side up displacement in addition to dextral slip. Earlier fabrics in components of this unit derived from Karakoram block lithologies, Saltoro Formation, Saltoro Molasse, and SSZ Mélange units are transposed into parallelism with the Karakoram Fault shear fabrics, and fabrics of this orientation can be traced for meters to tens of meters across the diffuse SW boundary of the Karakoram shear zone. The youngest structures interpreted to be associated with the Karakoram Fault shear zone are numerous subvertical brittle fault zones with uncertain displacement, found within the Saltoro Range within 10 km of the Nubra River. These structures are oriented parallel to the regional orientation of the Karakoram Fault system.

Geochronology

$^{40}Ar/^{39}Ar$ hornblende and U/Pb zircon geochronology, as well as U/Pb geochronology of detrital zircons, provide constraints on the ages of units and major faults in the field area and the provenance of the Saltoro Molasse. Uncertainties on all new dates presented in this paper are reported at the 2σ (ca. 95%) confidence level. See the Supporting Information section for a description of analytical methods for the geochronologic methods used in this paper and Tables A2 and A3 for run data.

$^{40}Ar/^{39}Ar$ Constraints on the Age of the Shyok Volcanics

My Shyok Volcanic eruptive rock samples contained no magmatic zircon suitable for U/Pb dating. My best available constraint on the age of the unit comes from a $^{40}Ar/^{39}Ar$ hornblende age on one of the cross-cutting hypabyssal dikes (NBUM10-45). The Ar isotopes degassed from twelve incremental heating steps all yielded Early Cretaceous apparent ages, but the release spectrum for this sample does not display a statistically defined plateau age (Figure 2.7). I refer this behavior to be indicative of contamination by a non-radiogenic, or 'excess', ^{40}Ar component (Kelley, 2002). Inverse isochron analysis of the NBUM10-45 data did not allow me to isolate the $^{40}Ar/^{36}Ar$ ratio of the trapped excess component, precluding determination of a precise date for the hornblende. I regard the ^{39}Ar abundance-weighted mean date for all steps in the release spectrum of 125.6 ± 6.1 Ma as my best (but imprecise) estimate for the apparent age of the hornblende. Because metamorphism of the Shyok Volcanics unit was restricted to lower greenschist facies, below the canonical $^{40}Ar/^{39}Ar$ hornblende closure temperature range of ca. 500-600ºC (Harrison, 1981), I interpret this date as a minimum estimate of the igneous age of the Shyok Volcanics succession. Better constraints would require a more exhaustive search for datable zircons in a variety of units in the volcanic succession or the associated dikes.

Detrital U/Pb Zircon Constraints on the Provenance and Age of the Saltoro Molasse

We conducted a detrital zircon U/Pb LA-ICPMS study on sample BCUM12-105 collected from within the Saltoro Molasse in order to constrain its possible provenance and maximum age. This sample is from a sandy layer interpreted to be a channel, with

both overlying and underlying conglomeratic strata. The 166 zircons dated from Saltoro Molasse sample BCUM12-105 range in $^{206}Pb/^{238}U$ age from Late Cretaceous to Neoarchean (Figure 2.8a). The majority of the grains from the sample (n=97) define a single major mode with a mean $^{206}Pb/^{238}U$ age of 92.43±0.24 Ma (Figure 2.8b). This is interpreted to be the oldest possible depositional age of the part of the Saltoro Molasse from which BCUM12-105 was collected. It seems unlikely that the actual depositional age is much younger because presumably post-collisional magmatic activity was ongoing in both the Kohistan-Ladakh and Karakoram blocks by at least 80 Ma (references here, I think, Nathaniel). Unfortunately, the internal stratigraphy of the molasse is not well constrained. However, my sense is that this sample comes from the lower part of the succession. It is plausible, though I think unlikely, that the depositional age of the basal Saltoro Molasse could be older than ca. 92 Ma.

Also shown in Figure 2.8a for comparison are compilations of zircon ages from the published literature for the Karakoram block and the Kohistan-Ladakh arc system in addition new data from this study. I note that the majority of the studies of these potential source regions focused on granitic rocks, and any older country rocks or inheritance are therefore likely underrepresented, skewing the probability density plots for these potential source regions toward younger dates. While the majority of ages from the Kohistan-Ladakh block are younger than the major mode of sample BCUM12-105, this mode overlaps in time with a small but significant mode of bedrock zircon dates from the Kohistan-Ladakh block. It matches less well with the known distribution of zircon ages for the Karakoram block. In fact, at the time of the deposition of the molasse, the ca. 105-90 Ma mode in the Kohistan-Ladakh spectra would have been the most significant mode

for that block, as all other larger modes reported from Kohistan-Ladakh are younger than BCUM12-105. Furthermore, twenty of the grains that form the major mode in sample BCUM12-105 fall in a time span for which there are no zircons of that date reported from the Karakoram block, and there are only three reported zircon grains from the Karakoram block in the date range of 95-85 Ma. I tentatively conclude that the most likely source region for most of the detrital zircons in the youngest mode of the Saltoro Molasse is the Kohistan-Ladakh block, but caution that the bedrock U/Pb zircon database for the Karakoram is sparse compared to those of other potential source regions and the full spectrum of potential Karakoram source region ages may not yet be known.

Both the Karakoram and Kohistan-Ladakh blocks seem viable contributors to the Early Cretaceous through Triassic zircon population present in the Saltoro Molasse. The Kohistan-Ladakh block population does contain a few Cambrian or older zircon grains that may have been the sources for some of the Cambrian or older crystals in the Saltoro Molasse, but a higher proportion of the Karakoram block zircons are Cambrian or Precambrian, making the Karakoram block the most likely source for these older grains. Given that zircons with a Th/U > 0.5 are most likely igneous (Hoskin and Schaltegger, 2003), the dates from BCU12-105 are interpreted to represent igneous activity throughout the entire range of dates represented in the molasse sample (Figure 2.9). Significant numbers of zircons with much lower Th/U also exist, which may indicate that both igneous and metamorphic zircons are included in the population. The similar correlations of Th/U scatter with $^{206}Pb/^{238}U$ date are also seen in the early Paleozoic and Precambrian zircons I dated from Karakoram block samples (see below). Given that: 1) the Saltoro Molasse is deposited on rocks likely originally deposited or erupted within or adjacent to

the Ladakh arc; 2) the most abundant zircons in the studied Saltoro molasse sample appear to come from a Ladakh arc source; and 3) the Karakoram block provides a better match for observed early Paleozoic and Precambrian zircons in the molasse sample, I interpret the Saltoro Molasse to be a post-collisional unit.

U/Pb LA-ICPMS Zircon Bedrock Geochronology

Karakoram Block Paragneiss

Sample NBNU10-41, a sheared Karakoram block paragneiss collected within the Karakoram Fault zone, contained euhedral zircons with both patchy and oscillatory zoning, and – in most examples – direct evidence for overgrowths of rim material on inherited cores. A total of 44 zircon core analyses yielded $^{206}Pb/^{238}U$ dates ranging from ca. 500 to 2600 Ma (Figure 2.10a). The concordance or near-concordance of many of these dates suggests the zircon cores are best interpreted as evidence of the incorporation of a range of Paleoproterozoic-Cambrian detrital zircons in the paragneiss protolith. Seventy-five rim analyses (Figure 2.10b) are scattered along or near concordia from ca. 1000 Ma to roughly 375 Ma. Many of these zircon rims have Th/U $\geq$ 0.5 and are likely igneous, but a significant number have much lower Th/U and may be metamorphic (Figure 2.9). It is thus unclear from the data whether or not these zircon rims are all inherited detrital zircon or if some of the overgrowths could be related to early phases of metamorphism in the Karakoram block. One zircon rim in the large population I analyzed yielded an unusually young (177.0 ± 3.0 Ma) $^{206}Pb/^{238}U$ date and Th/U = 0.02, which I tentatively interpret as indicating prograde metamorphism in the Karakoram block as recently as the Early Jurassic.

Thirty-three zircons from a granite sample ascribed to the Karakoram block (BCUM12-FG; Figure 2.3) yielded a distribution of concordant and near-concordant dates similar to the rim population of Karakoram block sample NBNU10-41 (Figure 2.10c). The sample contained euhedral zircons with both patchy and oscillatory zoning, and – in most examples – direct evidence for overgrowths of rim material on inherited zircon cores. One significant difference is that the 14 youngest grains are concordant with one another, yielding an error-weighted mean $^{206}Pb/^{238}U$ date of 162.8 ± 1.2 Ma (2σ; Figure 2.10d). I interpret this mean date as the crystallization age of the granite, and the older zircons as indicative of inheritance of older igneous and possibly metamorphic zircons. (Figure 2.9). Unfortunately, sample BCUM12-FG was not collected from an outcrop, but instead from a rockslide below an inaccessible outcrop occurring in the hanging wall of the structure I map as the MKT, the Waris thrust (Figure 2.3). The similarity of rock types present in such rockfalls with unquestionable outcrops of the Karakoram block northeast of the Karakoram Fault trace was the primary basis for my interpretation of the rocks above the Waris thrust in the Saltoro Range as belonging to the Karakoram block, but the similarity in inherited or detrital zircon age populations in NBNU10-41 and BCUM12-FG lends credence to that interpretation.

Felsic Aplitic Dike Cutting the Shyok Volcanics-Saltoro Molasse Contact

One sample (BCUM12-146a, collected from sampling locality BCUM12-146 shown on Figure 2.3) was collected from an aplitic dike that cuts the unconformity between the Shyok Volcanics and Saltoro Molasse (Figure 2.11). Zircons from this sample are mostly euhedral and concentrically zoned. Three of these zircon grains were

U/Pb LA-ICPMS dated, one with a distinctive core and two with no obvious cores. A total of five core and rim $^{206}Pb/^{238}U$ analyses from the three zircons yielded statistically indistinguishable dates. In fact, the data for all zircons from this sample are concordant (Figure 2.10e), yielding a mean $^{206}Pb/^{238}U$ date of 85.2 ± 3.8 Ma (Figure 2.10f). I interpret this date as the igneous age of the dike from which BCUM12-146a was collected and also, due to the cross-cutting relationship between the dike and the Shyok Volcanics-Saltoro Molasse unconformity, a minimum bound of the age of the Saltoro Molasse. Coupled with the ca. 92 Ma minimum age of detrital zircons in the molasse reported above, this date is consistent with Saltoro Molasse deposition beginning in the early Late Cretaceous.

Granites Intruding the SSZ

Two samples of granites cutting SSZ lithologies were collected for U/Pb geochronology: BCUM12-97, which intrudes the Shyok Volcanics unit, and BCUM12-135, which intrudes the Saltoro Formation (Figure 2.3). Both contained euhedral, concentrically zoned zircons, but only sample BCUM12-135 contained some crystals with obvious inherited cores. BCUM12-97 zircons are concordant (Figure 2.12a), and 24 $^{206}Pb/^{238}U$ dates for these zircon crystals have statistically indistinguishable results (Figure 2.12b) with a mean of 84.79 ± 0.68 Ma, which is interpreted to be the intrusive age of this granite. Although sample BCUM12-135 zircon cores yield Mesoproterozoic dates (Figure 2.12c), the majority (n = 23) of the $^{206}Pb/^{238}U$ zircon dates in this rock are statistically indistinguishable with a mean of 86.05 ± 0.67 Ma (Figure 2.12d), which is the interpreted igneous age of this body. These granites, in addition to the 85.2 ± 3.8 Ma

aplite dike sample (BCUM12-146a) also dated, suggest that Late Cretaceous (80-90 Ma) felsic igneous activity was widespread across all elements of the SSZ, providing a minimum age for amalgamation of the units within the suture zone. The Tirit Granite (Figure 2.3), for which Upadahay (2008) reported a 71.40 ± 0.36 Ma (2σ) TIMS U/Pb zircon age and Weinberg et al. (2000) reported a 68 ± 1 Ma (2σ) ion microprobe U-Pb zircon age, appears to be indicative of even more recent Cretaceous magmatism. There is no geochronologic evidence at present that plutons of equivalent age to the main Paleocene-Eocene intrusive phase of the Ladakh batholith occur in the SSZ.

Late Granodiorite Intruding the Karakoram Block

The youngest intrusive rock encountered in my study (NBWA10-95; Figure 2.3) is an undeformed granodiorite that intrudes older rocks of the Karakoram block and is cut by the Waris thrust. Eighteen euhedral zircons showing oscillatory zoning from this sample were dated. They yielded statistically indistinguishable $^{206}Pb/^{238}U$ results with a mean of 42.0 ± 1.7 Ma (Figure 2.12e), which I interpret as the rock's crystallization age; all zircons from this sample have Th/U > 0.5, indicating an igneous origin (Figure 2.9). The fact that this granodiorite is cut by the Waris thrust confirms that the thrust is one of the youngest structures in the study area, cut only by the Karakoram Fault system.

DISCUSSION AND CONCLUSIONS

Prior to tectonic activity on the Shyok suture zone, the major non-oceanic crustal elements currently exposed to the southwest and northeast (Ladakh and Karakoram, respectively) were separated by part of the Neotethys ocean basin. Although Late

Cretaceous-Miocene igneous activity in the Ladakh Range apparently took place in a continental arc environment (St-Onge et al., 2010), several researchers interpret older igneous activity in Ladakh and the correlative Kohistan arc to the west as happening in an oceanic arc environment (e.g., Burg, 2011; Bouilhol et al., 2013). I follow this argument in postulating that the Shyok suture zone manifests docking of this island arc with a Eurasian margin characterized by the Karakoram continental arc. My U/Pb geochronologic data from Karakoram block elements in the Saltoro Range confirm that this arc was well established by Early-Middle Jurassic times.

Most rock packages in the SSZ of the Saltoro Range represent volcanic and sedimentary rocks deposited in a near-marine or marine environment (Shyok Volcanics and Saltoro Formation), or rocks interpreted as indicative of either a subduction complex or a tectonic unit related to suturing (the Mélange unit). As noted above, research in the along-strike equivalent of the SSZ in Pakistan led Robertson and Collins (2002) to propose that likely equivalents of my Shyok Volcanics and Saltoro Formation (their Pakora formation) were deposited in a proximal back-arc basin environment of the Kohistan-Ladakh island arc, and I find such an interpretation equally suitable for the Saltoro Range exposures. Unfortunately, the eruptive age of the Shyok Volcanics is only constrained to $\geq 125.6 \pm 6.1$ (2σ) Ma by a $^{40}Ar/^{39}Ar$ date on an apparently igneous amphibole from a hypabyssal dike intrusive cutting that unit. I infer, however, that this dike intruded late in the eruptive history of the Shyok Volcanics, such that the volcanic unit is quite likely Early Cretaceous in age. My data provide no direct constraints on the age of the overlying Saltoro Formation in the Saltoro Range, but fossils identified by

Upadhyay (2014) suggest that deposition was ongoing over at least a portion of the Albian-Aptian interval.

At first glance, Cretaceous ages for the Shyok Volcanic unit and the Saltoro Formation might suggest a closer affinity of these units to the Karakoram block rather than the Kohistan-Ladakh block. However, both Rolland et al. (2000) and Robertson and Collins (2002) identified a similar succession immediately to the west that they correlated with the Kohistan-Ladakh block. These authors, as well as Upadyay (2014) and Weinberg et al. (2000), explicitly interpreted the Shyok Volcanics unit and Saltoro Formation as having formed in association with the Kohistan-Ladakh block. This interpretation is supported by some additional geological evidence in my field area. The Shyok Volcanics unit and the Saltoro Formation are separated from the Ladakh block by the steeply dipping Khalsar thrust. Barring significant rotation of that structure after its activity – something for which I have no evidence – it seems unlikely that the displacement on that structure was large enough to juxtapose units deposited near the Karakoram block against the Kohistan-Ladakh block. In light of the fact that I have no evidence from my study area to the contrary, I accept the interpretations of previous workers that the Shyok Volcanics unit and Saltoro Formation constitute some of the oldest preserved portion of the Kohistan-Ladakh block, and are not part of the Karakoram block.

If my interpretation is correct that marine units of the Shyok Volcanics and Saltoro Formation are Cretaceous, the age of suturing of the Kohistan-Ladakh arc to Eurasia can be no older that Early Cretaceous. A minimum age constraint is provided by the Saltoro Molasse, which is interpreted as largely or completely deposited in a post-

suturing continental environment. Unless existing zircon datasets for the Kohistan-Ladakh and Karakoram arcs are not indicative of the complete range of zircon U/Pb dates from the two distinctive crustal blocks, the simplest interpretation of the detrital zircon suite in the studied sample of the Saltoro Molasse (BCUM12-105) is that the molasse has a mixed zircon provenance from both Kohistan-Ladakh and the Karakoram even though the age distribution for my sample does not perfectly match that of either potential source block. The youngest U/Pb detrital zircon sub-population within sample BCUM12-105 implies deposition of most or all of the Saltoro Molasse at or after ca. 92 Ma, whereas the ca. 85 Ma $^{206}Pb/^{238}U$ date of a cross-cutting dike (BCUM12-146a) provides a minimum age. Following this line of reasoning, the Shyok suturing event must be no younger than Late Cretaceous (Santonian-Turonian). While this model is consistent with all of my data and the presently available and published zircon U/Pb datasets for both the Karakoram and Kohistan-Ladakh blocks, it must be noted that the datasets for both blocks are still sparse, and future datasets will be needed to further evaluate the model. A Cretaceous age for the Shyok suture zone is consistent with conventional wisdom (e.g., Clift et al., 2002; Petterson and Windley, 1985; Treloar et al., 1989; Searle, 1991; Searle et al., 1997; Robertson and Collins, 2002; Burtman, 2010; Rehman et al., 2011; Thanh et al., 2012), but it is inconsistent with two recent papers arguing for a ca. 50 or ca. 40 Ma age. Khan et al. (2009) inferred that the Kohistan-Ladakh intraoceanic arc collided with India at ca. 65-61 Ma, and Kohistan-Ladakh-India collided at ca. 50 Ma with the southern margin of Eurasia along the Shyok suture. To support this interpretation, they inferred that paleomagnetic data from India placed the Kohistan-Ladakh arc and the northern Indian margin near the equator at ca. 65-61 Ma, far south of the southern margin of Eurasia.

More recently, Bouilhol et al. (2013) employed U/Pb geochronology and the evolution of Hf, Nd, and Sr isotopic signatures with time in Kohistan-Ladakh plutonic rocks to argue instead for ca. 50 Ma collision of Kohistan-Ladakh with India, followed by ca. 40 Ma closure along the Shyok suture.

Neither the Khan et al. (2009) or Bouilhol et al. (2013) models can be reconciled with my data, which appear to imply that the continental Saltoro Molasse began to be deposited across the Shyok suture in the Late Cretaceous. Is there an alternative interpretation of my data that might eliminate this inconsistency? While the Saltoro Molasse was certainly not deposited in an oceanic setting and I infer from my detrital zircon U/Pb data that it contains sediment shed from both the Karakoram and Kohistan-Ladakh blocks, an argument could be made that existing U/Pb zircon datasets from these blocks are not yet sufficiently comprehensive to permit definitive provenance interpretations for this molasse. For example, a later collision between Kohistan-Ladakh and the Karakoram might be possible if the Saltoro Molasse was deposited on an emergent part of the Kohistan-Ladakh block, and that block contained an as-yet uncharacterized source for the Precambrian zircons in the molasse. Further evaluation of such possibilities will require more spatially comprehensive mapping of U/Pb age variations in the Karakoram and Ladakh blocks.

At the same time, there are good reasons for objective skepticism about models that invoke a Tertiary age for Shyok suturing. The Khan et al. (2009) model depends heavily on a paleolatitude estimate for the Kohistan arc derived from previously published paleomagnetic data for Paleocene volcanic rocks in northern Pakistan (Ahmed et al., 2000). Unfortunately, those data were obtained from deformed and remagnetized

rocks, calling into question the robustness of the estimated paleolatitude and the authors' rough estimate of the timing of the remagnetization event. Additionally, the Khan et al. (2009) model fails to take into account paleomagnetic evidence that is suggestive that Kohistan-Ladakh arc and Eurasia were close to each other in the middle to Late Cretaceous (Rehman et al., 2011; Zaman and Torii, 1999). It is fair to say that the Cretaceous-early Cenozoic paleolatitudes of the Kohistan-Ladakh arc remain very poorly constrained at present. In my opinion, any robust paleomagnetic model for timing of the Shyok suture needs to incorporate data from the Karakoram block, for which there are scant data.

The Bouilhol et al. (2013) model interprets a distinctive change in Ladakh arc isotopic geochemistry at ca. 40 Ma – indicative of a greater component of crustal contamination – as unambiguously related to southward underthusting of the Karakoram block beneath the Kohistan-Ladakh block during Shyok suturing. Indeed, direct field evidence exists for some limited degree of southward underthrusting of suture zone lithologies in the Saltoro Range beneath the Ladakh block along the Khalsar thrust (Figure 2.3). However, if this – or a similarly oriented structure – carries Karakoram rocks deeply enough to contaminate the source regions of Ladakh plutons after 40 Ma, it could have easily done so long after Shyok suturing. An even simpler explanation for the change in isotopic signature might be that it marks the arrival of Indian continental lithosphere within or above the Ladakh magma source area, especially inasmuch as most published models for the evolution of this part of the Himalaya feature collision of the Indian and Eurasian plates as well as ultrahigh pressure metamorphism of India's leading edge only ten or so million years earlier (e.g., Donaldson et al., 2013; Najman, et al.,

2010; St-Onge, et al., 2013). Similar Cretaceous-middle Tertiary geochemical transitions have been documented for the Gangdese arc in southern Tibet, and those have been interpreted as indicative of Indian plate crustal contamination or partial melting (e.g., Jiang et al., 2014)). On balance, I regard the Cretaceous age for the Shyok suture indicated by my study as being more consistent with regional geological constraints than either of the Tertiary ages proposed by Khan et al. (2009) and Bouilhol et al. (2013). If correct, my interpretation lends support to more traditional models of the Cretaceous-early Tertiary collisional history of this sector of the Himalaya, which hold that: 1) the early Kohistan-Ladakh island arc was incorporated into the southern margin of Eurasia in the Cretaceous and afterwards evolved as a continental arc over a north-facing subduction zone; and 2) final closure of the Neo-Tethys ocean occurred along the Indus suture to the south (Figure 2.13).

Existing geochronologic data from NW India suggest that Cretaceous accretion of the Ladakh arc may have resulted in a temporary reduction in activity within the Karakoram arc, but a northward expansion of igneous activity beyond the Ladakh Range and into the Shyok suture zone, accounting for the Tirit Granite and other bodies described and dated as part of my study. Such expansion is consistent with a model in which the subduction angle beneath the Ladakh arc flattened and the subduction rate increased in order to accommodate an additional component of India-Eurasia convergence rate after cessation of subduction beneath the Karakoram.

Apparent confirmation of a Cretaceous age for the Shyok suture strongly suggest that this suture is correlative with the similarly aged Bangong suture of central Tibet (Kapp et al., 2007; Liu et al., 2014), but not the Cenozoic Yarlung suture (Najman et al.,

2010). This correlation supports traditionally accepted tectonic scenarios in which a continuous, 'Transhimalayan', Andean-type arc system characterized the southern margin of Eurasia and accommodated northward subduction of the Neo-Tethys ocean basin prior to India-Eurasia collision (e.g., Hodges, 2000)). Today the remnants of this system are preserved as Late Cretaceous-Paleocene, intrusive and extrusive igneous rocks of the Gangdese arc in southern Tibet and the Kohistan-Ladakh arc in NW India and Pakistan.

Correlation of the Shyok and Bangong sutures across the Karakoram Fault constrain the total slip on that structure. I note that the SSZ immediately southeast of my study area includes two distinctive belts of ophiolitic material, truncated by the Karakoram Fault, which have similar appearance to two belts of what has been mapped by others (Kapp et al., 2003; Liu et al.,2014) as 'ophiolitic mélange' in the Bangong suture, where the southern of the two ophiolite bearing belts is sometimes referred to as the Shequanhe suture. These belts are also truncated by the Karakoram Fault in such a way as to suggest correlation with the belts in the Shyok suture zone (Figure 2.14). Matching the northernmost of these belts across the fault suggests an approximate total offset of ca. 130 km. The same exercise using the southernmost belts suggests an offset of ca. 190 km. The range in offsets likely results from contractional deformation, such as along the MKT, that postdates the initiation of the Karakoram Fault. These estimates can be compared with previous estimates of maximum Karakoram Fault offset ranging from ca. 120 km to ca. 200 km (Searle, 1996; Searle et al., 1998; Lacassin et al., 2004).

ACKNOWLEDGMENTS

We gratefully acknowledge that funding for the research reported here was provided by the U.S. National Science Foundation through awards EAR 1007929 (Tectonics) and EAR 0642731 (Sedimentary Geology and Paleobiology). I thank the Arizona LaserChron Center, supported by NSF-EAR 1338583, for use of their facilities, and C.P. Dorjay for field and logistical support. Associate Editor Paul Kapp and two anonymous reviewers provided useful feedback on the initial submission of this paper that substantially improved the final version.

FIGURE CAPTIONS

Figure 2.1. Regional tectonic sketch map, redrawn after Yin and Harrison (2000). MKT is the Main Karakoram thrust.

Figure 2.2. (a) Google Earth (map data: Google, CNES/Astrium, DigitalGlobe) image of the study area with major geographic features labeled. (b) Decorrelation stretched Landsat image of the study area which has the same field of view as Figure 2.2a

Figure 2.3. Geologic map and cross section of the Shyok suture zone, with the same field of view as Figure 2.2a-b. Unit colors are the same in the map and cross section, and there is no vertical exaggeration.

Figure 2.4: Schematic tectonic stratigraphy showing the relative positions of major units seen in the mapping area (a) within the Saltoro Range and (b) near the town of Skuru on the northern margin of the Ladakh batholith.

Figure 2.5. Classification diagrams for the Shyok Volcanics unit after (a) Winchester and Floyd (1977), (b) Hastie et al. (2007), and (c) Hollacher et al. (2012). Black squares are data from Shyok Volcanics rocks analyzed for my study.

Figure 2.6. Trace element geochemistry for the Shyok Volcanics (black) and ophiolites from within the SSZ (grey). Data from this study and Thanh et al. (2012), respectively.

Figure 2.7. $^{40}Ar/^{39}Ar$ step heating age spectrum, Ca/k Ratios and, percent radiogenic ^{40}Ar ($^{40}Ar^*$) for hornblende sample NBUM10-45, sampled from a dike within the Shyok Volcanics. The box heights shown for individual steps represent 2σ errors.

Figure 2.8. (a) Probability density plot for U/Pb zircon dates from the Karakoram and Kohistan-Ladakh blocks and the Saltoro Molasse. The plots are normalized such that the total area under curves is equal. Karakoram data (n=331) are taken from bedrock and detrital samples from active drainages from Fraser et al. (2001), Hueberger et al. (2007), Jain and Singh (2008), Lukens et al. (2012), Parrish et al. (1989), Phillips et al. (2004), Ravikant et al. (2009), Weinberg et al. (2000), and this study. Kohistan-Ladakh data (n=1342) is from bedrock supplied by Bosch et al. (2011), Bouihol et al. (2011), Bouilhol et al. (2013), Hueberger et al. (2007), Jagoutz et al. (2009), Khan et al. (2009), Ravikant

et al. (2009), and Sen et al. (2013). BCUM12-105 (n=166) data is from a detrital bedrock sample from the Saltoro Molasse within the SSZ. Grey boxes highlight the ages of peaks discussed in the main text. (b) Mean U/Pb age for the youngest zircon population in BCUM12-105; black horizontal line is shown at the mean age for the population.

Figure 2.9. Th/U vs. $^{206}Pb/^{238}U$ date plot for all zircon analyses from Saltoro Molasse sample BCUM12-105 and Karakoram block samples NBNU10-41,BCUM12-FG, and NBWA10-95. The horizontal red line is at Th/U = 0.5, above which zircons are most likely magmatic in origin (Hoskin and Schaltegger, 2003).

Figure 2.10. U/Pb zircon data from the SSZ. (a) Concordia diagram for cores from Karakoram affinity schist sample NBNU10-41. (b) Concordia diagram for rims from NBNU10-41. (c) Concordia diagram for all grains from Karakoram affinity granitic rockfall sample BCUM12-FG. (d) Mean age and dates for youngest population from BCUM12-FG. (e) Concordia diagram for all analyses from SSZ intruding dike sample BCUM12-146a. (f) Mean age and dates for all analyses from BCUM12-146a.

Figure 2.11. Field photo showing sampling site 146. The field of view looks west slopes away at a ca. 45° angle. The dike is ca. 4 m wide where it enters the Saltoro Molasse. Call-out shows the sampling location of for BCUM12-146a with geologist for scale.

Figure 2.12. (a) Concordia diagram for all grains from SSZ intruding granitic sample BCUM12-97. (b) Mean age and dates for all grains from BCUM12-97. (c) Concordia

diagram for all grains from SSZ intruding granitic sample BCUM12-135. (d) Mean age and dates for youngest population from BCUM12-135. (e) Mean age and dates for all grains from Karakoram affinity granitic sample NBWA10-95.

Figure 2.13. Tectonic cartoon showing my model for the timing of the formation of the SSZ.

Figure 2.14. My preferred offsets along the Karakoram Fault correlating ophiolitic segments of the SSZ and Bangong suture zone superimposed over Google Earth imagery, with zones/boundaries of possible correlation labeled. The position of this figure is shown in Figure 1. 1: The Waris thrust (MKT) and northern ophiolitic mélange zone in the SSZ. 2: The Khalsar thrust and the southern ophiolitic mélange zone in the SSZ. 3: Northern extent of the Bangong suture zone as mapped by Phillips (2008) and Van Buer et al. (2015). 4: Northern extent of ophiolitic mélange extended to the west from Kapp et al. (2003) and Liu et al. (2014) and also the southern extent of the Bangong suture zone from Phillips (2008) and Van Buer et al. (2015). 5: Southern extent of ophiolitic mélange extended to the west from Kapp et al. (2003) and Liu et al. (2014). 6: Northern extent of ophiolitic mélange in the Shequanhe suture zone from Kapp et al. (2003). 7: Southern extent of ophiolitic mélange in the Shequanhe suture zone from Kapp et al. (2003). 8: Karakoram Fault. The offset of 130 km corresponds to the position of the Waris thrust and associated ophiolitic mélange within the SSZ and out proposed correlation to the northernmost mapped extent of ophiolitic mélange within the Bangong suture zone. The offset of 190 km corresponds to the position of the Khalsar and associated ophiolitic

mélange within the SSZ and out proposed correlation to the northernmost mapped extent of ophiolitic mélange within the Shequanhe suture segment of the Bangong suture zone.

REFERENCES

Ahmed, M. N.; Yoshida, M.; Yoshiki, F., 2000, Paleomagnetic study of Utror volcanic formation; remagnetizations and postfolding rotations in Utror area, Kohistan arc, northern Pakistan, Earth, Planets and Space, 52, 425–36.

Aitchison, J.C.; Xia, X.; Baxter, A.T.; Ali, J.R., 2011, Detrital zircon U-Pb ages along the Yarlung-Tsangpo suture zone, Tibet: Implications for oblique convergence and collision between India and Asia, Gondwana Research, 20, 691-709, 10.1016/j.gr.2011.04.002.

Allen, T.; Chamberlain, C.P., 1991, Metamorphic evidence for an inverted crustal section, with constraints on the Main Karakoram thrust, Baltistan, northern Pakistan, Journal Of Metamorphic Geology, JUL, 9, 4, 403-418, 10.1111/j.1525-1314.1991.tb00535.x.

Bosch, D.; Garrido, C.J.; Bruguier, O.; Dhuime, B.; Bodinier, J.-L.; Padron-Navarta, J.A.; Galland, B., 2011, Building an island-arc crustal section: Time constraints from a LA-ICP-MS zircon study, Earth and Planetary Science Letters, 309, 268-279, 10.1016/j.epsl.2011.07.016.

Bouilhol, P.; Jagoutz, O.; Hanchar, J.M.; Dudas, F.O., 2013, Dating the India-Eurasia collision through arc magmatic records, Earth and Planetary Science Letters, 366, 163-175, 10.1016/j.epsl.2013.01.023.

Bouilhol, P.; Schaltegger, U.; Chiaradia, M.; Ovtcharova, M.; Stracke, A.; Burg, J.-P.; Dawood, H., 2011, Timing of juvenile arc crust formation and evolution in the Sapat Complex (Kohistan-Pakistan), Chemical Geology, 280, 243-256, 10.1016/j.chemgeo.2010.11.013.

Brown, E. T.; Bendick, R.; Bourles, D. L.; Gaur, V.; Molnar, P.; Raisbeck, G. M.; Yiou, F., 2002, Slip rates of the Karakorum fault, Ladakh, India, determined using cosmic ray exposure dating of debris flows and moraines, Journal of Geophysical Research-Solid Earth, 107, B9.

Burg, J.P., 2011, The Asia–Kohistan–India collision. Review and discussion, In: Brown, D., Ryan, P. D. (Eds.), Arc-Continent Collision, Springer, Berlin Heidelberg, 279-309.

Burtman, V. S., 2010, Tien Shan, Pamir, and Tibet: History and geodynamics of Phanerozoic oceanic basins, Geotectonics, 44, 5, 388-404.

Clift, P.D.; Hannigan, R.; Blusztajn, J.; Draut, A.E.; 2002, Geochemical evolution of the Dras-Kohistan Arc during collision with Eurasia; evidence from the Ladakh Himalaya, India, Island Arc, 11, 4, 255-273.

Cooper, F. J.; Adams, B. A.; Edwards, C. S.; Hodges K.V., 2012, Large normal-sense displacement on the South Tibetan fault system in the eastern Himalaya, Geology, 40, 11, 971-974, 10.1130/G33318.1.

Crawford, M.B.; Searle, M.P., 1992, Field Relationships and Geochemistry of Pre-collisional (India-Asia) Granitoid Magmatism in the Central Karakoram, Northern Pakistan, Tectonophysics, 206, 171-192, 10.1016/0040-1951(92)90375-G.

DeCelles, P. G.; Kapp, P.; Gehrels, G. E.; Ding, L., 2014, Paleocene-Eocene foreland basin
evolution in the Himalaya of southern Tibet and Nepal: Implications for the age of initial India-Asia collision, Tectonics, 33, 5, 824-849.

Donaldson, D.G.; Webb, A.A.G.; Menold, C.A.; Kylander-Clark, A.R.C.; Hacker, B.R., 2013, Petrochronology of Himalayan ultrahigh-pressure eclogite, Geology, 41, 8, 835-838, DOI:10.1130/G33699.1.

Ehiro, M.; Kojima, S.; Sato, T.; Ahmad, T.; Ohtani, T., 2007, Discovery of Jurassic ammonoids from the Shyok suture zone to the northeast of Chang La pass, Ladakh, northwest India and its tectonic significance, Island Arc, 16, 124-132, doi:10.1111/j.1440-1738.2007.00562. x.

Fraser, J.E.; Searle, M.P.; Parrish, R.R.; Noble, S.R., 2001, Chronology of deformation, metamorphism, and magmatism in the southern Karakoram mountains, Geological Society of America Bulletin, 113, 1443-1455, 10.1130/0016-7606(2001)113<1443:CODMAM>2.0.CO;2.

Dunlap, W.J.; Wysoczanski, R., 2002, Thermal evidence for early Cretaceous metamorphism in the Shyok suture zone and age of the Khardung volcanic rocks, Ladakh, India, Journal Of Asian Earth Sciences, 20, 5, 481, 490, PII S1367-9120(01)00042-6, 10.1016/S1367-9120(01)00042-6.

Harrison, T. M., 1981, Diffusion of ^{40}Ar in hornblende, Contributions to Mineralogy And Petrology, 78, 324-331.

Hastie, A. R.; Kerr, A.C.; Pearce, J.A.; Mitchell, S.F., 2007, Classification of altered volcanic island arc rocks using immobile trace elements: Development of the Th-Co discrimination diagram, Journal of Petrology, 48, 2341-2357, 10.1093/petrology/egm062.

Heuberger, S.; Schaltegger, U.; Burg, J.-P.; Villa, I.M.; Frank, M.; Dawood, H.; Hussain, S.; Zanchi, A., 2007, Age and isotopic constraints on magmatism along the Karakoram-Kohistan Suture Zone, NW Pakistan: evidence for subduction and continued convergence after India-Asia collision, Swiss Journal of Geosciences, 100, 85-107, 10.1007/s00015-007-1203-7.

Hodges, K.V., 2000, Tectonics of the Himalaya and southern Tibet from two perspectives, Geological Society of America Bulletin, 112, 324-350, 10.1130/0016-7606(2000)112<0324:TOTHAS>2.3.CO;2.

Hollocher, K.; Robinson, P.; Walsh, E.; Roberts, D., 2012, geochemistry of amphibolite-facies volcanics and gabbros of the Storen nappe in extensions west and southwest of Trondheim, western gneiss region, Norway: a key to correlations and paleotectonic settings, American Journal of Science, 312, 357-416, 10.2475/04.2012.01.

Horton, F.; Leech, M.L., 2013, Age and origin of granites in the Karakoram shear zone and Greater Himalaya Sequence, NW India, Lithosphere, 5, 300-320, 10.1130/L213.1.

Hoskin, P.W.O.; Schaltegger, U., 2003, The composition of zircon and igneous and metamorphic petrogenesis, Reviews in Mineralogy and Geochemistry, 53, 27-62, 10.2113/0530027.

Jagoutz, O.E.; Burg, J.-P.; Hussain, S.; Dawood, H.; Pettke, T.; Iizuka, T.; Maruyama, S., 2009, Construction of the granitoid crust of an island arc part I: geochronological and geochemical constraints from the plutonic Kohistan (NW Pakistan), Contributions To Mineralogy and Petrology, 158, 739-755, 10.1007/s00410-009-0408-3.

Jagoutz, O.; Royden, L.; Holt, A. F.; Becker, T. W., 2015, Anomalously fast convergence of India and Eurasia caused by double subduction, Nature Geoscience, 8, 475-478.

Jain, A.K.; Singh, S., 2008, Tectonics of the southern Asian plate margin along the Karakoram Shear Zone: Constraints from field observations and U-Pb SHRIMP ages, Tectonophysics, 451, 186-205, 10.1016/j.tecto.2007.11.048.

Jiang, Z. Q., Wang, Q., Wyman, D. A., Li, Z. X., Yang, J. H., Shi, X. B., Ma, L., Tang, G. J., Gou, G. N., Jia, X. H., and Guo, H. F., 2014, Transition from oceanic to continental lithosphere subduction in southern Tibet: Evidence from the Late Cretaceous-Early Oligocene (~ 91-30 Ma) intrusive rocks in the Chanang-Zedong area, southern Gangdese, Lithos, 196, 213-231.

Ji, W.-Q.; Wu, F.-Y.; Chung, S.-L.; Li, J.-Xi.; Liu, C.-Z., 2009, Zircon U-Pb geochronology and Hf isotopic constraints on petrogenesis of the Gangdese batholith, southern Tibet, Chemical Geology, 262, 3-4, 229, 245, 10.1016/j.chemgeo.2009.01.020.

Jolliffe, I.T., 2002, Principal Component Analysis, 2nd edition, Springer, New York, 32 p.

Juyal, K.P., 2006, Foraminiferal biostratgraphy of the Early Cretaceous Hundiri Formation, lower Shyok area, eastern Karakoram, India, Current Science, 91, 1096-1101.

Kapp, P.; DeCelles, P.G.; Gehrels, G.E.; Heizier, M.; Ding, L., 2007, Geological records of the Lhasa-Qiangtang and Indo-Asian collisions in the Nima area of central Tibet, Geological Society of America Bulletin, 119, 917-932, 10.1130/B26033.1.

Kapp, P.; Murphy, M.A.; Yin, A.; Harrison, T.M.; Ding, L.; Guo, J.H., 2003, Mesozoic and Cenozoic tectonic evolution of the Shiquanhe area of western Tibet, Tectonics, JUL 9, 22, 4, 1029, 10.1029/2001TC001332.

Kelley, S, 2002, Excess argon in K-Ar and Ar-Ar geochronology, Chemical Geology, 188, 1-2, 1-22, PII S0009-2541(02)00064-5, 10.1016/S0009-2541(02)00064-5.

Khan, S.D.; Walker, D.J.; Hall, S.A.; Burke, K.C.; Shah, M.T.; Stockli, L., 2009, Did the Kohistan-Ladakh island arc collide first with India?, Geological Society of America Bulletin, 121, 366-384, 10.1130/B26348.1.

Lacassin, R., Valli, F., Arnaud, N., Leloup, P. H., Paquette, J. L., Haibing, L., Tapponnier, P., Chevalier, M. L., Guillot, S., Maheo, G., and Xu, Z. Q., 2004, Large-scale geometry, offset and kinematic evolution of the Karakorum fault, Tibet, Earth and Planetary Science Letters, 219, 3-4, 255-269.

Lister, G. S.; Snoke, A. W., 1984, S-C mylonites, Journal of Structural Geology, 6, 617-638.

Liu, W.-L.; Xia, B.; Zhong, Y.; Cai, J.-X.; Li, J.-F.; Liu, H.-F.; Cai, Z.-R.; Sun, Z.-L., 2014, Age and composition of the Rebang Co and Julu ophiolites, central Tibet: implications for the evolution of the Bangong Meso-Tethys, International Geology Review, 56, 430-447, 10.1080/00206814.2013.873356.

Lukens, C.E.; Carrapa, B.; Singer, B.S.; Gehrels, G., 2012, Miocene exhumation of the Pamir revealed by detrital geothermochronology of Tajik Rivers, Tectonics, 31, TC2014, 10.1029/2011TC003040.

McDermid, I.R.C.; Aitcheson, J.C.; Davis, A.M.; Harrison, T.M.; Grove, M.; 2002, The Zedong terrane: a Late Jurassic intra-oceanic magmatic arc within the Yarlung-Tsangpo suture zone, southeastern Tibet, Chemical Geology, 187, 267-277.

Najman, Y., Appel, E., Boudagher-Fadel, M., Bown, P., Carter, A., Garzanti, E., Godin, L., Han, J. T., Liebke, U., Oliver, G., Parrish, R., and Vezzoli, G., 2010, Timing of India-

Asia collision: Geological, biostratigraphic, and palaeomagnetic constraints, Journal of Geophysical Research-Solid Earth, 115, doi: 10.1029/2010jb007673.

Parrish, R.R.; Tirrul, R., 1989, U-Pb age of the Baltoro granite, northwest himalaya, and implications for monazite U-Pb systematics, Geology, 17, 1076-1079, 10.1130/0091-7613(1989)017<1076:UPAOTB>2.3.CO;2

Petterson, M. G., and Windley, B. F., 1985, Rb-Sr dating of the Kohistan arc-batholith in the Trans-Himalaya of north Pakistan, and tectonic implications, Earth and Planetary Science Letters, 74, 45-57.

Phillips, R.J.; Parrish, R.R.; Searle, M.P., 2004, Age constraints on ductile deformation and long-term slip rates along the Karakoram Fault zone, Ladakh, Earth and Planetary Science Letters, 226, 305-319, 10.1016/j.epsl.2004.07.037.

Phillips, R.J., 2008, Geological map of the Karakoram Fault zone, Eastern Karakoram, Ladakh, NW Himalaya, Journal Of Maps, 21-37

Phillips, R. J.; Searle, M. P., 2007, Macrostructural and microstructural architecture of the Karakoram Fault: Relationship between magmatism and strike-slip faulting, Tectonics, 26, 3, doi: 10.1029/2006tc001946.

Rai, H., 1982, Geological evidence against the Shyok palaeo-suture, Ladakh Himalaya, Nature, 297, 142, 144, 10.1038/297142a0

Rao, D.R.; Rai, H., 2009, Geochemical Studies of Granitoids from Shyok Tectonic Zone of Khardung-Panamik Section, Ladakh, India, Journal of the Geological Society of India, 73, 553-566.

Ravikant, V.; Wu, F.-Y.; Ji, W.-Q., 2009, Zircon U-Pb and Hf isotopic constraints on petrogenesis of the Cretaceous-Tertiary granites in eastern Karakoram and Ladakh, India, Lithos, 110, 153-166, 10.1016/j.lithos.2008.12.013.

Raz, U.; Honegger, K., 1989, Magmatic and tectonic evolution of the Ladakh block from field studies, Tectonophysics, 161, 107, 118, 10.1016/0040-1951(89)90306-5

Rehman, H.U.; Seno, T.; Yamamoto, H.; Khan, Tahseenullah, 2011, Timing of collision of the Kohistan-Ladakh Arc with India and Asia: Debate, Island Arc, 20, 308-328, 10.1111/j.1440-1738.2011.00774.x.

Rex, A. J.; Searle, M. P.; Tirrul, R.; Crawford, M.B.; Prior, D.J.; Rex, D. C.; Barnicoat, A., 1988, The geochemical and tectonic evolution of the central Karakoram, North Pakistan, Philosophical Transactions of the Royal Society of London, 326, 229-255.

Robertson, A.H.F.; Collins, A.S., 2002, Shyok Suture Zone, N Pakistan: late Mesozoic-Tertiary evolution of a critical suture separating the oceanic Ladakh Arc from the Asian continental margin, Journal of Asian Earth Sciences, 20, 309-351, 10.1016/S1367-9120(01)00041-4.

Rolland, Y.; Maheo, G.; Pecher, A.; Vila, I. M., 2009, Syn-kinematic emplacement of the Pangong metamorphic and magmatic complex along the Karakorum Fault (N Ladakh), Journal of Asian Earth Sciences, 34, 1, 10-25.

Rolland, Y.; Pecher, A.; Picard, C., 2000, Middle Cretaceous back-arc formation and arc evolution along the Asian margin: the Shyok Suture Zone in northern Ladakh (NW Himalaya), Tectonophysics, 325, 145-173, 10.1016/S0040-1951(00)00135-9.

Rowley, D.B., 1996, Age of initiation of collision between India and Asia: A review of stratigraphic data, Earth and Planetary Science Letters, DEC, 145, 1-4, 1-13, 10.1016/S0012-821X(96)00201-4.

Schwab, M; Ratschbacher, L; Siebel, W; McWilliams, M.; Minaev, V.; Lutkov, V.; Chen, F.K.; Stanek, K.; Nelson, B.; Frisch, W.; Wooden, J.L., 2004, Assembly of the Pamirs: Age and origin of magmatic belts from the southern Tien Shan to the southern Pamirs and their relation to Tibet, Tectonics, 23, 4, TC4002, 10.1029/2003TC001583.

Searle, M. P., 1991, Geology and Tectonics of the Karakoram Mountains, John Wiley & Sons, Chichester, U.K.

Searle, M.P., 1996, Geological evidence against large-scale pre-Holocene offsets along the Karakoram Fault: Implications for the limited extrusion of the Tibetan plateau, Tectonics, 15, 171-186, 10.1029/95TC01693.

Searle, M.P.; Tirrul, R., 1991, Structural and thermal evolution of the Karakoram crust, Journal of the Geological Society, 148, 65-82, 10.1144/gsjgs.148.1.0065.

Searle, M., Corfield, R. I., Stephenson, B., and McCarron, J., 1997, Structure of the North Indian continental margin in the Ladakh-Zanskar Himalayas: implications for the timing of obduction of the Spontang ophiolite, India-Asia collision and deformational events in the Himalaya, Geological Magazine, 134, 297-316.

Searle, M. P.; Weinberg, R. F.; Dunlap, W. J., 1998, Transpressional tectonics along the Karakoram Fault zone, northern Ladakh: constraints on Tibetan extrusion, in Holdsworth, R. E., Strachan, R. A., and Dewey, J. F., eds., Continental Transpressional and Transtensional Tectonics, London, Geological Society of London, Special Publications 135, 307-326.

Searle, M.P.; Khan, M.A.; Fraser, J.E.; Gough, S.J.; Jan, M.Q., 1999, The tectonic evolution of the Kohistan-Karakoram collision belt along the Karakoram Highway transect, north Pakistan, Tectonics, 18, 929-949, 10.1029/1999TC900042.

Searle, M.P.; Parrish, R.R.; Thow, A.V.; Noble, S.R.; Phillips, R.J.; Waters, D.J., 2010, Anatomy, age and evolution of a collisional mountain belt: the Baltoro granite batholith and Karakoram Metamorphic Complex, Pakistani Karakoram, Journal of the Geological Society, 167, 183-202, 10.1144/0016-76492009-043.

Sen, K.; Collins, A.S., 2013, Dextral transpression and late Eocene magmatism in the trans-Himalayan Ladakh Batholith (North India): implications for tectono-magmatic evolution of the Indo-Eurasian collisional arc, International Journal of Earth Sciences, 102, 1895-1909, 10.1007/s00531-012-0826-8.

St-Onge, M. R.; Rayner, N.; and Searle, M. P.; 2010, Zircon age determinations for the Ladakh batholith at Chumathang (Northwest India): Implications for the age of the India-Asia collision in the Ladakh Himalaya, Tectonophysics, 495, 3-4, 171-183.

St-Onge, M. R.; Rayner, N.; Palin, R. M.; Searle, M. P.; and Waters, D. J., 2013, Integrated pressure-temperature-time constraints for the Tso Morari dome (Northwest India): implications for the burial and exhumation path of UHP units in the western Himalaya, Journal of Metamorphic Geology, 31, 5, 469-504.

Thanh, N.X.; Itaya, T.; Ahmad, T.; Kojima, S.; Ohtani, T.; Ehiro, M., 2010, Mineral chemistry and K-Ar ages of plutons across the Karakoram Fault in the Shyok-Nubra confluence of northern Ladakh Himalaya, India, Gondwana Research, 17, 1, 180-188, 10.1016/j.gr.2009.08.002.

Thanh, N.X.; Rajesh, V.J.; Itaya, T.; Windley, B.; Kwon, S.; Park, C.-S., 2012, A Cretaceous forearc ophiolite in the Shyok suture zone, Ladakh, NW India: Implications for the tectonic evolution of the Northwest Himalaya, Lithos, 155, 81-93, 10.1016/j.lithos.2012.08.016.

Treloar, P.J.; Rex, D.C.; Guise, P.G.; Coward, M.P.; Searle, M.P.; Windley, B.F.; Petterson, M.G.; Jan, M.Q.; Luff, I.W., 1989, K-Ar and Ar-Ar geochronology of the Himalayan collision in NW Pakistan - constraints on the timing of suturing, deformation, metamorphism and uplift, Tectonics, 8, 881-909, 10.1029/TC008i004p00881

Tripathy-Lang, A.; Hodges, K.V.; van Soest, M.C.; Ahmad, T., 2013, Evidence of pre-Oligocene emergence of the Indian passive margin and the timing of collision initiation between India and Eurasia, Lithosphere, 5, 501-506, 10.1130/L273.1.

Upadhyay, R., 2008, Implications of U-Pb zircon age of the Tirit granitoids on the closure of the Shyok suture zone, northern Ladakh, India, Current Science, 94, 1635-1640.

Upadhyay, R., 2014, Palaeogeographic significance of 'Yasin-type' rudist and orbitolinid fauna of the Shyok Suture Zone, Saltoro Hills, northern Ladakh, India, Current Science, 106, 223-228.

Valli, F.; Leloup, P.H.; Paquette, J.-L.; Arnaud, N.; Li, H.; Tapponnier, P.; Lacassin, R.; Guillot, S.; Liu, D.; Deloule, E.; Xu, Z.; Maheo, G., 2008, New U-Th/Pb constraints on timing of shearing and long-term slip-rate on the Karakorum fault, Tectonics, 27, TC5007, 10.1029/2007TC002184.

Van Buer, N. J.; Jagoutz, O.; Upadhyay, R.; Guillong, M., 2015, Mid-crustal detachment beneath western Tibet exhumed where conjugate Karakoram and Longmu–Gozha Co faults intersect, Earth and Planetary Science Letters, 413, 144-157.

van Hinsbergen, D.J.J.; Lippert, P.C.; Dupont-Nivet, G.; McQuarrie, N.; Doubrovine, P.V.; Spakman, W.; Torsvik, T.H., 2012, Greater India Basin hypothesis and a two-stage Cenozoic collision between India and Asia, Proceedings of the National Academy of Sciences Of The United States Of America, MAY 15, 109, 20, 7659-7664, 10.1073/pnas.1117262109.

Weinberg, R.F.; Dunlap, W.J., 2000, Growth and deformation of the Ladakh batholith, northwest Himalayas: Implications for timing of continental collision and origin of calc-alkaline batholiths, Journal of Geology, 108, 303-320, 10.1086/314405.

Weinberg, R.F.; Dunlap, W.J.; Whitehouse, M 2000, New field, structural and geochronological data from the Shyok and Nubra Valleys, northern Ladakh: linking Kohistan to Tibet, Geological Society, London, Special Publications 2000, 170, 253-275, 10.1144/GSL.SP.2000.170.01.14.

White, L. T., Ahmad, T., Ireland, T. R., Lister, G. S., and Forster, M. A., 2011, Deconvolving episodic age spectra from zircons of the Ladakh Batholith, northwest Indian Himalaya, Chemical Geology, 289, 3-4, 179-196.

Winchester, J.A.; Floyd, P.A., 1977, Geochemical discrimination of different magma series and their differentiation products using immobile elements, Chemical Geology, 20, 4, 325-343, 10.1016/0009-2541(77)90057-2.

Wu, F.Y.; Ji, W.Q.; Wang, J.G.; Liu, C.Z.; Chung, S.L.; Clift, P.D., 2014, Zircon U-Pb and Hf isotopic constraints on the onset time of India-Asia collision, American Journal of Science, 314, 548 -579, doi10.2475/02.2014.04.

Yin, A., 2010, Cenozoic tectonic evolution of Asia: A preliminary synthesis, Tectonophysics, 488, 1-4, SI, 293-325, 10.1016/j.tecto.2009.06.002.

Yin, A.; Harrison, T.M., 2000, Geologic evolution of the Himalayan-Tibetan orogen, Annual Review of Earth and Planetary Sciences, 28, 211-280, 10.1146/annurev.earth.28.1.211.

Zaman H.; Torii M., 1999, Paleomagnetic study of Cretaceous red beds from the eastern Hindukush ranges, northern Pakistan; paleoarc construction of the Kohistan-Karakoram composite unit before the India-Asia collision, Geophysical Journal International, 136, 719–38.

Zhang, L.-L.; Liu, C.-Z.; Wu, F.-Y.; Ji, W.-Q.; Wang, J.-G., 2014, Zedong block revisited: An intra-oceanic arc within Neo-Tethys or a part of the Asian active continental margin?, Journal of Asian Earth Sciences, 80, 34-55, 10.1016/j.jseaes.2013.10.029.

FIGURE 2.1

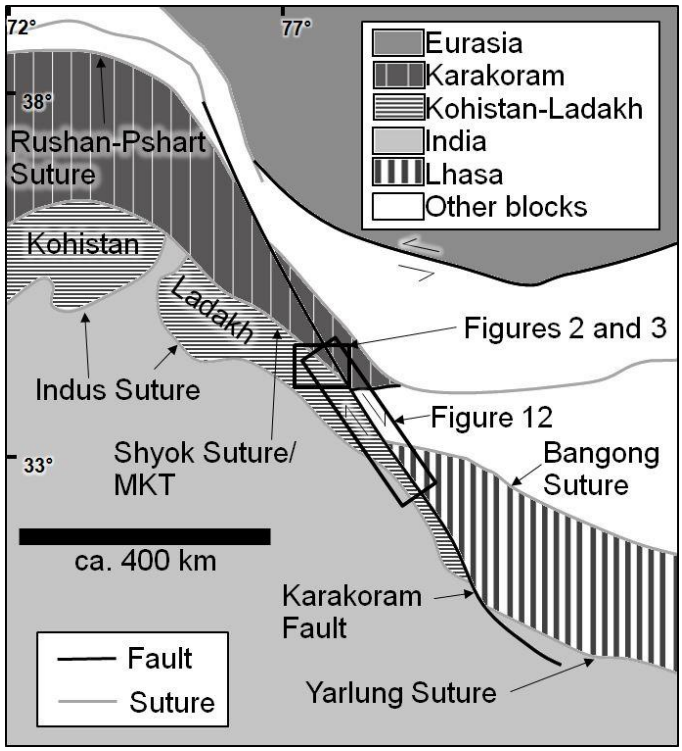
72°
77°
38°
33°
Eurasia
Karakoram
Kohistan-Ladakh
India
Lhasa
Other blocks
Rushan-Pshart Suture
Kohistan
Ladakh
Figures 2 and 3
Indus Suture
Figure 12
Shyok Suture/ MKT
Bangong Suture
ca. 400 km
Karakoram Fault
Fault
Suture
Yarlung Suture

FIGURE 2.2

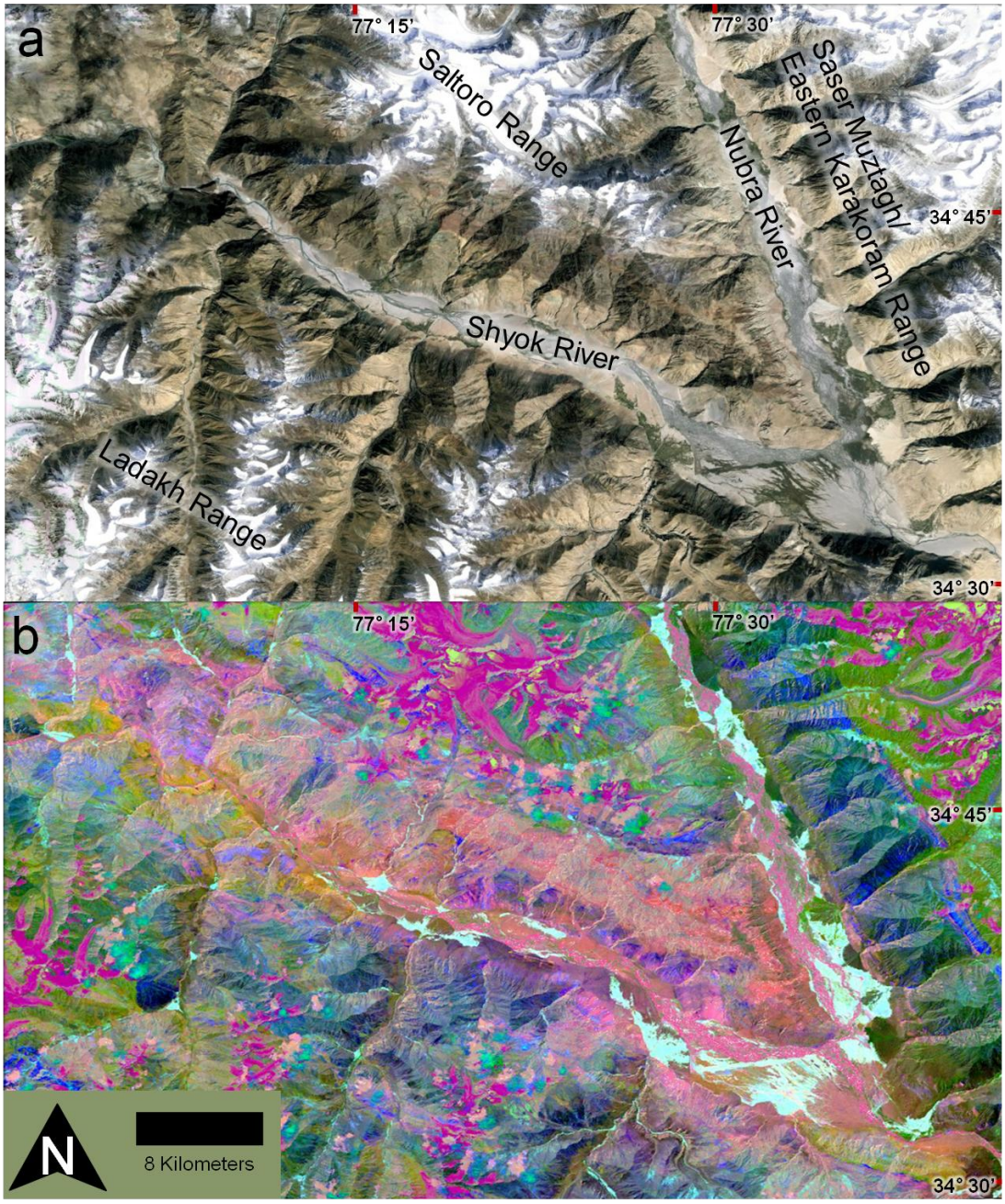
a
77° 15'
77° 30'
Saltoro Range
Nubra River
Saser Muztagh/
Eastern Karakoram Range
34° 45'
Shyok River
Ladakh Range
34° 30'
b
77° 15'
77° 30'
34° 45'
N
8 Kilometers
34° 30'

FIGURE 2.3

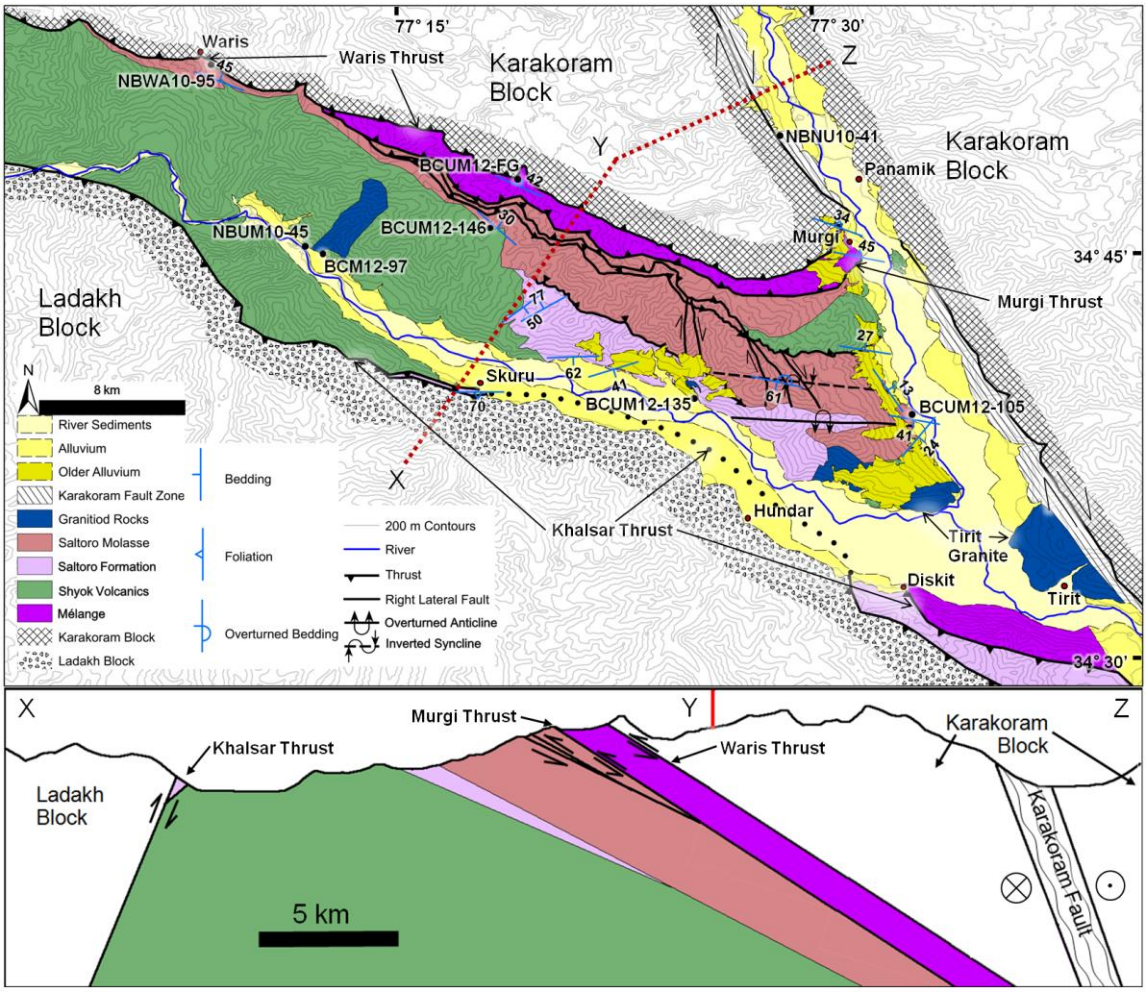
77° 15'
77° 30'
34° 45'
34° 30'
Waris
Waris Thrust
NBWA10-95
Karakoram Block
Y
Z
NBNU10-41
Panamik
Karakoram Block
BCUM12-FG
NBUM10-45
BCUM12-146
BCM12-97
Murgi
Murgi Thrust
Ladakh Block
Skuru
BCUM12-135
BCUM12-105
X
Khalsar Thrust
Hundar
Tirit Granite
Diskit
Tirit
N
8 km
River Sediments
Alluvium
Older Alluvium
Karakoram Fault Zone
Granitiod Rocks
Saltoro Molasse
Saltoro Formation
Shyok Volcanics
Mélange
Karakoram Block
Ladakh Block
Bedding
Foliation
Overturned Bedding
200 m Contours
River
Thrust
Right Lateral Fault
Overturned Anticline
Inverted Syncline
X
Y
Z
Murgi Thrust
Khalsar Thrust
Waris Thrust
Karakoram Block
Ladakh Block
Karakoram Fault
5 km

FIGURE 2.4

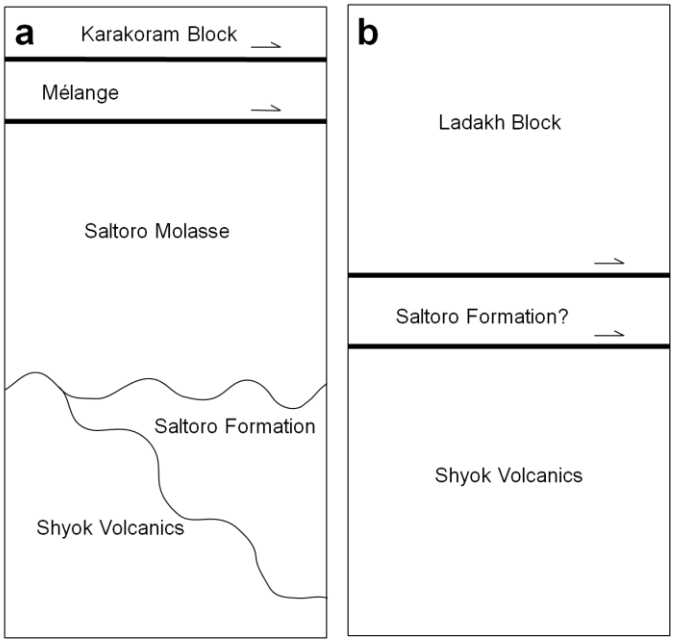
a
Karakoram Block
Mélange
Saltoro Molasse
Saltoro Formation
Shyok Volcanics
b
Ladakh Block
Saltoro Formation?
Shyok Volcanics

FIGURE 2.5

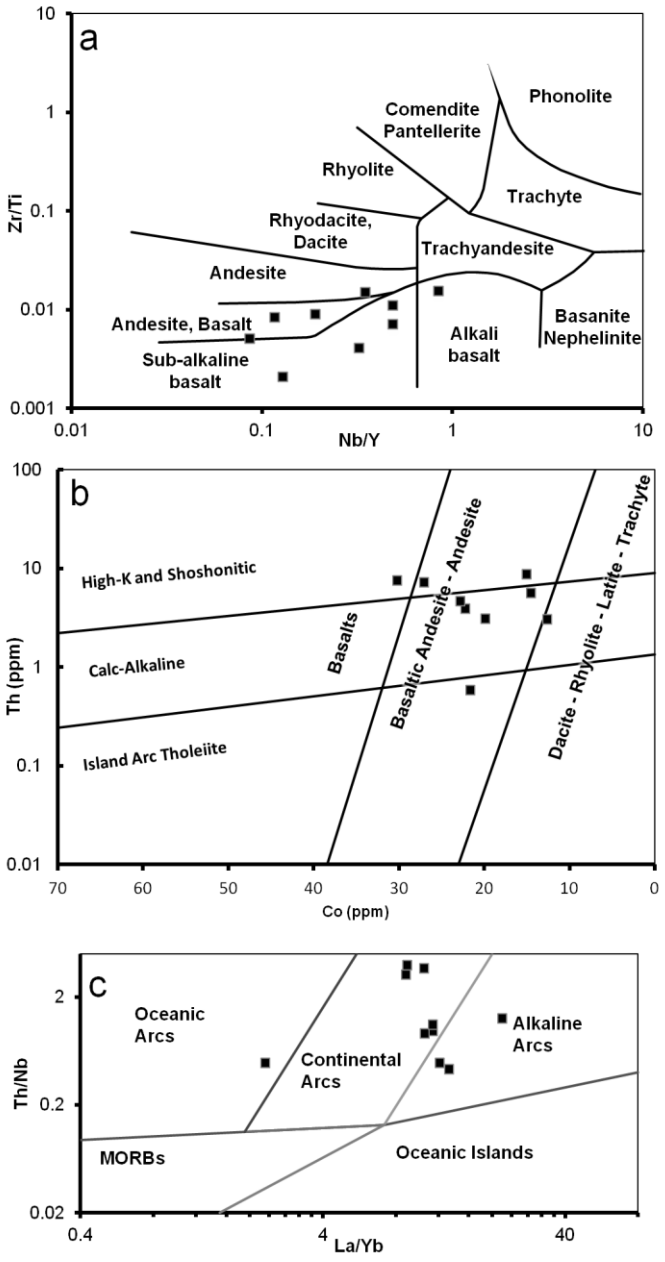
a
Phonolite
Comendite
Pantellerite
Rhyolite
Trachyte
Rhyodacite,
Dacite
Trachyandesite
Andesite
Andesite, Basalt
Alkali
basalt
Basanite
Nephelinite
Sub-alkaline
basalt
Zr/Ti
Nb/Y
10
1
0.1
0.01
0.001
0.01
0.1
1
10
b
High-K and Shoshonitic
Calc-Alkaline
Island Arc Tholeiite
Basalts
Basaltic Andesite - Andesite
Dacite - Rhyolite - Latite - Trachyte
Th (ppm)
Co (ppm)
100
10
1
0.1
0.01
70
60
50
40
30
20
10
0
c
Oceanic
Arcs
Continental
Arcs
Alkaline
Arcs
MORBs
Oceanic Islands
Th/Nb
La/Yb
2
0.2
0.02
0.4
4
40

FIGURE 2.6

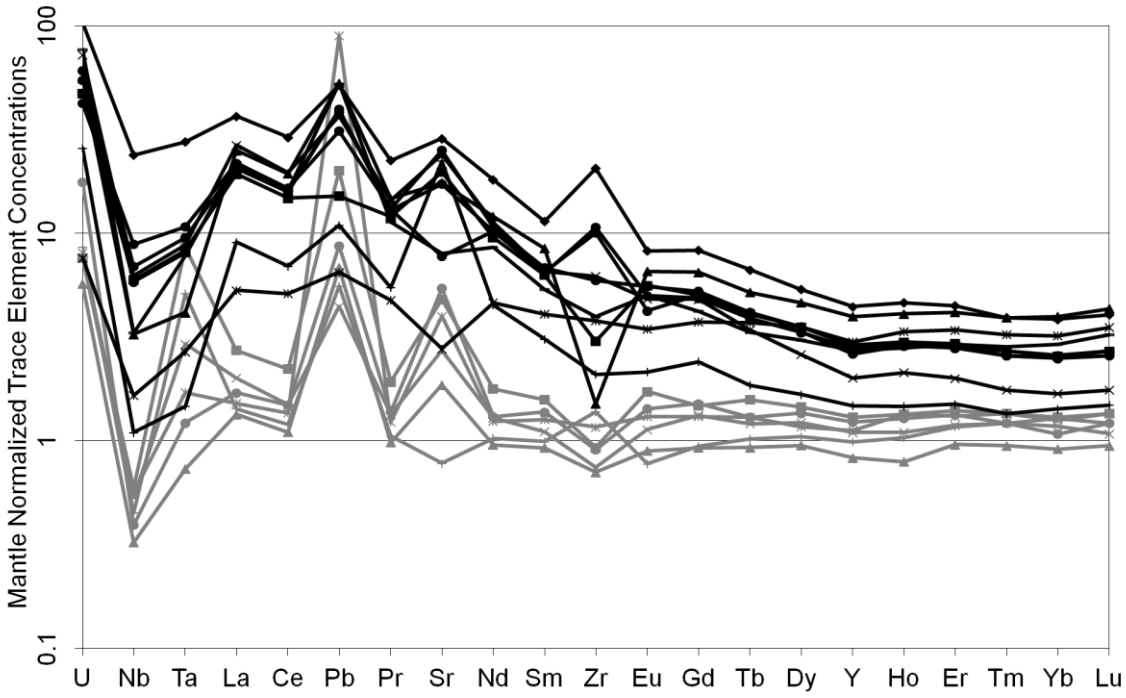
Mantle Normalized Trace Element Concentrations
100
10
1
0.1
U
Nb
Ta
La
Ce
Pb
Pr
Sr
Nd
Sm
Zr
Eu
Gd
Tb
Dy
Y
Ho
Er
Tm
Yb
Lu

FIGURE 2.7

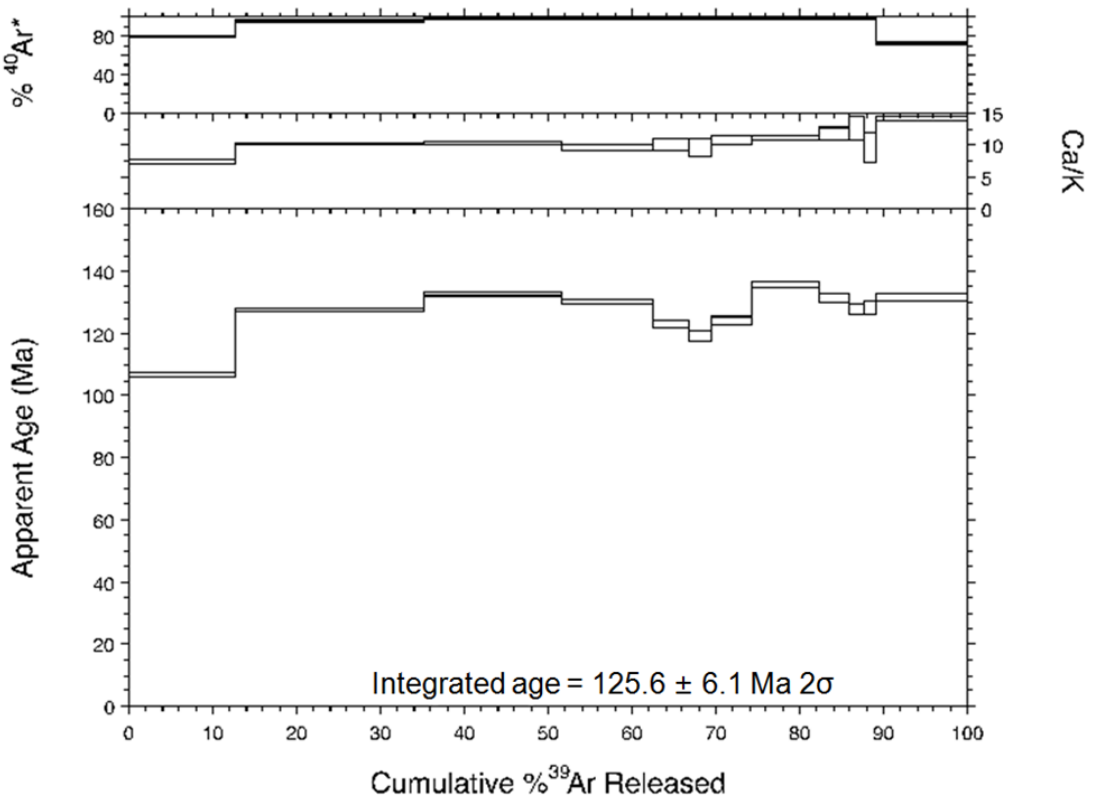
% 40Ar*
80
40
0
15
10
5
0
Ca/K
160
140
120
100
80
60
40
20
0
Apparent Age (Ma)
Integrated age = 125.6 ± 6.1 Ma 2σ
0
10
20
30
40
50
60
70
80
90
100
Cumulative %39Ar Released

FIGURE 2.8

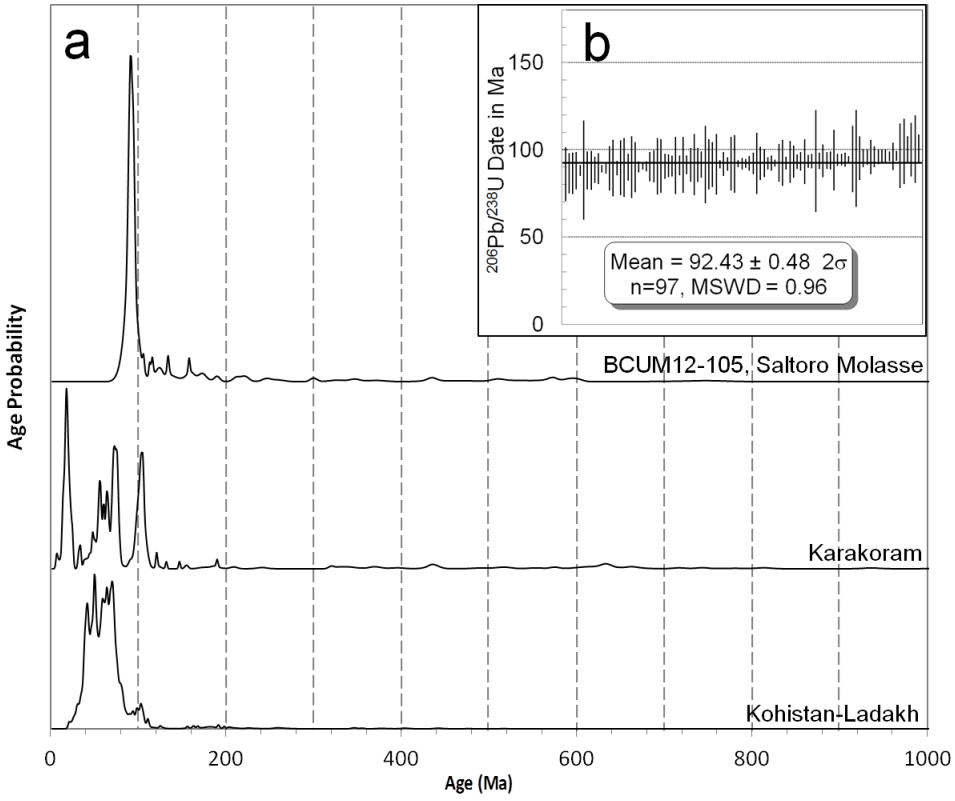
a
b
Age Probability
$^{206}Pb/^{238}U$ Date in Ma
150
100
50
0
Mean = 92.43 ± 0.48 2σ
n=97, MSWD = 0.96
BCUM12-105, Saltoro Molasse
Karakoram
Kohistan-Ladakh
0
200
400
600
800
1000
Age (Ma)

FIGURE 2.9

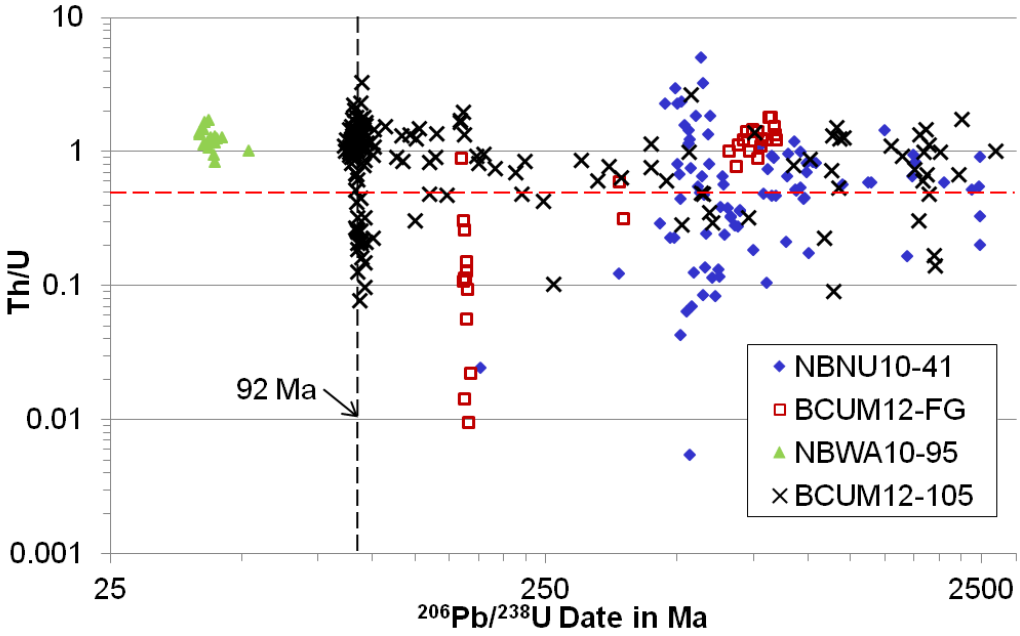
10
1
0.1
0.01
0.001
Th/U
92 Ma
25
250
2500
206Pb/238U Date in Ma
NBNU10-41
BCUM12-FG
NBWA10-95
BCUM12-105

FIGURE 2.10

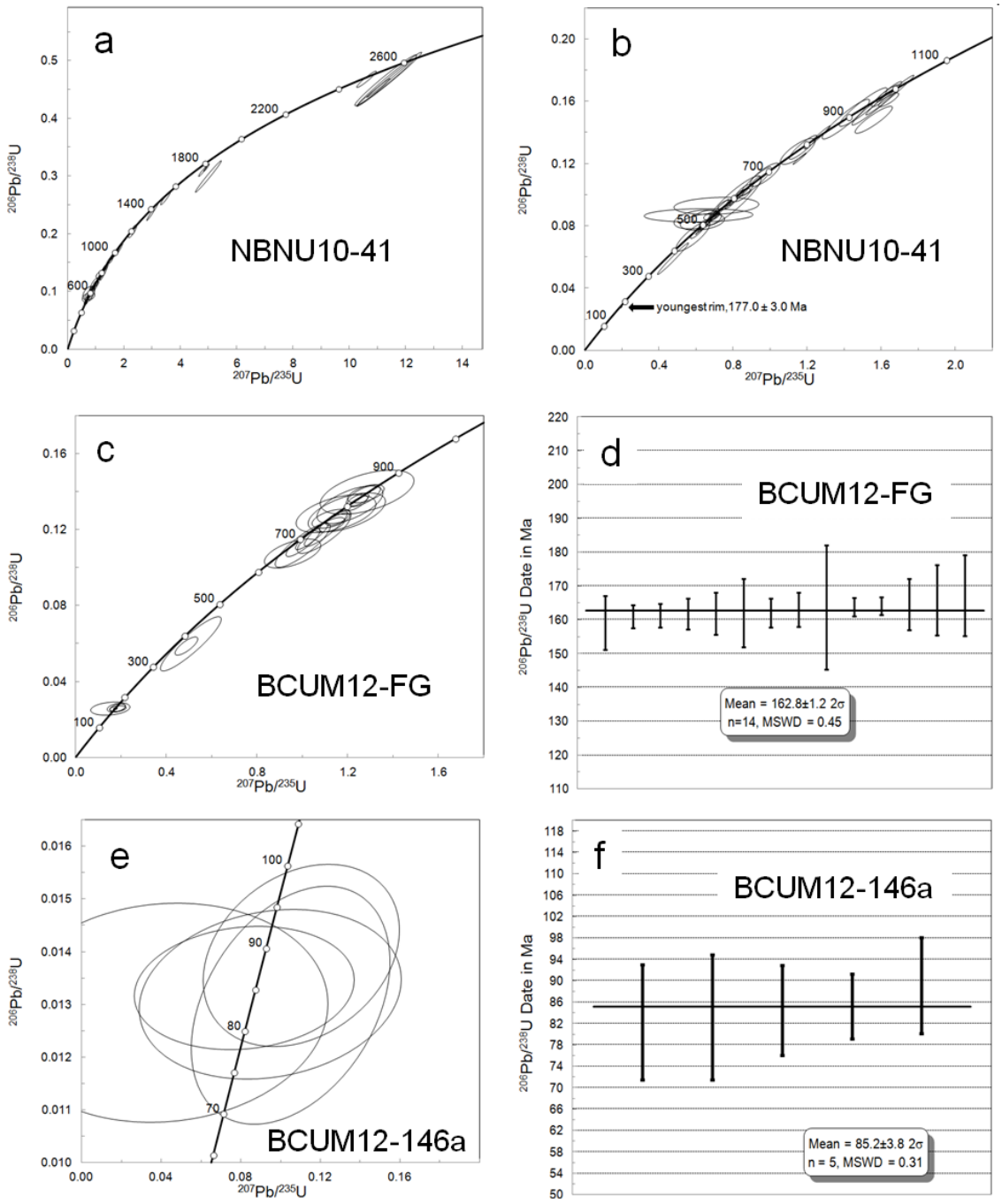
a
NBNU10-41
2600
2200
1800
1400
1000
600
$^{206}Pb/^{238}U$
$^{207}Pb/^{235}U$
b
NBNU10-41
1100
900
700
500
300
100
youngest rim, 177.0 ± 3.0 Ma
c
BCUM12-FG
900
700
500
300
100
d
BCUM12-FG
$^{206}Pb/^{238}U$ Date in Ma
Mean = 162.8±1.2 2σ
n=14, MSWD = 0.45
e
BCUM12-146a
100
90
80
70
f
BCUM12-146a
Mean = 85.2±3.8 2σ
n = 5, MSWD = 0.31

FIGURE 2.11

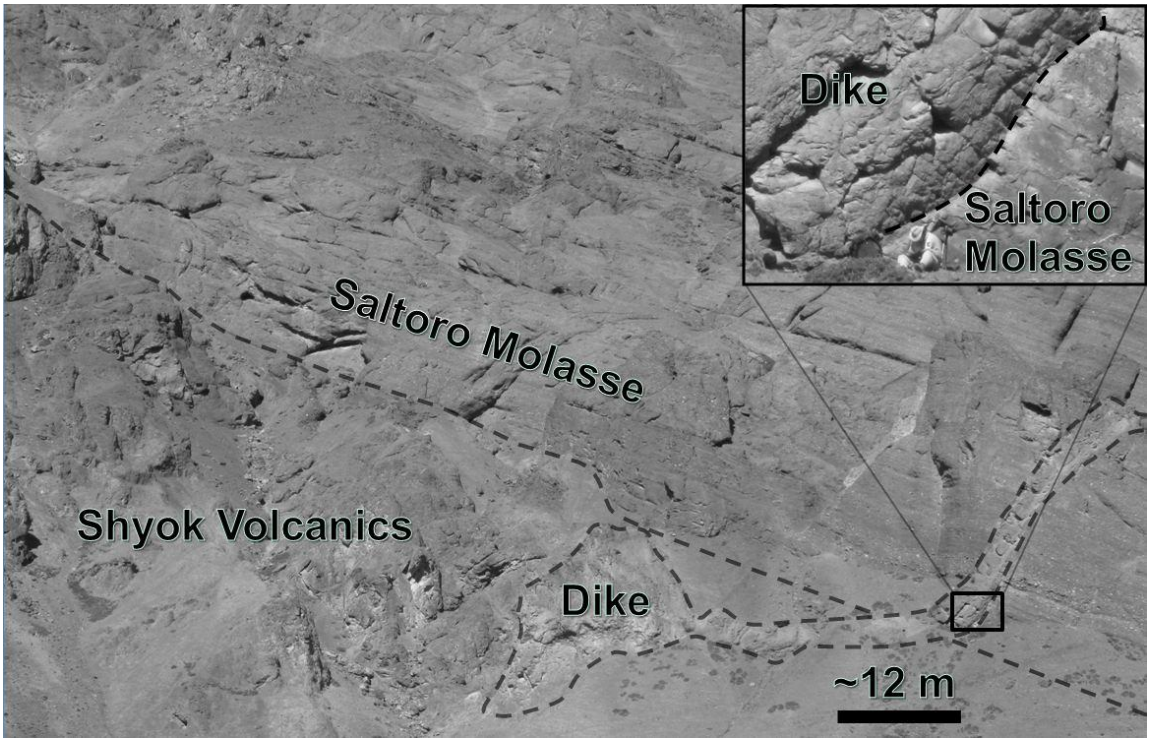
Dike
Saltoro Molasse
Saltoro Molasse
Shyok Volcanics
Dike
~12 m

FIGURE 2.12

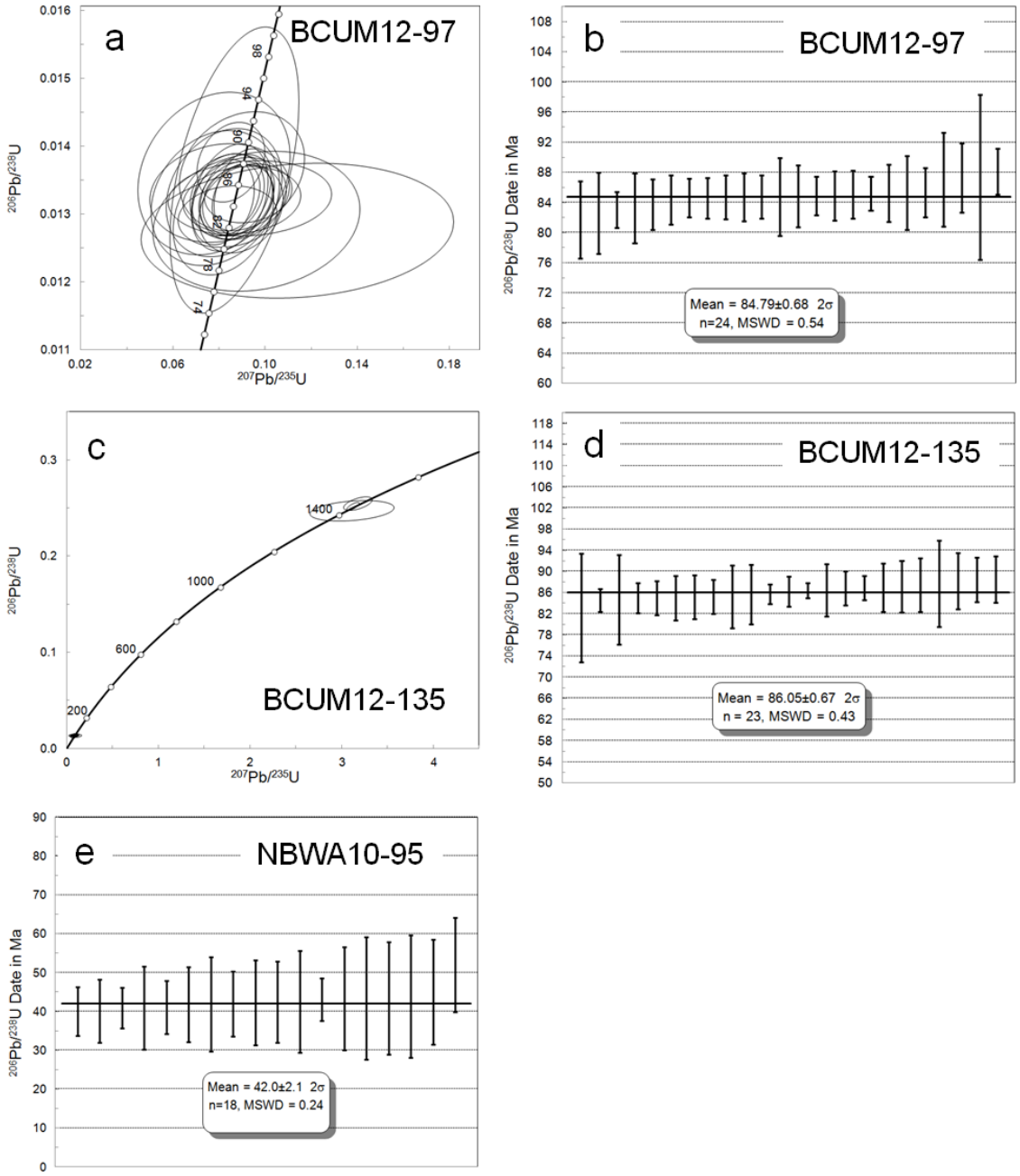
a
BCUM12-97
$^{206}Pb/^{238}U$
$^{207}Pb/^{235}U$
b
BCUM12-97
$^{206}Pb/^{238}U$ Date in Ma
Mean = 84.79±0.68 2σ
n=24, MSWD = 0.54
c
BCUM12-135
1400
1000
600
200
$^{206}Pb/^{238}U$
$^{207}Pb/^{235}U$
d
BCUM12-135
$^{206}Pb/^{238}U$ Date in Ma
Mean = 86.05±0.67 2σ
n = 23, MSWD = 0.43
e
NBWA10-95
$^{206}Pb/^{238}U$ Date in Ma
Mean = 42.0±2.1 2σ
n=18, MSWD = 0.24

FIGURE 2.13

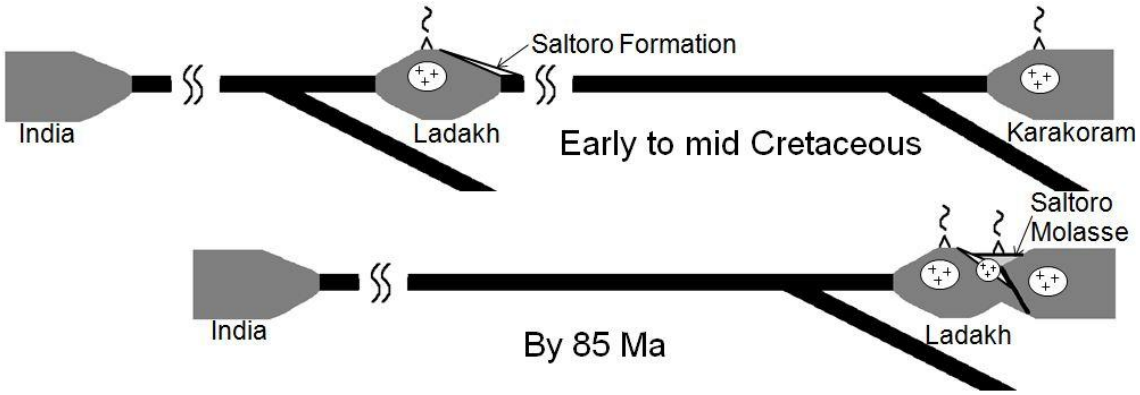
Saltoro Formation
India
Ladakh
Early to mid Cretaceous
Karakoram
Saltoro
Molasse
India
By 85 Ma
Ladakh

FIGURE 2.14

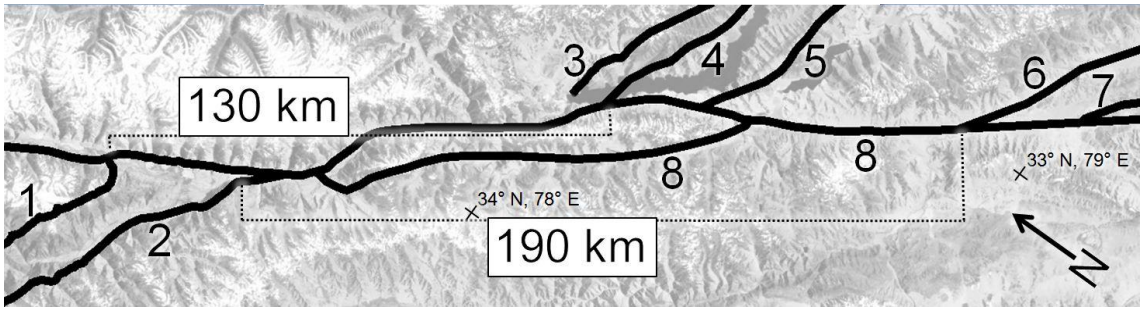

CHAPTER 3

EVIDENCE FOR THE EMPLACEMENT AGE OF THE NEW IDRIA SERPENTINITE DIAPIR FROM ^{40}AR/^{39}AR NEPTUNITE AND (U-TH)/PB JOAQUINITE GEOCHRONOLOGY

ABSTRACT

It is generally believed that northward passage of the Mendocino Triple Junction triggered rapid ascent of a serpentinite diapir at New Idria, in the Diablo Range of California. Unfortunately, establishing the precise age of diapirism at New Idria – and therefore the initiation age of the San Andreas fault system at this latitude – has proven to be challenging. An unusual metasomatic assemblage – containing the minerals benitoite, neptunite, and joaquinite – crystallized in the diapir during its ascent at temperatures of < 250˚C and pressures of ca. 500 MPa. I have discovered that neptunite and joaquinite from this assemblage are amenable to ^{40}Ar/^{39}Ar and ^{208}Pb/^{232}Th chronology, respectively. These chronometers record statistically indistinguishable dates, and I regard the more precise neptunite ^{40}Ar/^{39}Ar plateau date of 12.375 ± 0.082 Ma as the best available constraint on the timing of diapirism at New Idria. This age is consistent with previous, less precise estimates for the timing of initiation of the San Andreas system in this area based on paleomagnetic constraints.

INTRODUCTION

The Coast Range province of westernmost California records the complex geologic history of an active continental margin. A transformative part of this history was the development of the San Andreas Fault System as a consequence of northward propagation of the Mendocino Triple Junction (Furlong and Schwartz, 2004). The primary method for measuring past positions of the triple junction has involved plate circuit reconstructions, but the temporal accuracy of these estimates depend on calibrations of the paleomagnetic record to the absolute time scale (Atwater and Stock, 1998). As such, independent constraints on the timing of the passage of the Mendocino Triple Junction are valuable as independent checks on plate reconstructions and provide temporal piercing points, especially if such constraints are relatively precise. One place where such constraints may be possible to obtain is the New Idria region of west-central California. In that area, a widely accepted interpretation is that the passage of the Mendocino Triple Junction triggered the development of a serpentinite diapir at New Idria that ascended quickly from mid-crustal levels to the surface in less than a million years (Coleman, 1996; Vermeesch et al., 2006). As noted by Van Baalen (2004), this event apparently was coeval with the crystallization of a rare mineral assemblage within the diapir: benitoite ($BaTiSi_3O_9$), neptunite ($KNa_2Li(Fe, Mn, Mg)_2Ti_2Si_8O_{24}$)), and joaquinite ($NaBa_2REE_2FeTi_2Si_8O_{26}$ $(OH, F)\cdot H_2O$). Here I demonstrate that neptunite and joaquinite (respectively) show promise as $^{40}Ar/^{39}Ar$ and (U-Th)/Pb chronometers, and suggest that these tools can be used to improve my understanding of the timing of triple junction passage and San Andreas development at the latitude of New Idria.

GEOLOGIC BACKGROUND

The New Idria serpentinite occurs in the southernmost Diablo Range, within the subduction-accretion Coast Range province of California. Exposures are found only in the core of the active Coalinga Antiform. Partly because occurrences of similar rocks are limited, the initial tectonic setting of the New Idria body is not well constrained. Reasonable interpretations are that it represents an underplated abyssal peridotite complex, as a fragment of the Coast Range ophiolite, or as a serpentinized forearc mantle wedge (Tsujimori et al., 2007). The serpentinite body has been thrust westward over ophiolite-bearing subduction mélange of the Franciscan Formation (Figures 3.1, B1). Both the New Idria serpentinite and the Franciscan rocks structurally beneath them have been structurally emplaced over Cretaceous marine sedimentary rocks of the Great Valley Sequence on a succession of complex, often overturned thrust faults (Coleman, 1996). Sedimentary rocks of the Late Cretaceous–Recent San Joaquin Basin depositionally overlie the Great Valley Sequence, but are not in direct contact with the serpentinite.

The serpentinite body is bound by faults with shear-sense indicators indicative of upward movement of the serpentinite relative to adjacent rocks, something that has long been considered conclusive evidence for diapiric emplacement (e.g. Coleman, 1961; Coleman, 1996). More recently, Vermeesch et al. (2006) presented a model in which the New Idria serpentinite rose rapidly from as deep as 20 km (where blueschist facies conditions prevailed) and expanded out onto Earth's surface, providing a source for the Big Blue Formation, a sedimentary serpentinite in the San Joaquin Basin

As the name implies, the New Idria body's predominant rock type is serpentinite (lizardite + chrysotile ± antigorite). Its protolith lithologies were predominately dunite and harzburgite, with subordinate lherzolite and pyroxenite (Van Baalen, 2004). Entrained within it are exotic blocks of eclogite, garnet amphibolite, blueschist, and greenstone (Laurs et al., 1997; Tsujimori et al., 2007). Greenstone blocks within the serpentinite are unquestionably sourced from the Franciscan Formation (Van Baalen, 2004). Several nepheline normative syenite stocks (containing abundant alkali feldspar and kaersustite) intrude the serpentinite.

Previously published work suggests that that the New Idria serpentinite contains three different generations of metamorphic assemblages, here referred to, from oldest to youngest, as M_1, M_2, and M_3. Tsujimori et al. (2007) argued that the peak metamorphism (M_1) resulted in the growth of one of two different eclogite assemblages in different rocks: Grt ($Alm_{50-62}Grs_{29-36}Prp_{9-17-17}Sps_{1-8}$) + Cpx ($Jd_{10-18}Aug_{67-80}Aeg_{10-15}$) + Rt ± Clz ± Qz, and Grt ($Alm_{48-57}Grs_{22-32}Prp_{12-17}Sps_{<3)}$ + Cpx ($Jd_{38-47}Aug_{45-55}Aeg_{2-11}$) + Rt ± Clz ± Qz . (In this contribution, I employ mineral abbreviations from Whitney and Evans, 2010.) In one garnet amphibolite sample, they also reported the M_1 assemblage Grt ($Alm_{45-50}Grs_{34-41}Prp_{8-15}Sps_{1-7}$ + Cpx ($Jd_{4-13}Aug_{83-89}Aeg_{0-6}$) +Ed to Ts Hbl + Rt + Qz). Based on Jd+Qz (Holland, 1983) and Grt+Cpx (Krogh-Ravna, 2000) equilibria, Tsujimori et al. (2007) interpreted the M_1 crystallization conditions of the eclogite assemblages to have been 580-620 °C and >1.3 GPa. For the garnet amphibolite, they inferred 630-680 and 0.8-1.0 GPa based on Jd+Qz and Grt+Cpx equilibria.

Eclogite and amphibolite grade M_1 assemblages are overprinted by M_2 blueschist facies assemblages implying pressure and temperature conditions of > 1 GPa and 200-

290 °C based on the presence of pumpellyite and pure jadeite and absence of albite (Harlow and Sorenson, 2005; Kim et al., 2013; Maruyama and Liou, 1988; Tsujimori et al., 2007). Typical blueschist facies assemblages associated with M_2 are Gln to Fgl ± Jd ± Pmp ± Lws ± Chl ± Ttn ± Ph, though essentially pure jadeitite pods within the serpentinite body likely also represent M_2 (Coleman, 1961; Tsujimori et al., 2007). In addition to more typical blueschists described above, M_2 conditions also led to the metamorphism of pyroxenite blocks to Chl + Di + Ti-rich Grt rocks that are lithologically similar to rodingites. In many exotic blocks, the growth of M_2 assemblages was synkinematic with the development of a distinctive penetrative foliation (Van Baalen, 2004).

Van Baalen (2004) argued that low temperature (<400 °C) metamorphism within the New Idria serpentinite occurred in two discrete events, and I refer to his later event as M_3. The M_3 assemblage is found in veins that fill cracks that crosscut earlier foliation developed synchronously with M_2. One type of vein-filling assemblage is Chl + Di + Ti-rich Grt in rodingite-like blocks. The M_3 chlorite is depleted in the Tschermak component relative to M_2 chlorite, leading Van Baalen (2004) to conclude that M_3 occurred at lower temperatures than M_2 (Laird, 1988), specifically at <250 °C based on the upper stability limit of natrolite (Peacor, 1973).

A second M_3 assemblage, found filling cracks in blueschist blocks at New Idria, includes benitoite, neptunite, and joaquinite that apparently formed in equilibrium with apatite, albite, actinolite, and various zeolite minerals. The crystallization of these rare minerals was closely followed by the crystallization of nearly pure natrolite, which filled the remaining interstices in the veins (Laurs et al., 1997). While benitoite and joaquinite

group minerals have since been found at other localities (e.g. Sakai and Akai, 1994), New Idria remains the only known location hosting the assemblage benitoite + neptunite + joaquinite and the only known locality of large, gem-quality benitoite crystals. This rarity, combined with benitoite's high dispersive and refractive indices and deep blue color, contributed to its designation as the state gemstone of California.

The exact roles played by metasomatism in M_3 metamorphism (including the paragenesis of benitoite and associated rare minerals) remain unclear. Van Baalen (2004) argued that very localized metasomatism between blueschist and Franciscan greenstone blocks entrained within the New Idria serpentinite mobilized the trace elements that are concentrated in the rare minerals, with transport occurring in Na-rich, Si-poor fluids. This process is fundamentally limited to the local scale based on the immobility of Ti (Van Baalen, 1993). Laurs et al. (1997) agreed with Van Baalen on the whole, but showed that the rare mineralization did not require the presence of the greenstone blocks based on the numerous localities within the New Idria serpentinite where benitoite is found only in association with blueschist blocks. Laurs et al. (1997) further argued that fluids involved in benitoite production were likely Mg-Ca rich fluids based on the bulk composition of benitoite-bearing veins. I favor the interpretation that the fluids that led to benitoite formation were Na-rich, as the westernmost benitoite-bearing blocks near Clear Creek are in close proximity to blocks bearing M_3 jadeite veins (Laurs et al., 1997; Coleman 1961). The jadeite veins must have formed in Na-rich fluid saturated conditions (Harlow and Sorenson, 2005; Sorenson et al., 2006). Sorenson et al. (2006) further proposed that the most likely source for the jadeite-forming fluids is derived from devolitalizing blueschists whose protoliths had undergone Na-metasomatism (spilitization).

A reasonable interpretation of the M_1-M_3 paragenetic sequences found at New Idria is that M_1 and M_2 assemblages record incorporation of the New Idria body into the Coast Range subduction-accretion environment, while M_3 records the late-stage, diapiric ascent of the body from high-pressure (blueschist facies) conditions to the upper crust (e.g., Tsujimori et al., 2007). M_1 has been inferred to be older than 135 ± 7 Ma (confidence level unspecified) by Tsujimori et al. (2007) based on a 'preliminary' K/Ar cooling date for M_1 hornblende within the garnet. M_2 metamorphism has not been directly dated at New Idria, but K/Ar phengite and glaucophane ages from blueschists in various western California and Oregon localities range over 150-120 Ma (Coleman and Lanphere, 1971). There have been no previously reported direct constraints on the possible age of M_3 metamorphism. Van Baalen (2004) reported (as a personal communication from M. Lanphere) a total-fusion $^{40}Ar/^{39}Ar$ date of 12.4 ± 0.8 Ma for amphibole (presumably kaersutite) from one of the syenite stocks that intruded the serpentinite diapir during its ascent, but the data have not been published and it is unclear what confidence level is represented by the quoted uncertainty. If it is correct, the model of Vermeesch et al. (2006) that the New Idria serpentinite provided the source for the Big Blue Formation sedimentary serpentinite argues that that age of the diapir must be the same as the biostratigraphically constrained age of that formation – between 14 and 11 Ma (Johnson and Graham, 2007). In addition, Vermeesch et al. (2006) report fission-track apparent ages of detrital zircons collected from the Great Valley Sequence immediately adjacent to the diapir of 13.1 ± 1 Ma (confidence level unspecified), which they interpreted as reflecting resetting during diapir emplacement.

Paleomagnetic reconstructions suggest that the Mendocino Triple Junction passed by the New Idria region at ca. 12 Ma, with the associated plate boundary tectonic environment changing from a subduction zone to the initiation of the San Andreas Fault (McQuarrie and Wernicke, 2005; Stock and Hodges 1989). General consensus has been reached by geologists working in the region that this change in tectonic environment triggered the rise of the New Idria diapir, but there remains disagreement with regard to the exact mechanism of interaction. Coleman (1996) argued that transpression caused by the San Andreas Fault pumped water into peridotites, causing them to serpentinize, become less dense, and rise to the surface as the New Idria diapir. Vermeesch et al. (2006) favored the interpretation that the passage of the Mendocino Triple Junction exposed formerly insulated crust to hot mantle rock. In their model, such heating would have caused the overlying rocks to dehydrate, and the fluids released would have led to the serpentinization of previously obducted ophiolites, triggering rise of the diapir.

NEW CONSTRAINTS ON THE AGE OF M_3 AND NEW IDRIA DIAPIRISM

Recently, in the course of a study aimed at better establishing the chemistry of unusual minerals of the New Idria M_3 assemblage, I discovered that the neptunites contained a significant amount of potassium (7.6-8.3 wt. % K_2O) and the joaquinites contained a significant amount of U and Th (0.23-0.32 wt% UO_3, and 0.45-0.72 wt% ThO_2, respectively). As a consequence, I elected to apply the (U-Th)/Pb geochronologic method to the joaquinites and the $^{40}Ar/^{39}Ar$ method to the neptunites in an effort to better constrain the age of the M_3 event. (Analytical details may be found in Appendix B.)

(U-Th)/Pb Joaquinite Geochronology

We determined (U-Th)/Pb dates for three DGM joaquinites by laser ablation ICPMS in the Group 18 Laboratories at Arizona State University. The analytical protocols and data reduction strategies used are described in the Appendix B and analytical data for the DGM joaquinites are shown in Table B3. For each crystal, between five and ten ablation experiments were performed. I found no obvious variation in the apparent ages determined for various spots within the crystals, nor did I see intercrystal variations in apparent ages. I did, however, find that the calculated $^{206}Pb/^{238}U$, $^{207}Pb/^{235}U$, and $^{208}Pb/^{232}Th$ dates for each crystal were not concordant, with the $^{206}Pb/^{238}U$ and $^{207}Pb/^{235}U$ dates consistently older than the $^{208}Pb/^{232}Th$ dates. Given the low U/Th ratios of the State Gem Mine joaquinites (ca. 0.5), I attribute the lack of concordance to initial intermediate daughter product disequilibrium caused by excess ^{230}Th incorporation at the time of formation (e.g. Schoene, 2014). Intermediate daughter products are relatively short lived for the $^{232}Th \rightarrow {}^{208}Pb$ decay chain (as compared to $^{238}U \rightarrow {}^{206}Pb$ and $^{235}U \rightarrow {}^{207}Pb$), such that it reaches secular equilibrium more quickly and is thus less susceptible to problems related to the incorporation of excess intermediate daughter products (Harrison et al., 2002). As a consequence, I have elected to interpret the $^{208}Pb/^{232}Th$ dates in Table B3 as the most reliable. Figure 3.2 illustrates that these dates for all joaquinite analyses fall within analytical uncertainty of one another, with an inverse error-weighted mean date of 12.08 ± 0.59 Ma (all new dates in this paper are reported at the 2σ level). I interpret this date as a robust estimate for the ^{208}Pb closure age of joaquinite from New Idria.

$^{40}Ar/^{39}Ar$ Neptunite Geochronology

We conducted $^{40}Ar/^{39}Ar$ incremental heating experiments on four neptunite fragments from the same sample in the Group 18 Laboratories. For these experiments, a CO_2 laser was used at successively higher power levels for each heating increment, and the liberated gasses were analyzed by gas source, magnetic sector mass spectrometry (see Appendix B for protocols and Table B4 for the $^{40}Ar/^{39}Ar$ data). The resulting incremental release spectra are shown in Figures 3.3 and B3. Each sample behaved in a relatively straightforward way, with high (> 90%) radiogenic ^{40}Ar yields for each increment. Ca/K ratios for each increment are relatively uniform, consistently low, and similar to the values calculated from my ICPMS data. Each experiment yielded a statistically significant plateau age (Fleck et al., 1977), and those ages were indistinguishable from integrated ages for all steps. All four crystals yielded indistinguishable plateau ages, and I regard the inverse error-weighted mean age for all four samples (12.375 ± 0.082 Ma) as a robust estimate for the ^{40}Ar closure age of New Idria neptunite.

DISCUSSION AND CONCLUSIONS

Although neither $^{40}Ar/^{39}Ar$ dates for neptunite nor (U-Th)/Pb dates for joaquinite have been published previously, I found that both mineral-isotopic systems yield robust results for the rare mineral suite that characterizes M_3 metamorphism in the New Idria serpentinite diapir. The statistical equivalence of my preferred $^{40}Ar/^{39}Ar$ neptunite date (12.375 ± 0.082 Ma) and my preferred $^{208}Pb/^{232}Th$ joaquinite date (12.08 ± 0.59 Ma) imply that both are crystallization rather than cooling ages, and together provide strong evidence that M_3 metamorphism occurred at ca. 12.0-12.5 Ma. My results thus support

the earlier inference of this age for M_3 by Van Baalen (2004) based on unpublished data. Although the minerals neptunite and joaquinite are extremely rare, my positive experiences suggest that $^{40}Ar/^{39}Ar$ neptunite and $^{208}Pb/^{232}Th$ joaquinite may be valuable geochronometers for other localities where these minerals are found. If New Idria M_3 P-T conditions are generally indicative of the conditions under which these unusual minerals form, it is likely that the chronometers based on them record crystallization, and not cooling, ages.

The Tertiary tectonics of California have been profoundly influenced by the development and evolution of slab windows beneath the western North America as a consequence of impingement of the Pacific-Farallon Ridge System and the Farallon-North American Trench and subsequent northward and southward migrations of the Mendocino and Rivera Triple Junctions on either end of the San Andreas transform plate boundary (e.g., Atwater and Stock, 1998; Furlong and Schwartz, 2004). Most recent plate reconstructions place the Mendocino Triple Junction at the approximate position of the New Idria diapir at 13-12 Ma. My new results invite correlation of passage of the slab window related to the triple junction to development of the diapir coincident with M_3, as hypothesized earlier by Van Baalen (2004). If correct, this has important implications for the rate of emplacement of the diapir.

Although Van Baalen could not constrain the pressure conditions of M_3, Coleman (1961) observed veins containing the assemblage Jd + Ab crosscutting M_2 blueschist blocks with later stage Ab + Ntr + Thm + Anl filling gaps in the veins. In these veins, jadeite is common towards the margins and jadeite-bearing assemblages grade continuously into zeolite-bearing assemblages towards the vein interiors, as well as where

the veins penetrate deeper into the exotic block. Based on the M_2-crosscutting nature of these veins, Tsujimori and Harlow (2012) observed that these veins musts postdate M_2. Harlow et al. (2015) further noted that jadeite formation is commonly associated with Ba mineralization. For these reasons, I tentatively group the jadeite bearing vein formation at New Idria with M_3. The transition from assemblages where jadeite is stable to where jadeite is unstable within M_3 veins implies M_3 occurred near the lower stability limit of jadeite. The association of Ab + Jd at <250 °C near the lower stability limit of jadeite implies pressures of ca. 0.5 GPa, conditions near the upper pressure limit of the greenschist facies (Harlow and Sorenson, 2005; Harlow et al., 2015). I suggest that the change in pressure associated with M_3 is also responsible for the retrogression of M_2 Lws- and Jd-bearing blueschists to the assemblage Ab + Gln + Act + Ttn ± Stp ± Qz ± Kfs ± Ep ± Ap, which is commonly observed in association with benitoite-bearing veins (Laurs et al., 1997).

Taking 0.5 GPa as minimum pressure during initiation of diapirism implies 17 km of exhumation for the New Idria serpentinite since 12.375 ± 0.082 Ma, my preferred neptunite age for M_3. Accepting the arguments of Vermeesch et al. (2006), stratigraphic constraints from the Big Blue Formation require the diapir to have reached the surface by 11 Ma. These two ages argue that emplacement of the diapir from mid-crustal levels to the surface took less than 1.4 Ma, requiring very rapid diapiric rise (12 km/Ma). Accepting the commonly assumed causal link between the initiation of diapiric rise and the change in plate boundary environment, my data might be reasonably interpreted as indicative of a 12.375 ± 0.082 Ma age for passage of the Mendocino Triple Junction and initiation of the San Andreas Fault at New Idria.

ACKNOWLEDGEMENTS

Analytical aspects of my research were supported by a grant from the U.S. National Science Foundation's Continental Dynamics program (EAR 1007929) to K.V. Hodges. I thank the U.S. National Science Foundation's Earth Sciences Instrumentation and Facilities program for partial support for the acquisition of analytical instrumentation in the Group 18 Laboratories. The author also expresses his gratitude to ASU's GeoClub for providing logistical support at New Idria, and for subsidizing costs associated with sample procurement.

FIGURE CAPTIONS

Figure 3.1. Geologic map of the New Idria serpentinite and associated rocks. After Coleman (1962), Kim et al. (2013), Laurs et al. (1997), and Tsujimori et al. (2007). Lin of section indicates location of figure B1.

Figure 3.2. Mean $^{208}Pb/^{232}Th$ date for all joaquinite grains analyzed from sample DGM. Vertical lines are individual analyses with 2σ errors. Horizontal bar is the mean.

Figure 3.3. $^{40}Ar/^{39}Ar$ laser step heating spectra for neptunite sample SGM-1. The top, middle, and bottom panels show the percent radiogenic yield, the Ca/K ratio, and the date (respectively) for each heating step. Errors shown for each step reflect both analytical errors and errors in J, and are reported at 2σ. Integrated total gas date is indicated at the bottom. Plateau segments are marked by the arrows with associated date labeled.

REFERENCES

Atwater, T.; Stock, J.; 1998, Pacific North America plate tectonics of the Neogene southwestern United States, An update, International Geology Review, 40, 375-402.

Coleman, R.G., 1961, Jadeite deposits of the Clear Creek area, New Idria district, San Benito County, California, Journal of Petrology, 2, 209–247.

Coleman, R. G., 1996, New Idria Serpentinite: A land management dilemma, Environmental & Engineering Geoscience, 2, 9–22.

Coleman, R.G.; Lanphere, M.A., 1971, Distribution and age of high-grade blueschists, associated eclogites, and amphiboles from Oregon and California , Geological Society of America Bulletin, 82, 2397-2412.

Fleck, R.J.; Sutter, J.F.; Elliot, D.H., 1977, Interpretation of discordant $^{40}Ar/^{39}Ar$ age spectra of Mesozoic tholeiites from Antarctica, Geochimica et Cosmochimica Acta, 41, 15-32.

Furlong, K.; Schwartz, S.Y., 2004, Influence of the Mendocino Triple Junction on the tectonics of coastal California, Annual Review of Earth and Planetary Sciences, 32, 403-433.

Harlow, G.E.; Sorensen, S.S., 2005, Jade (Nephrite and Jadeitite) and Serpentinite, Metasomatic connections , International Geology Review, 47, 2, 113-146, 10.2747/0020-6814.47.2.113.

Harlow, G.E.; Tsujimori, T.; Sorenson S.S., 2015, Jadeitites and plate tectonics, Annual Review of Earth and Planetary Science , 43, 105-138, doi: 10.1146/annurev-earth-060614-105215.

Harrison, T.M.; Catlos, E.J.; Montel, J.-M., 2002, U–Th–Pb dating of phosphate minerals, *in* Kohn, M.J., Rakovan, J., Hughes, J. eds., Phosphates, Geochemical, Geobiological, and Materials Importance, Mineralogical Society of America, Washington, D.C, 523–558.

Holland, T.J.B., 1983, The experimental determination of activities in disordered and shot-range ordered jadeitic pyroxenes, Contributions to Mineralogy and Petrology, 82, 214-220, doi ,10.1007/BF01166616.

Johnson, C.L.; Graham S.A., 2007 Middle Tertiary Stratigraphic Sequences of the San Joaquin Basin, California, *in* Scheirer A.H. (ed.) Petroleum Systems and Geologic Assessment of Oil and Gas in the San Joaquin Basin Province, California, 6, doi ,10.3133/pp1713.ch06.

Kim, D.; Katayama, I.; Michibayashi, K.; Tsujimori, T., 2013, Rheological contrast between glaucophane and lawsonite in naturally deformed blueschist from Diablo Range, California, Island Arc, 22, 1, 63-73, 10.1111/iar.12003.

Krogh-Ravna, E., 2000, The garnet-clinopyroxene Fe^{2+}-Mg geothermometer, An updated calibration , Journal of Metamorphic Geology, 18, 211-219, doi ,10.1046/j.1525-1314.2000.00247.x.

Laird, J., 1988, Chlorites - metamorphic petrology, Reviews In Mineralogy, 19, 405-453.

Laurs, B.M.; Rohtert, W.R.; Gray, M., 1997, Benitoite from the New Idria District, San Benito County, California, Gems & Gemology, 33, 166–187.

Maruyama, S.; Liou, J.G., 1988, Petrology of Franciscan metabasites along the jadeite glaucophane type facies series, Cazadero, California, Journal Of Petrology, 29, 1, 1, 37.

McQuarrie, N.; Wernicke, B., 2005, An animated tectonic reconstruction of southwestern North America since 36 Ma, Geosphere, 1, 3, 147-172, 10.1130/GES00016.1.

Peacor, D.R., 1973, High-temperature, single-crystal x-ray study of natrolite, American Mineralogist, 58, vol. 7-8, 676-680.

Sakai, M., Akai, J., 1994, Strontium, barium and titanium-bearing minerals and their host rocks from Ohmi, Japan , Scientific Reports Niigata University, Series E, 9, 97-118.

Schoene, B., 2014, U-Th-Pb Geochronology, *in* Rudnick R. (ed.) Treatise on Geochemistry (Second Edition), The Crust, 4, 341-388.

Sorenson, S.; Harlow, G.E.; Rumble, D., 2006, The origin of jadeitite-forming subduction-zone fluids, CL-guided SIMS oxygen-isotope and trace-element evidence , American Mineralogist, 91, 979-996.

Stock, J.M.; Hodges, K., 1989, Pre-Pliocene extension around the Gulf of California and the transfer of Baja California to the Pacific Plate , Tectonics, 8, 1, 99-115, 10.1029/TC008i001p00099.

Tsujimori, T.; Harlow, G.E., 2012, Petrogenetic relationships between jadeitite and associated high-pressure and low-temperature metamorphic rocks in worldwide jadeitite localities , A review , European Journal of Mineralogy, 24, 371-390, DOI , 10.1127/0935-1221/2012/0024-2193.

Tsujimori, T.; Liou, G. J.; Coleman, R. G., 2007, Finding of high-grade tectonic blocks from the New Idria serpentinite body, Diablo Range, California, Petrologic constraints on the tectonic evolution of an active serpentinite diapir, *in* Cloos, M., Carlson, W. D., Gilbert, M. C., Liou, J. G. and Sorensen, S. S. (eds.) Convergent Margin Terranes and Associated Regions , A Tribute to W. G. Ernst , Geological Society of America, Special Papers 419, 67–80.

Van Baalen, M.R., 1993, Titanium mobility in metamorphic systems, A review , Chemical Geology, 110, 233–249.

Van Baalen, M.R., 2004, Migration of the Mendocino triple junction and the origin of titanium- rich mineral suites at new Idria, California , International Geology Review, 46, 8, 671-692, 10.2747/0020-6814.46.8.671.

Vermeesch, P.; Miller, D.D., Graham, S.A., De Grave, J., McWilliams, M.O., 2006, Multimethod detrital thermochronology of the Great Valley Group near New Idria, California, Geological Society Of America Bulletin, 118, 1-2, 210-218, 10.1130/B25797.1.

Whitney D.L.; Evans B.W., 2010, Abbreviations for names of rock-forming minerals , American Mineralogist, 95, 185-187.

FIGURE 3.1

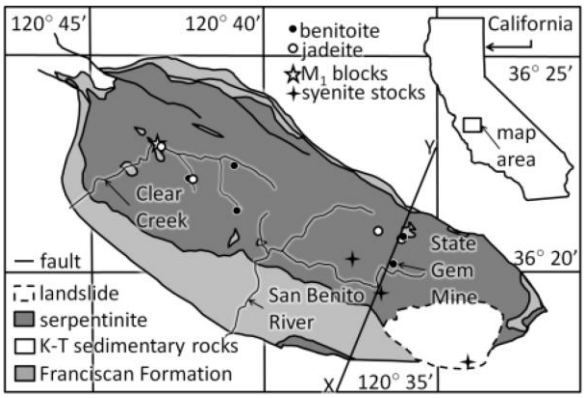
120° 45′
120° 40′
benitoite
jadeite
M1 blocks
syenite stocks
California
36° 25′
map
area
Y
Clear
Creek
State
Gem
Mine
36° 20′
fault
landslide
serpentinite
K-T sedimentary rocks
Franciscan Formation
San Benito
River
X
120° 35′

FIGURE 3.2

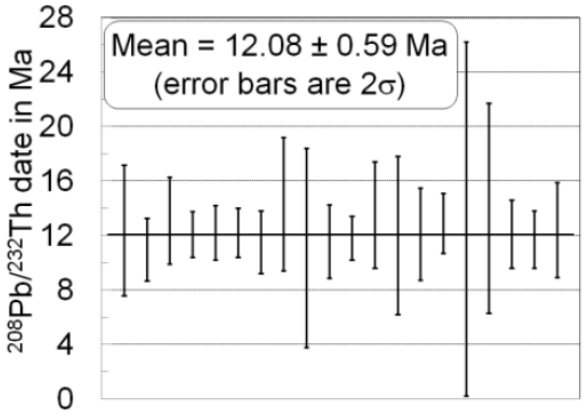
Mean = 12.08 ± 0.59 Ma
(error bars are 2σ)
$^{208}Pb/^{232}Th$ date in Ma
28
24
20
16
12
8
4
0

FIGURE 3.3

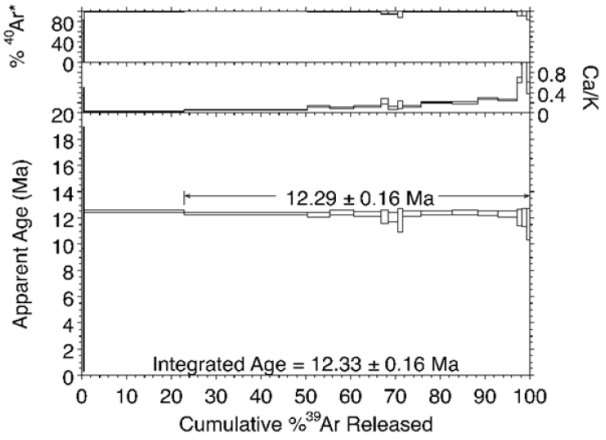
% 40Ar*
80
40
0
Ca/K
0.8
0.4
0
20
18
16
14
12
10
8
6
4
2
0
Apparent Age (Ma)
12.29 ± 0.16 Ma
Integrated Age = 12.33 ± 0.16 Ma
0 10 20 30 40 50 60 70 80 90 100
Cumulative %39Ar Released

CHAPTER 4

IMPLICATIONS OF EXOTIC META-TRONDHJEMITE MINERALS FOR THE METAMORPHIC CONDITIONS AND EXHUMATION HISTORY OF THE SANGSANG OPHIOLITE, YARLUNG SUTURE ZONE, SOUTHERN TIBET

ABSTRACT

Meta-trondhjemite pods found within serpentinite matrix mélange rocks of the Sangsang ophiolite complex of the Yarlung suture zone in south central Tibet contain the rare metamorphic assemblages albite ± winchite ± katophorite and neptunite ± benitoite ± joaquinite. This first assemblage implies metamorphism under high-pressure epidote-amphibolite-facies conditions. I interpret it, as well as associated magnesio-riebeckite-bearing, blueschist-facies assemblages within the suture zone at Sangsang, as having formed within a subduction accretion complex along the southern margin of Eurasia prior to the India-Eurasia collision. Although there are no constraints on the pressure and temperature conditions associated with the second assemblage, comparisons with other known occurrences suggest that it may form during metasomatism related to exhumation of high-pressure epidote-amphibolte or blueschist terrains. Structurally higher units in the Sangsang ophiolite complex did not experience the epidote-amphibolite to blueschist facies event, as evidenced by the existence of a ca. 120 Ma unconformity between uppermost Sangsang ophiolite complex and the overlying, essentially unmetamorphosed Xigaze Group forearc sedimentary succession. I attribute this metamorphic discontinuity to a previously unrecognized normal fault within the ophiolite complex, with a minimum tectonic denudation by normal faulting of ca. 17 km, close in age to India-Eurasia collision. As such, the initiation of this fault may record the timing of collision.

INTRODUCTION

Several ophiolites have been described within the Yarlung suture zone (Figure 4.1a), which marks the zone of collision between the Indian and Eurasian plates within the Himalayan-Tibetan orogenic system (e.g. Hébert et al., 2012; Hodges, 2000; Yin and Harrison, 2000). Despite their tectonic significance, there have been relatively few studies of the deformational and metamorphic histories of these complexes because most are extensively serpentinized and do not readily yield metamorphic pressure (P) and temperature (T) constraints. Unfortunately, many of the metasedimentary rocks within the suture zone also have been found to have high-variance mineral assemblages that frustrate attempts to reconstruct their PT histories. Most successful studies rely heavily on rare and unusual metamorphic assemblages found in the ophiolites and associated rocks (e.g. Guilmette et al., 2008; Guilmette et al., 2009). In this study, I report the existence of one such assemblage within meta-trondhjemite pods in the Sangsang ophiolite of southwestern Tibet. These pods contain the rare minerals winchite, katophorite, benitoite, neptunite, and joaquinite, which help constrain the exhumation history of Yarlung suture zone metamorphic rocks prior to India-Eurasia collision.

GEOLOGY OF THE SANGSANG OPHIOLITE

The Sangsang ophiolite (Figure 4.1b) is primarily represented by a massive serpentinite body, though recognizable protoliths are preserved both as blocks within the serpentinite and as fault-bounded slices both immediately north and south of the serpentinites (Bédard et al., 2009). The lithologic variety of relict metaigneous rocks in the serpentinite (dunite, harzburgite, websterite, gabbro, diabase, basalt, and andesite), as

well as the presence of exotic blocks of low-grade metasedimentary rocks (metasandstone, chert, and marble), imply that the serpentinite body is best described as a serpentinitic mélange. The majority of the serpentine matrix is massive and green to brown with minor chrysotile. Mafic protolith lithologies are commonly rodingitized. The serpentinitic mélange is bound to the north by a depositional unconformity, above which lie essentially unmetamorphosed rocks of the Xigaze Group forearc sediments (Maffione et al., 2015). Based on its current dip, the unconformity underlying the Xigaze Group has been rotated a minimum of roughly 90°. The base of the serpentinitic mélange has been mapped as a discrete thrust fault: the 'Yarlung Zangbo Mantle thrust' of Ding et al. (2005). Structurally deeper rocks are even more chaotic sedimentary to metamafic matrix subduction mélanges that include diagnostic blueschist facies metamorphic assemblages (Ding et al., 2005).

Bédard et al. (2009) interpreted the Sangsang ophiolite as representing oceanic crust from a forearc, supra-subduction zone environment. There have been few published geochronologic results that constrain the eruptive age of Sangsang oceanic crust, its metamorphism, and emplacement within the suture zone. Contact relationships with the Xigaze forearc sequence require only that serpentinization (and therefore exposure of the serpentinized rocks on the seafloor) must predate the unconformity that separates them inasmuch as basal Xigaze units contain serpentinite clasts. This unconformity is no older than 129 Ma based on the U/Pb ages of the youngest detrital zircons found in the basal Xigaze Group (Huang et al., 2015; Maffione et al., 2015). Zircon U/Pb geochronology of oceanic crustal fragments within the nearby (and better preserved) Xigaze ophiolite require eruption of oceanic crust between 127 and 124 Ma, and similar $^{40}Ar/^{39}Ar$

hornblende dates for the garnet-amphibolite-facies metamorphic sole of the ophiolite imply rapid disruption (fragmentation) of this crust soon after eruption (Guilmette et al., 2009). A similar history has been proposed for the Sangsang ophiolite by Bédard et al. (2009).

At least part of the disruption of the Sangsang ophiolite occurred in an ocean floor environment, probably through hyperextension and development of oceanic metamorphic core complexes as envisioned by Maffione et al. (2015). Ding et al. (2005) interpreted ca. 63 Ma $^{40}Ar/^{39}Ar$ amphibole dates from lowermost blueschist facies rocks immediately below the Yarlung Zangbo Mantle thrust as indicative of obduction of the ophiolite over the subduction mélange at that time. Emplacement of the Sangsang ophiolite at its present structural level presumably occurred no more recently than during India-Eurasia collision, which – in this sector of the Himalaya – has been inferred as occurring between the Paleocene (Ding et al., 2005; DeCelles et al., 2015) and early Oligocene (Aitchison et al., 2007).

META-TRONDHJEMITES WITHIN THE SANGSANG OPHIOLITE

Although the structural geology of the Sangsang ophiolite is beyond the scope of this contribution, one of the more important structures identified within the serpentinite thus far is a steeply-dipping (near-vertical) shear zone that strikes roughly parallel to the regional outcrop pattern of the ophiolite (Figure 4.1b). Based on a restoration of the basal unconformity beneath the Xigaze Group farther north to its original paleo-horizontal orientation, it is likely that the shear zone (which is nearly parallel to the unconformity) originally dipped shallowly. Where studied I studied this shear zone in detail, the

structure is marked by several tens to roughly 100 meters of shearing, with anastomosing shear fabrics subparallel to the overall orientation of the shear zone. Much of this highly deformed zone is characterized by quartz veining and the conversion of serpentinite to soapstone. I was unable to find fabrics within the shear zone that definitively indicate shear sense.

Along this shear zone, I discovered three resistant lenses (herein called 'pods') of an exotic, albite-rich rock type unlike the surrounding serpentinite or other exotic lithologies within the serpentinite (Figure 4.1b). Based on the lithologic and mineralogic similarities among these pods and rocks from a comparable geologic setting in central Japan (Sakai and Akai 1994), I interpret the pods to be metamorphosed trondhjemites (plagiogranites) within the ophiolite. Distributed over a distance of roughly 2 km, these pods range in size (as measured on the outcrop surface) from 250 m x 100 m to 10 m x 5 m. Only the westernmost pod (Figure 4.2a) cropped out in such a way as to reveal its thickness (ca. 25 m). All are elongate parallel to the shear zone and mantled by thin (≤ 10 cm) rims of characteristically light blue serpentine and talc with nodules of tremolite and diopside. These alteration rims were not observed around other exotic blocks elsewhere within the ophiolitic mélange. The unusual lithology of the pods, the fact that all three occur within 20 km of one another, and their shared structural position along the vertical shear zone within the serpentinitic mélange invite the interpretation that all three were once part of a single disrupted block.

The eastern and western pods express similarly in outcrop. Both are schistose to phyllitic, displaying alternating layers of a blue amphibole and albite with grain sizes of up to about a millimeter. Long axes of the amphiboles are aligned parallel to foliation.

This primary foliation is itself deformed by numerous mesoscopic to macroscopic folds of multiple orientations and cut by microscopic to mesoscopic quartz veins. Mineral proportions for the eastern and western pods are ~90% albite with the remainder amphibole.

Unlike the other pods, the middle pod is unfoliated (Figure 4.2b and c). It is typically coarser grained, with major phases ranging from 0.1 to 2 mm. While the mineralogy of this pod is also mostly albite and blue amphibole, up to 10% by modal proportion is benitoite and/or neptunite, with minor amounts of joaquinite and zircon. The albites in this pod (white) commonly exhibit dueteric alteration and grain boundary bulging (Figure 4.2b). Individual amphiboles are deep blue to blue green. Larger crystals occur as spindly bundles, often with concave margins, often connected by amphibole "stringers." Smaller (ca 0.5 mm) aggregates of amphiboles form stellate clusters. The benitoites are mostly colorless to dichroic (colorless to blue), euhedral to subhedral, and have the tabular dipyramidal habit typical of the species. Some benitoites contain joaquinite inclusions, making them appear yellow. All benitoites fluoresce bright blue under short-wave ultraviolet light. The neptunites form deep red, poorly terminated prisms that occasionally exhibit "elbow" twinning. Joaquinite grains are yellow and exhibit lamellar twinning. They have habits similar to the larger amphibole grains that often mantle them. Zircons are usually square dipyramids, with dimensions of ca. 100 µm by ca. 40 µm. All phases except zircon and amphibole are observed to form euhedral crystals on the surfaces of ca. 1 mm vugs in the middle pod.

MINERAL CHEMISTRY

In order to establish the chemistry of the unusual minerals found in the Sangsang meta-trondhjemites, I analyzed individual crystals by laser ablation, inductively coupled, plasma-source mass spectrometry (LA-ICPMS) in the Group 18 Laboratories at Arizona State University.

Methods

Minerals were separated from field samples using conventional gravimetric and magnetic procedures, and then were hand-picked to ensure that the analyzed crystals were as inclusion free as possible and showed no signs of alteration (based on microscopic examination). The crystals were then embedded in epoxy and polished prior to analysis. Material extractions were done using a Photon Machines *Analyte G2* instrument package that features an *Atlex 300* ArF excimer ultraviolet (193 nm) laser and HelEx ablation cell and the chemical analyses were performed using a Thermo Scientific *iCAP Q* quadrupole ICPMS.

Ablations involved rastering a 20 µm laser spot across the sample over a distance of ~600 µm. In doing so, I applied a 4 mJ laser energy at 50% output power and a pulse frequency of 4 Hz for a total of ca. 60 s. Ablated material was continuously transferred into the plasma source of the *iCAP Q* using a mixed He+Ar carrier gas. For most analyses, a plasma RF power of 1400 W was used. Prior to each unknown and standard analysis, a 20 s background run was done, and a 20 s washout followed each analysis. I selected isotopes to measure based on the reported compositions of minerals in the joaquinite and neptunite groups. Measured isotopes were: ^{7}Li, ^{23}Na, ^{24}Mg, ^{27}Al, ^{29}Si, ^{44}Ca, ^{47}Ti, ^{51}V, ^{55}Mn, ^{57}Fe, ^{64}Zn, ^{88}Sr, ^{89}Y, ^{93}Nb, ^{125}Te, ^{129}Xe, ^{134}Ba, ^{139}La, ^{140}Ce, ^{141}Pr,

^{146}Nd, ^{147}Sm, ^{153}Eu, ^{157}Gd, ^{159}Tb, ^{163}Dy, ^{165}Ho, ^{166}Er, ^{169}Tm, ^{172}Yb, ^{175}Lu, ^{232}Th, and ^{238}U for joaquinite, ^{7}Li, ^{23}Na, ^{24}Mg, ^{27}Al, ^{29}Si, ^{39}K, ^{44}Ca, ^{47}Ti, ^{51}V, ^{55}Mn, ^{57}Fe, ^{64}Zn, ^{88}Sr for amphiboles, ^{23}Na, ^{27}Al, ^{29}Si, ^{47}Ti, ^{51}V, ^{55}Mn, ^{57}Fe, ^{88}Sr, and ^{134}Ba for benitoite, and ^{7}Li, ^{23}Na, ^{24}Mg, ^{27}Al, ^{29}Si, ^{39}K, ^{44}Ca, ^{47}Ti, ^{51}V, ^{55}Mn, ^{57}Fe, and ^{64}Zn for neptunite. For all analyses, I used NIST glass SRM 610 as my primary standard, and a standard analysis was run between every 5 unknowns, between measurements on different minerals, and at the beginning and end of every day's analytical session. Data were reduced using the *Iolite* software package (Paton et al., 2011) using its trace element data reduction scheme (Woodhead et al., 2007), which results in an output of semi-quantitative elemental weight percentages for each analysis. These data were then normalized such that all measured elements summed to 100 weight percent. At the 2σ (~ 95%) confidence level, assumed uncertainties for major elements were ~5 % of the reported values, whereas those for trace elements were ~10 %. Based on comparable analyses of different parts of the crystals within each raster, I found no evidence for substantial intracrystalline zoning in any of the studied phases.

Results

We analyzed five amphiboles from the middle pod and six from the eastern pod. The results (Table 4.1) are suggestive of two distinctive mineral compositions. Using charge balance to calculate the relative proportions of Fe^{3+}, I obtained the following average formulas:

$$(Na_{0.06}K_{0.56})_{\Sigma=0.62}(Na_{1.28}Ca_{0.72})(Fe^{2+}_{2.48}Fe^{3+}_{0.70}Al_{0.03}Mg_{1.67}Mn_{0.01}Li_{0.04}Ti_{0.07})(Si_{7.92}Al_{0.08})O_2{}_2OH_2,$$

and

$(Na_{0.02}K_{0.12})_{\Sigma=0.14}(Na_{0.78}Ca_{1.22})(Fe^{2+}_{2.20}\ Fe^{3+}_{0.40}Al_{0.26}Mg_{2.19}Mn_{0.01}Li_{0.04}Ti_{0.02})Si_8O_{22}OH_2$.

Based on their chemistry and the recent classification scheme of Hawthorne et al. (2012), the first composition represents a type of katophorite, whereas the second represents a type of winchite. Both katophorite and winchite are confirmed to exist in the eastern pod, whereas only the former is confirmed to exist in the middle pod.

Seven translucent benitoites from the middle pod (six blue and one colorless) were analyzed (Table 4.2). All yielded similar results, indicating an average chemical formula of:

$$Ba_{0.94}Ti_{1.03}(Si_{2.97}Ti_{0.02}Al_{0.01})_{\Sigma=3}O_9.$$

Our analyses of this rare mineral are consistent with previously reported results from the type locality in San Benito County, California in addition to localities in Japan and Arkansas (Laird and Albee 1972; Laurs et al., 1997).

We obtained LA-ICPMS compositional data for fifteen individual crystals of neptunite from the middle pod (Table 4.3). The calculated average chemical formula for these neptunites is:

$$(K_{0.93}Na_{0.04}Li_{0.03})_{\Sigma=1}Na_2Li(Fe_{1.67}Mg_{0.34}Mn_{0.01})_{\Sigma=2.02}Ti_{1.97}Si_{8.02}O_{24},$$

which is well within the variation observed for other neptunite analyses (Laird and Albee, 1972; Zadov et al., 2011).

Ten joaquinite crystals from the middle pod were analyzed, yielding a relatively narrow range of compositions (Table 4.4). Since joaquinite is variably hydrous, I normalized the compositional data such that Si + Al =8 for the purposes of calculating a chemical formula:

$$Ba_2(Na_{0.79}Ca_{0.24})_{\Sigma=1.03}(REE_{1.47}Sr_{0.48}Th_{0.04})_{\Sigma=1.99}(Fe_{0.90}Mg_{0.02}Li_{0.20}Ti_{0.17}Nb_{0.01})_{\Sigma=1.30}Ti_2$$

$$(Si_{7.98}Al_{0.02})_{\Sigma=8}O_{26}(OH_{0.41}O_{0.59})_{\Sigma=1}\cdot H_2O,$$

where the relative abundances of OH and O are based on total charge balance. While the apparent excess of atoms in the Fe and, to a lesser extent, the Na site seem to violate stoichiometry, it should be noted that charge deficiencies caused by Li, Sr, and Al in sites where they are not dominant are nearly balanced out by charge excesses created by similarly out of place Ca, Ti, Nb, Th, and U. (For this discussion, sites in joaquinite are referred to by their dominant cation.) The apparent deficiencies can be eliminated easily by interpreting 0.05 atoms per formula unit of either Fe or Mn as Fe^{3+} or Mn^{3+}instead. Furthermore, adding up the species with their typical charges (using Fe^{2+} and Mn^{2+}) requires 26.79 O for charge balance, which is within the acceptable range for joaquinite due to O and OH solid solution. Notably, excess in the Fe and Na sites of joaquinite has been documented in the literature (e.g., Chihara et al., 1974; Laid and Albee, 1972; Matsubara et al., 2001).

PT CONDITIONS FOR METAMORPHISM OF THE META-TRONDHJEMITE ASSEMBLAGES

Assuming that albite + blue amphibole (katophorite and/or winchite) and neptunite + benitoite + joaquinite represent diagnostic equilibrium assemblages within the Sangsang meta-trondhjemites, I considered what the likely equilibrium PT conditions would have been at the time of crystallization. Unfortunately, most thermodynamic databases do not contain sufficient data for these minerals within the appropriate composition space, and thus quantitative thermobarometry or thermodynamic modeling is

not possible. The ubiquity of albite – rather than jadeite + quartz – requires that metamorphism occurred at pressures of less than ca. 1 GPa (Harlow, 1994). Other occurrences of the unusual Ti-rich minerals in this assemblage (benitoite, joaquinite, and neptunite) are found in high P – low T (blueschist facies) metamorphic terrains, but they are commonly interpreted as related to alkali fluid alteration and thus may not have formed at blueschist-facies conditions (Laurs et al., 1997; Sakai and Akai, 1994; Van Baalen 2014). While thin section textures observed for samples from the middle pod at Sangsang do not show obvious evidence that these Ti-rich minerals are secondary, and I interpret them to be part of an equilibrium metasomatic assemblage that formed after the blue amphiboles but at similar P-T conditions. Unfortunately, the unfoliated character of the middle pod does not allow me to evaluate whether or not the blue amphiboles in this assemblage were definitively coeval with the fabric-forming blue amphiboles in the other pods; it is possible, perhaps likely, that the pods collectively provide evidence for multiple generations of blue amphiboles.

Potentially, my most useful P-T constraints might be provided by the occurrence of winchite in the eastern pod. While there is general agreement that winchite has a limited stability field, there is some disagreement as to the P-T limits for natural assemblages. On Figure 4.3, I show two different stability fields suggested by Otsuki and Banno (1990) and Okamoto and Toriumi (2004). Although there is some overlap between these two fields, Otsuki and Banno generally favor lower P and T for the stability field than Okamoto and Toriumi. The higher PT stability field of Okamoto and Toriumi seems more compatible with albite deformation textures in the Sangsang samples. While the majority of the albite is fractured in the eastern and western pods, which exhibit better

tectonite fabrics, some larger crystals exhibit undulatory extinction, indicative of a degree of plastic deformation. Although a variety of factors may influence the temperature range of the brittle-crystal plastic transition for albite (e.g., Eberlei et al., 2014; Fitz Gerald and Stünitz, 1993), most work has suggested that the onset of crystal plastic behavior begins at ca. 450˚C. This temperature is near the upper temperature limit of winchite favored by Otsuki and Banno (1990), but well within the winchite temperature field of Okamoto and Toriumi (2004). On balance, I feel that the Okamoto and Toriumi (2004) stability field better represents the possible range of pressures and temperatures at which winchite formed at Sangsang.

Unfortunately, the stability field of katophorite is not constrained by experimental data to the best of my knowledge. However, known occurrences of katophorite are limited to two localities where the mineral formed during high-pressure Na-metasomatism (Ali and Arai, 2013; Oberti et al., 2015). In their re-examination of holotype katophorite, Oberti et al. (2015) argued that katophorite is the initial high-P low-T metasomatic phase created as a precursor to the production of jadeitites. It is worth noting that katophorite from both of these localities are more Mg and Cr rich/Fe and K poor than my samples, which has unknown implications for katophorite stability. The textural relationships between katophorite and winchite in the eastern meta-trondhjemite pod imply that the two amphiboles crystallized under approximately the same P-T conditions. Assuming that all of the pods were once part of the same block, I infer that the blue amphiboles+albite meta-trondhjemite assemblage – though perhaps not including the unusual suite of Ti-rich minerals found within these rocks – crystallized within the stability field of winchite at temperatures of ca. 450-500˚C and at pressures in

the range of 500-1000 MPa, equivalent to paleodepths of 20 to 35 km. These PT conditions also fall within the stability field of jadeite (Harlow et al., 2015), and are therefore also consistent with what little is known about katophorite stability. Adopting the metamorphic facies boundaries of Tsai et al. (2013), these pressure and temperature ranges are indicative of high-pressure epidote amphibolite facies conditions.

A conundrum is introduced by evidence of grain boundary migration (bulging) in rare, coarser-grained albite aggregates found in the middle pod (Figure 4.2b). This mode of feldspar deformation is generally thought to be indicative of high temperature (> 600˚C; Fitz Gerald and Stünitz, 1993; Rosenberg and Stünitz, 2003). However, there is no mineralogical evidence in the pods for such high-grade metamorphism. Unless albite grain boundary migration can take place at lower temperatures than is commonly assumed, the most likely explanation for albite grain bulging is that the affected grains are relict porphyrocrysts that experienced older, high-temperature metamorphism earlier in the tectonic evolution of the ophiolite.

COMPARISON OF THE SANGSANG OCCURRENCE OF RARE TITANIUM MINERALS WITH OTHER EXAMPLES

The Sangsang occurrence of benitoite + neptunite + joaquinite adds to a very small number of known localities for these rare Ti minerals. Previously described occurrences fall into two categories, both suggestive of a metamorphic and/or metasomatic origin. The first and more reported occurrence is as minor constituents in association with alkali igneous rocks, typically a class of nepheline syenites known as agpaites (Chakhmouradian et al., 2002; Laurs, 1997; Matsubara et al., 2001; Sørenson,

1997; Zadov et al., 2011; Zubkova et al., 2004). In this category, textural evidence indicates that the rare Ti-minerals post-date the initial magmatic assemblages. The second type of occurrence is as metamorphic minerals within blocks containing Na-amphiboles that, in turn, occur within serpentinites. These examples are only found where the serpentinites contain blueschists, jadeitites, and non-agapaitic alkali intrusions (Laurs, 1997; Sakai and Akai, 1994). The second type is also notable for containing the only previously known, non-microscopic crystals of benitoite; in this form, benitoite is a highly sought after gem mineral. The meta-trondhjemite assemblage described here is most closely related to this category of occurrence.

The classical locality for this assemblage – and the type locality for benitoite and joaquinite – is within a serpentinite diapir at New Idria, San Benito County, California (Coleman, 1957). The diapirism is thought to represent a significant mantle exhumation event of high-pressure rocks that included, in its later stages, crystallization of the rare Ti mineral suite (Van Baalen, 2004; Vermeesch et al., 2006; Tsujimori et al., 2007). Benitoite, neptunite, and joaquinite from New Idria and Sangsang are compositionally similar, and the Sangsang meta-trondhjemites bear a general similarity to the host rocks of the assemblage found at New Idria, although the New Idria host rocks are associated with jadeitites, which I did not observe at Sangsang. However, the presence of katophorite at Sangsang may be taken as indicative that the meta-trondhjemites did undergo limited metasomatism, but that the pods may not have remained at depth long enough prior to exhumation for the metasomatic event to have resulted in the growth of jadeite.

Our pods also are similar to the albitites found in a serpentinite body near Ohmi, Niigata Prefecture, Central Japan (Sakai and Akai, 1994). The Ohmi albitite host pod is of similar size to the larger Sangsang pods, and similarly occurs within a shear zone. Like the eastern and western pods at Sangsang, the Ohmi host body is highly tectonized, but it includes some apparently more rigid, unfoliated domains similar in many ways to the middle pod at Sangsang. The mineralogy of the Ohmi pod is also similar, characterized by a predominance of albite with subordinate amphiboles. Both are dominantly albite with subordinate blue amphibole and lesser abundances of the rare Ti minerals. At the same time, the two localities display some differences. First, the Ohmi albitites lack neptunite. This could simply be due to differences in bulk compositions of the host rocks, with the Japanese rocks lacking sufficient Li. Second, the Ohmi occurrence, like the New Idria occurrence, is associated with jadeitites. Thirdly, blocks of essentially undeformed rock with recognizable trondhjemite texture and mineralogy are preserved within the albitite, confirming the protolith for the pod.

THE TECTONIC SIGNIFICANCE OF THE SUBVERTICAL SHEAR ZONE AT SANGSANG

The assemblages found within the meta-trondhjemites indicate equilibrium pressures inconsistent with their structural position. The part of the ophiolite exposed north of these pods is structurally continuous with the unmetamorphosed base of the Xigaze Group (Figure 4.1). This implies that the shear zone along which the pods are found is tectonically significant. I found no mineral assemblages that closely constrain PT conditions within the serpentinitic mélange south of the shear zone and north of the

Yarlung Zangbo Mantle thrust. However, the sedimentary-matrix mélange in the footwall of that thrust contains metamorphic assemblages compatible with the PT conditions implied by my meta-trondhjemite assemblages (Ding et al., 2005). It is thus plausible that the entire succession of ophiolites and serpentinitic and subduction mélange to the south acted as a coherent structural unit at the time of slip on the shear zone.

The juxtaposition of meta-trondhjemite pods in the shear zone that crystallized at a minimum pressure of ca. 500 MPa and rocks to the north that were likely no more than a kilometer or so beneath the surface at the time of faulting implies that the structure accommodated a minimum of ca. 17 km of tectonic denudation by normal faulting. The presence of the second assemblage in addition to the Na-Ca amphiboles suggests that this denudation was coeval with the growth of Ti-minerals during metamorphism.

CONCLUSIONS

Meta-trondhjemite pods found within the serpentinitic mélange of the Sangsang ophiolite provide important information regarding minimum pressures of subduction-related metamorphism immediately prior to the India-Eurasia collision and the degree of subsequent tectonic exhumation during Yarlung suture zone development. Based on the presence of the assemblage winchite ± katophorite, I infer a minimum of 17 km of vertical displacement along what is currently a vertically oriented shear zone. If this assemblage is coeval with or postdates previously documented metamorphism at similar conditions nearby at ca. 63 Ma (Ding et al., 2005), the extensional event described in this contribution must have occurred subsequently and may be a secondary effect related to the early stages of India-Eurasia collision, long after the hyperextension event in a forearc

setting that has been described as affecting the Sangsang ophiolite at ca. 120 Ma (Maffione et al., 2015). The Ti-minerals, by comparison with New Idria (Van Baalen, 2004), it may be associated with decompression related to slip on the extensional structure.

ACKNOWLEDGEMENTS

Analytical aspects of my research were supported by a grant from the U.S. National Science Foundation's Continental Dynamics program (EAR 1007929) to K.V. Hodges. I thank the U.S. National Science Foundation's Earth Sciences Instrumentation and Facilities program for partial support for the acquisition of analytical instrumentation in the Group 18 Laboratories.

FIGURE CAPTIONS

Figure 4.1. Maps of the study area modified from Maffione et al. (2015) to show the position of the shear zone within serpentinite and the albitite pods. Frame 1a shows a regional overview of the ophioltes within the Yalung suture zone and surrounding rocks with local names for reference. Frame 1b shows a detailed view of the Sangsang ophiolite overlayed on a satellite image with major rock units and structures labeled. Meta-trondjhemite pods are highlighted in red.

Figure 4.2. Frame a: Field photo of the western meta-trondhjemite pod looking due west from the eastern pod. Frames b and c: Unpolarized photomicrographs of a middle pod

sample with important rare minerals indicated: Bn – benitoite; Jq – joaquinite; Kt – katophorite; Nt – neptunite. Bulges in the albite indicated by the red arrow.

Figure 4.3. Pressure-temperature diagram highlighting the stability field of winchite with respect to the major metamorphic facies. Two proposed stability fields for winchite are shown: Otsuki and Banno (1990; darker shading) and Okamoto and Toriumi (2004; lighter shading). Facies boundaries are after Tsai et al. (2013).

REFERENCES

Aitchison, J.C.; Ali J.R.; Davis A.M., 2007, When and where did India and Asia collide? Journal of Geophysical Research – Solid Earth, 112, B5, doi, 10.1029/2006jb004706.

Ali, M.; Arai, S., 2013, Cr-rich magnesiokatophorite as an indicator of mantle metasomatism by hydrous Na-rich carbonatite, J Miner Petrol Sci, 108, 215-226, 10.1180/minmag.2015.079.2.13

Bédard, E.; Hébert, R.; Guilmette, C.; Lesage, G.; Wang, C.S.; Dostal, J., 2009, Petrology and geochemistry of the Saga and Sangsang ophiolitic massifs, Yarlung Zangbo Suture Zone, Southern Tibet, Evidence for an arc-back-arc origin, Lithos, 113, 1-2, 48-67, 10.1016/j.lithos.2009.01.011.

Chakhmouradian, A.R.; Mitchell, R.H., 2002, The mineralogy of Ba- and Zr-rich alkaline pegmatites from Gordon Butte, Crazy Mountains Montana, USA, comparisons between potassic and sodic agpaitic pegmatites, Contrib Mineral Petr, 143, 1, 93, 114, 10.1007/s00410-001-0333-6.

Chihara, K.; Komatsu, M.; Mizota, T.; 1974, A joaquinite-like mineral from Ohmi, Niigata Prefecture, Central Japan, Mineralogical Journal, 7, 4, 395-399.

Coleman, R.G., 1957, Mineralogy and petrology of the New Idria district, California. Dissertation, Stanford University.

Dai, J.G.; Wang, C.S.; Polat, A.; Santosh, M.; Li,Y.L.; Ge, Y.K., 2013, Rapid forearc spreading between 130 and 120 Ma, Evidence from geochronology and geochemistry of the Xigaze ophiolite, southern Tibet, Lithos. 172, 1, 16. 10.1016/j.lithos.2013.03.011.

Ding, L.; Kapp, P.; Wan X.Q.; 2005, Paleocene-Eocene record of ophiolite obduction and initial India-Asia collision, south central Tibet, Tectonics, 24, 3, TC3001, 10.1029/2004TC001729.

Eberlei, T.; Habler, G.; Grasemann, B.; Abart, R., 2014, Upper–greenschist facies intragrain deformation of albite in mylonitic meta–pegmatite and the influence of crystallographic anisotropy on microstructure formation, J Struct Geol, 69, 47-58

Fitz Gerald, J.D.; Stunitz, H., 1993, Deformation of granitoids at low metamorphic grade. 1. Reactions and grain-size reduction. Tectonophysics, 221, 3-4, 269-297, 10.1016/0040-195193,90163-E.

Guilmette, C.; Hébert, R.; Dupuis, C.; Wang, C.S.; Li, Z.J., 2008, Metamorphic history and geodynamic significance of high-grade metabasites from the ophiolitic melange beneath the Yarlung Zangbo ophiolites, Xigaze area, Tibet, J Asian Earth Sci, 32, 5-6, 423-437, 10.1016/j.jseaes.2007.11.013.

Guilmette, C.; Hébert, R.; Wang, C.S.; Villeneuve. M., 2009, Geochemistry and geochronology of the metamorphic sole underlying the Xigaze Ophiolite, Yarlung Zangbo Suture Zone, South Tibet, Lithos, 112, 1-2, 149-162, 10.1016/j.lithos.2009.05.027

Harlow, G.;E.; 1994, Jadeitites, albitites and related rocks from the Motagua fault zone, Guatemala, J Metamorph Geol, 12, 1, 49-68, 10.1111/j.1525-1314.1994.tb00003.x.

Hawthorne, F.C.; Oberti, R.; Harlow, G.E.; Maresch, W.V.; Martin, R.F.; Schumacher, J.C.; Welch, M.D., 2012, Nomenclature of the amphibole supergroup, Am Mineral, 97, 11-12, 2031-2048, 10.2138/am.2012.4276.

Hébert, R.; Bezard. R.; Guilmette. C.; Dostal. J.; Wang, C.S.; Liu, Z.F., 2012, The Indus-Yarlung Zangbo ophiolites from Nanga Parbat to Namche Barwa syntaxes, southern Tibet, First synthesis of petrology, geochemistry, and geochronology with incidences on geodynamic reconstructions of Neo-Tethys, Gondwana Res, 22, 2, SI, 377-397, 10.1016/j.gr.2011.10.013.

Hodges, K.V., 2000, Tectonics of the Himalaya and southern Tibet from two perspectives, Geol Soc Am Bull, 112, 3, 324-350, 10.1130/0016-76062000,112<0324, TOTHAS>2.3.CO;2.

Huang, W.T.; van Hinsbergen, D.J.J.; Maffione, M.; Orme D.A.; Dupont-Nivet, G.; Guilmette, C.; Ding, L.; Guo, Z.J.; Kapp, P., 2015, Lower Cretaceous Xigaze ophiolites formed in the Gangdese forearc, Evidence from paleomagnetism, sediment provenance, and stratigraphy, Earth Planet Sc Lett, 415, 142-153, 10.1016/j.epsl.2015.01.032.

Laird, J.; Albee, A.L., 1972, Chemical composition and physical, optical, and structural properties of benitoite, neptunite, and joaquinite, Am Mineral, 57, 1-2, 85-102.

Laurs, B.M.; Rohtert, W.; Gray M., 1997, Benitoite from the New Idria District, San Benito County, California. Gems Gemol. 33, 166–187.

Leake, B,E.; Woolley, A.R.; Arps, C.E.S.; Birch, W.D.; Gilbert, M.C.; Grice, J.D.; Hawthorne, F.C.; Kato, A.; Kisch, H.J.; Krivovichev, V.G.; Linthout, K.; Laird, J.; Mandarino, J.A.; Maresch, W.V.; Nickel, E.H.; Rock, N.M.S.; Schumacher, J.C.; Smith, D.C.; Stephenson, N.C.N.; Ungaretti, L.; Whittaker, E.J.W.; Guo, YZ., 1997, Nomenclature of amphiboles, Report of the subcommittee on amphiboles of the International Mineralogical Association, commission on new minerals and mineral names, Am Mineral, 82, 9-10, 1019-1037.

Maffione, M.; van Hinsbergen, D.J.J.; Koornneef, L.M.T.; Guilmette, C.; Hodges, K.; Borneman, N.; Huang, W.; Ding, L.; Kapp, P.A., 2015, Forearc hyperextension dismembered the South Tibetan ophiolites, Geology, 42, 475-478,10.1130/G36472.1.

Matsubara, S.; Mandarino, J.A.; Semenov, E.I.; 2008, Redefinition of a mineral in the joaquinite group, Orthojoaquinite-La, Can Mineral, 39, 3, 757-760, 10.2113/gscanmin.39.3.757.

Oberti, R.; Boiocchi, M.; Hawthorne, F.C.; Ball, N.A.; Harlow, G.E., 2015, Katophorite from the Jade Mine Tract, Myanmar, mineral description of a rare grandfathered, endmember of the amphibole supergroup, Mineral Mag, 79, 355-363, 10.1180/minmag.2015.079.2.13.

Okamoto, A.; Toriumi, M., 2004, Optimal mixing properties of calcic and subcalcic amphiboles, application of Gibbs' method to the Sanbagawa schists, SW Japan, Contrib Mineral Petr, 146, 5, 529-545.

Otsuki, M.; Banno, S., 1990, Prograde and retrograde metamorphism of hematite-bearing basic schists in the Sambagawa belt in central Shikoku, J Metamorph Geol, 8, 4, 425-439. 10.1111/j.1525-1314.1990.tb00629.x.

Paton, C.; Hellstrom, J.; Paul, B.; Woodhead, J.; Hergt, J., 2011, Iolite, freeware for the visualization and processing of mass spectrometric data, J Anal Atom Spectrom, 26, 12, 2508-2518.

Rosenberg, C.L.; Stünitz, H., 2003, Deformation and recrystallization of plagioclase along a temperature gradient, an example from the Bergell tonalite, J Sruct Geol, 25, 389-408.

Sakai, M.; Akai, J., 1994, Strontium, barium and titanium-bearing minerals and their host rocks from Ohmi, Japan, Scientific Reports Niigata University, Series E, 9, 97-118.

Stipp, M.; Stunitz, H.; Heilbronner, R.; Schmid, S.M., 2002, The eastern Tonale fault zone, a 'natural laboratory' for crystal plastic deformation of quartz over a temperature range from 250 to 700 degrees C, J Struct Geol, 24, 12, 1861-1884, 10.1016/S0191-814102,00035-4.

Tsai. C.H.; Iizuka, Y., Ernst, W.G., 2013, Diverse mineral compositions, textures, and metamorphic P-T conditions of the glaucophane-bearing rocks in the Tamayen melange, Yuli belt, eastern Taiwan, J Asian Earth Sci, 63, SI, 218-233, 10.1016/j.jseaes.2012.09.019.

Tsujimori, T.; Matsumoto, K.; Wakabayashi, J.; Liou, J.G.; 2006, Franciscan eclogite revisited, Reevaluation of the P-T evolution of tectonic blocks from Tiburon Peninsula, California, USA, Mineral Petrol, 88, 1-2, 243-267, 10.1007/s00710-006-0157-1.

Van Baalen, M.R., 2004, Migration of the mendocino triple junction and the origin of titanium-rich mineral suites at new Idria, California, Int Geol Rev, 46, 8, 671-692, 10.2747/0020-6814.46.8.671.

van Staal. C.R.; Currie, K.L.; Rowbotham, G.; Goodfellow, W.; Rogers, N., 2008, Pressure-temperature paths and exhumation of Late Ordovician-Early Silurian blueschists and associated metamorphic nappes of the Salinic Brunswick subduction complex, northern Appalachians, Geol Soc Am Bull, 120, 11-12, 1455-1477, 10.1130/B26324.1.

Vermeesch, P.; Miller, D.D.; Graham, S.A.; De Grave, J.; McWilliams, M.O.; 2006, Multimethod detrital thermochronology of the Great Valley Group near New Idria, California, Geol Soc Am Bull, 118, 1-2, 210-218, 10.1130/B25797.1.

Woodhead, J.D.; Hellstrom, J.; Hergt, J.M.; Greig, A.; Maas, R., 2007, Isotopic and elemental imaging of geological materials by laser ablation inductively coupled plasma-mass spectrometry, Geostand Geoanal Res, 31, 4, 331-343.

Zadov, A.E.; Gazeev, V.M.; Karimova, O.V.; Pertsev, N.N.; Pekov, I.V.; Galuskin, E.V.; Galuskina, I.O.; Gurbanov, A.G.; Belakovsky, D.I.; Borisovsky, S.E.; Kartashov, P.M.; Ivanova, A.G.; Yakubovich, O.V., 2011, Magnesioneptunite, KNa2LiMg,Fe,2,Ti2Si8O24, a new mineral species of the neptunite group. Geol Ore Deposit+, 53, 8, 775-782, 10.1134/S1075701511080186.

Zolotarev, A.A.; Krivovichev, S.V.; Yakovenchuk, V.N., 2007, Refinement of the mangan-neptunite crystal structure, Geol Ore Deposit+, 49, 8, 835-838, 10.1134/S1075701507080181.

Zubkova, N.V.; Pushcharovskii, D.Y.; Giester, G.; Tillmanns, E.; Pekov, I.V.; Krotova, O.D., 2004, Crystal structure of byelorussite-Ce, NaMnBa2Ce2TiO,2,[Si4O12]2,F,OH, center dot H2O, Crystallogr Rep+, 49, 6, 964-968, 10.1134/1.1828140.

FIGURE 4.1

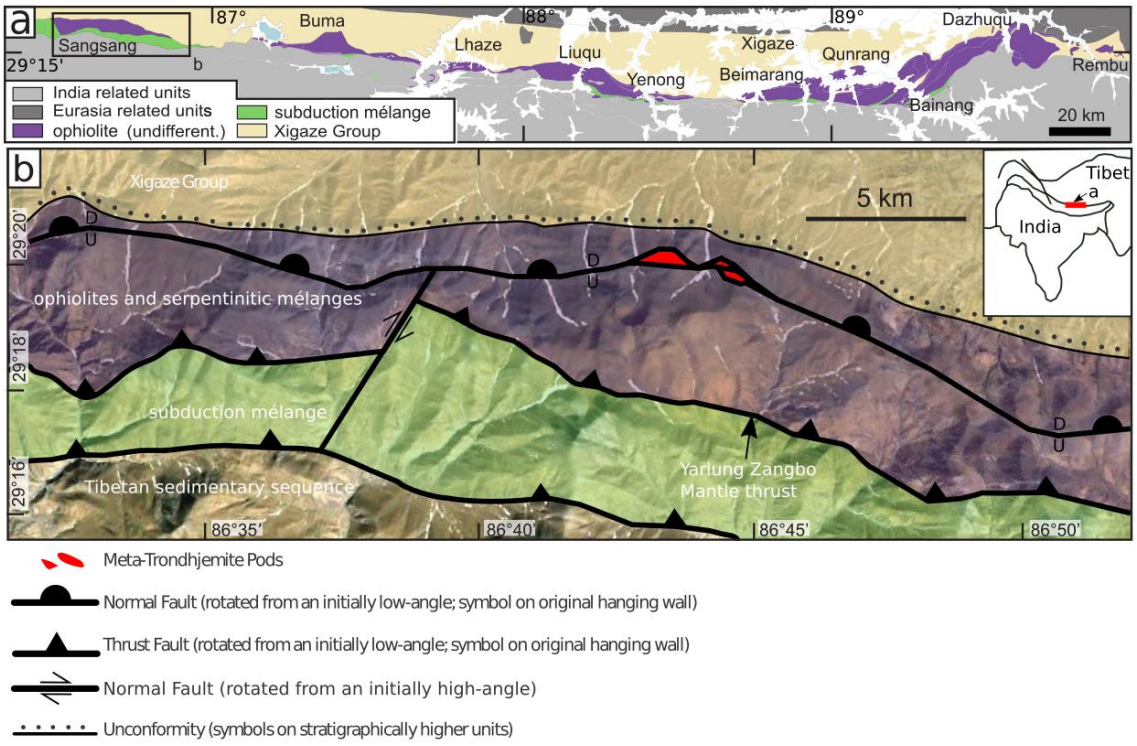
a
Sangsang
87°
88°
89°
29°15'
b
Buma
Lhaze
Liuqu
Yenong
Xigaze
Beimarang
Qunrang
Dazhuqu
Rembu
Bainang
20 km
India related units
Eurasia related units
ophiolite (undifferent.)
subduction mélange
Xigaze Group
b
Xigaze Group
5 km
Tibet
a
India
29°20'
29°18'
29°16'
ophiolites and serpentinitic mélanges
subduction mélange
Tibetan sedimentary sequence
Yarlung Zangbo
Mantle thrust
86°35'
86°40'
86°45'
86°50'
Meta-Trondhjemite Pods
Normal Fault (rotated from an initially low-angle; symbol on original hanging wall)
Thrust Fault (rotated from an initially low-angle; symbol on original hanging wall)
Normal Fault (rotated from an initially high-angle)
Unconformity (symbols on stratigraphically higher units)

FIGURE 4.2

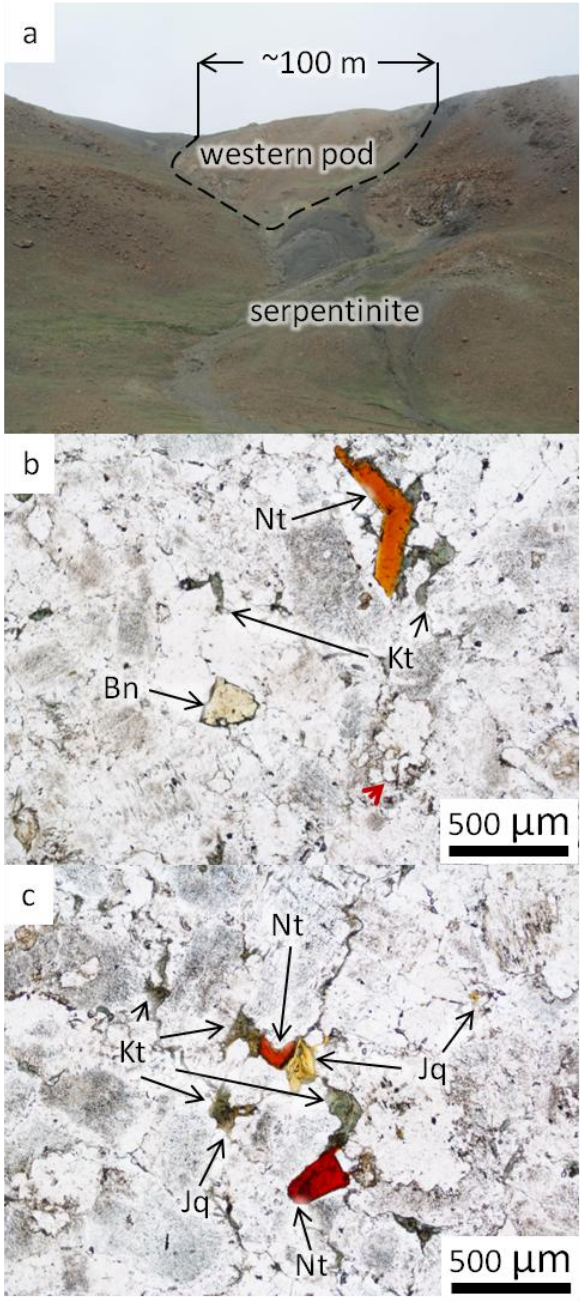
a
~100 m
western pod
serpentinite
b
Nt
Kt
Bn
500 µm
c
Nt
Kt
Jq
Jq
Nt
500 µm

FIGURE 4.3

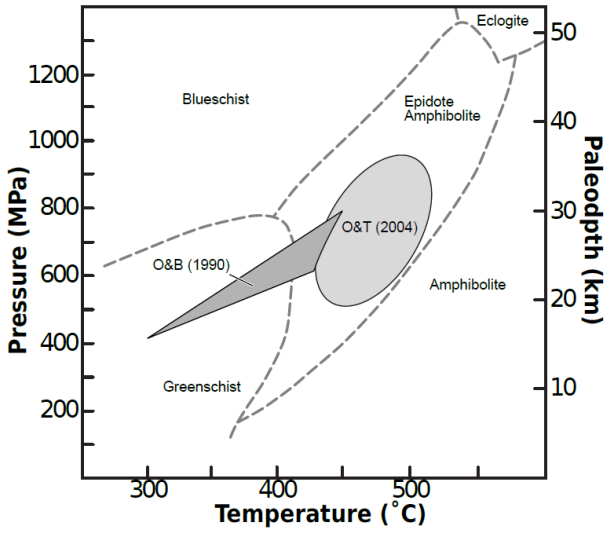
Eclogite
Blueschist
Epidote
Amphibolite
O&T (2004)
O&B (1990)
Amphibolite
Greenschist
Pressure (MPa)
1200
1000
800
600
400
200
300
400
500
Temperature (˚C)
50
40
30
20
10
Paleodpth (km)

Table 4.1: LA-ICPMS analyses of amphiboles

	Middle Pod					Eastern Pod					
	1a	2a	2b	2c	2d	1a	1b	1c	2a	3a	3c
wt%											
SiO_2	52	54	53	53	54	55	55	55	57	58	57
FeO	27	25	26	25	25	22	22	21	18	18	20
MgO	7.0	7.9	7.7	7.4	7.7	10	10	10	10	7.1	7.5
Na_2O	4.5	4.7	4.7	4.6	4.7	2.5	2.4	2.5	4.2	6.3	6.1
CaO	4.3	4.4	4.5	4.7	4.6	8.5	8.7	8.5	5.9	3.5	3.4
K_2O	3.2	2.8	2.9	3.3	2.7	0.65	0.64	0.64	0.65	1.4	1.4
Al_2O_3	1.1	0.52	0.47	0.34	0.63	0.93	0.92	0.90	3.5	3.8	2.5
TiO_2	0.49	0.54	0.65	0.73	0.57	0.13	0.13	0.13	0.19	1.7	2.0
MnO	0.08	0.08	0.08	0.10	0.09	0.29	0.29	0.29	0.20	0.22	0.23
ppm											
Li	310	340	330	220	340	8.9	9.3	9.8	17	8.0	9.4
Sr	350	250	290	370	250	57	57	56	41	480	440
Zn	160	210	210	190	190	260	250	250	280	330	350
V	34	42	43	41	41	240	240	230	260	210	250
a.p.f.u.[a]											
Si	7.8	8.0	7.9	8.0	8.0	8.0	8.0	8.0	8.1	8.2	8.2
Al	0.19	0.090	0.083	0.060	0.11	0.16	0.16	0.15	0.57	0.64	0.42
Ti	0.055	0.060	0.073	0.082	0.063	0.014	0.014	0.014	0.020	0.19	0.21
Fe	3.4	3.1	3.2	3.2	3.1	2.6	2.6	2.6	2.1	2.2	2.4
Mg	1.6	1.7	1.7	1.7	1.7	2.2	2.2	2.2	2.2	1.5	1.6
Mn	0.010	0.010	0.011	0.013	0.011	0.036	0.035	0.036	0.024	0.027	0.029
Li	0.040	0.043	0.042	0.028	0.044	0.0011	0.0012	0.0012	0.0021	0.0010	0.0012
Na	1.3	1.3	1.3	1.3	1.4	0.69	0.68	0.69	1.14	1.75	1.71
Ca	0.69	0.70	0.71	0.75	0.72	1.3	1.3	1.3	0.90	0.53	0.52
K	0.61	0.52	0.55	0.63	0.50	0.12	0.12	0.12	0.12	0.25	0.25
I.D.	katophorite	katophorite	katophorite	katophorite	katophorite	winchite	winchite	winchite	winchite	katophorite	katophorite

[a] a.p.f.u is atoms per formula unit. Each a.p.f.u analysis normalized to 23 O. Sample numbers represent individual grains, letters represent specific analyses on a given grain.

Table 4.2: LA-ICPMS analyses of benitoite

	1	2	3	4	5	6	7
wt%							
SiO_2	44	44	44	44	44	44	45
BaO	36	36	36	35	36	36	35
TiO_2	21	21	21	21	21	21	20
ppm							
Al	210	390	290	180	580	400	1990
Fe	160	140	130	120	180	140	310
Sr	88	75	75	78	72	68	110
Na	46	35	53	43	47	62	530
V	2.0	1.9	1.6	2.0	1.6	1.7	1.4
Mn	0.32	0.23	0.11	0.078	0.26	0.0015	5.9
a.p.f.u.[a]							
Si	3.0	3.0	3.0	3.0	3.0	3.0	3.0
Ti	1.1	1.1	1.0	1.1	1.1	1.1	1.0
Ba	0.95	0.95	0.95	0.94	0.95	0.95	0.92

[a] a.p.f.u is atoms per formula unit. Each a.p.f.u analysis normalized to 9 O. All Fe is calculated as Fe^{2+}.

Table 4.3: LA-ICPMS analyses of neptunite

	1	2	3	4	5	6	7	8	9	10	11	12	13	15	15
wt%															
SiO_2	54	54	54	54	53	54	54	54	54	54	54	54	54	54	54
TiO_2	18	17	18	18	19	18	18	17	17	18	17	17	17	17	17
FeO	13	14	13	12	13	13	13	14	13	14	14	14	13	15	15
Na_2O	7.1	7.0	7.0	7.0	7.1	7.1	7.1	7.1	7.1	7.1	7.1	7.1	7.1	7.0	7.0
K_2O	4.7	4.6	4.6	4.7	4.7	4.6	4.6	4.7	4.6	4.6	4.3	4.3	4.5	4.4	4.4
Li_2O	1.8	1.7	1.7	1.8	1.8	1.8	1.7	1.7	1.7	1.7	1.7	1.7	1.7	1.7	1.7
MgO	1.6	1.6	1.3	2.1	1.6	1.6	1.4	1.6	1.6	1.3	1.3	1.4	1.7	1.5	1.4
	0.08	0.08			0.07	0.07	0.07	0.08		0.08	0.07				
MnO	5	2	0.075	0.029	6	9	6	4	0.062	2	9	0.10	0.069	0.074	0.062
ppm															
Al	160	260	120	230	120	110	180	230	210	220	130	310	70	300	200
Ca	48	140	140	59	27	n.d.	170	91	5.9	55	n.d.	90	120	70	n.d.
Zn	50	40	49	48	53	54	46	44	44	55	52	46	57	42	40
V	12	11	8.1	21	13	11	10	10	15	11	8.1	16	9.5	9.1	10
a.p.f.u[a]															
Si	8.0	8.0	8.0	8.0	7.9	8.0	8.0	8.0	8.0	8.0	8.0	8.0	8.0	8.0	8.0
Ti	2.0	1.9	2.0	2.0	2.1	2.0	2.0	1.9	1.9	2.0	2.0	1.9	1.9	1.9	1.9
Fe	1.7	1.7	1.7	1.5	1.6	1.5	1.7	1.7	1.6	1.7	1.7	1.7	1.6	1.8	1.8
Mg	0.36	0.35	0.30	0.45	0.35	0.36	0.31	0.35	0.36	0.29	0.29	0.31	0.39	0.34	0.31
	0.01	0.01	0.009	0.003	0.01	0.01	0.01	0.01	0.007	0.01	0.01	0.01	0.008	0.009	0.007
Mn	1	0	4	6	0	0	0	1	8	0	0	3	6	4	8
Li	1.1	1.0	1.0	1.0	1.1	1.1	1.0	1.0	1.0	1.0	1.0	1.0	1.0	1.0	1.0
Na	2.1	2.0	2.0	2.0	2.0	2.0	2.1	2.0	2.0	2.1	2.0	2.1	2.0	2.0	2.0
K	0.95	0.93	0.92	0.92	0.92	0.93	0.94	0.93	0.94	0.95	0.92	0.94	0.94	0.94	0.95

[a] a.p.f.u is atoms per formula unit. Each a.p.f.u analysis normalized to 24 O. All Fe is calculated as Fe^{2+}. n.d. means not detected above background.

Table 4.4: LA-ICPMS analyses of joaquinite

	1	2	3	4	5	6	7	8	9	10
wt%										
SiO_2	34	35	36	35	36	35	34	35	34	35
BaO	22	22	22	22	22	22	23	22	23	23
TiO_2	13	12	12	13	13	13	13	12	13	13
Ce_2O_3	7.9	8.5	7.9	7.7	7.7	7.4	7.7	8.2	7.7	7.8
La_2O_3	4.8	5.1	4.2	4.7	4.2	4.3	4.1	5.6	4.4	4.5
FeO	4.7	4.8	4.8	4.5	4.6	4.6	4.6	4.9	4.8	4.7
Nd_2O_3	3.7	4.0	4.3	3.6	4.0	3.1	3.9	3.2	3.5	3.5
SrO	3.5	2.8	3.4	3.6	3.5	4.2	4.0	3.2	3.9	3.8
Na_2O	1.8	1.9	1.8	1.8	1.9	1.7	1.7	1.8	1.7	1.8
CaO	0.94	0.75	0.92	0.96	0.95	1.2	1.0	0.89	1.1	1.1
Pr_2O_3	0.91	0.96	0.98	0.88	0.94	0.81	0.95	0.87	0.90	0.88
ThO_2	0.68	0.61	0.56	0.73	0.65	0.81	0.62	0.69	0.86	0.79
Sm_2O_3	0.55	0.50	0.57	0.45	0.55	0.41	0.58	0.29	0.40	0.45
Gd_2O_3	0.23	0.16	0.18	0.14	0.17	0.14	0.20	0.06	0.11	0.14
Li_2O	0.22	0.19	0.21	0.22	0.24	0.24	0.25	0.20	0.20	0.23
Nb_2O_{10}	0.16	0.17	0.15	0.15	0.15	0.21	0.14	0.15	0.25	0.24
ppm										
Mg	500	440	610	290	330	360	330	560	350	400
Al	380	520	630	320	440	180	270	600	250	310
Y	340	160	160	110	140	110	180	34	78	110
Dy	250	140	140	100	120	100	150	27	62	93
Zn	170	170	180	180	190	220	250	160	180	210
Mn	160	120	66	120	110	79	130	100	130	210
U	140	110	220	130	150	220	190	100	150	170
Eu	120	85	100	76	94	110	110	38	64	81
Tb	110	66	74	52	64	51	78	18	38	51
Er	24	11	11	7.4	8.7	8.7	11	3.1	6.2	8.3
Ho	21	10.0	11	6.7	8.5	6.8	11	1.7	4.7	6.4
Yb	12	4.7	4.2	1.8	3.9	3.5	3.6	0.59	1.8	3.2
V	5.6	6.0	7.1	4.9	5.8	2.9	6.4	4.1	4.7	4.8
Tm	1.9	0.68	0.68	0.34	0.67	0.66	0.74	0.13	0.35	0.55
Lu	1.8	0.72	0.68	0.34	0.60	0.50	0.54	0.13	0.31	0.46
a.p.f.u.[a]										
Si	8.0	8.0	8.0	8.0	8.0	8.0	8.0	8.0	8.0	8.0
Al	0.020	0.026	0.031	0.016	0.022	0.009	0.014	0.031	0.013	0.016
Ti	2.2	2.1	2.1	2.2	2.1	2.2	2.3	2.1	2.2	2.2
Nb	0.013	0.013	0.012	0.011	0.012	0.016	0.011	0.011	0.020	0.019
Fe	0.92	0.91	0.89	0.85	0.86	0.86	0.90	0.92	0.94	0.92
Mg	0.029	0.025	0.034	0.016	0.018	0.020	0.019	0.031	0.020	0.023
Li	0.20	0.17	0.19	0.20	0.22	0.22	0.23	0.18	0.19	0.21
Na	0.81	0.82	0.80	0.79	0.81	0.73	0.78	0.79	0.78	0.79
Ca	0.23	0.18	0.22	0.23	0.23	0.30	0.26	0.22	0.27	0.26
Sr	0.48	0.36	0.44	0.47	0.46	0.55	0.54	0.42	0.53	0.51
Ba	2.0	1.9	1.9	2.0	1.9	2.0	2.1	2.0	2.1	2.0
ΣREE	1.5	1.6	1.5	1.4	1.4	1.3	1.5	1.5	1.5	1.5
Th	0.036	0.031	0.029	0.038	0.033	0.041	0.033	0.036	0.046	0.042

[a] a.p.f.u is atoms per formula unit. Each a.p.f.u analysis normalized to Si+Al=8. All Fe is calculated as Fe^{2+}.

CHAPTER 5

PROLONGED OCEANIC SUBDUCTION ALONG THE SOUTHERN MARGIN OF EURASIA PRECEDED INDIA-EURASIA COLLISION: EVIDENCE FROM THE SANGSANG OPHIOLITE OF SOUTHERN TIBET

ABSTRACT

Despite decades of research, the timing of the India-Eurasia collision along the Yarlung suture remains controversial. Surprisingly few attempts to constrain the age of collision focus on the rocks of the suture zone themselves, even though their magmatic and metamorphic ages would place lower bounds on the possible age of collision. New mapping and (U-Th)/Pb and $^{40}Ar/^{39}Ar$ geochronologic data from the Sangsang ophiolite in south-central Tibet indicate a prolonged evolution of the subduction margin between the Gangdese continental arc (along the southern edge of Eurasia) and the Neo-Tethys ocean basin to the south, ranging from at least ca. 130 Ma into the early Eocene. The data suggest large-scale, arc-normal hyperextension of the Gangdese forearc from ca. 130 Ma to at least 111 Ma. This extension potentially reconciles the recently reported presence of Eurasian detritus in Paleocene sedimentary rocks deposited on Indian plate rocks, even though available paleomagnetic constraints suggest that India was hundreds of kilometers south of Eurasia at that time. The youngest metamorphic event in the Sangsang ophiolite, related to the late stages of subduction zone activity, involved growth of a rare, low temperature-high pressure (blueschist facies) metasomatic assemblage that includes the minerals neptunite and joaquinite. These minerals yield concordant, early Eocene

(Ypresian) metamorphic ages, which may closely correspond to the timing of India-Eurasia collision or, at the very least, place a constraint on the maximum age of collision.

INTRODUCTION

The India-Eurasia collision along the Yarlung suture and subsequent evolution of the Himalaya may have been the most significant geologic event of the Cenozoic, with global ramifications (Broeker, 2015). Unfortunately, the age of initial collision is still debated, with most recent estimates ranging between 60-40 Ma. Most Himalayan researchers are persuaded by the available evidence that the Yarlung suture is an Eocene structure (e.g., Najman et al., 2010; St-Onge et al., 2010; Rowley, 1996; van Hinsbergen et al., 2012), but some researchers have concluded that the suture formed later (e.g., Oligocene; Aitcheson et al., 2011) or earlier (e.g., early Paleocene; DeCelles et al., 2014).

Studies of the timing of collision have employed a variety of observations, including quantifications of changes in sediment source, paleomagnetic measurements of plate movements, and changes in isotopic signals of magmatic rocks but generally have not focused on rocks within the Yarlung suture. In support of this prior body of work, here I report the results of such a study of the Sangsang section of the Yarlung suture in south central Tibet (Figure 5.1a). The Sangsang section is unique in that it contains one of the few reported occurrences in the Yarlung suture zone of mineral assemblages indicative of low-temperature, high-pressure rocks in a subduction zone environment. Such rocks are useful for constraining the timing of collision inasmuch as the geodynamic conditions that allow for their formation do not persist beyond the start of

collision. As I show below, the Sangsang rocks include a variety of pre- to syn-collisional mineral assemblages that include minerals suitable for robust isotope geochronology.

GEOLOGIC BACKGROUND: THE PRINCIPAL TECTONIC ELEMENTS OF SOUTHERN TIBET

Rocks in southern Tibet belong to one of three broad groups: those of obvious Eurasian plate affinity, those of obvious Indian plate affinity, and those found in the Yarlung suture zone (Figure 5.1a). While the region now comprising the Tibetan plateau had a long history of accretionary tectonics stretching back through the Mesozoic (Yin and Harrison, 2000), I focus here on the southernmost portion of Eurasia consisting of the Lhasa block (Figure 5.1a). The oldest portions of Lhasa block formed in the Precambrian, transitioning to a sedimentary platform in the Devonian to Cretaceous (Hodges, 2000), and accreting to Eurasia ca. 110-88 Ma (Borneman et al., 2015; Kapp et al., 2007, Kapp et al., 2003; Yin and Harrison, 2000). Currently, the southernmost Lhasa block is composed primarily of the Gangdese batholith and its volcanic equivalent, the Linzizong Volcanics (Ding et al., 2005). The Gangdese batholith first intruded the Lhasa block in the Late Triassic and remained more or less continuously active through the mid-Miocene (e.g. Jiang et al., 2014). The batholith is thought to represent a continental margin ("Andean"-type) arc formed as a consequence of north-directed subduction of Neo-Tethys oceanic lithosphere beneath Eurasia (e.g. Hodges, 2000), though the presence of Miocene rocks younger than even the youngest estimates for collision require some degree of crustal anatexis (Ding et al., 2005; Yin and Harrison, 2000).

As a consequence of such a long duration of arc magmatism, it is reasonable to infer that Late Triassic-Miocene sedimentary strata derived from the batholith will likely contain at least some detrital zircons of similar age to the depositional age of the sediment (e.g. zircons derived from volcanic component of the Gangdese arc), a characteristic that improves my ability to determine the ages of those strata through detrital zircon U/Pb geochronology. One tectonically significant sedimentary package that has been dated in this way is the early Cretaceous-early Eocene Xigaze Group, which represents the forearc basin of the Gangdese batholith (Huang et al., 2015a; Ding et al., 2005; Wang et al., 2012; Orme et al., 2015). Facies within the forearc are highly variable, including both limestones and clastic sediments ranging from mud rocks to conglomerates. Currently, the Xigaze Group is thrust over the Oligocene-Miocene Kailas Formation, a succession of rocks commonly inferred to be postcollisional (DeCelles et al., 2011), along the south-dipping Great Counter thrust (Yin and Harrison, 2000). The Kailas formation in turn sits unconformably on the Gangdese batholith to the north (DeCelles et al., 2011). The southern boundary of the Xigaze Group is poorly understood, but has typically been interpreted as a high angle strand of the Great Counter thrust that places rocks of the Yarlung Suture over the forearc (Ding et al., 2005). However, recent re-examinations of the southern limit of the forearc in several areas have resulted in the re-interpretation of the southern contact as an unconformity (Huang et al., 2015a; Maffione et al., 2015).

South of both Eurasian-affinity rocks and the Yarlung suture are the Paleozoic to Eocene marine strata of the Tibetan Sedimentary sequence (Gaetani and Garzanti, 1991). These units were deposited on the passive margin of India and encompass the portions of

the Indian continent most proximal to Eurasia prior to collision. To the south, the Tibetan Sedimentary sequence is separated from other Indian-affinity rocks of the Himalayan realm by the Miocene to recent South Tibetan detachment system (Hodges, 2000). To the north, Indian-affinity rocks are typically thrust over rocks of the Yarlung suture zone (Orme et al, 2015).

The suture itself consists primarily of dismembered ophiolites and mélanges in a typically 15 km-wide zone (Ding et al., 2005). In places, rocks representing the suture are absent and Indian rocks are thrust over Eurasian rocks along the Great Counter thrust (Orme et al., 2015). Typically, ophiolites of the Yarlung suture are thrust to the south over mélanges. A common point of confusion within the Yarlung suture is that many of the ophiolites are best termed ophiolitic mélanges, and some of the mélanges are dominated by ophiolites with nominally sedimentary matrix. Consequently, a brief discussion of these rocks follows immediately, with a more detailed description reserved for discussion of the Sangsang section in detail.

Ophiolites range in degree of alteration and intactness from fresh and intact (such as exposures near the city of Xigaze) to completely metasomatized and dismembered (such as exposures near the town of Sangsang). The entire range of ophiolitic lithologies, ultramafic rocks through pelagic cherts, is present within the Yarlung suture. The ophiolites have Early Cretaceous magmatic ages and a supra-subduction zone (SSZ) magmatic signature (Hébert et al., 2012 and references therein). While Yarlung suture ophiolites likely sample distinct segments of the ocean lithosphere that once separated India and Eurasia (Hébert et al., 2012), paleomagnetic constraints place the formation of the Sangsang and Xigaze ophiolites in the Gangdese forearc (Huang et al., 2015a).

$^{40}Ar/^{39}Ar$ hornblende dates from amphibolites from within the Xigaze section are ca. 128-124 Ma, which has been interpreted to represent the metamorphic age of the rocks, with metamorphism driven by either a subduction initiation or a ridge subduction event (Guilmette et al., 2009).

The mélanges are lithologically very diverse and poorly studied. However, the most detailed examination of the Yarlung suture mélanges to date (Cai et al., 2012) was done in the Xigaze region. Mélanges in this sector of the Yarlung suture, typically with sedimentary matrices, are inferred to be of Mesozoic age on the basis of the spectrum of U/Pb dates of the detrital zircons they contain. Cai et al. (2012) distinguished three mélange formations: the chert-rich Tangga, the mud-rich Pomunong, and the mostly intact terriginous clastic material-bearing Rongmawa. These mélanges are structurally chaotic, and were interpreted to represent a southward younging subduction zone accretionary complex.

PREVIOUS ESTIMATES OF THE AGE OF INDIA-EURASIA COLLISION

Currently, estimates for the timing of collision fall into three time spans: 40-35 Ma, 55-50 Ma, and 60-59 Ma. A 40-35 Ma collision has been proposed on the basis of the inferred presence of an intra-oceanic "Zedong" arc through the Eocene (Aitchison et al., 2011), and the appearance of continental isotopic signatures in magmatic rocks in the Kohistan and Ladakh regions of the westernmost portion of the Himalayan-Tibetan orogen (Bouilhol et al., 2013). This interpretation also figures prominently in a recent model of India-Eurasia convergence that features two subduction zones operating in parallel within the Tethys ocean basin over the Cretaceous-early Tertiary interval

(Jagoutz et al., 2015). However, recent work suggests that the postulated Zedong arc is most likely correlative to the Gangdese Arc (Zhang et al., 2014), and studies that place depositional age constraints on molasse sediments that overlap suture zone rocks suggest that suturing in Ladakh was no younger than 50 Ma (Tripathy-Lang et al., 2013; Borneman et al., 2015).

The most widely accepted age for India-Eurasia is collision is 55-50 Ma, as reviewed by Hodges (2000). This time period is consistent with paleomagnetic reconstructions (van Hinsbergen et al., 2013; Huang et al., 2015b), and stratigraphic data constraining the first appearance of post-collisional sediments (Najman et al., 2010; Rowley, 1996). These constraints typically have uncertainties up to 2 Ma.

Evidence for a 60-59 Ma collision comes primarily from the Sangdanlin Formation, a sedimentary succession found south of the Yarlung suture that depositionally overlies Tibetan Sedimentary sequence rocks but contains primarily Eurasian-derived detritus (Hu et al., 2015; Orme et al., 2015). This relationship reasonably implies that India and Eurasia had docked with one another prior to Sangdanlin Formation deposition, which has been constrained to ca. 60-59 Ma (DeCelles et al., 2014; Hu et al., 2015; Wu et al., 2014). A major drawback of this hypothesis is that most recent paleomagnetic reconstructions call for ca. 1000 km of separation between India and Eurasia at 60 Ma (e.g., Huang et al., 2015b).

TECTONIC STRATIGRAPHY OF SANGSANG SECTION OF THE YARLUNG SUTURE

The geologic basis for my work was developed by field mapping and sample collection for a total of one month spread over two field seasons in 2011 and 2013. During the course of this work, I conducted three complete, roughly N-S mapping transects through the entire Yarlung suture, as well as several partial transects that allowed me to examine all major lithologic packages and almost every contact in multiple locations. Bedrock exposure in the area is excellent, and topography is not sufficiently extreme to limit access. My field mapping was further aided by examination of both Google Earth and ASTER satellite imagery (Figure 5.1b).

Xigaze Group

The northernmost and stratigraphically highest rocks in my study area are the mudstones and turbiditic sandstones of the Xigaze Group. These rocks were originally deposited between the margin of the southern Eurasian Gangdese arc and the associated trench (An et al., 2014; Huang et al., 2015a; Wang et al., 2012). In the Sangsang region, the Xigaze Group lies depositionally on ophiolites and also contains ophiolitic detritus. This contact marks the northern boundary of my mapping area. The maximum age of deposition of the Xigaze Group is ca. 129 Ma based on the U/Pb detrital zircon spectra from a sample collected immediately above its basal unconformity (Huang et al., 2015a).

Ophiolites

Ophiolitic rocks occur immediately south of the basal unconformity. The bulk of these rocks are best described as Serpentinitic Mélange, with most exposures dominated by massive green to brown serpentine with occasional chrysotile-rich domains. Primary lithologies are preserved as isolated pods of various sizes distributed throughout. In this contribution, I use the word 'pod' to denote a block in a dissimilar matrix without connotation of genetic relationship. Primary igneous lithologies range from peridotite to basalt. Many of these mafic to felsic lithologies have been interpreted as dikes, some showing signs of heavy alteration, primarily rodingitization (Bédard et al., 2009). Notable among altered meta-igneous pods are three consisting of meta-trondhjemite (Figure 5.1b). The metamorphic mineralogy of these pods includes the rare amphibole assemblage winchite + katophorite, and the rare Ti-silicate assemblage neptunite + benitoite + joaquinite. (Two of these minerals, neptunite and joaquinite, provide important constraints on the age of the suture zone, as I discuss below.) Amphibolite pods similar to those found in the Xigaze ophiolite are also common within the Sangsang Serpentinitic Mélange. In addition, I also identified rare pods of radiolarite-bearing limestones, presumably of marine origin. Bédard et al. (2009) conducted an extensive survey of primary lithologies preserved at Sangsang and inferred that the ophiolites most likely formed in a supra-subduction zone environment in a manner similar to the Xigaze ophiolites.

In addition to the pods of primary lithologies scattered within the Serpentinitic Mélange, there are several larger, more or less coherent blocks of oceanic crustal rocks mapped on Figure 5.1b. Within these blocks, evidence for metamorphism is minimal.

Mafic lithologies are typically grey to black, but are occasionally green. The block to the north of the serpentinite mélange in the eastern portion of the field area preserves massive basalts, diabases, and gabbros. Those in the central portions of the field area to the south of the serpentinite mélange consist mainly of massive basalts. In the eastern portion of the field area and south of the serpentinite mélange, two juxtaposed blocks occur. The more northern of the two is broadly similar to those described above. The more southern of the two preserves a primary depositional contact of fine-grained limestone on pillow basalt. Here, the limestones are grey to orange, moderately deformed, contain minor interlayers of mudstone, and are bedded on the 1-5 cm scale.

U/Pb zircon constraints on the crystallization ages of the meta-trondhjemites

A thick section of one sample of the middle meta-trondhjemite pod (sample 254) contains roughly 100 x 40 μm, euhedral dipyramidal square prisms of zircon. Fabric relationships observed in thin section suggest that these zircons were part of the primary magmatic assemblage of trondhjemite, not the subsequent metamorphic assemblages winchite + katophorite and neptunite + benitoite + joaquinite. The pressure-temperature stability fields of these metamorphic assemblages are not terribly well constrained (Oberti et al., 2015; Van Baalen, 2004), but the diffusivity of radiogenic Pb in zircon at the likely temperature ranges of the observed assemblages is sufficiently sluggish that I would expect U/Pb ages for pre-metamorphic zircons to reflect magmatic growth rather than metamorphic resetting (Cherniak and Watson, 2001).

We determined the U/Pb dates of four zircon crystals in sample 254 by *in situ* excimer laser ablation, inductively coupled plasma source mass spectrometry (LA-

ICPMS). Analytical procedures for this work may be found in the Appendix. A total of six $^{206}Pb/^{238}U$ dates for the four zircons (Table C1; Figure 5.2) yielded statistically indistinguishable dates based on the mean weighted standard deviation (MSWD; Wendt and Carl, 1991). Collectively, the six dates have an inverse variance-weighted mean of 111.2 ± 2.2 Ma (2σ), which I interpret as the magmatic age of the trondhjemite.

Subduction Mélanges

Immediately to the south of a fault contact with the ophiolitic lithologies is a distinctive sequence of mélanges with mixed sedimentary and igneous components. These rocks are highly strained, with grain sizes rarely over 100 μm and commonly under 50 μm. In the field, I divided these lithologies into two categories: one that includes mixed phyllitic metasedimentary rocks and blueschists and is exposed primarily to the north, and one that lacks blueschists, exposed primarily in the south.

The phyllites ranged in color from red to yellow to white, with color variations on scales of centimeters to as much as ten meters. They contain variable amounts of quartz and sericite. I interpret the protolith of the red phyllites to be red pelagic cherts based on their near pure silica composition and distinct color. Greenschist phyllites are also abundant, with the assemblage chlorite + quartz + plagioclase + titanite ± tremolite ± epidote ± sericite. Rarely, greenschist phyllites contain lenses of deformed stretched pebble conglomerates, with clasts typically ca. 1 cm by 0.5 cm to as thin as 1 mm. These clasts have assemblages similar to the rest of the greenschists, but are typically lighter colored than their host matrix.

Na-amphiboles were originally identified by Ding et al. (2005) in the Sangsang region; rocks bearing Na-amphiboles have assemblages consistent with transitional high-pressure epidote amphibolite to blueschist facies. Here I will refer to these lithologies simply as blueschists. They are a distinct deep navy blue and are present in discrete zones up to 0.5 km thick near the contact of the Subduction Mélanges unit and the ophiolites to the north. The typical blueschist assemblage is Na-amphibole + chlorite + quartz + titanite ± epidote ± phengite ± albite. Ding et al. (2005) dated Na-amphiboles from these rocks to ca. 63 Ma using the $^{40}Ar/^{39}Ar$ technique, and interpreted that to be the "age of uplift" for the blueschists. Blueschist horizons become progressively less common toward structurally lower levels of the Subduction Mélanges unit before disappearing altogether. The southern boundary of the blueschist-bearing mélange unit is gradational into the phyllitic lithologies.

Relatively undeformed rocks are rare within the mélanges, but are occasionally found as discrete pods on the 10 m scale. Most are massive, greenschist facies metabasalts. I found one occurrence of a massive, medium-grained sandstone within phyllitic metasedimentary subunit, several kilometers south of the nearest blueschist outcrops. I infer a continental shelf depositional environment for this sandstone base on its grain size and nearly pure quartz composition.

Based on the pervasive deformation of these rocks, their highly heterogeneous nature, and their incorporation of ophiolitic lithologies, I interpret this package of phyllites and blueschists to be a subduction mélange. While they share many similarities with the Xigaze mélanges to the east, the presence of blueschist facies rocks and more

deformed nature of the rocks at Sangsang are sufficient to preclude straightforward lithologic correlation of the Xigaze and Sangsang mélanges.

Detrital zircon U/Pb constraints on the age and provenance of sandstone in the Subduction Mélanges

The U/Pb systematics of detrital zircons can place important constraints on the maximum depositional age of a sedimentary rock – it can be no older than the zircons it contains – and can indicate probable sediment provenance (Gehrels, 2012). I applied this technique to zircon crystals separated from a sandstone sample (234) collected from within the phyllitic metasedimentary subunit of the Subduction Mélanges. Employing LA-ICPMS, I acquired 198 $^{206}Pb/^{238}U$ dates ranging from Late Cretaceous to Archean (Table C1, Figure 5.3). (Analytical procedures for this work are also articulated in the Appendix.) The three youngest crystals in the sample, with an inverse variance-weighted mean $^{206}Pb/^{238}U$ age of 81.85 ± 0.82 Ma, are statistically indistinguishable, and I interpret their mean as the maximum depositional age of the sandstone. The many Mesozoic zircons in this sample strongly suggest derivation from the pre-collisional Gangdese arc to the north (Cai et al., 2012; DeCelles et al., 2014; Zhang et al., 2014). Considering the presence of Paleozoic and older zircons as well, which is suggestive of a continental source, I infer a predominately Eurasian marginal provenance for the studied sandstone.

Tibetan Sedimentary sequence

South of the Subduction Mélanges unit is a package of rocks showing strong similarities to Indian continental margin rocks mapped throughout southern Tibet as the

Tibetan Sedimentary sequence (Gaetani and Garzanti, 1991). I did not examine these exposures in detail because they were exposed only along the southern boundary of my study area, but the lithologies there consisted of brown sandstones, mudstones, and impure limestones of unconstrained age. While these rocks are also complexly folded on the outcrop to kilometer scale, they preserve primary centimeter- to meter-scale bedding. Near the steep, poorly exposed contact between this unit and the Subduction Mélanges, I observed a series of slices of pillow basalts juxtaposed with Tibetan Sedimentary sequence rocks, presumably by imbricate thrusts. (These structures are not shown on Figure 5.1 because of their scales.) I take these as evidence that the contact between the two mapping units is tectonic in nature.

STRUCTURAL GEOLOGY

Other than the unconformity at the base of the Xigaze Group, the contacts between all of the major mapping units described above are faults. These steeply dipping structures are well exposed and easily mapped in the field, even though actual exposures of the fault surfaces are rare or nonexistent. My interpretation that they are faults is based on the observations that they juxtapose rocks with apparently distinctive metamorphic histories, and that they can be seen to truncate compositional layering or, in some cases, older faults. Unfortunately, most rocks in the study area contain few deformational fabrics diagnostic of shear sense, and I am left to interpret the kinematics of the mapped structures from the nature of their metamorphic discontinuities.

We infer that the present, near-vertical orientation of the Xigaze basal unconformity places an important constraint on the original configuration of faults within

the study area. If I assume that this unconformity was subhorizontal at the time of deposition and that its rotation to a steep dip today resulted from post-collisional deformation – consistent with previous inferences for steep structures in southern Tibet (Hodges, 2000; Yin and Harrison, 2000) – many or all of the major faults (that presumably do not postdate the unconformity) in my study area had low dip angles at the time of unconformity development. In the paragraphs below, I described mapped structures with respect to a reconstructed 'Xigaze unconformity horizontal' frame of reference.

Fault 1: A pre-unconformity ocean floor detachment?

Maffione et al. (2015) speculated that the Xigaze basal unconformity developed on the remnant footwall of a detachment in an oceanic core complex, which might have formed around the same time as the maximum depositional age of the Xigaze Group at Sangsang, ca. 129 Ma. I identified one potential candidate in the form of a currently steep fault (labeled Fault 1 on Figure 5.1) that strikes WNW-ESE across the eastern part of the study area. It juxtaposes relatively unmetamorphosed mafic rocks to the north against Serpentinitic Mélange to the south. In the central part of the study area, this fault disappears beneath the Xigaze basal unconformity, placing an important constraint on the structure's age. In the Xigaze unconformity horizontal frame of reference, Fault 1 would be an essentially horizontal fault carrying mafic rocks in its hanging wall. I interpret this structure to have been an oceanic low-angle normal fault (detachment) that omitted substantial crustal section, emplacing ophiolitic upper crust (represented by the mafic rocks) over ophiolitic mantle represented by its footwall serpentinites.

Subduction complex-related faults within the suture zone

Several faults with a variety of kinematics were mapped within the Sangsang sector of the Yarlung suture. An anastamosing system of high-angle faults – moderately low-angle in the Xigaze unconformity horizontal frame of reference – separate the ophiolites from the structurally underlying Subduction Mélanges. These were previously mapped collectively as the Yarlung Zangbo Mantle thrust (Ding et al., 2005; Figure 5.1). A thrust interpretation (serpentinites over Subduction Mélanges) is supported by S-C fabrics preserved in phyllite outcrops immediately south of the trace of the structure.

The trace of the Yarlung Zangbo Mantle thrust is notably offset in an apparent left-lateral sense by a high-angle, NE–SE-striking, 60˚SE dipping fault labeled Fault 2 on Figure 5.1. Although the total offset on this structure is unconstrained, I estimate a separation of ≥ 2.5 km based on reconstructing the map offset of the trace of the Yarlung Zangbo Mantle thrust strand carrying ophiolitic rocks in its immediate hanging wall. In the Xigaze unconformity horizontal frame of reference, Fault 2 would have been a high-angle structure at the time of its inception, and the sense of offset of the Yarlung Zangbo Mantle thrust system in this frame of reference suggests that Fault 2 likely initiated as a normal fault.

To the north, Fault 2 is apparently cut by another structure (Fault 3) that lies entirely within the Serpentinitic Mélange, striking subparallel with Fault 1. Unfortunately, my observations from the field and remote sensing imagery do not show a cross-cutting relationship between Fault 1 and Fault 3 that might allow me to evaluate the relative ages of the two structures, but the pre-unconformity age of Fault 1 and the post-Fault 2 – and thus post-Yarlung Zangbo Mantle thrust – age of Fault 3 implies that the

two are of different ages. Reconstruction of Fault 3 to Xigaze unconformity horizontal suggests that it, like Fault 1, initiated as a low-angle structure, carrying lithologically similar Serpentinitic Mélange in both its hanging wall and footwall.

One key to understanding the tectonic significance of Fault 3 is the existence along it of structural slices containing meta-trondhjemite with the high-pressure metamorphic minerals winchite + katophorite. In the Xigaze unconformity horizontal frame of reference, Fault 3 occurs only 1-2 km beneath the unconformity, implying that Fault 3 hanging wall rocks occupied an upper crustal position at the time of faulting. However, the winchite + katophorite assemblage in the meta-trondhjemite slices along this structure are characteristic of high-pressure epidote amphibolite or possibly intermediate- to high-pressure blueschist facies metamorphism and could not have formed in the upper crust. Katophorite, for example, has only been reported previously as a product of high-pressure Na metasomatism (Oberti et al., 2015), and has also been identified as precursor mineral to the formation of jadeitites, which are only known to form above a de-watering subducting crust (Harlow et at., 2015). Moreover, most diagnostic mineral assemblages in the more distal footwall of Fault 3 – the blueschists within the Subduction Mélanges, for example – also indicate a deeper crustal growth environment. As a consequence, I interpret Fault 3 as a normal-sense structure that, while apparently established at a low-angle, cut deeply enough to enable exhumation of the meta-trondhjemites to upper crustal levels. Cross-cutting relationships between Fault 3, Fault 2, and the Yarlung Zangbo Mantle thrust indicate that Fault 3 is the youngest major structure entirely within the suture zone.

Fault 4: The southern boundary of the suture zone

The southern boundary of the Subduction Mélanges is marked by a fault that is especially poorly exposed because fluvial drainages commonly follow its surface expression. Regardless, it was not difficult to locate due to the sudden change from highly deformed phyllites to un-metamorphosed sedimentary rocks across it. This structure – labeled Fault 4 on Figure 5.1 –strikes E-W and dips 60-75° to the south. In the Xigaze unconformity horizontal frame of reference, Fault 4 would have dipped north at approximately 30°, with Subduction Mélanges in its hanging wall and Tibetan Sedimentary sequence rocks in its footwall. Where exposed, Fault 4 is primarily cataclastic in nature, containing 10 m-scale to sub-mm breccia fragments derived from both footwall and hanging wall rocks. Chatter marks on slickensides and cm-scale σ-shaped clasts associated with the footwall indicate a footwall down sense of shear in the fault's original orientation, consistent with thrusting.

Fabric characteristics within the suture zone

Although the overall appearance of most metamorphic units within the suture zone is structurally chaotic, penetrative fabrics are only well-preserved within the phyllitic lithologies of the Subduction Mélanges unit. Rocks from the immediate footwall of the Yarlung Zangbo Mantle thrust and immediate hanging wall of Fault 4 are typically oriented with their dominant foliation parallel to the adjacent structures. At greater distances from the faults, the phyllitic fabrics are complexly folded on the m- to km-scale. Lineations are common throughout the phyllites and typically plunge parallel to the local dip of the predominant phyllitic fabric. While apparent shear sense indicators in the

form of deformed clasts, S-C fabrics, and asymmetric folds are common throughout the phyllites, they often imply contradictory motions in individual outcrops not proximate to the Yarlung Zangbo Mantle thrust or Fault 4.

CONSTRAINTS ON THE AGES OF METAMORPHIC ASSEMBLAGES

$^{40}Ar/^{39}Ar$ geochronology

$^{40}Ar/^{39}Ar$ incremental heating experiments were performed on eleven amphibole multi-grain aliquots from amphibolite, meta-trondhjemite, and blueschist samples from both within the ophiolites and the Subduction Mélange (Table C2; see Appendix C for methods). These samples fall into two groups: hornblendes from amphibolites that yielded Cretaceous dates vs. Na-Ca-amphiboles and Na-amphiboles from meta-trondhjemites and blueschists that yielded early Tertiary dates.

For the hornblendes from amphibolites, integrated ages range over 125-80 Ma (Figure 5.4). For steps within individual samples, younger ages, lower Ca/K ratios, and lower radiogenic ^{40}Ar contents (i.e. high excess ^{40}Ar, Kelley, 2002) are roughly correlative, indicating the samples may have been affected by a metasomatic fluid after primary metamorphism. Five of the seven samples exhibit statistically significant plateau ages (Fleck et al., 1977) ranging from 125.1 ± 3.8 Ma down to 87.2 ± 2.3 Ma. Plateau steps have uniformly high (≥ 80%) radiogenic ^{40}Ar yields and low Ca/K ratio variation. These dates are most conservatively interpreted as closure dates for the amphiboles, but the probable metamorphic temperatures for the amphibole-bearing assemblages are sufficiently low that I follow previous researchers working on the Yarlung suture zone in interpreting them as crystallization ages (cf., Guilmette et al., 2009). The lack of plateaus

for samples ISZ and WPT03 discourage me from interpreting their spectra further, and data for neither sample yielded an inverse isochron when plotted in $^{36}Ar/^{40}Ar$ vs. $^{39}Ar/^{40}Ar$ space.

Three of four Na-Ca-amphiboles and Na-amphiboles from meta-trondhjemite and blueschist samples yielded plateau dates of 62.26 ± 0.32 Ma, 61.11 ± 0.31 Ma, and 61.05 ± 0.30 Ma (Figure 5.5). The oldest of these was for a Na-amphibole from a blueschist, whereas the two younger and statistically indistinguishable dates were for meta-trondhjemite Na-Ca amphiboles. High (≥ 90%) radiogenic ^{40}Ar yields and relatively uniform Ca/K ratios characterized all of the plateaus. I interpret the inverse variance-weighted mean of the samples 249 and 254 (61.08 ± 0.22 Ma) as the best available estimate of the ^{40}Ar closure age of meta-trondhjemite Na-Ca amphiboles. The slightly older (62.26 ± 0.32 Ma) sodic amphibole plateau date from blueschist sample KMBS is also slightly younger than the ca. 63 Ma blueschist dates for the same unit as determined by Ding et al. (2005). Based on the similarity and near overlapping nature of these dates, I interpret these dates to represent a single metamorphic event that spanned ca. 63-61 Ma at various structural levels within the Sangsang ophiolite.

(U-Th)/Pb joaquinite and $^{40}Ar/^{39}Ar$ neptunite geochronology

Recent work on joaquinites and neptunites from their type locality in the Diablo Range of California has established that (U-Th)/Pb dating of the former and $^{40}Ar/^{39}Ar$ dating of the latter can provide valuable constraints on the crystallization ages of these rare low-temperature, possibly moderately high-pressure metasomatic minerals (Borneman et al., in preparation; Chapter 3). I applied both chronometers to minerals

separated from meta-trondhjemite sample 254. (See Appendix for analytical methods.) LA-ICPMS (U-Th)/Pb data for 34 joaquinite crystals (a total of 54 analyses in all) are reported in Table C3. These crystals contain large amounts of common (non-radiogenic) Pb but have high Th/U ratios (~ 27) making them highly suitable for Th/Pb dating. On a conventional $^{232}Th/^{204}Pb$ vs. $^{208}Pb/^{204}Pb$ isotope correlation diagram (Figure 5.6), data for all 34 crystals define a statistically significant isochron corresponding to a crystallization age of 51.9 ± 1.6 Ma.

$^{40}Ar/^{39}Ar$ incremental heating experiments were performed on three neptunite crystals from the sample, and the results are shown in Table C2 and Figure 5.7. Each crystal exhibited relatively straightforward behavior during the experiment, with high (> 90%) radiogenic ^{40}Ar yields and low and relatively uniform Ca/K ratios for all increments. Each experiment yielded a statistically significant plateau age, and all three plateaus were within uncertainty of each other. The inverse variance-weighted mean of all three (52.38 ± 0.61 Ma) is statistically indistinguishable from the less precise Th/Pb isochron age of the joaquinite, and I regard it as the best available constraint on the age of the high-Ti metasomatic assemblage in the meta-trondhjemite pods.

DISCUSSION

The ages of oceanic crustal components within the Sangsang ophiolite

Recently, Chan et al. (2015) reviewed previously published and new U/Pb zircon constraints on the ages of mafic rocks of oceanic crustal origin within various ophiolitic massifs along the Yarlung suture zone. They interpreted those data to indicate the existence of oceanic rocks in the suture zone of various ages ranging from Late Jurassic

to middle Cretaceous. Potentially, this variety implies the existence of several intraoceanic subduction zones within Neo-Tethys prior to India-Eurasia collision, with both mid-ocean ridge and supra-subduction zone oceanic crust now preserved as imbricate slices in the suture (Hébert et al., 2012). If previous workers are correct in their inference that the Xigaze basal unconformity at Sangsang developed at about the time of the youngest detrital zircons found above the unconformity (Maffione et al., 2015; Huang et al., 2015a), then at least some of the ophiolitic mélange must be no younger than ca. 129 Ma. U/Pb zircon dates for gabbros and quartz diorites from the nearby Xigaze ophiolite, ranging from 132-126 Ma, are roughly consistent with this inference (Malpas et al., 2003; Wang et al., 2006; Chan et al., 2015). Unfortunately, my work on the mafic rocks of the ophiolitic mélange at Sangsang did not lead to the identification of zircons suitable for U/Pb dating. However, my U/Pb data for meta-trondhjemite sample 254 indicate the existence of oceanic crustal components at least as young as late Early Cretaceous (ca. 111 Ma) in the Sangsang ophiolite south of Fault 3. At present, this represents the youngest known igneous oceanic rock found in the Yarlung suture and, in conjunction with previously published data, suggests the continuation of supra-subduction zone oceanic crust development in the northern Neo-Tethys ocean basin throughout much of the Early Cretaceous. Furthermore, the similar age of Fault 1(as constrained by the Xigaze unconformity) allows that the formation of detachments in this region was coeval with magmatism and amphibolites facies metamorphism. Such an association of magmatism and normal faulting is common in slow spreading ridge environments (Smith et al., 2006; Maffione et al., 2015).

Older $^{40}Ar/^{39}Ar$ dates for amphiboles in the Sangsang ophiolite (ca. 125 Ma) are similar to those from amphibolite bodies found in the Xigaze ophiolite (Guilmette et al., 2009). The Xigaze dates were interpreted by Guilmette and co-workers as indicative of the early stages of supra-subduction zone oceanic crust formation. If this hypothesis is extended to explain the oldest amphibolite ages at Sangsang, the early oceanic crust could have been produced in a proximal mid ocean ridge that was subsequently subducted beneath Eurasia at some point prior to obduction of the Sangsang ophiolite. The plausible timing of this hypothetical event is poorly constrained, but an application of simple math can narrow the possibilities. If V_s is the subduction rate under Sangsang and V_r is the ridge spreading rate, then V_c, the convergence rate across both the ridge and subduction zone is

$$V_c = V_s - V_r \quad (1)$$

prior to ridge subduction, and

$$V_c = V_s \quad (2)$$

after ridge subduction. Through these equations we predict an increase in convergence associated with the ridge subduction event. Paleomagnetic data record an increase in the India-Eurasia convergence rate at ca. 120-70 Ma (van Hinsbergen et al., 2012). While the oldest amphibole age at Sangsang (125.1 ± 3.8 Ma) is slightly older than this range, realistic uncertainties on the geochronologic and paleomagnetic data make it plausible that the subduction of a mid-ocean ridge and associated hot lithosphere at ca. 125 Ma could account for both the increase in convergence rate and amphibolite generation.

However, the full ca. 125-87 Ma range of amphibole ages from amphibolite bodies at Sangsang suggests protracted oceanic crust formation as envisioned for

ophiolites in other settings by Dewey and Casey (2011). Recently, Chan et al. (2015) speculated that ca. 130-120 Ma and ca. 90-80 Ma amphibolites identified along the Yarlung suture may be related to a continuous oceanic-crust forming event. my data for the Sangsang ophiolite, demonstrating the existence in a single segment of the suture of amphiboles that crystallized across the entire age range identified by Chan and co-workers, supports their idea.

Development of the Subduction Mélanges and preservation of high-pressure assemblages

The gradational contact between the blueschists and the phyllitic metasedimentary units of the Subduction Mélanges unit is significant in that it implies that the entire package experienced high-pressure metamorphism even though the phyllites contain high thermodynamic-variance assemblages that do not include minerals uniquely indicative of it. My Na-amphibole $^{40}Ar/^{39}Ar$ data for the blueschist, along with the previously published data of Ding et al. (2005), require the Subduction Mélanges package to have been assembled prior to metamorphism at ca. 62-63 Ma. The ca. 82 Ma maximum age of a sandstone bed found within this package provides a useful upper bound on the age of assembly.

The preservation of high-pressure mineral assemblages within the Subduction Mélanges implies that some process interrupted trench evolution such that the high-pressure assemblages were rapidly transported to the upper crust without substantial retrogression. The existence of similarly high-pressure relict assemblages of essentially the same age within the meta-trondhjemites of the ophiolitic mélanges to the north

strongly suggests that this exhumation event affected the entire forearc region during the early Paleocene.

Possible implications of early Paleocene accretionary wedge exhumation for the southward extent of Eurasian detritus

The presence of detrital zircons of Eurasian provenance in the Subduction Mélanges potentially helps to resolve a vexing tectonic paradox. The oldest known sedimentary deposits along the suture zone in southern Tibet that contain mixed Indian and Eurasian detritus is the ca. 60-58 Ma Sangdanlin Formation (DeCelles et al., 2014; Hu et al., 2015). Those authors reasonably suggested that this might be interpreted as evidence of Paleocene or earlier India-Eurasia collision. However, the most reliable paleomagnetic data pertinent to the timing of collision (e.g., Huang et al., 2015b) suggest that the northern margin of India was roughly 1000 km south of the southern margin of Eurasia at ca. 60 Ma. Building on an earlier suggestion by Orme et al. (2015) that a regional exhumation event may have triggered the influx of Eurasian detritus to the Sangdanlin Formation, I suggest that uplift and erosion of the Subduction Mélanges, which contain Eurasian zircons, provided a secondary source for the Eurasian zircons identified in the Sangdanlin Formation. In this model, I envision an Early Cretaceous Eurasian margin forearc that extended southward several hundred kilometers from the Lhasa block to the subduction zone in which the Sangsang mélanges formed. (Forearcs of such dimensions exist today such as the ca. 430 km Makran forearc region to the immediate west of the India-Eurasia collision zone; Nicholson et al., 2010.) Given the evidence for late Early Cretaceous extension in the supra-subduction zone oceanic basin

to the north – presented here as well as by Maffione et al. (2015) and Hunziker et al. (2015) – it is possible that the total width of the modified forearc at the time of deposition of the Sangdanlin Formation was plausibly as much as 500 km. I know from the distance from shore to the edge of the continental rise of modern land masses (e.g., NW Australia; Heezen, 1974) that offshore continental sediment transport distances can be up to at least ca. 500 km. If the reworked detritus from the uplifted distal Eurasian forearc were transported similar distances southward, it is thus possible that they may have been deposited onto Indian crust well before India-Eurasia collision, eliminating the need to interpret the presence of mixed Indian-Eurasian detritus in the Sangdanlin Formation as evidence for pre-60 Ma India-Eurasia collision.

Based on my work at Sangsang, I are unable to ascribe a discrete tectonic event that led to the uplift and subsequent erosion of the forearc in the Paleocene, though I can propose several possible models. In the first, portions of the accretionary wedge could have been obducted onto the northern margin of India at this time. This model has broad support for evidence of similar obduction events in the Paleocene (Chan et al., 2015; Ding et al., 2005). However, this model requires one of two unlikely scenarios in Sangsang. Either the Indian passive margin and the Eurasia forearc were much closer than current paleomagnetic models suggest, or the accretionary wedge portion of the forearc had been rifted ca. 1000 km from Eurasia, putting it in proximity to India at ca. 60 Ma. Any southward obduction onto India must have taken place after the deposition of the Sangdanlin Formation, as obduction would have overridden any basin on the Indian plate.

In a second model, the forearc sequence at Sangsang could have been obducted southward onto an intra-oceanic arc. There are varying degrees of evidence for multiple intra-oceanic arcs between India and Eurasia prior to collision (e.g., the Spong arc; Pederson, 2011). Since paleomagnetic constraints make it likely that the Sangsang forearc was the northernmost forearc between India and Eurasia (Huang et al., 2015a), any intervening intra-oceanic arc(s) would have been to the south of the paleo-positions of the rocks exposed at Sangsang. Thus, if such an arc were to impinge on the trench south of the Sangsang accretionary wedge, Sangsang could have been obducted and uplifted southward onto that arc. I do not favor this model, however, inasmuch as there is currently no evidence for an intra-oceanic arc colliding at Sangsang.

We find a third model to be the most plausible. It holds that high sedimentation rates into the trench led to a "sediment choked" subduction zone. Here, influx of new material to the bottom of accretionary wedge would cause uplift to the surface. Currently such a sediment choked and actively eroding accretionary wedge exist off of Iran and Pakistan (Smith et al., 2014). This example also exists without the influence of a second continental mass on the opposite side of the trench. Evidence of this model comes from An et al., (2014), who showed that thickening of the forearc succession though the Campanian requires a commensurate growth in the accretionary wedge that acted to contain the basin.

Tectonic significance of extensional activity on Fault 3

Slip on Fault 3 was likely in a normal sense given the presence of the high-pressure Na-Ca amphiboles found within the meta-trondhjemite slices found along it and

high-pressure Na-amphiboles found in the more distal footwall. If I reasonably infer that fault slip is responsible for the exhumation of the meta-trondhjemite from depth, Fault 3 must have been active at ca. 61 Ma or more recently based on the $^{40}Ar/^{39}Ar$ dates presented here. I prefer the interpretation that tectonic denudation related to Fault 3 was more recent and coincident with retrograde overprinting of the high-pressure winchite + katophorite assemblage by the neptunite + benitoite + joaquinite metasomatic assemblage in these rocks during the exhumation process. If this interpretation is correct, the most likely age for the most significant offset on Fault 3 is ca. 52 Ma based on my Th/Pb and $^{40}Ar/^{39}Ar$ data for the joaquinite and neptunite in the metasomatic assemblage.

Evidence for extensional faulting close in timing to collision at first seems counter-intuitive, but I provide two models that can explain this phenomenon. The first builds on the "sediment choked" scenario described above. In this model, the volume of sedimentary rocks entering the subduction zone and being added to the forearc accretionary wedge would have increased as India and Eurasia approached each other. This extra sediment could have led to the wedge exceeding its critical taper, leading to either collapse and normal faulting or forward propagation of the wedge. A second model involves the hydration of ultramafic material in the footwall of Fault 3. Heating during collision could dehydrate deeper rocks, causing fluid to migrate into structurally higher ultramafic rocks. The hydration of ultramafic rocks to serpentinites leads to a decrease in density. This density decrease could then drive the diapiric rise of the now serpentinitic material (and blocks entrained within it) upwards along normal sense faults. Such a diapiric rise has been invoked at the other locality for the rare Ti minerals in the New Idria serpentinite diapir of California (Van Baalen, 2004)

Tectonic significance of the Yarlung Zangbo Mantle thrust

The most important contractional structure identified in my study area is the Yarlung Zangbo Mantle thrust of Ding et al. (2005). It marks a major metamorphic discontinuity, juxtaposing hanging wall ophiolitic mélanges and footwall blueschist facies rocks of the Subduction Mélanges. The age of serpentinization in the hanging wall is not well constrained, but the associated amphibolites yield ca. 125 to ca. 87 Ma $^{40}Ar/^{39}Ar$ amphibole plateaus. A growing body of $^{40}Ar/^{39}Ar$ Na-amphibole data (including those presented here and by Ding et al., 2005) indicates that the high-pressure metamorphism of the footwall was an early Paleocene (ca. 63-62 Ma) phenomenon. The observed metamorphic pressure-temperature and age discontinuity across the Yarlung Zangbo Mantle thrust requires that the structure must be active after the time of footwall metamorphism.

The observation that Fault 2 offsets the Yarlung Zangbo Mantle thrust but is truncated by Fault 3 places additional constraints on the age of thrusting. If I accept the interpretation that principal movement on Fault 3 occurred during the development of the ca. 52 Ma high-Ti metasomatic assemblage in the meta-trondhjemites, then Fault 2 must be older. The observed relationship between this fault and the Yarlung Zangbo Mantle thrust, as well the limit on the age of thrusting, effectively constrain the age of the Yarlung Zangbo Mantle thrust to between ca. 63 and ca. 52 Ma.

Implications for the age of India-Eurasia collision

The assemblage of the rare Ti-minerals neptunite + benitoite + joaquinite may help constrain the timing of India-Eurasia collision at the longitude of Sangsang. The rarity of these minerals also makes it likely that the relatively rare conditions for their

formation can be tied to a discrete geologic event. For example, the only other known occurrence of this complete assemblage – in the New Idria region, California – is generally interpreted to have formed coincident with the cessation of a subduction event, in that instance related to passage of the Mendocino triple junction (Van Baalen, 2004). If a similar event was responsible for crystallization of the assemblage at Sangsang, the ca. 52 Ma age of that assemblage may date India-Eurasia collision. Independent paleomagnetic data, which indicate 52 Ma as the best estimate for the timing of contact between the Tibetan Sedimentary Sequence and the southern margin of the Eurasian plate (Huang et al., 2015b), lend credence to this idea.

A model for the pre-collisional – collisional transition in the Sangsang and Xigaze regions

My research on the Sangsang segment of the Yarlung suture, the new geochronologic data in particular, complement the results of previous studies and help refine my understanding of the processes of India-Eurasia convergence and eventual collision in this area. In particular, the rocks present in Sangsang collect in one area evidence for tectonic events reported only in separate sections elsewhere in the orogen. One viable model of the geologic history recorded along this segment is shown in Figure 5.8.

Prior to 130 Ma, mid ocean ridge affinity rocks of Late Jurassic and Late Jurassic to Early Cretaceous supra-subduction zone rocks require at least one mid-ocean ridge and subduction zone separated India and Eurasia (Chan et al., 2015; Hébert et al., 2012). Paleomagnetic constraints (Huang et al., 2015b) and the $^{40}Ar^{39}Ar$ amphibolites dates

from this study make it likely that the subduction zone (or the most northerly subduction zone if there were indeed multiple subduction zones) was immediately south of the Eurasian continent.

By ca. 132 Ma (Chan et al., 2015), supra subduction zone magmatism in the forearc region had initiated. This may have been triggered by subduction of a mid-ocean ridge in the Eurasia-proximal subduction zone. This magmatism lasted until at least ca. 111 Ma based on the magmatic age from a meta-trondhjemite presented in this study. Spreading in this SSZ environment was likely slow based on the presence of low-angle normal faults that date from this time and the propensity for extension of that style near slow-spreading ridges (Smith et al., 2006). These faults that denuded forearc mantle rocks allowed Xigaze Forearc strata to be deposited on the same recently formed ophiolites. At the same time, continuing subduction of young and warm oceanic crust originally developed south of the ridge triggered amphibolite facies metamorphism in the subduction-accretion wedge until at least ca. 80 Ma. Tectonic processes during this period of coeval subduction and extension resulted in hyperextension of the Gangdese forearc, possibly increasing its N-S extent to as much as 500 km based on the above paleomagnetic arguments.

Subduction continued until the early Paleocene, allowing the Xigaze forearc to be thrust over the accretionary wedge. I suggest that, at 63-61 Ma, accretion of material to the bottom of the accretionary wedge began to drive uplift of the accretionary wedge and forearc, causing the wedge to breach the ocean's surface as constrained by the erosion of the wedge at this time (Orme et al., 2015). The Yarlung Zangbo Mantle thrust appears to have been related to wedge deformation during this process. Uplift of the wedge would

have permitted both it and the overlying distal Xigaze Forearc to erode. As a consequence, reworked Eurasian detritus could have reached as far as the northernmost margin of India to the south, where it was deposited as part of the 60-59 Ma Sangdanlin Formation.

Based on paleomagnetic estimates and interpretation of Huang et al. (2015b), the Indian plate should have reached the southern margin of the hyperextended forarc at ca. 52 Ma. This requires that the accretionary wedge made contact with and was obducted onto India after Sangdanlin Formation deposition but before the final collision of continental India and Eurasia. The relative timing of these events is heavily dependent on whether or not the forearc retreated northward toward Eurasia during the course of normal subduction after ca. 60 Ma.

The conventional wisdom that initial collision between the Indian and Eurasian plates occurred during the early Eocene (Ypresian) is consistent with my geological observations and geochronologic data for Sangsang. I specifically infer that final suturing triggered rapid exhumation of high-pressure metamorphic rocks within the subduction zone, leading to the crystallization of an assemblage of rare Ti-rich metasomatic minerals found in the meta-trondhjemite pods at Sangsang. Thus, I regard the growth of these minerals, dated to ca. 52 Ma using both the U/Pb and $^{40}Ar/^{39}Ar$ geochronologic techniques, as the best available estimate for the timing of final collision at Sangsang. As India-Eurasia convergence continued, the Sangsang section rotated to the near-vertical orientation it has today.

CONCLUSIONS

The geologic record as preserved at Sangsang places important constraints on the timing, style, and location of convergence between India and Eurasia. The region preserves evidence for supra-subduction zone magmatism, metamorphism, and extension within the forearc immediately south of Eurasia over much of the Cretaceous Period. This long-lived process was interrupted in the Paleocene by poorly understood event that led to uplift and erosion of the accretionary wedge. Previously reported evidence for Eurasian detritus in the 60-59 Ma Sangdanlin Formation deposited on the Indian continental margin– which was interpreted as evidence for Paleocene India-Eurasia collision (DeCelles et al., 2014; Hu et al., 2015; Wu et al., 2014) – may instead indicate the transport of reworked Eurasian material from the eroded accretionary wedge. I suggest that the final collision between continental India and Eurasia at the longitude of Sangsang resulted in the crystallization of an unusual metasomatic mineral assemblage in the ophiolite at 52 Ma.

ACKNOWLEDGEMENTS

Analytical aspects of my research were supported by a grant from the U.S. National Science Foundation's Continental Dynamics program (EAR 1007929) to K.V. Hodges. I thank the U.S. National Science Foundation's Earth Sciences Instrumentation and Facilities program for partial support for the acquisition of analytical instrumentation in the Group 18 Laboratories.

FIGURE CAPTIONS

Figure 5.1. a: Overview of the Yarlung suture adjacent to the Sangsang section. b: Geologic map of the Sangsang section showing topography, structures, rock attitudes, and sample locations. c and d: Cross sections through the study area emphasizing original fault motions. No vertical exaggeration. YZMT is the Yarlung Zangbo Mantle thrust.

Figure 5.2. U/Pb zircon data for meta-trondhjemite sample 254. The inverse variance-weighted mean of 111.2 ± 2.2 Ma is interpreted as the magmatic age of the trondhjemite Vertical bars are individual dates with errors, horizontal bar is the mean age.

Figure 5.3. Detrital zircon age spectrum for sandstone sample 234 from the phyllitic metasedimentary subunit of the Subduction Mélanges. Left inset shows a zoomed in version the same spectrum on the same axes. Right inset shows the $^{206}Pb/^{238}U$ dates and uncertainties (at 2□) for the three youngest crystals.

Figure 5. 4. $^{40}Ar/^{39}Ar$ step heating release spectra for hornblendes from amphibolites pods within the serpentinized ophiolites. Plateau dates are bracketed were appropriate.

Figure 5.5. $^{40}Ar/^{39}Ar$ step heating release spectra for Na/Na-Ca amphiboles. Plateau dates are bracketed were appropriate.

Figure 5.6. Th/Pb isochron for sample 254 joaquinite. The date calculated from this isochron is 51.9 ± 1.6 Ma, the initial 208Pb/204Pb ratio is 38.51 ±0.51, the MSWD for the date is 0.71. All errors are 2σ.

Figure 5.7. $^{40}Ar/^{39}Ar$ step heating release spectra for neptunite from sample 254. Plateau dates are bracketed were appropriate.

Figure 5.8. Subduction and collision model for the Sangsang section of the Yarlung suture. See Conclusion section for discussion. Half arrows emphasize fault movements during the time of slip.

REFERENCES

Aitchison, J.C.; Xia, X.; Baxter, A.T.; Ali, J.R., 2011, Detrital zircon U-Pb ages along the Yarlung-Tsangpo suture zone, Tibet: Implications for oblique convergence and collision between India and Asia, Gondwana Research, 20, 4, 691-709, 10.1016/j.gr.2011.04.002.

An, W.; Hu, X.M.; Garzanti, E.; BouDagher-Fadel, M.K.; Wang, J.G.; Sun, G.Y., 2014, Xigaze forearc basin revisited (South Tibet): Provenance changes and origin of the Xigaze Ophiolite, Geological Society of America Bulletin, 126, 11-12, 1595-1613, 10.1130/B31020.1.

Borneman, L.; Hodges, K.; van Soest, M.C.; Bohon, W.; Wartho, J.-A.; Cronk, S.S.; Ahmad, T., 2014, Age and structure of the Shyok suture in the Ladakh region of northwestern India: Implications for slip on the Karakoram fault system, Tectonics, 34, 10, 2011-2033, 10.1002/2015TC003933.

Bédard, E.; Hébert, R.; Guilmette, C.; Lesage, G.; Wang, C.S.; Dostal, J., 2009, Petrology and geochemistry of the Saga and Sangsang ophiolitic massifs, Yarlung Zangbo Suture Zone, Southern Tibet: Evidence for an arc-back-arc origin, Lithos, 113, 1-2, 48-67, 10.1016/j.lithos.2009.01.011.

Bouilhol, P.; Jagoutz, O.; Hanchar, J.M.; Dudas, F.O., 2013, Dating the India-Eurasia collision through arc magmatic records, Earth and Planetary Science Letters, 366, 163-175, 10.1016/j.epsl.2013.01.023.

Broecker, W., 2015, The collision that changed the world, Elementa Science of the Anthropocene, 3, 000061, 10.12952/journal.elementa.

Cai, F.L.; Ding, L.; Leary, R.J.; Wang, H.Q.; Xu, Q.; Zhang, L.Y.; Yue, Y.H., 2012, Tectonostratigraphy and provenance of an accretionary complex within the Yarlung-Zangbo suture zone, southern Tibet: Insights into subduction-accretion processes in the Neo-Tethys, Tectonophysics, 574, 181-192, 10.1016/j.tecto.2012.08.016.

Chan, G.H.; Aitchison, J.C.; Crowley, Q.G.; Horstwood, M.S.A.; Searle, M.; Parrish, R.R.; Chan, J.S-L., 2015, U-Pb zircon ages for Yarlung Tsangpo suture zone ophiolites, southwestern Tibet and their tectonic implication, Gondwana Research, 27, 719-732.

Cherniak, D.J.; Watson, E.B., 2001, Pb diffusion in zircon Chemical Geology, 172, 5-24.

Chew, D.M.; Petrus, J.A.; Kamber, B.S.; 2014, U-Pb LA-ICPMS dating using accessory mineral standards with variable common Pb, Chemical Geology, 363, 185-199, 10.1016/j.chemgeo.2013.11.006.

Coleman, R.G., 1961, Jadeite deposits of the Clear Creek area, New Idria district, San Benito County, California, Journal of Petrology, 2, 209-211.

DeCelles, G.; Kapp, P.; Gehrels, G.E.; Ding, L., 2014, Paleocene-Eocene foreland basin evolution in the Himalaya of southern Tibet and Nepal: Implications for the age of initial India-Asia collision, Tectonics, 33, 5, 824-849, 10.1002/2014TC003522.

DeCelles, G.; Kapp, P.; Quade, J.; Gehrels, G.E., 2011, Oligocene-Miocene Kailas basin, southwestern Tibet: Record of postcollisional upper-plate extension in the Indus-Yarlung suture zone, Geological Society of America Bulletin, 123, 7-8, 1337-1362, 10.1130/B30258.1.

Dewey, J.F.; Casey, J.F., 2011, The Origin of Obducted Large-Slab Ophiolite Complexes. *in* Brown, D., and Ryan, D., eds., Arc–Continent Collision, Berlin Heidelberg, Springer, 431–444.

Ding, L., Kapp, P., and Wan, X.Q., 2005, Paleocene-Eocene record of ophiolite obduction and initial India-Asia collision, south central Tibet, Tectonics, 24, 3, TC3001, 10.1029/2004TC001729.

Gaetani, M.; Garzanti, E., 1991, Multicyclic history of the northern India continental-margin (northwestern Himalaya), AAPG Bulletin-American Association of Petroleum Geologists, 75, 9, 1427-1446.

Gehrels, G., 2012, Detrital zircon U-Pb geochronology: Current methods and new opportunities, *in* Busby, C., and Perez, A.A., eds., Tectonics of Sedimentary Basins: Recent Advances: Oxford, Blackwell, 47-62.

Gehrels, G.; Kapp, P.; DeCelles, P.; Pullen, A.; Blakey, R.; Weislogel, A.; Ding, L.; Guynn, J.; Martin, A.; McQuarrie, N.; Yin, A., 2011, Detrital zircon geochronology of pre-Tertiary strata in the Tibetan-Himalayan orogen, Tectonics, 30, TC5016, 10.1029/2011TC002868.

Gehrels, G.E.; Valencia, A.; Ruiz, J., 2008, Enhanced precision, accuracy, efficiency, and spatial resolution of U-Pb ages by laser ablation-multicollector-inductively coupled plasma-mass spectrometry, Geochemistry Geophysics Geosystems, 9, Q03017, 10.1029/2007GC001805.

Guilmette, C.; Hébert, R.; Wang, C.S.; Villeneuve, M., 2009, Geochemistry and geochronology of the metamorphic sole underlying the Xigaze Ophiolite, Yarlung Zangbo Suture Zone, South Tibet, Lithos, 112, 1-2, 149-162, 10.1016/j.lithos.2009.05.027.

Harlow, G.E.; Tsujimori, T.; Sorensen, S.S., 2015, Jadeitites and Plate Tectonics, Annual Review of Earth and Planetary Sciences, 43, 105-138, 10.1146/annurev-earth-060614-105215.

Hébert, R.; Bezard, R.; Guilmette, C.; Dostal, J.; Wang, C.S.; Liu, Z.F., 2012, The Indus-Yarlung Zangbo ophiolites from Nanga Parbat to Namche Barwa syntaxes, southern Tibet: First synthesis of petrology, geochemistry, and geochronology with incidences on geodynamic reconstructions of Neo-Tethys, Gondwana Research, 22, 2, 377-397, 10.1016/j.gr.2011.10.013.

Heezen, B.C., 1974, Atlantic type continental margins, *in* Burk, C.A., and Drake, C.L., eds., The Geology of Continental Margins: New York, Springer, 13-24.

Hodges, K., 2000, Tectonics of the Himalaya and southern Tibet from two perspectives, Geological Society of America Bulletin, 112, 3, 324-350, 10.1130/0016-7606(2000)112<0324:TOTHAS>2.3.CO;2.

Hodges, K., 2013, Thermochronology in orogenic systems, *in* Rudnick R. ed., Treatise on Geochemistry (Second Edition): The Crust, 281-308.

Hu, X.; Garzanti, E.; Moore, T.; Raffi, I., 2015, Direct stratigraphic dating of India-Asia collision onset at the Selandian (middle Paleocene, 59 ± 1 Ma), Geology, 43, no. 10, 859-862, doi:10.1130/G36872.1.

Huang, W.T.; van Hinsbergen, D.J.J.; Maffione, M.; Orme, D.A.; Dupont-Nivet, G.; Guilmette, C.; Ding, L.; Guo, Z.J.; and Kapp, P., 2015a, Lower Cretaceous Xigaze ophiolites formed in the Gangdese forearc: Evidence from paleomagnetism, sediment

provenance, and stratigraphy, Earth and Planetary Science Letters, 415, 142-153, 10.1016/j.epsl.2015.01.032.

Huang, W.; van Hinsbergen, D.J.J.; Lippert, C.; Guo, Z.; Dupont-Nivet, G., 2015b, Paleomagnetic tests of tectonic reconstructions of the India-Asia collision zone, Geophysical Research Letters, 42, 8, 2642-2649, 10.1002/2015GL063749.

Hunziker, D.; Burg, J., Bouilhol, P.; von Quadt, A., 2015, Jurassic rifting at the Eurasian Tethys margin: Geochemical and geochronological constraints from granitoids of North Makran, southeastern Iran, Tectonics, 34, 571-593, 10.1002/2014TC003768.

Jagoutz, O.; Royden, L.; Holt, A.F.; Becker, T.W., 2015, Anomalously fast convergence of India and Eurasia caused by double subduction, Nature Geoscience, 8, 6, 475-478, 10.1038/NGEO2418.

Jiang, Z.Q.; Wang, Q.; Wyman, D.A.; Li, Z.X.; Yang, J.H.; Shi, X.B.; Ma, L.; Tang, G.J.; Gou, G.; Jia, X.H.; Guo, H.F., 2014, Transition from oceanic to continental lithosphere subduction in southern Tibet: Evidence from the Late Cretaceous-Early Oligocene (similar to 91-30 Ma) intrusive rocks in the Chanang-Zedong area, southern Gangdese, Lithos, 196, 213-231, 10.1016/j.lithos.2014.03.001.

Kapp, P.; Murphy, M.A.; Yin, A.; Harrison, T.M.; Ding, L.; Guo, J.H., 2003, Mesozoic and Cenozoic tectonic evolution of the Shiquanhe area of western Tibet, Tectonics, 22, 4, TC1029, 10.1029/2001TC001332.

Kapp, P.; DeCelles, G.; Gehrels, G.E.; Heizier, M.; Ding, L., 2007, Geological records of the Lhasa-Qiangtang and Indo-Asian collisions in the Nima area of central Tibet, Geological Society of America Bulletin, 119, 7-8, 917-932, 10.1130/B26033.1.

Kelley, S., 2002, Excess argon in K-Ar and Ar-Ar geochronology, Chemical Geology, 188, 1-2, 1-22, 10.1016/S0009-2541(02)00064-5.

Long, S.; McQuarrie, N., Tobgay, T.; Coutand, I.; Cooper, F.J.; Reiners, W.; Wartho, J.-A.; Hodges, K., 2012, Variable shortening rates in the eastern Himalayan thrust belt, Bhutan: Insights from multiple thermochronologic and geochronologic data sets tied to kinematic reconstructions, Tectonics, 31, TC5004, 10.1029/2012TC003155.

Maffione, M.; van Hinsbergen, D.J.J.; Koornneef, L.M.T.; Guilmette, C.; Hodges, K., Borneman, N.; Huang, W.; Ding, L.; Kapp, , 2015, Forearc hyperextension dismembered the South Tibetan ophiolites, Geology, 43, 475–478, doi:10.1130/G36472.1.

Malpas, J.; Zhou, M.-F.; Robinson, T.; Reynolds, H., 2003, Geochemical and geochronological constraints on the origin and emplacement of the Yarlung Zangbo ophiolites, Southern Tibet, Geological Society, London, Special Publications 218, 191–206.

Najman, Y.; Appel, E.; Boudagher-Fadel, M.; Bown, P.; Carter, A.; Garzanti, E.; Godin, L.; Han, J.T.; Liebke, U.; Oliver, G.; Parrish, R., Vezzoli, G., 2010, Timing of India-Asia collision: Geological, biostratigraphic, and palaeomagnetic constraints, Journal of Geophysical Research-Solid Earth, 115, B12416, 10.1029/2010JB007673.

Nicholson, K.; Khan, M.; Mahmood, K., 2012, Geochemistry of the Chagai-Raskoh arc, Pakistan: Complex arc dynamics spanning the Cretaceous to Quaternary, Lithos, 118, 338-348, 10.1016/j.lithos.2010.05.008.

Oberti, R.; Boiocchi, M.; Hawthorne, F.C.; Ball, A.; Harlow, G.E., 2015, Katophorite from the Jade Mine Tract, Myanmar: mineral description of a rare (grandfathered) endmember of the amphibole supergroup, Mineralogical Magazine, 79, 355-363, 10.1180/minmag.2015.079.2.13.

Orme, D.A.; Carrapa, B.; Kapp, P., 2015, Sedimentology, provenance and geochronology of the upper Cretaceous-lower Eocene western Xigaze forearc basin, southern Tibet, Basin Research, 27, 4, 387-411, 10.1111/bre.12080.

Paton, C.; Hellstrom, J.; Paul, B.; Woodhead, J.; Hergt, J., 2011, Iolite: Freeware for the visualisation and processing of mass spectrometric data, Journal Of Analytical Atomic Spectrometry, 26, 12, 2508-2518, 10.1039/c1ja10172b.

Rowley, D.B., 1996, Age of initiation of collision between India and Asia: A review of stratigraphic data, Earth and Planetary Science Letters, 145, 1-4, 1-13, 10.1016/S0012-821X(96)00201-4.

Sakai, M.; Akai, J., 1994, Strontium, barium and titanium-bearing minerals and their host rocks from Ohmi, Japan, Scientific Reports Niigata University, Series E, 9, 97-118.

Schoene, B.; Bowring, S.A., 2006, U-Pb systematics of the McClure Mountain syenite: thermochronological constraints on the age of the Ar-40/Ar-39 standard MMhb, Contributions to Mineralogy and Petrology, 151, 5, 615-630, 10.1007/s00410-006-0077-4.

Schwarz, W.H.; Trieloff, M., 2007, Intercalibration of Ar-40-Ar-39 age standards NL-25, HB3gr hornblende, GA1550, SB-3, HD-B1 biotite and BMus/2 muscovite, Chemical Geology, 242, 1-2, 218-231, 10.1016/j.chemgeo.2007.03.016.

Slama, J.; Dunkley, D.J.; Kachlik, P.; Kusiak, M.A., 2008, Transition from island-arc to passive setting on the continental margin of Gondwana: U-Pb zircon dating of Neoproterozoic metaconglomerates from the SE margin of the Tepla-Barrandian Unit, Bohemian Massif, Tectonophysics, 461, 1-4, 44-59, 10.1016/j.tecto.2008.03.005.

Smith, D. K.; Cann, J. R.; Escartín, J., 2006, Widespread active detachment faulting and core complex formation near 13°N on the Mid-Atlantic Ridge: Nature, 442, 440-443.

Smith, G.L.; McNeill, L.C.; Henstock, T.J.; Arraiz, D.; Spiess, 2014, Fluid generation and distribution in the highest sediment input accretionary margin, the Makran, Earth and Planetary Science Letters, 403, 131-143, 10.1016/j.epsl.2014.06.030.

Steiger, R.H.; Jäger, E., 1977, Subcommission on geochronology: Convention on the use of decay constants in geo- and cosmochronology, Earth And Planetary Science Letters, 36, 21-23.

St-Onge, M. R.; Rayner, P.; Searle, M., 2010, Zircon age determinations for the Ladakh batholith at Chumathang (Northwest India): Implications for the age of the India-Asia collision in the Ladakh Himalaya, Tectonophysics, 495, 3-4, 171-183.

Sun, J.F.; Yang, J.H.; Wu, F.Y.; Xie, L.W.; Yang, Y.H.; Liu, Z.C.; Li, X.H., 2012, In situ U-Pb dating of titanite by LA-ICPMS, Chinese Science Bulletin, 57, 20, 2506-2516, 10.1007/s11434-012-5177-0.

Tripathy-Lang, A.; Hodges, K.; van Soest, M.C.; Ahmad, T., 2013, Evidence of pre-Oligocene emergence of the Indian passive margin and the timing of collision initiation between India and Eurasia, Lithosphere, 5, 5, 501-506, 10.1130/L273.1.

Van Baalen, M.R., 2004, Migration of the Mendocino triple junction and the origin of titanium-rich mineral suites at new Idria, California, International Geology Review, 46, 8, 671-692, 10.2747/0020-6814.46.8.671.

van Hinsbergen, D.J.J.; Lippert, C.; Dupont-Nivet, G.; McQuarrie, N.; Doubrovine, P., Spakman, W.; Torsvik, T.H., 2012, Greater India Basin hypothesis and a two-stage Cenozoic collision between India and Asia, Proceedings of the National Academy of Sciences of the United States of America, 109, 20, 7659-7664, 10.1073/pnas.1117262109.

Wang, C.S.; Li, X.H.; Liu, Z.F.; Li, Y.L.; Jansa, L.; Dai, J.G.; Wei, Y.S., 2012, Revision of the Cretaceous-Paleogene stratigraphic framework, facies architecture and provenance of the Xigaze forearc basin along the Yarlung Zangbo suture zone, Gondwana Research, 22, 2, 415-433, 10.1016/j.gr.2011.09.014.

Wang, R.; Xia, B.; Zhou, G.Q.; Zhang, Y.Q.; Yang, Z.Q.; Li, W.Q.; Wei, D.L.; Zhong, L.F.; Xu, L.F., 2006, SHRIMP zircon U–Pb dating for gabbro from the Tiding ophiolite in Tibet, Chinese Science Bulletin 51, 1776–1779.

Wendt, I.; Carl, C., 1991, The statistical distribution of the mean squared weighted deviation, Chemical Geology, 86, 275-285.

Wu, F.Y.; Ji, W.Q.; Wang, J.G.; Liu, C.Z.; Chung, S.L.; Clift, D., 2014, Zircon U-Pb and Hf isotopic constraints on the onset time of India-Asia collision, American Journal of Science, 314, 2, 548-579, 10.2475/02.2014.04.

Yin, A.; Harrison, T.M., 2000, Geologic evolution of the Himalayan-Tibetan orogen, Annual Review of Earth and Planetary Sciences, 28, 211-280, 10.1146/annureearth.28.1.211.

Zhang, L.L.; Liu, C.Z.; Wu, F.Y.; Ji, W.Q.; Wang, J.G., 2014, Zedong terrane revisited: An intra-oceanic arc within Neo-Tethys or a part of the Asian active continental margin? Journal of Asian Earth Sciences, 80, 34-55, 10.1016/j.jseaes.2013.10.029.

FIGURE 5.1

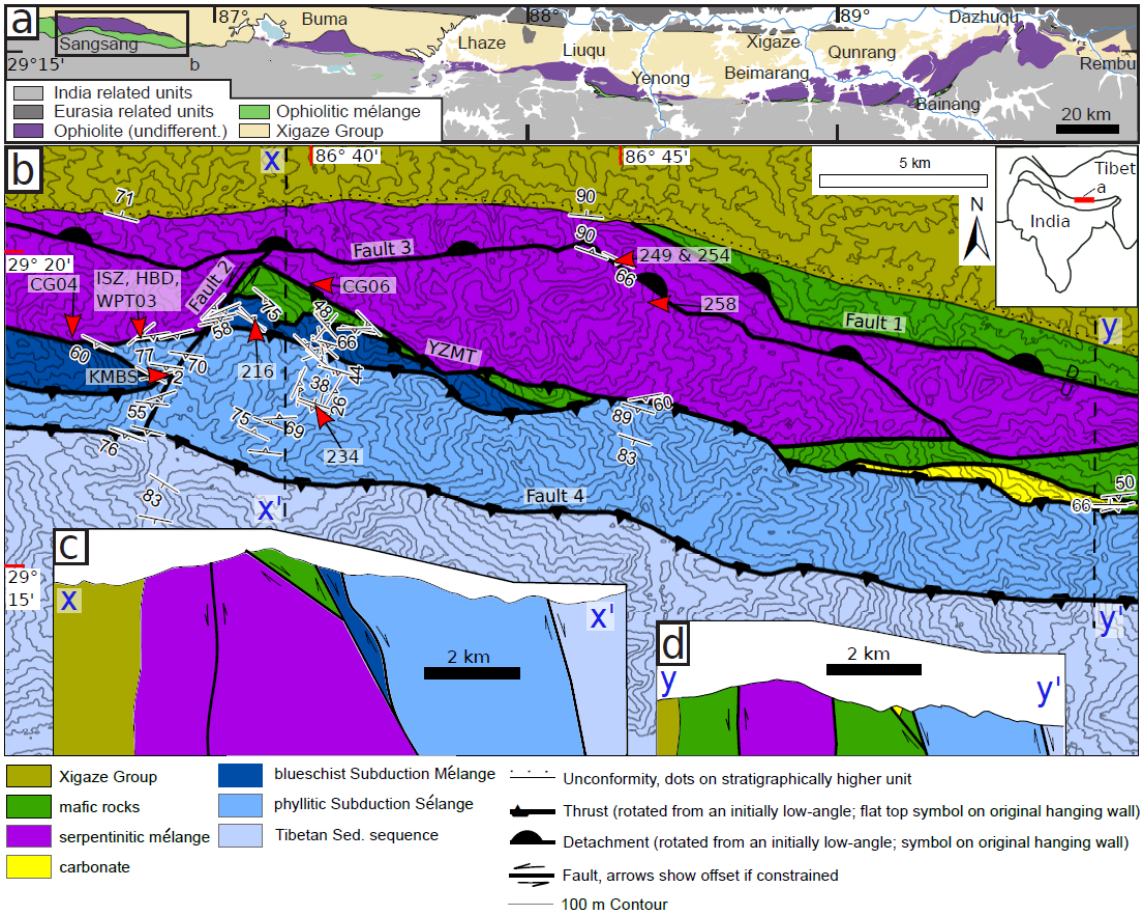
a
Sangsang
87°
Buma
88°
Lhaze
Liuqu
89°
Xigaze
Qunrang
Dazhuqu
Rembu
Yenong
Beimarang
Bainang
29°15'
b
20 km
India related units
Eurasia related units
Ophiolite (undifferent.)
Ophiolitic mélange
Xigaze Group
b
x
x'
86° 40'
86° 45'
5 km
N
Tibet
a
India
71
90
90
249 & 254
66
258
Fault 3
Fault 2
Fault 1
29° 20'
CG04
ISZ, HBD,
WPT03
CG06
78
48
66
58
60
77
70
KMBS
216
YZMT
38
29
55
75
69
234
76
83
89
60
83
50
66
y
y'
Fault 4
c
29°
15'
x
x'
2 km
d
2 km
y
y'
Xigaze Group
mafic rocks
serpentinitic mélange
carbonate
blueschist Subduction Mélange
phyllitic Subduction Sélange
Tibetan Sed. sequence
Unconformity, dots on stratigraphically higher unit
Thrust (rotated from an initially low-angle; flat top symbol on original hanging wall)
Detachment (rotated from an initially low-angle; symbol on original hanging wall)
Fault, arrows show offset if constrained
100 m Contour

Figure 5.2

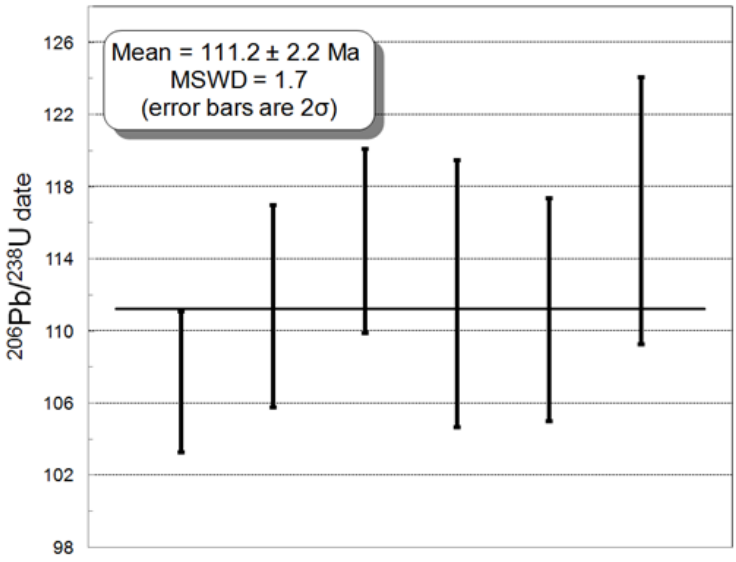
Mean = 111.2 ± 2.2 Ma
MSWD = 1.7
(error bars are 2σ)
126
122
118
114
110
106
102
98
206Pb/238U date

FIGURE 5.3

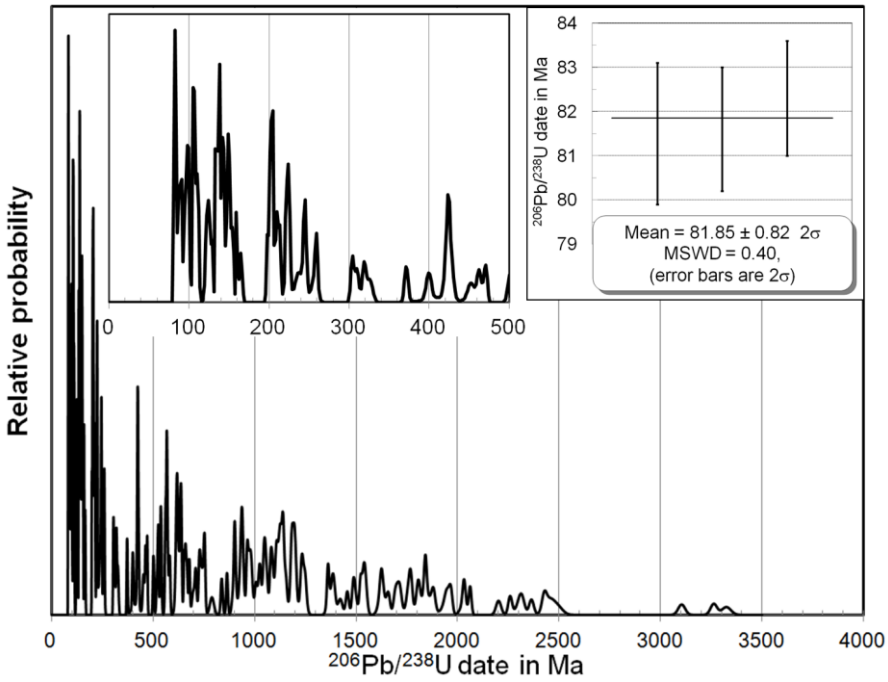
Relative probability
0
500
1000
1500
2000
2500
3000
3500
4000
206Pb/238U date in Ma
0
100
200
300
400
500
84
83
82
81
80
79
206Pb/238U date in Ma
Mean = 81.85 ± 0.82 2σ
MSWD = 0.40,
(error bars are 2σ)

FIGURE 5.4

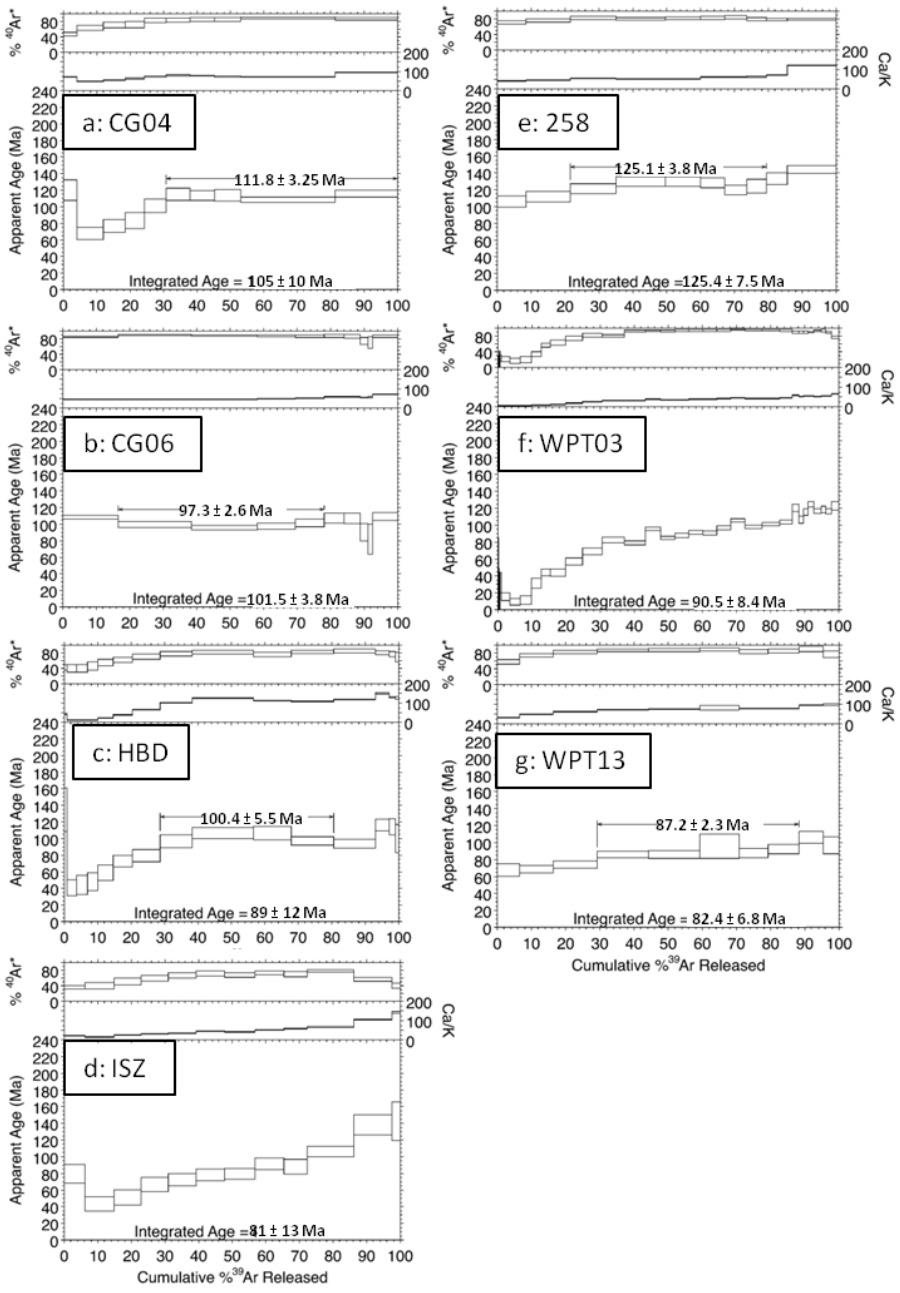
a: CG04
111.8 ± 3.25 Ma
Integrated Age = 105 ± 10 Ma
b: CG06
97.3 ± 2.6 Ma
Integrated Age = 101.5 ± 3.8 Ma
c: HBD
100.4 ± 5.5 Ma
Integrated Age = 89 ± 12 Ma
d: ISZ
Integrated Age = 81 ± 13 Ma
e: 258
125.1 ± 3.8 Ma
Integrated Age = 125.4 ± 7.5 Ma
f: WPT03
Integrated Age = 90.5 ± 8.4 Ma
g: WPT13
87.2 ± 2.3 Ma
Integrated Age = 82.4 ± 6.8 Ma
% 40Ar*
Ca/K
Apparent Age (Ma)
Cumulative %39Ar Released

FIGURE 5.5.

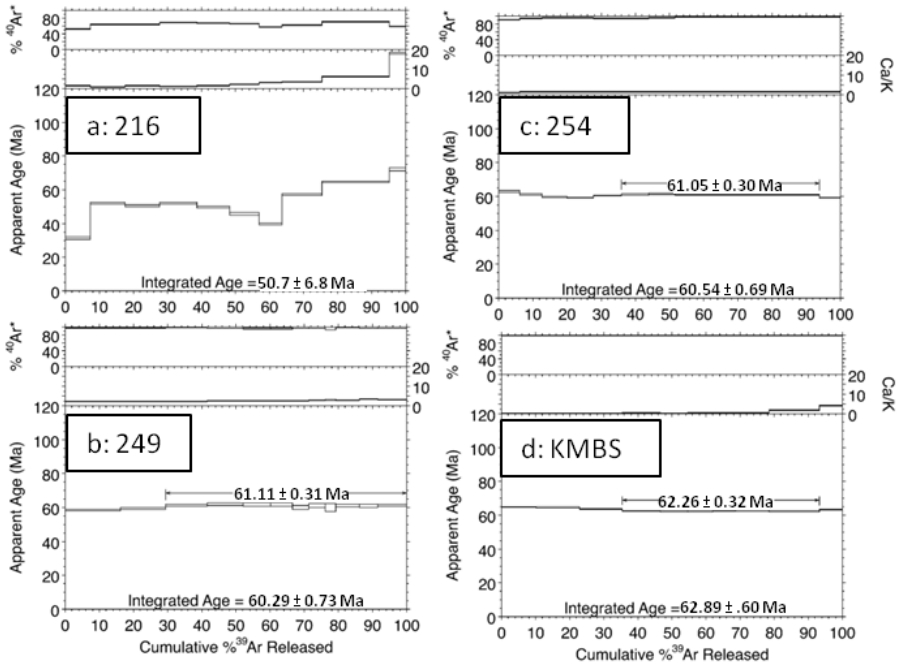
a: 216
Integrated Age =50.7 ± 6.8 Ma
b: 249
61.11 ± 0.31 Ma
Integrated Age = 60.29 ± 0.73 Ma
c: 254
61.05 ± 0.30 Ma
Integrated Age =60.54 ± 0.69 Ma
d: KMBS
62.26 ± 0.32 Ma
Integrated Age =62.89 ± .60 Ma
% 40Ar*
Ca/K
Apparent Age (Ma)
Cumulative %39Ar Released

FIGURE 5.6

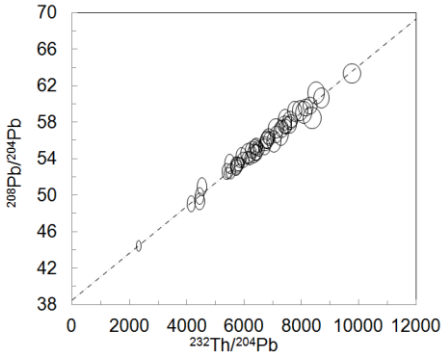
70
66
62
58
54
50
46
42
38
$^{208}Pb/^{204}Pb$
0
2000
4000
6000
8000
10000
12000
$^{232}Th/^{204}Pb$

FIGURE 5.7

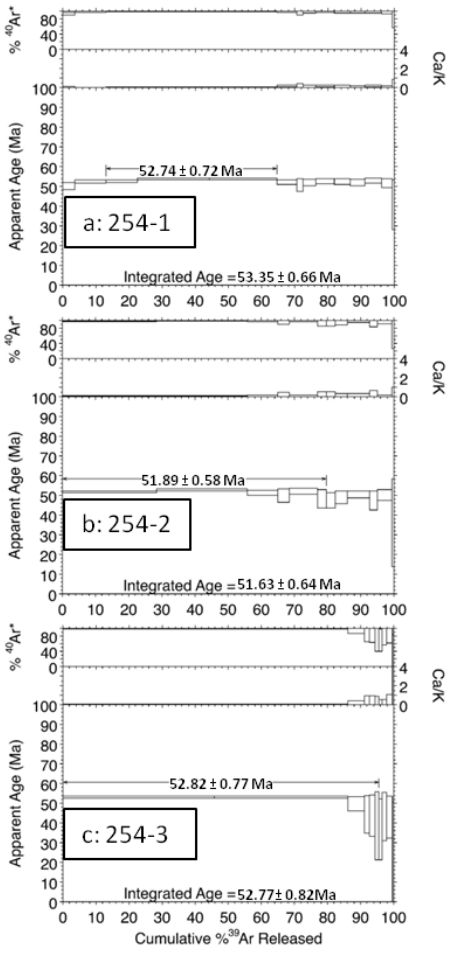
% 40Ar*
Ca/K
Apparent Age (Ma)
52.74 ± 0.72 Ma
a: 254-1
Integrated Age = 53.35 ± 0.66 Ma
51.89 ± 0.58 Ma
b: 254-2
Integrated Age = 51.63 ± 0.64 Ma
52.82 ± 0.77 Ma
c: 254-3
Integrated Age = 52.77 ± 0.82 Ma
Cumulative %39Ar Released

FIGURE 5.8

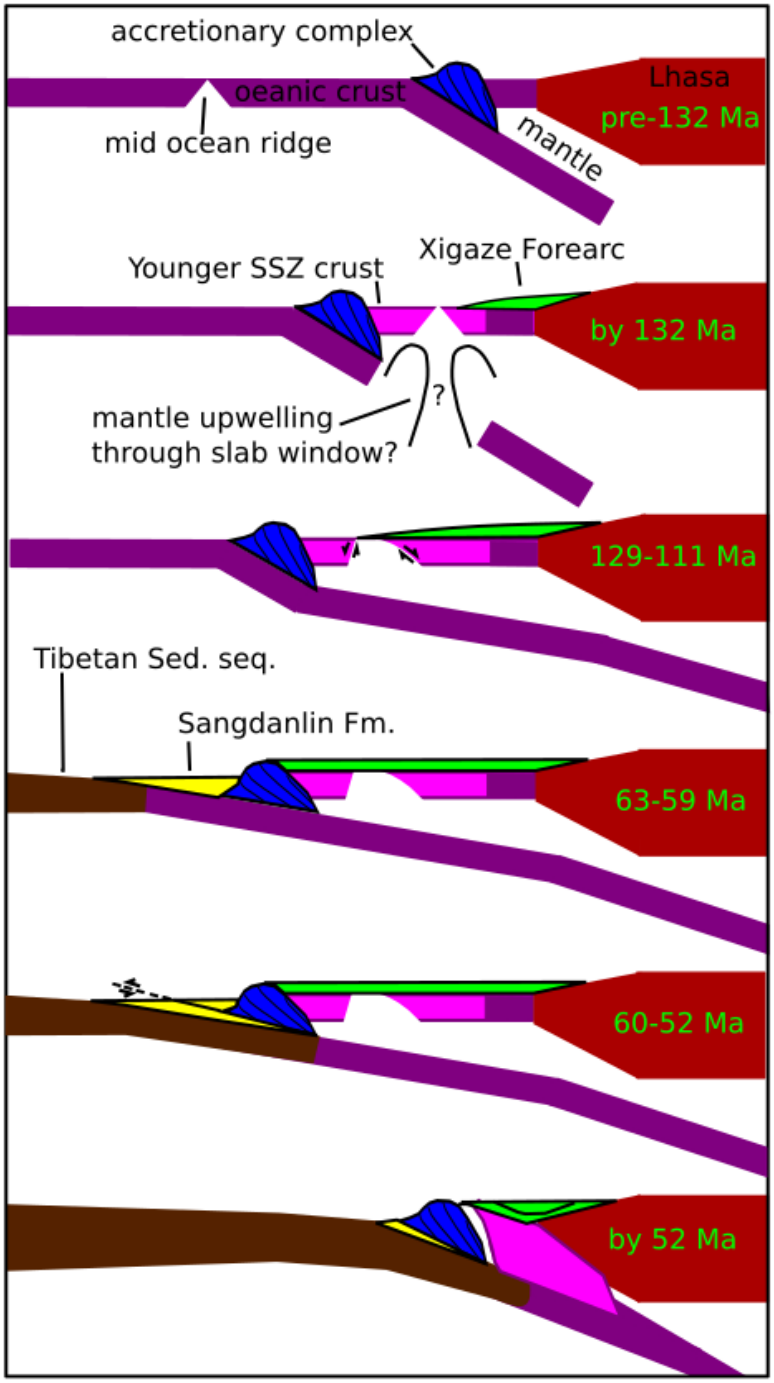
accretionary complex
oeanic crust
mid ocean ridge
mantle
Lhasa
pre-132 Ma
Younger SSZ crust
Xigaze Forearc
by 132 Ma
mantle upwelling
through slab window?
?
129-111 Ma
Tibetan Sed. seq.
Sangdanlin Fm.
63-59 Ma
60-52 Ma
by 52 Ma

CHAPTER 6

SYNTHESIS

In this dissertation, I have endeavored to place new constraints on the timing of the India-Eurasia collision using a multi-faceted approach that combines field mapping, remote sensing data interpretation, geochemistry, and the application of multiple (and sometimes novel) geochronologic and thermochronologic techniques. In this chapter I summarize my main findings and explore avenues for further research.

SUMMARY OF FINDINGS

Constraints on the evolution of the Himalayan-Tibetan orogen from Shyok suture research

Chapter 2 focuses on the timing of formation of the Shyok suture zone in an effort to test the competing hypotheses that the Kohistan-Ladakh block accreted to the Karakoram block in either Cretaceous (e.g. Rehman et al., 2011) or Eocene (Bouilhol et al, 2013) time. In retrospect, the bulk of my argument could have been made from a single outcrop where Shyok Volcanics (within the suture zone) are depositionally overlain by the post-collisional Saltoro Molasse, and both units crosscut by a datable felsic, aplitic dike. (However, an extensive field campaign was required to find this outcrop!) I correlated the Shyok Volcanics unit in this outcrop to a portion of the Ladakh block through comparisons of rock descriptions, and by using geochemistry to show that the Shyok Volcanics are distinct from nearby suture zone ophiolites. The Saltoro Molasse has a detrital zircon spectrum that requires sediment input from the Karakoram Range to the north (part of Eurasia) and also indicates likely sediment input from the Ladakh block

to the south. The maximum depositional age of the Saltoro Molasse (as constrained by $^{206}Pb/^{238}U$ ages of the youngest detrital zircons it contains) is ca. 92 Ma. The cross-cutting dike has a $^{206}Pb/^{238}U$ zircon age of ca. 85 Ma. These data bracket the depositional age of the Saltoro Molasse, requiring that Karakoram- and possibly Ladakh-derived sediments were deposited onto the Ladakh block in the 92-85 Ma interval. This time range also serves as a minimum age of collision along the Shyok suture. A Cretaceous age for the Shyok suture is inconsistent with published interpretations that collision between India and Eurasia took place at ca. 40 Ma along this feature (Bouilhol et al., 2013; Jagoutz et al. 2015).

My constraint on the timing of closure also allows for correlation of the Shyok suture to the Cretaceous Bangong suture across the Karakoram Fault. This consequently limits total offset on the central Karakoram Fault to 130-190 km, with almost all of the range in that offset due to uncertainty of the location of the Bangong suture caused by its duplication by thrusting after initiation.

Constraints on the evolution of the southern Eurasian margin and the timing of collision

My results from Sangsang are broadly consistent with previous models for the evolution of the Tethyan ocean basin between India and Eurasia prior to collision (e.g. Chan et al., 2015), but they – as well as new paleomagnetic indications that the Sangsang rocks were proximal to Eurasia prior to collision (Maffione et al., 2015; Huang et al., 2015a) – suggests a few key modifications to existing models. While supra-subduction zone magmatism, rifting, and metamorphism falling within ca. 130-80 Ma has been

reported elsewhere along much of the Yarlung suture (Chan et al., 2015), my work demonstrates that these supra-subduction events were both more prolonged than previously thought and (at least in the Sangsang and Xigaze regions) occurred in a forearc setting adjacent to Eurasia. In light of new $^{40}Ar/^{39}Ar$ age data in the dissertation, I have been able to use previously published evidence for uplift in the forearc region, as well as evidence for deposition of Eurasian detritus onto the Indian margin, to explain how it is possible for the geologic record to contain Eurasian sediments overlying Indian affinity rocks at a time when paleomagnetic constraints place the two continents far apart. In my model, the early supra-subduction rifting served to extend the forearc off of Eurasia while the resulting expanded basin was constantly filling. This allowed Eurasian-affinity forearc material (now much closer to India than is typically assumed) to then be eroded and redeposited on the Indian passive margin.

Finally, an assemblage of rare Ti-minerals found in the ophiolites of Sangsang share a ca. 52 Ma age with the current best paleomagnetic estimates for the timing of collision (Huang et al., 2015b). The age of these minerals also places key constraints on fault movements at ca. 52 Ma, supporting the hypothesis that a major structural reorganization at this time may have been related to collision.

Development of the joaquinite and neptunite geochronometers

In my pursuit of placing geochronologic constraint on the timing of the India-Eurasia collision, I also developed the $^{40}Ar/^{39}Ar$ neptunite and (U-Th)/Pb joaquinite geochronometers. In a test of the application of these systems, I showed that the resulting dates fit in well with the prevailing tectonic model for their occurrence in California, in

which initiation of the San Andreas Fault drove diapirism and metasomatism that formed these phases at ca. 12 Ma (Van Baalen, 2004). In addition, my date (12.375 ± 0.082 Ma) for neptunite from this region serves as one of the highest precision constraints for the age of intuition of the San Andreas Fault anywhere along its length.

My application of these chronometers in Tibet was also successful, with their ca. 52 Ma age coeval with the timing of collision. Overall, I showed that both of these chronometers yield reproducible, internally consistent ages. Applications of these chronometers to two localities demonstrate that they are robust and would be valuable tools for studies of other occurrences of this rare assemblage. An advantage of these chronometers is that they allow for the dating of subduction zone metamorphism which has proved generally difficult using more traditional mineral-isotopic systems.

FURTHER RESEARCH DIRECTIONS

Developing and expanding the use of joaquinite and neptunite as geochronometers

There are several outstanding questions that complicate tectonic interpretation of $^{40}Ar/^{39}Ar$ neptunite and (U-Th)/Pb joaquinite geochronometric results. The pressure-temperature conditions leading to the formation of these phases remains unclear. The close association of these two phases (and benitoite) with blueschists (Sangsang, California, and Japan, this study; Van Baalen, 2004; and Sakai and Akai, 1994, respectively) and jadeite mineralization (in California and Japan) lead me to suspect that the assemblage benitoite + joaquinite + neptunite forms under high pressure (blueschist facies) conditions. This could either be because these minerals require high-pressure conditions, or because some combination of high pressure conditions and the

geochemical gradient between serpentine and blueschist are required to drive the metasomatism that forms these minerals. Experimentally testing these hypotheses would be difficult, inasmuch as reactions become more sluggish at lower temperatures. A second, more easily undertaken study would be to see if benitoite, neptunite, and joaquinite are in isotopic equilibrium with either high-pressure phases (jadeite, Na-Ca/Na-amphiboles) or low-pressure phases (zeolites, greenschist minerals) where they are found. For such a study, it would be possible to use Li and Sr, as both are highly mobile in fluids and therefore their isotopic signatures would likely reflect the fluids involved in their formation.

Additionally, the application of these chronometers is limited by the extreme rarity of the phases, although my discovery of them at Sangsang suggests that careful mineralogical studies of similar blueschist facies terrains may yield new examples. Part of the reason that so few have been identified thus far is that their typical occurrence within pods in serpentinitic mélanges. Such mélanges typically lack lithologic boundaries that invite geologic mapping. As a result, the internal characteristics of serpentinitic mélanges are rarely studied in sufficient detail to find specific exotic block that may preserve neptunite and/or joaquinite. One known locality with the potential for dating is the Ohmi jade region of Japan, which contains benitoite and joaquinite (Sakai and Akai, 1994). Based on my experiences with California and Tibet occurrences, dating joaquinite from Ohmi would likely constrain the uplift of high pressure rocks in this region, providing better controls on subduction-accretion processes in Japan. Other jadeite localities (Burma, Guatemala) may also host these rare phases, allowing for application of these techniques to those localities if they are found.

Developing a better understanding of the Karakoram Fault

Much work remains to be done on the role of the Karakoram Fault in the Himalayan-Tibetan orogen. Additional mapping of the structure in the India-Tibet border region, as well as coordinated study of the Bangong suture zone and isolated ophiolitic fragments in that area, may yield better constraints on the total offset of that structure. A key goal of such a study would be to link piercing points within the Bangong suture to piercing points within the seemingly less deformed Shyok suture. Unfortunately, regions where such studies would be possible are presently inaccessible for geopolitical reasons. In addition, studies similar to those in this dissertation could be conducted on sutures further to the northwest along the Karakoram Fault. While sutures are known to exist (e.g. Valli et al., 2008), their ages are much more poorly constrained than those of sutures to the southeast.

The history of the Karakoram block

Both Chapter 2 in this contribution and Bouilhol et al. (2013) cite the lack of data regarding the magmatic history of the Karakoram block as a major obstacle to refining my understanding of the history of the Shyok suture. Currently, little is known about Karakoram magmatism, especially in comparison to the Kohistan-Ladakh and Gangdese batholiths. Almost all of what is known about the timing of Karakoram magmatism relates only to post-collisional granites (e.g. Fraser et al., 2001). Any ca. 40 Ma or older geochemical and/or age data from the Karakoram would therefore be helpful in testing among collision age hypotheses. Unfortunately, accessing most of the Karakoram block (which lies mostly in Pakistan) is difficult due to its extreme topography and geopolitical

circumstances. Luckily, the portion of the Karakoram block in the Nubra valley is in a relatively safe area and features less severe topography owing to its adjacency to large drainages. The data presented in Chapter 2 imply that much of this portion of the Karakoram block is older than the youngest proposed collision age. Since the precollisional, Eurasian-marginal subduction zone dipped under the Karakoram block prior to suturing, a combined U/Pb and geochemical study of the Karakoram rocks in Nubra similar to that conducted by Bouilhol et al. (2013) on the Kohistan-Ladakh block could reveal changes in magma sources related to suturing. Such a study would also serve to better constrain bedrock zircon sources that could have contributed detritus to the Saltoro Molasse and allow for a more rigorous comparison of the Saltoro molasse and Karakoram block zircon populations.

The Cenozoic uplift history of the Karakoram block is similarly poorly constrained. The high, geomorphically young appearance of the region has led to the general consensus that the region must have undergone recent uplift along a reactivation of the Shyok suture known as the Main Karakoram Thrust (MKT, Searle et al., 1996). Evidence for a ca. 7-6 Ma age for such activity is sparse (Fraser et al., 2001), and what does exist has been alternately interpreted to record intrusive activity (Rolland et al., 2006). The only firm constraint on Karakoram uplift and MKT activity comes in the form of ca. 3.5 Ma dikes that cross-cut the MKT, providing a minimum age (Searle et al., 2010). Exposures of the MKT within the Nubra study area provide a good opportunity to compare low-temperature thermochronometric (such as (U-Th)/He) data from the hanging and foot walls of the MKT. A disparity in dates across the MKT would constrain

the MKT to having been active at the time recorded by a younger hanging wall date, and thereby also likely date uplift of the Karakoram Range as a whole.

Expanding studies of the Yarlung suture

As shown in Chapter 6, great strides have been made in the last decade and a half toward understanding and constraining tectonic activity that is currently structurally condensed along the Yarlung suture. Much of this progress is due to the discovery and study of previously undescribed rocks – such as the Sangdanlin section (DeCelles et al., 2014; Hu et al., 2015; Orme et al., 2015) – as well as some of the work presented in this study. These recent results emphasize the need to characterize the entirety of the Yarlung suture, much of which currently remains unstudied except at the broadest scale. The need for detailed mapping is underscored by the fact that sutures represent scattered fragments of 100's to 1000's of kilometers of missing geology that are not easily reassembled into a coherent record. Thus, a productive way to achieved a better understanding of the timing of the India-Eurasia collision might be to carefully map out the entire Yarlung suture, rather than "drive-by" sampling of easily accessed outcrops for which there is little context.

REFERENCES

Bouilhol, P.; Jagoutz, O.; Hanchar, J.M.; Dudas, F.O., 2013, Dating the India-Eurasia collision through arc magmatic records, Earth and Planetary Science Letters, 366, 163-175, 10.1016/j.epsl.2013.01.023.

Chan, G.H.; Aitchison, J.C.; Crowley, Q.G.; Horstwood, M.S.A.; Searle, M.P.; Parrish, R.R.; Chan, J.S-L., 2015, U-Pb zircon ages for Yarlung Tsangpo suture zone ophiolites, southwestern Tibet and their tectonic implication, Gondwana Research, 27, 719-732.

DeCelles, P.G; Kapp, P.; Gehrels, G.E.; Ding, L., 2014, Paleocene-Eocene foreland basin evolution in the Himalaya of southern Tibet and Nepal: Implications for the age of initial India-Asia collision, Tectonics, 33, 5, 824-849, 10.1002/2014TC003522.

Fraser, J.E.; Searle, M.P.; Parrish, R.R.; Noble, S.R., 2001, Chronology of deformation, metamorphism, and magmatism in the southern Karakoram Mountains, Geological Society of America Bulletin, 113, 11, 1443-1455, 10.1130/0016-7606(2001)113<1443: CODMAM>2.0.CO;2.

Hu, X.; Garzanti, E.; Moore, T.; Raffi, I., 2015, Direct stratigraphic dating of India-Asia collision onset at the Selandian (middle Paleocene, 59 ± 1 Ma), Geology, 43, 10, 859-862, 10.1130/G36872.1.

Huang, W.T.; van Hinsbergen, D.J.J.; Maffione, M.; Orme, D.A.; Dupont-Nivet, G.; Guilmette, C.; Ding, L.; Guo, Z.J.; Kapp, P., 2015a, Lower Cretaceous Xigaze ophiolites formed in the Gangdese forearc: Evidence from paleomagnetism, sediment provenance, and stratigraphy, Earth and Planetary Science Letters, 415, 142-153, 10.1016/j.epsl.2015.01.032.

Huang, W.; van Hinsbergen, D.J.J.; Lippert, P.C.; Guo, Z.; Dupont-Nivet, G., 2015b, Paleomagnetic tests of tectonic reconstructions of the India-Asia collision zone, Geophysical Research Letters, 42, 8, 2642-2649, 10.1002/2015GL063749.

Jagoutz, O.; Royden, L.; Holt, A.F.; Becker, T.W., 2015, Anomalously fast convergence of India and Eurasia caused by double subduction, Nature Geoscience, 6, 475, U78, 10.1038/NGEO2418.

Maffione, M.; van Hinsbergen, D.J.J.; Koornneef, L. M.T.; Guilmette, C.; Hodges, K.; Borneman, N.; Huang, W.; Ding, L.; and Kapp, P., 2015, Forearc hyperextension dismembered the South Tibetan ophiolites, Geology, 43, 475–478, doi:10.1130/G36472.1.

Orme, D.A.; Carrapa, B.; Kapp, P., 2015, Sedimentology, provenance and geochronology of the upper Cretaceous-lower Eocene western Xigaze forearc basin, southern Tibet, Basin Research, 4, 387-411, 10.1111/bre.12080.

Rehman, H.U.; Seno, T.; Yamamoto, H.; Khan, Tahseenullah, 2011, Timing of collision of the Kohistan-Ladakh Arc with India and Asia: Debate, Island Arc, 20, 308-328, 10.1111/j.1440-1738.2011.00774.x.

Rolland, Y.; Carrio-Schaffhauser, E.; Sheppard, S.M.F.; Pecher, A.; Esclauze, L., 2006, Metamorphic zoning and geodynamic evolution of an inverted crustal section (Karakorum margin, N Pakistan), evidence for two metamorphic events, International Journal of Earth Sciences, 95, 2, 288-305, 10.1007/s00531-005-0026-x.

Sakai, M.; Akai, J., 1994, Strontium, barium and titanium-bearing minerals and their host rocks from Ohmi, Japan, Scientific Reports Niigata University, Series E, 9, 97-118.

Searle, M. P., 1991, Geology and Tectonics of the Karakoram Mountains, John Wiley & Sons, Chichester, U.K.

Searle, M. P.; Parrish, R. R.; Thow, A. V.; Noble, S. R.; Phillips, R. J.; Waters, D. J., 2010, Anatomy, age and evolution of a collisional mountain belt: the Baltoro granite batholith and Karakoram Metamorphic Complex, Pakistani Karakoram, Journal of the Geological Society, 167, 1, 183-202, 10.1144/0016-76492009-043.

Valli, F.; Leloup, P. H.; Paquette, J.-L.; Arnaud, N.; Li, H.; Tapponnier, P.; Lacassin, R.; Guillot, S.; Liu, D.; Deloule, E.; Xu, Z.; Maheo, G., 2008, New U-Th/Pb constraints on timing of shearing and long-term slip-rate on the Karakorum Fault, Tectonics, 27, TC5007, 10.1029/2007TC002184.

Van Baalen, M.R., 2004, Migration of the Mendocino Triple Junction and the origin of titanium-rich mineral suites at New Idria, California, International Geology Review, 46, 8, 671-692, 10.2747/0020-6814.46.8.671.

REFERENCES

Ahmed, M. N.; Yoshida, M.; Yoshiki, F., 2000, Paleomagnetic study of Utror volcanic formation; remagnetizations and postfolding rotations in Utror area, Kohistan arc, northern Pakistan, Earth, Planets And Space, 52, 425–36.

Aitchison, J.C.; Xia, X.; Baxter, A.T.; Ali, J.R., 2011, Detrital zircon U-Pb ages along the Yarlung-Tsangpo suture zone, Tibet: Implications for oblique convergence and collision between India and Asia, Gondwana Research, 20, 691-709, 10.1016/j.gr.2011.04.002.

Aitchison, J.C.; Ali J.R.; Davis A.M., 2007, When and where did India and Asia collide? J Geophys Res-Sol Ea, 112, B5, doi, 10.1029/2006jb004706.

Ali, M.; Arai, S., 2013, Cr-rich magnesiokatophorite as an indicator of mantle metasomatism by hydrous Na-rich carbonatite, J Miner Petrol Sci, 108, 215-226, 10.1180/minmag.2015.079.2.13

Allen, T.; Chamberlain, C.P., 1991 ,Metamorphic evidence for an inverted crustal section, with constraints on the Main Karakoram thrust, Baltistan, northern Pakistan, Journal Of Metamorphic Geology, JUL, 9, 4, 403-418, 10.1111/j.1525-1314.1991.tb00535.x.

An, W.; Hu, X.M.; Garzanti, E.; BouDagher-Fadel, M.K.; Wang, J.G.; Sun, G.Y., 2014, Xigaze forearc basin revisited (South Tibet): Provenance changes and origin of the Xigaze Ophiolite, Geological Society of America Bulletin, 126, 11-12, 1595-1613, 10.1130/B31020.1.

Atwater, T.; Stock, J.; 1998, Pacific North America plate tectonics of the Neogene southwestern United States, An update , International Geology Review, 40, 375-402.

Beck, R. A., 1995, Stratigraphic evidence for an early collision between northwest India and Asia, Nature, 373, 55–58.

Bédard, E.; Hébert, R.; Guilmette, C.; Lesage, G.; Wang, C.S.; Dostal, J., 2009, Petrology and geochemistry of the Saga and Sangsang ophiolitic massifs, Yarlung Zangbo Suture Zone, Southern Tibet: Evidence for an arc-back-arc origin, Lithos, 113, 1-2, 48-67, 10.1016/j.lithos.2009.01.011.

Borneman, L.; Hodges, K.; van Soest, M.C.; Bohon, W.; Wartho, J.-A.; Cronk, S.S.; Ahmad, T., 2014, Age and structure of the Shyok suture in the Ladakh region of northwestern India: Implications for slip on the Karakoram fault system, Tectonics, 34, 10, 2011-2033, 10.1002/2015TC003933.

Bosch, D.; Garrido, C.J.; Bruguier, O.; Dhuime, B.; Bodinier, J.-L.; Padron-Navarta, J.A.; Galland, B., 2011, Building an island-arc crustal section: Time constraints from a LA-

ICP-MS zircon study, Earth And Planetary Science Letters, 309, 268-279, 10.1016/j.epsl.2011.07.016.

Bouilhol, P.; Jagoutz, O.; Hanchar, J.M.; Dudas, F.O., 2013, Dating the India-Eurasia collision through arc magmatic records, Earth And Planetary Science Letters, 366, 163-175, 10.1016/j.epsl.2013.01.023.

Bouilhol, P.; Schaltegger, U.; Chiaradia, M.; Ovtcharova, M.; Stracke, A.; Burg, J.-P.; Dawood, H., 2011, Timing of juvenile arc crust formation and evolution in the Sapat Complex (Kohistan-Pakistan), Chemical Geology, 280, 243-256, 10.1016/j.chemgeo.2010.11.013.

Broecker, W., 2015, The collision that changed the world, Elementa Science of the Anthropocene, 3, 000061, 10.12952/journal.elementa

Brown, E. T.; Bendick, R.; Bourles, D. L.; Gaur, V.; Molnar, P.; Raisbeck, G. M.; Yiou, F., 2002, Slip rates of the Karakorum fault, Ladakh, India, determined using cosmic ray exposure dating of debris flows and moraines, Journal Of Geophysical Research-Solid Earth, 107, B9.

Burg, J.P., 2011, The_Asia–Kohistan–India collision. Review and discussion, In: Brown, D., Ryan, P. D. (Eds.), Arc-Continent Collision, Springer, Berlin Heidelberg, 279-309.

Burtman, V. S., 2010, Tien Shan, Pamir, and Tibet: History and geodynamics of Phanerozoic oceanic basins, Geotectonics, 44, 5, 388-404.

Cai, F.L.; Ding, L.; Leary, R.J.; Wang, H.Q.; Xu, Q.; Zhang, L.Y.; Yue, Y.H., 2012, Tectonostratigraphy and provenance of an accretionary complex within the Yarlung-Zangpo suture zone, southern Tibet: Insights into subduction-accretion processes in the Neo-Tethys, Tectonophysics, 574, 181-192, 10.1016/j.tecto.2012.08.016.

Chakhmouradian, A.R.; Mitchell, R.H., 2002, The mineralogy of Ba- and Zr-rich alkaline pegmatites from Gordon Butte, Crazy Mountains Montana, USA, comparisons between potassic and sodic agpaitic pegmatites, Contrib Mineral Petr, 143, 1, 93, 114, 10.1007/s00410-001-0333-6.

Chan, G.H.; Aitchison, J.C.; Crowley, Q.G.; Horstwood, M.S.A.; Searle, M.; Parrish, R.R.; Chan, J.S-L., 2015, U-Pb zircon ages for Yarlung Tsangpo suture zone ophiolites, southwestern Tibet and their tectonic implication, Gondwana Research, 27, 719-732.

Cherniak, D.J.; Watson, E.B., 2001, Pb diffusion in zirco Chemical Geology, 172, 5-24.

Chihara, K.; Komatsu, M.; Mizota, T.; 1974, A joaquinite-like mineral from Ohmi, Niigata Prefecture, Central Japan, Mineralogical Journal, 7, 4, 395-399.

Chew, D.M.; Petrus, J.A.; Kamber, B.S.; 2014, U-Pb LA-ICPMS dating using accessory mineral standards with variable common Pb, Chemical Geology, 363, 185-199, 10.1016/j.chemgeo.2013.11.006.

Clift, P.D.; Hannigan, R.; Blusztajn, J.; Draut, A.E.; 2002, Geochemical evolution of the Dras-Kohistan Arc during collision with Eurasia; evidence from the Ladakh Himalaya, India, Island Arc, 11, 4, 255-273.

Coleman, R.G., 1957, Mineralogy and petrology of the New Idria district, California. Dissertation, Stanford University.

Coleman, R.G., 1961, Jadeite deposits of the Clear Creek area, New Idria district, San Benito County, California, Journal of Petrology, 2, 209-211.
Coleman, R. G., 1996, New Idria Serpentinite: A land management dilemma , Environmental & Engineering Geoscience, 2, 9–22.

Coleman, R.G.; Lanphere, M.A., 1971, Distribution and age of high-grade blueschists, associated eclogites, and amphiboles from Oregon and California , Geological Society of America Bulletin, 82, 2397-2412.

Cooper, F. J.; Adams, B. A.; Edwards, C. S.; Hodges K.V., 2012, Large normal-sense displacement on the South Tibetan fault system in the eastern Himalaya, Geology, 40, 11, 971-974, 10.1130/G33318.1.

Crawford, M.B.; Searle, M.P., 1992, Field Relationships and Geochemistry of Pre-collisional (India-Asia) Granitoid Magmatism in the Central Karakoram, Northern Pakistan, Tectonophysics, 206, 171-192, 10.1016/0040-1951(92)90375-G.

Dai, J.G.; Wang, C.S.; Polat, A.; Santosh, M.; Li,Y.L.; Ge, Y.K., 2013, Rapid forearc spreading between 130 and 120 Ma, Evidence from geochronology and geochemistry of the Xigaze ophiolite, southern Tibet, Lithos. 172, 1, 16. 10.1016/j.lithos.2013.03.011.

DeCelles, P. G.; Kapp, P.; Gehrels, G. E.; Ding, L., 2014, Paleocene-Eocene foreland basin evolution in the Himalaya of southern Tibet and Nepal: Implications for the age of initial India-Asia collision, Tectonics, 33, 5, 824-849.

DeCelles, G.; Kapp, P.; Quade, J.; Gehrels, G.E., 2011, Oligocene-Miocene Kailas basin, southwestern Tibet: Record of postcollisional upper-plate extension in the Indus-Yarlung suture zone, Geological Society of America Bulletin, 123, 7-8, 1337-1362, 10.1130/B30258.1.

Dewey, J.F.; Casey, J.F., 2011, The Origin of Obducted Large-Slab Ophiolite Complexes. *in* Brown, D., and Ryan, D., eds., Arc–Continent Collision, Berlin Heidelberg, Springer, 431–444.

Ding, L., Kapp, P., and Wan, X.Q., 2005, Paleocene-Eocene record of ophiolite obduction and initial India-Asia collision, south central Tibet, Tectonics, 24, 3, TC3001, 10.1029/2004TC001729.

Donaldson, D.G.; Webb, A.A.G.; Menold, C.A.; Kylander-Clark, A.R.C.; Hacker, B.R., 2013, Petrochronology of Himalayan ultrahigh-pressure eclogite, Geology, 41, 8, 835-838, DOI:10.1130/G33699.1.

Dunlap, W.J.; Wysoczanski, R., 2002, Thermal evidence for early Cretaceous metamorphism in the Shyok suture zone and age of the Khardung volcanic rocks, Ladakh, India, Journal Of Asian Earth Sciences, 20, 5, 481, 490, PII S1367-9120(01)00042-6, 10.1016/S1367-9120(01)00042-6.

Eberlei, T.; Habler, G.; Grasemann, B.; Abart, R., 2014, Upper–greenschist facies intragrain deformation of albite in mylonitic meta–pegmatite and the influence of crystallographic anisotropy on microstructure formation, J Struct Geol, 69, 47-58.

Ehiro, M.; Kojima, S.; Sato, T.; Ahmad, T.; Ohtani, T., 2007, Discovery of Jurassic ammonoids from the Shyok suture zone to the northeast of Chang La pass, Ladakh, northwest India and its tectonic significance, Island Arc, 16, 124-132, doi:10.1111/j.1440-1738.2007.00562.x.

Fitz Gerald, J.D.; Stunitz, H., 1993, Deformation of granitoids at low metamorphic grade. 1. Reactions and grain-size reduction. Tectonophysics, 221, 3-4, 269-297, 10.1016/0040-195193,90163-E.

Fleck, R.J.; Sutter, J.F.; Elliot, D.H., 1977, Interpretation of discordant $^{40}Ar/^{39}Ar$ age spectra of Mesozoic tholeiites from Antarctica , Geochimica et Cosmochimica Acta, 41, 15-32.

Fraser, J.E.; Searle, M.P.; Parrish, R.R.; Noble, S.R., 2001, Chronology of deformation, metamorphism, and magmatism in the southern Karakoram mountains, Geological Society Of America Bulletin, 113, 1443-1455, 10.1130/0016-7606(2001)113<1443:CODMAM>2.0.CO;2.

Furlong, K.; Schwartz, S.Y., 2004, Influence of the Mendocino Triple Junction on the tectonics of coastal California , Annual Review of Earth and Planetary Sciences, 32, 403-433.

Gaetani, M.; Garzanti, E., 1991, Multicyclic history of the northern India continental-margin (northwestern Himalaya), AAPG Bulletin-American Association of Petroleum Geologists, 75, 9, 1427-1446.

Gehrels, G., 2012, Detrital zircon U-Pb geochronology: Current methods and new opportunities, *in* Busby, C., and Perez, A.A., eds., Tectonics of Sedimentary Basins: Recent Advances: Oxford, Blackwell, 47-62.

Gehrels, G.; Kapp, P.; DeCelles, P.; Pullen, A.; Blakey, R.; Weislogel, A.; Ding, L.; Guynn, J.; Martin, A.; McQuarrie, N.; Yin, A., 2011, Detrital zircon geochronology of pre-Tertiary strata in the Tibetan-Himalayan orogen, Tectonics, 30, TC5016, 10.1029/2011TC002868.

Gehrels, G.E.; Valencia, A.; Ruiz, J., 2008, Enhanced precision, accuracy, efficiency, and spatial resolution of U-Pb ages by laser ablation-multicollector-inductively coupled plasma-mass spectrometry, Geochemistry Geophysics Geosystems, 9, Q03017, 10.1029/2007GC001805.

Guilmette, C.; Hébert, R.; Dupuis, C.; Wang, C.S.; Li, Z.J., 2008, Metamorphic history and geodynamic significance of high-grade metabasites from the ophiolitic melange beneath the Yarlung Zangbo ophiolites, Xigaze area, Tibet, J Asian Earth Sci, 32, 5-6, 423-437, 10.1016/j.jseaes.2007.11.013.

Guilmette, C.; Hébert, R.; Wang, C.S.; Villeneuve, M., 2009, Geochemistry and geochronology of the metamorphic sole underlying the Xigaze Ophiolite, Yarlung Zangbo Suture Zone, South Tibet, Lithos, 112, 1-2, 149-162, 10.1016/j.lithos.2009.05.027.

Harlow, G.;E.; 1994, Jadeitites, albitites and related rocks from the Motagua fault zone, Guatemala, J Metamorph Geol, 12, 1, 49-68, 10.1111/j.1525-1314.1994.tb00003.x.

Harlow, G.E.; Sorensen, S.S., 2005, Jade (Nephrite and Jadeitite) and Serpentinite , Metasomatic connections , International Geology Review, 47, 2, 113-146, 10.2747/0020-6814.47.2.113.

Harlow, G.E.; Tsujimori, T.; Sorensen, S.S., 2015, Jadeitites and Plate Tectonics, Annual Review of Earth and Planetary Sciences, 43, 105-138, 10.1146/annurev-earth-060614-105215.

Harrison, T. M., 1981, Diffusion of ^{40}Ar in hornblende, Contributions To Mineralogy and Petrology, 78, 324-331.

Harrison, T.M.; Catlos, E.J.; Montel, J.-M., 2002, U–Th–Pb dating of phosphate minerals, *in* Kohn, M.J., Rakovan, J., Hughes, J. eds., Phosphates, Geochemical, Geobiological, and Materials Importance , Mineralogical Society of America, Washington, D.C, 523–558.

Hastie, A. R.; Kerr, A.C.; Pearce, J.A.; Mitchell, S.F., 2007, Classification of altered volcanic island arc rocks using immobile trace elements: Development of the Th-Co discrimination diagram, Journal of Petrology, 48, 2341-2357, 10.1093/petrology/egm062.

Hébert, R.; Bezard, R.; Guilmette, C.; Dostal, J.; Wang, C.S.; Liu, Z.F., 2012, The Indus-Yarlung Zangbo ophiolites from Nanga Parbat to Namche Barwa syntaxes, southern Tibet: First synthesis of petrology, geochemistry, and geochronology with incidences on

geodynamic reconstructions of Neo-Tethys, Gondwana Research, 22, 2, 377-397, 10.1016/j.gr.2011.10.013.

Heezen, B.C., 1974, Atlantic type continental margins, *in* Burk, C.A., and Drake, C.L., eds., The Geology of Continental Margins: New York, Springer, 13-24.

Henderson, A.L.; Najman, Y.; Parrish, R.; Mark, D.F.; Foster, G.L., 2011, Constraints to the timing of India-Eurasia collision: a re-evaluation of evidence from the Indus Basin sedimentary rocks of the Indus-Tsangpo Suture Zone, Ladakh, India, Earth-Science Reviews, 106, 265-292.

Heuberger, S.; Schaltegger, U.; Burg, J.-P.; Villa, I.M.; Frank, M.; Dawood, H.; Hussain, S.; Zanchi, A., 2007, Age and isotopic constraints on magmatism along the Karakoram-Kohistan Suture Zone, NW Pakistan: evidence for subduction and continued convergence after India-Asia collision, Swiss Journal Of Geosciences, 100, 85-107, 10.1007/s00015-007-1203-7.

Hodges, K.V., 2000, Tectonics of the Himalaya and southern Tibet from two perspectives, Geological Society Of America Bulletin, 112, 324-350, 10.1130/0016-7606(2000)112<0324:TOTHAS>2.3.CO;2.

Hodges, K., 2013, Thermochronology in orogenic systems, *in* Rudnick R. ed., Treatise on Geochemistry (Second Edition): The Crust, 281-308.

Holland, T.J.B., 1983, The experimental determination of activities in disordered and shot-range ordered jadeitic pyroxenes , Contributions to Mineralogy and Petrology, 82, 214-220, doi ,10.1007/BF01166616.

Hollocher, K.; Robinson, P.; Walsh, E.; Roberts, D., 2012, geochemistry of amphibolite-facies volcanics and gabbros of the Storen nappe in extensions west and southwest of Trondheim, western gneiss region, Norway: a key to correlations and paleotectonic settings, American Journal Of Science, 312, 357-416, 10.2475/04.2012.01.

Horton, F.; Leech, M.L., 2013, Age and origin of granites in the Karakoram shear zone and Greater Himalaya Sequence, NW India, Lithosphere, 5, 300-320, 10.1130/L213.1.

Hoskin, P.W.O.; Schaltegger, U., 2003, The composition of zircon and igneous and metamorphic petrogenesis, Reviews in Mineralogy ad Geochemistry, 53, 27-62, 10.2113/0530027.

Hu, X.; Garzanti, E.; Moore, T.; Raffi, I., 2015, Direct stratigraphic dating of India-Asia collision onset at the Selandian (middle Paleocene, 59 ± 1 Ma), Geology, 43, no. 10, 859-862, doi:10.1130/G36872.1.

Huang, W.T.; van Hinsbergen, D.J.J.; Maffione, M.; Orme, D.A.; Dupont-Nivet, G.; Guilmette, C.; Ding, L.; Guo, Z.J.; and Kapp, P., 2015a, Lower Cretaceous Xigaze

ophiolites formed in the Gangdese forearc: Evidence from paleomagnetism, sediment provenance, and stratigraphy, Earth and Planetary Science Letters, 415, 142-153, 10.1016/j.epsl.2015.01.032.

Huang, W.; van Hinsbergen, D.J.J.; Lippert, C.; Guo, Z.; Dupont-Nivet, G., 2015b, Paleomagnetic tests of tectonic reconstructions of the India-Asia collision zone, Geophysical Research Letters, 42, 8, 2642-2649, 10.1002/2015GL063749.

Hunziker, D.; Burg, J., Builhol, P.; von Quadt, A., 2015, Jurassic rifting at the Eurasian Tethys margin: Geochemical and geochronological constraints from granitoids of North Makran, southeastern Iran, Tectonics, 34, 571-593, 10.1002/2014TC003768.

Jagoutz, O.E.; Burg, J.-P.; Hussain, S.; Dawood, H.; Pettke, T.; Iizuka, T.; Maruyama, S., 2009, Construction of the granitoid crust of an island arc part I: geochronological and geochemical constraints from the plutonic Kohistan (NW Pakistan), Contributions To Mineralogy And Petrology, 158, 739-755, 10.1007/s00410-009-0408-3.

Jagoutz, O.; Royden, L.; Holt, A.F.; Becker, T.W., 2015, Anomalously fast convergence of India and Eurasia caused by double subduction, Nature Geoscience, 8, 6, 475-478, 10.1038/NGEO2418.

Jain, A.K.; Singh, S., 2008, Tectonics of the southern Asian plate margin along the Karakoram Shear Zone: Constraints from field observations and U-Pb SHRIMP ages, Tectonophysics, 451, 186-205, 10.1016/j.tecto.2007.11.048.

Jiang, Z. Q., Wang, Q., Wyman, D. A., Li, Z. X., Yang, J. H., Shi, X. B., Ma, L., Tang, G. J., Gou, G. N., Jia, X. H., and Guo, H. F., 2014, Transition from oceanic to continental lithosphere subduction in southern Tibet: Evidence from the Late Cretaceous-Early Oligocene (~ 91-30 Ma) intrusive rocks in the Chanang-Zedong area, southern Gangdese, Lithos, 196, 213-231.

Ji, W.-Q.; Wu, F.-Y.; Chung, S.-L.; Li, J.-Xi.; Liu, C.-Z., 2009, Zircon U-Pb geochronology and Hf isotopic constraints on petrogenesis of the Gangdese batholith, southern Tibet, Chemical Geology, 262, 3-4, 229, 245, 10.1016/j.chemgeo.2009.01.020.

Johnson, C.L.; Graham S.A., 2007 Middle Tertiary Stratigraphic Sequences of the San Joaquin Basin, California, *in* Scheirer A.H. (ed.) Petroleum Systems and Geologic Assessment of Oil and Gas in the San Joaquin Basin Province, California, 6, doi ,10.3133/pp1713.ch06.

Jolliffe, I.T., 2002, Principal Component Analysis, 2nd edition, Springer, New York, 32 p.

Juyal, K.P., 2006, Foraminiferal biostratgraphy of the Early Cretaceous Hundiri Formation, lower Shyok area, eastern Karakoram, India, Current Science, 91, 1096-1101.

Kapp, P.; DeCelles, P.G.; Gehrels, G.E.; Heizier, M.; Ding, L., 2007, Geological records of the Lhasa-Qiangtang and Indo-Asian collisions in the Nima area of central Tibet, Geological Society Of America Bulletin, 119, 917-932, 10.1130/B26033.1.

Kapp, P.; Murphy, M.A.; Yin, A.; Harrison, T.M.; Ding, L.; Guo, J.H., 2003, Mesozoic and Cenozoic tectonic evolution of the Shiquanhe area of western Tibet, Tectonics, JUL 9, 22, 4, 1029, 10.1029/2001TC001332.

Kelley, S, 2002, Excess argon in K-Ar and Ar-Ar geochronology, Chemical Geology, 188, 1-2, 1-22, PII S0009-2541(02)00064-5, 10.1016/S0009-2541(02)00064-5.

Khan, S.D.; Walker, D.J.; Hall, S.A.; Burke, K.C.; Shah, M.T.; Stockli, L., 2009, Did the Kohistan-Ladakh island arc collide first with India?, Geological Society Of America Bulletin, 121, 366-384, 10.1130/B26348.1.

Kim, D.; Katayama, I.; Michibayashi, K.; Tsujimori, T., 2013, Rheological contrast between glaucophane and lawsonite in naturally deformed blueschist from Diablo Range, California , Island Arc, 22, 1, 63-73, 10.1111/iar.12003.

Klootwijk, C.; Gee, J.; Peirce, J.; Smith, G; McFadden, P., 1992, An early India-Asia contact: Paleomagnetic constraints from the Ninetyeast Ridge, ODP Leg 121, Geology, 20, 395–398.

Krogh-Ravna, E., 2000, The garnet-clinopyroxene Fe^{2+}-Mg geothermometer , An updated calibration , Journal of Metamorphic Geology, 18, 211-219, doi ,10.1046/j.1525-1314.2000.00247.x.

Lacassin, R., Valli, F., Arnaud, N., Leloup, P. H., Paquette, J. L., Haibing, L., Tapponnier, P., Chevalier, M. L., Guillot, S., Maheo, G., and Xu, Z. Q., 2004, Large-scale geometry, offset and kinematic evolution of the Karakorum fault, Tibet, Earth And Planetary Science Letters, 219, 3-4, 255-269.

Laird, J., 1988, Chlorites - metamorphic petrology , Reviews In Mineralogy, 19, 405-453.

Laird, J.; Albee, A.L., 1972, Chemical composition and physical, optical, and structural properties of benitoite, neptunite, and joaquinite, Am Mineral, 57, 1-2, 85-102.

Laurs, B.M.; Rohtert, W.R.; Gray, M., 1997, Benitoite from the New Idria District, San Benito County, California , Gems & Gemology, 33, 166–187.

Leake, B,E.; Woolley, A.R.; Arps, C.E.S.; Birch, W.D.; Gilbert, M.C.; Grice, J.D.; Hawthorne, F.C.; Kato, A.; Kisch, H.J.; Krivovichev, V.G.; Linthout, K.; Laird, J.; Mandarino, J.A.; Maresch, W.V.; Nickel, E.H.; Rock, N.M.S.; Schumacher, J.C.; Smith, D.C.; Stephenson, N.C.N.; Ungaretti, L.; Whittaker, E.J.W.; Guo, YZ., 1997, Nomenclature of amphiboles, Report of the subcommittee on amphiboles of the

International Mineralogical Association, commission on new minerals and mineral names, Am Mineral, 82, 9-10, 1019-1037.

Lister, G. S.; Snoke, A. W., 1984, S-C mylonites, Journal of Structural Geology, 6, 617-638.

Liu, W.-L.; Xia, B.; Zhong, Y.; Cai, J.-X.; Li, J.-F.; Liu, H.-F.; Cai, Z.-R.; Sun, Z.-L., 2014, Age and composition of the Rebang Co and Julu ophiolites, central Tibet: implications for the evolution of the Bangong Meso-Tethys, International Geology Review, 56, 430-447, 10.1080/00206814.2013.873356.

Long, S.; McQuarrie, N., Tobgay, T.; Coutand, I.; Cooper, F.J.; Reiners, W.; Wartho, J.-A.; Hodges, K., 2012, Variable shortening rates in the eastern Himalayan thrust belt, Bhutan: Insights from multiple thermochronologic and geochronologic data sets tied to kinematic reconstructions, Tectonics, 31, TC5004, 10.1029/2012TC003155.

Lukens, C.E.; Carrapa, B.; Singer, B.S.; Gehrels, G., 2012, Miocene exhumation of the Pamir revealed by detrital geothermochronology of Tajik Rivers, Tectonics, 31, TC2014, 10.1029/2011TC003040.

Maffione, M.; van Hinsbergen, D.J.J.; Koornneef, L.M.T.; Guilmette, C.; Hodges, K., Borneman, N.; Huang, W.; Ding, L.; Kapp, , 2015, Forearc hyperextension dismembered the South Tibetan ophiolites, Geology, 43, 475–478, doi:10.1130/G36472.1.

Malpas, J.; Zhou, M.-F.; Robinson, T.; Reynolds, H., 2003, Geochemical and geochronological constraints on the origin and emplacement of the Yarlung Zangbo ophiolites, Southern Tibet, Geological Society, London, Special Publications 218, 191–206.

Matsubara, S.; Mandarino, J.A.; Semenov, E.I.; 2008, Redefinition of a mineral in the joaquinite group, Orthojoaquinite-La, Can Mineral, 39, 3, 757-760, 10.2113/gscanmin.39.3.757.

Maruyama, S.; Liou, J.G., 1988, Petrology of Franciscan metabasites along the jadeite glaucophane type facies series, Cazadero, California , Journal Of Petrology, 29, 1, 1, 37.

McDermid, I.R.C.; Aitcheson, J.C.; Davis, A.M.; Harrison, T.M.; Grove, M.; 2002, The Zedong terrane: a Late Jurassic intra-oceanic magmatic arc within the Yarlung-Tsangpo suture zone, southeastern Tibet, Chemical Geology, 187, 267-277.

McQuarrie, N.; Wernicke, B., 2005, An animated tectonic reconstruction of southwestern North America since 36 Ma , Geosphere, 1, 3, 147-172, 10.1130/GES00016.1.

Najman, Y., Appel, E., Boudagher-Fadel, M., Bown, P., Carter, A., Garzanti, E., Godin, L., Han, J. T., Liebke, U., Oliver, G., Parrish, R., and Vezzoli, G., 2010, Timing of India-

Asia collision: Geological, biostratigraphic, and palaeomagnetic constraints, Journal Of Geophysical Research-Solid Earth, 115, doi: 10.1029/2010jb007673.

Nicholson, K.; Khan, M.; Mahmood, K., 2012, Geochemistry of the Chagai-Raskoh arc, Pakistan: Complex arc dynamics spanning the Cretaceous to Quaternary, Lithos, 118, 338-348, 10.1016/j.lithos.2010.05.008.

Oberti, R.; Boiocchi, M.; Hawthorne, F.C.; Ball, N.A.; Harlow, G.E., 2015, Katophorite from the Jade Mine Tract, Myanmar, mineral description of a rare grandfathered, endmember of the amphibole supergroup, Mineral Mag, 79, 355-363, 10.1180/minmag.2015.079.2.13.

Okamoto, A.; Toriumi, M., 2004, Optimal mixing properties of calcic and subcalcic amphiboles, application of Gibbs' method to the Sanbagawa schists, SW Japan, Contrib Mineral Petr, 146, 5, 529-545.

Orme, D.A.; Carrapa, B.; Kapp, P., 2015, Sedimentology, provenance and geochronology of the upper Cretaceous-lower Eocene western Xigaze forearc basin, southern Tibet, Basin Research, 4, 387-411, 10.1111/bre.12080.

Otsuki, M.; Banno, S., 1990, Prograde and retrograde metamorphism of hematite-bearing basic schists in the Sambagawa belt in central Shikoku, J Metamorph Geol, 8, 4, 425-439. 10.1111/j.1525-1314.1990.tb00629.x.

Parrish, R.R.; Tirrul, R., 1989, U-Pb age of the Baltoro granite, northwest himalaya, and implications for monazite U-Pb systematics, Geology, 17, 1076-1079, 10.1130/0091-7613(1989)017<1076:UPAOTB>2.3.CO;2.

Paton, C.; Hellstrom, J.; Paul, B.; Woodhead, J.; Hergt, J., 2011, Iolite: Freeware for the visualisation and processing of mass spectrometric data, Journal Of Analytical Atomic Spectrometry, 26, 12, 2508-2518, 10.1039/c1ja10172b.

Peacor, D.R., 1973, High-temperature, single-crystal x-ray study of natrolite , American Mineralogist, 58, vol. 7-8, 676-680.
Petterson, M. G., and Windley, B. F., 1985, Rb-Sr dating of the Kohistan arc-batholith in the Trans-Himalaya of north Pakistan, and tectonic implications, Earth And Planetary Science Letters, 74, 45-57.

Phillips, R.J.; Parrish, R.R.; Searle, M.P., 2004, Age constraints on ductile deformation and long-term slip rates along the Karakoram Fault zone, Ladakh, Earth And Planetary Science Letters, 226, 305-319, 10.1016/j.epsl.2004.07.037.

Phillips, R.J., 2008, Geological map of the Karakoram Fault zone, Eastern Karakoram, Ladakh, NW Himalaya, Journal Of Maps, 21-37

Phillips, R. J.; Searle, M. P., 2007, Macrostructural and microstructural architecture of the Karakoram Fault: Relationship between magmatism and strike-slip faulting, Tectonics, 26, 3, doi: 10.1029/2006tc001946.

Rai, H., 1982, Geological evidence against the Shyok palaeo-suture, Ladakh Himalaya, Nature, 297, 142, 144, 10.1038/297142a0

Rao, D.R.; Rai, H., 2009, Geochemical Studies of Granitoids from Shyok Tectonic Zone of Khardung-Panamik Section, Ladakh, India, Journal Of The Geological Society Of India, 73, 553-566.

Ravikant, V.; Wu, F.-Y.; Ji, W.-Q., 2009, Zircon U-Pb and Hf isotopic constraints on petrogenesis of the Cretaceous-Tertiary granites in eastern Karakoram and Ladakh, India, Lithos, 110, 153-166, 10.1016/j.lithos.2008.12.013.

Raz, U.; Honegger, K., 1989, Magmatic and tectonic evolution of the Ladakh block from field studies, Tectonophysics, 161, 107, 118, 10.1016/0040-1951(89)90306-5.

Rehman, H.U.; Seno, T.; Yamamoto, H.; Khan, Tahseenullah, 2011, Timing of collision of the Kohistan-Ladakh Arc with India and Asia: Debate, Island Arc, 20, 308-328, 10.1111/j.1440-1738.2011.00774.x.

Rex, A. J.; Searle, M. P.; Tirrul, R.; Crawford, M.B.; Prior, D.J.; Rex, D. C.; Barnicoat, A., 1988, The geochemical and tectonic evolution of the central Karakoram, North Pakistan, Philosophical Transactions Of The Royal Society Of London, 326, 229-255.

Robertson, A.H.F.; Collins, A.S., 2002, Shyok Suture Zone, N Pakistan: late Mesozoic-Tertiary evolution of a critical suture separating the oceanic Ladakh Arc from the Asian continental margin, Journal Of Asian Earth Sciences, 20, 309-351, 10.1016/S1367-9120(01)00041-4.

Rolland, Y.; Maheo, G.; Pecher, A.; Vila, I. M., 2009, Syn-kinematic emplacement of the Pangong metamorphic and magmatic complex along the Karakorum Fault (N Ladakh), Journal Of Asian Earth Sciences, 34, 1, 10-25.

Rolland, Y.; Pecher, A.; Picard, C., 2000, Middle Cretaceous back-arc formation and arc evolution along the Asian margin: the Shyok Suture Zone in northern Ladakh (NW Himalaya), Tectonophysics, 325, 145-173, 10.1016/S0040-1951(00)00135-9.

Rosenberg, C.L.; Stünitz, H., 2003, Deformation and recrystallization of plagioclase along a temperature gradient, an example from the Bergell tonalite, J Sruct Geol, 25, 389-408.

Rowley, D.B., 1996, Age of initiation of collision between India and Asia: A review of stratigraphic data, Earth And Planetary Science Letters, DEC, 145, 1-4, 1-13, 10.1016/S0012-821X(96)00201-4.

Sakai, M.; Akai, J., 1994, Strontium, barium and titanium-bearing minerals and their host rocks from Ohmi, Japan, Scientific Reports Niigata University, Series E, 9, 97-118.

Schoene, B.; Bowring, S.A., 2006, U-Pb systematics of the McClure Mountain syenite: thermochronological constraints on the age of the Ar-40/Ar-39 standard MMhb, Contributions to Mineralogy and Petrology, 151, 5, 615-630, 10.1007/s00410-006-0077-4.

Schwab, M; Ratschbacher, L; Siebel, W; McWilliams, M.; Minaev, V.; Lutkov, V.; Chen, F.K.; Stanek, K.; Nelson, B.; Frisch, W.; Wooden, J.L., 2004, Assembly of the Pamirs: Age and origin of magmatic belts from the southern Tien Shan to the southern Pamirs and their relation to Tibet, Tectonics, 23, 4, TC4002, 10.1029/2003TC001583.

Schwarz, W.H.; Trieloff, M., 2007, Intercalibration of Ar-40-Ar-39 age standards NL-25, HB3gr hornblende, GA1550, SB-3, HD-B1 biotite and BMus/2 muscovite, Chemical Geology, 242, 1-2, 218-231, 10.1016/j.chemgeo.2007.03.016.

Searle, M. P., 1991, Geology and Tectonics of the Karakoram Mountains, John Wiley & Sons, Chichester, U.K.

Searle, M.P., 1996, Geological evidence against large-scale pre-Holocene offsets along the Karakoram Fault: Implications for the limited extrusion of the Tibetan plateau, Tectonics, 15, 171-186, 10.1029/95TC01693.

Searle, M.P.; Tirrul, R., 1991, Structural and thermal evolution of the Karakoram crust, Journal Of The Geological Society, 148, 65-82, 10.1144/gsjgs.148.1.0065.

Searle, M., Corfield, R. I., Stephenson, B., and McCarron, J., 1997, Structure of the North Indian continental margin in the Ladakh-Zanskar Himalayas: implications for the timing of obduction of the Spontang ophiolite, India-Asia collision and deformational events in the Himalaya, Geological Magazine, 134, 297-316.

Searle, M. P.; Weinberg, R. F.; Dunlap, W. J., 1998, Transpressional tectonics along the Karakoram Fault zone, northern Ladakh: constraints on Tibetan extrusion, in Holdsworth, R. E., Strachan, R. A., and Dewey, J. F., eds., Continental Transpressional And Transtensional Tectonics, London, Geological Society of London, Special Publications 135, 307-326.

Searle, M.P.; Khan, M.A.; Fraser, J.E.; Gough, S.J.; Jan, M.Q., 1999, The tectonic evolution of the Kohistan-Karakoram collision belt along the Karakoram Highway transect, north Pakistan, Tectonics, 18, 929-949, 10.1029/1999TC900042.

Searle, M.P.; Parrish, R.R.; Thow, A.V.; Noble, S.R.; Phillips, R.J.; Waters, D.J., 2010, Anatomy, age and evolution of a collisional mountain belt: the Baltoro granite batholith and Karakoram Metamorphic Complex, Pakistani Karakoram, Journal Of The Geological Society, 167, 183-202, 10.1144/0016-76492009-043.

Sen, K.; Collins, A.S., 2013, Dextral transpression and late Eocene magmatism in the trans-Himalayan Ladakh Batholith (North India): implications for tectono-magmatic evolution of the Indo-Eurasian collisional arc, International Journal Of Earth Sciences, 102, 1895-1909, 10.1007/s00531-012-0826-8.

Slama, J.; Dunkley, D.J.; Kachlik, P.; Kusiak, M.A., 2008, Transition from island-arc to passive setting on the continental margin of Gondwana: U-Pb zircon dating of Neoproterozoic metaconglomerates from the SE margin of the Tepla-Barrandian Unit, Bohemian Massif, Tectonophysics, 461, 1-4, 44-59, 10.1016/j.tecto.2008.03.005.

Smith, D. K.; Cann, J. R.; Escartín, J., 2006, Widespread active detachment faulting and core complex formation near 13°N on the Mid-Atlantic Ridge:Nature, 442, 440-443.

Smith, G.L.; McNeill, L.C.; Henstock, T.J.; Arraiz, D.; Spiess, , 2014, Fluid generation and distribution in the highest sediment input accretionary margin, the Makran, Earth and Planetary Science Letters, 403, 131-143, 10.1016/j.epsl.2014.06.030.

Sorenson, S.; Harlow, G.E.; Rumble, D., 2006, The origin of jadeitite-forming subduction-zone fluids , CL-guided SIMS oxygen-isotope and trace-element evidence , American Mineralogist, 91, 979-996.

Steiger, R.H.; Jäger, E., 1977, Subcommission on geochronology: Convention on the use of decay constants in geo- and cosmochronology, Earth And Planetary Science Letters, 36, 21-23.

Stipp, M.; Stunitz, H.; Heilbronner, R.; Schmid, S.M., 2002, The eastern Tonale fault zone, a 'natural laboratory' for crystal plastic deformation of quartz over a temperature range from 250 to 700 degrees C, J Struct Geol, 24, 12, 1861-1884, 10.1016/S0191-814102,00035-4.

Stock, J.M.; Hodges, K., 1989, Pre-pliocene extension around the Gulf of California and thetransfer of Baja California to the Pacific Plate , Tectonics, 8, 1, 99-115, 10.1029/TC008i001p00099.

St-Onge, M. R.; Rayner, N.; and Searle, M. P.; 2010, Zircon age determinations for the Ladakh batholith at Chumathang (Northwest India): Implications for the age of the India-Asia collision in the Ladakh Himalaya, Tectonophysics, 495, 3-4, 171-183.

St-Onge, M. R.; Rayner, N.; Palin, R. M.; Searle, M. P.; and Waters, D. J., 2013, Integrated pressure-temperature-time constraints for the Tso Morari dome (Northwest

India): implications for the burial and exhumation path of UHP units in the western Himalaya, Journal Of Metamorphic Geology, 31, 5, 469-504.

Sun, J.F.; Yang, J.H.; Wu, F.Y.; Xie, L.W.; Yang, Y.H.; Liu, Z.C.; Li, X.H., 2012, In situ U-Pb dating of titanite by LA-ICPMS, Chinese Science Bulletin, 57, 20, 2506-2516, 10.1007/s11434-012-5177-0.

Thanh, N.X.; Itaya, T.; Ahmad, T.; Kojima, S.; Ohtani, T.; Ehiro, M., 2010, Mineral chemistry and K-Ar ages of plutons across the Karakoram Fault in the Shyok-Nubra confluence of northern Ladakh Himalaya, India, Gondwana Research, 17, 1, 180-188, 10.1016/j.gr.2009.08.002.

Thanh, N.X.; Rajesh, V.J.; Itaya, T.; Windley, B.; Kwon, S.; Park, C.-S., 2012, A Cretaceous forearc ophiolite in the Shyok suture zone, Ladakh, NW India: Implications for the tectonic evolution of the Northwest Himalaya, Lithos, 155, 81-93, 10.1016/j.lithos.2012.08.016.

Treloar, P.J.; Rex, D.C.; Guise, P.G.; Coward, M.P.; Searle, M.P.; Windley, B.F.; Petterson, M.G.; Jan, M.Q.; Luff, I.W., 1989, K-Ar and Ar-Ar geochronology of the Himalayan collision in NW Pakistan - constraints on the timing of suturing, deformation, metamorphism and uplift, Tectonics, 8, 881-909, 10.1029/TC008i004p00881

Tripathy-Lang, A.; Hodges, K.V.; van Soest, M.C.; Ahmad, T., 2013, Evidence of pre-Oligocene emergence of the Indian passive margin and the timing of collision initiation between India and Eurasia, Lithosphere, 5, 501-506, 10.1130/L273.1.

Tsai, C.H.; Iizuka, Y., Ernst, W.G., 2013, Diverse mineral compositions, textures, and metamorphic P-T conditions of the glaucophane-bearing rocks in the Tamayen melange, Yuli belt, eastern Taiwan, J Asian Earth Sci, 63, SI, 218-233, 10.1016/j.jseaes.2012.09.019.

Tsujimori, T.; Harlow, G.E., 2012, Petrogenetic relationships between jadeitite and associated high-pressure and low-temperaturemetamorphic rocks in worldwide jadeitite localities , A review , European Journal of Mineralogy, 24, 371-390, DOI , 10.1127/0935-1221/2012/0024-2193.

Tsujimori, T.; Liou, G. J.; Coleman, R. G., 2007, Finding of high-grade tectonic blocks from the New Idria serpentinite body, Diablo Range, California , Petrologic constraints on the tectonic evolution of an active serpentinite diapir, *in* Cloos, M., Carlson, W. D., Gilbert, M. C., Liou, J. G. and Sorensen, S. S. (eds.) Convergent Margin Terranes and Associated Regions , A Tribute to W. G. Ernst , Geological Society of America, Special Papers 419, 67–80.

Upadhyay, R., 2008, Implications of U-Pb zircon age of the Tirit granitoids on the closure of the Shyok suture zone, northern Ladakh, India, Current Science, 94, 1635-1640.

Upadhyay, R., 2014, Palaeogeographic significance of 'Yasin-type' rudist and orbitolinid fauna of the Shyok Suture Zone, Saltoro Hills, northern Ladakh, India, Current Science, 106, 223-228.

Valli, F.; Leloup, P.H.; Paquette, J.-L.; Arnaud, N.; Li, H.; Tapponnier, P.; Lacassin, R.; Guillot, S.; Liu, D.; Deloule, E.; Xu, Z.; Maheo, G., 2008, New U-Th/Pb constraints on timing of shearing and long-term slip-rate on the Karakorum fault, Tectonics, 27, TC5007, 10.1029/2007TC002184.

Van Baalen, M.R., 2004, Migration of the mendocino triple junction and the origin of titanium-rich mineral suites at new Idria, California, International Geology Review, 46, 8, 671-692, 10.2747/0020-6814.46.8.671.

Van Buer, N. J.; Jagoutz, O.; Upadhyay, R.; Guillong, M., 2015, Mid-crustal detachment beneath western Tibet exhumed where conjugate Karakoram and Longmu–Gozha Co faults intersect, Earth And Planetary Science Letters, 413, 144-157.

Van Baalen, M.R., 1993, Titanium mobility in metamorphic systems , A review , Chemical Geology, 110, 233–249.

Van Baalen, M.R., 2004, Migration of the mendocino triple junction and the origin of titanium-rich mineral suites at new Idria, California, International Geology Review, 46, 8, 671-692, 10.2747/0020-6814.46.8.671.

van Hinsbergen, D.J.J.; Lippert, P.C.; Dupont-Nivet, G.; McQuarrie, N.; Doubrovine, P.V.; Spakman, W.; Torsvik, T.H., 2012, Greater India Basin hypothesis and a two-stage Cenozoic collision between India and Asia, Proceedings Of The National Academy Of Sciences Of The United States Of America, MAY 15, 109, 20, 7659-7664, 10.1073/pnas.1117262109.

van Staal. C.R.; Currie, K.L.; Rowbotham, G.; Goodfellow, W.; Rogers, N., 2008, Pressure-temperature paths and exhumation of Late Ordovician-Early Silurian blueschists and associated metamorphic nappes of the Salinic Brunswick subduction complex, northern Appalachians, Geol Soc Am Bull, 120, 11-12, 1455-1477, 10.1130/B26324.1.

Vermeesch, P.; Miller, D.D., Graham, S.A., De Grave, J., McWilliams, M.O., 2006, Multimethod detrital thermochronology of the Great Valley Group near New Idria, California , Geological Society Of America Bulletin, 118, 1-2, 210-218, 10.1130/B25797.1.

Wang, C.S.; Li, X.H.; Liu, Z.F.; Li, Y.L.; Jansa, L.; Dai, J.G.; Wei, Y.S., 2012, Revision of the Cretaceous-Paleogene stratigraphic framework, facies architecture and provenance of the Xigaze forearc basin along the Yarlung Zangbo suture zone, Gondwana Research, 22, 2, 415-433, 10.1016/j.gr.2011.09.014.

Wang, R.; Xia, B.; Zhou, G.Q.; Zhang, Y.Q.; Yang, Z.Q.; Li, W.Q.; Wei, D.L.; Zhong, L.F.; Xu, L.F., 2006, SHRIMP zircon U–Pb dating for gabbro from the Tiding ophiolite in Tibet, Chinese Science Bulletin 51, 1776–1779.

Weinberg, R.F.; Dunlap, W.J., 2000, Growth and deformation of the Ladakh batholith, northwest Himalayas: Implications for timing of continental collision and origin of calc-alkaline batholiths, Journal Of Geology, 108, 303-320, 10.1086/314405.

Weinberg, R.F.; Dunlap, W.J.; Whitehouse, M 2000, New field, structural and geochronological data from the Shyok and Nubra Valleys, northern Ladakh: linking Kohistan to Tibet, Geological Society, London, Special Publications 2000, 170, 253-275, 10.1144/GSL.SP.2000.170.01.14.

Wendt, I.; Carl, C., 1991, The statistical distribution of the mean squared weighted deviation, Chemical Geology, 86, 275-285.

Whitney D.L.; Evans B.W., 2010, Abbreviations for names of rock-forming minerals , American Mineralogist, 95, 185-187.

White, L. T., Ahmad, T., Ireland, T. R., Lister, G. S., and Forster, M. A., 2011, Deconvolving episodic age spectra from zircons of the Ladakh Batholith, northwest Indian Himalaya, Chemical Geology, 289, 3-4, 179-196.

Winchester, J.A.; Floyd, P.A., 1977, Geochemical discrimination of different magma series and their differentiation products using immobile elements, Chemical Geology, 20, 4, 325-343, 10.1016/0009-2541(77)90057-2.

Woodhead, J.D.; Hellstrom, J.; Hergt, J.M.; Greig, A.; Maas, R., 2007, Isotopic and elemental imaging of geological materials by laser ablation inductively coupled plasma-mass spectrometry, Geostand Geoanal Res, 31, 4, 331-343.

Wu, F.Y.; Ji, W.Q.; Wang, J.G.; Liu, C.Z.; Chung, S.L.; Clift, P.D., 2014, Zircon U-Pb and Hf isotopic constraints on the onset time of India-Asia collision, American Journal of Science, 314, 548 -579, doi10.2475/02.2014.04.

Yin, A., 2010, Cenozoic tectonic evolution of Asia: A preliminary synthesis, Tectonophysics, 488, 1-4, SI, 293-325, 10.1016/j.tecto.2009.06.002.

Yin, A.; Harrison, T.M., 2000, Geologic evolution of the Himalayan-Tibetan orogen, Annual Review Of Earth And Planetary Sciences, 28, 211-280, 10.1146/annurev.earth.28.1.211.

Zadov, A.E.; Gazeev, V.M.; Karimova, O.V.; Pertsev, N.N.; Pekov, I.V.; Galuskin, E.V.; Galuskina, I.O.; Gurbanov, A.G.; Belakovsky, D.I.; Borisovsky, S.E.; Kartashov, P.M.; Ivanova, A.G.; Yakubovich, O.V., 2011, Magnesioneptunite,

KNa2LiMg,Fe,2,Ti2Si8O24, a new mineral species of the neptunite group. Geol Ore Deposit+, 53, 8, 775-782, 10.1134/S1075701511080186.

Zaman H.; Torii M., 1999, Paleomagnetic study of Cretaceous red beds from the eastern Hindukush ranges, northern Pakistan; paleoarc construction of the Kohistan-Karakoram composite unit before the India-Asia collision, Geophysical Journal International, 136, 719–38.

Zhang, L.-L.; Liu, C.-Z.; Wu, F.-Y.; Ji, W.-Q.; Wang, J.-G., 2014, Zedong block revisited: An intra-oceanic arc within Neo-Tethys or a part of the Asian active continental margin?, Journal Of Asian Earth Sciences, 80, 34-55, 10.1016/j.jseaes.2013.10.029.

Zolotarev, A.A.; Krivovichev, S.V.; Yakovenchuk, V.N., 2007, Refinement of the mangan-neptunite crystal structure, Geol Ore Deposit+, 49, 8, 835-838, 10.1134/S1075701507080181.

Zubkova, N.V.; Pushcharovskii, D.Y.; Giester, G.; Tillmanns, E.; Pekov, I.V.; Krotova, O.D., 2004, Crystal structure of byelorussite-Ce, NaMnBa2Ce2TiO,2,[Si4O12]2,F,OH, center dot H2O, Crystallogr Rep+, 49, 6, 964-968, 10.1134/1.1828140.

APPENDIX A

CHAPTER 2 APPENDIX

TRACE ELEMENT GEOCHEMISTRY METHODS

Trace element geochemistry of 8 samples from the Shyok Volcanics unit was measured at Arizona State University in the Group 18 laboratories using a Thermo Scientific *iCap Q* Inductively Coupled Plasma Mass Spectrometer (ICP-MS). Non-weathered portions of samples were powdered and dissolved in HF, HNO_3, and HCl using standard techniques. Concentration from solution was determined using stock solutions. Samples were co-aspirated with an internal standard to control for time-variable sensitivity, and the data were blank corrected. USGS rock powder standards BHVO-2 and GSP-2 were run as check standards. My measurements for BHVO-2 fall within published uncertainties, whereas my data for GSP-2 is in good agreement with the exceptions of Y, Hf, Zr, and Gd Reaczek et al., 2001.

^{40}AR/^{39}AR METHODS

^{40}Ar/^{39}Ar geochronology of hornblende sample NBUM10-45 was conducted in the Group 18 Laboratories at Arizona State University. The sample was crushed, sieved, and then hand-picked in order to avoid altered grains. Using a row 8 medium-flux sample position at the McMaster University nuclear reactor, the Cd-shielded sample was co-irradiated with standard HD-B1 (24.18 ± 0.09 Ma; 1σ; Schwarz and Trieloff, 2007 as an irradiation monitor, as well as synthetic Ca and K salts to permit corrections for interfering isotopic reactions. Gasses were liberated for analysis in an ultra-high vacuum extraction line using a 970 nm IPG Photonics diode laser operated at successively higher power levels until the sample was fused. After gettering to eliminate active gasses, the purified gas was admitted to a Nu Instruments Noblesse, magnetic-sector mass

spectrometer for isotopic analysis. ^{39}Ar, ^{38}Ar, ^{37}Ar, and ^{36}Ar signals were measured on a single ETP ion counting multiplier by peak jumping. ^{40}Ar was measured using a $1x10^{11}$ Ohm Faraday detector or an ETP ion counting multiplier, depending upon the ^{40}Ar signal size. Detector intercalibration for ^{40}Ar was performed using multiple air shots. Average blank values were 3.19×10^{-16}, 2.60×10^{-18}, 2.78×10^{-19}, 5.59×10^{-18}, and 1.37×10^{-18} moles for ^{40}Ar, ^{39}Ar, ^{38}Ar, ^{37}Ar, and ^{36}Ar, respectively. The mass discrimination factor was 1.01546 ± 0.00060 per amu (2σ). The entire run was automated and computer controlled using the Mass Spec program. $^{40}Ar/^{39}Ar$ ages were calculated using the decay constant, branching ratio, and atmospheric $^{40}Ar/^{36}Ar$ ratio recommended by Steiger and Jäger (1977). Further details of the methods used at Arizona State University can be found in Long et al. (2012).

U/PB METHODS

U/Pb analyses were performed at the Arizona Laserchron facility at the University of Arizona on mineral separates prepared in the Group 18 Laboratories. The samples were crushed and sieved then separated using magnetic and heavy liquid methods. Zircons were hand-picked to avoid inclusions, but morphology was ignored to minimize sample bias. The zircons were mounted in epoxy and polished. Each grain mount was mapped as a back-scattered electron image on a scanning electron microscope to identify inclusions and zoning using a Hitachi 3400N SEM equipped with a Gatan Chroma Cathodoluminescence (CL) system. Non-detrital samples were also mapped using CL. U/Pb dates were obtained by laser-ablation-multicollecter inductively coupled plasma mass spectrometry (LA-MC-ICPMS). Grains were ablated using a 193 nm eximer UV

laser, with the laser spots being 30 microns in diameter and ~15 microns deep. Ablated material was carried by He into the plasma source of a *Nu HR* ICP-MS. U, Th, and Pb were measured simultaneously. ^{238}U, ^{232}Th, ^{208}Pb-^{206}Pb were measured on Faraday detectors with $3x10^{11}$ ohm resistors while ^{204}Pb and ^{202}Hg were measured on discrete dynode ion counters. Analyses started with a 15 s background measurement with the laser off, followed by a 15 s analysis with the laser firing, and ending with a 30 s washout. ^{204}Hg interference with ^{204}Pb was corrected for by my measuring ^{202}Hg and using the natural $^{202}Hg/^{204}Hg$ of 4.35 to subtract out ^{204}Hg. Common Pb was corrected for using the Hg-corrected ^{204}Pb and assuming a common Pb composition from Stacey and Kramers 1975. Fractionation was corrected for by running Laserchron zircon standard SL between every 5 unknowns (every 4 unkowns for igneous rocks). SL has a known age of 563.5 ± 3.2 Ma (2σ error), U = 518 ppm, and Th = 68 ppm. Zircon R33 is run as a check standard (Black et al., 2004; Gehrels et al., 2008). For this setup, $^{206}Pb/^{238}U$ dates < ~900 Ma have smaller uncertainties, but samples with ages > ~900 Ma, the $^{206}Pb/^{207}Pb$ dates have smaller uncertaimnties. Selecting $^{206}Pb/^{238}U$ dates younger than ~900 Ga and $^{206}Pb/^{207}Pb$ dates older than ~900 Ga results in uncertainties of 1-2% at the 2σ level. Detailed data reduction procedures are contained in Gehrels et al. (2008). Individual populations were delineated in multi-modal data sets using the Hampel identifier (Davies and Gather, 1993), excluding dates with an outlier limit value greater than 4. Data within populations were then combined into a single error weighted average. Detrital zircon datasets are plotted as probability distribution plots showing date versus relative probability. Igneous and metamorphic zircon datasets are plotted on concordia plots.

$^{206}Pb/^{238}Pb$ mean date plots are included for the youngest population in a given sample.

The data were plotted using Isoplot 4 (Ludwig, 2008).

REFERENCES

Davies, L.; Gather, U., 1993, the identification of multiple outliers, Journal of the American Statistical Association, 88, 782-792, 10.2307/2290763

Gehrels, G.E.; Valencia, V.A.; Ruiz, J., 2008, Enhanced precision, accuracy, efficiency, and spatial resolution of U-Pb ages by laser ablation-multicollector-inductively coupled plasma-mass spectrometry, Geochemistry Geophysics Geosystems, 9, Q03017, 10.1029/2007GC001805.

Long, S.P.; McQuarrie, N.; Tobgay, T.; Coutland, I.; Cooper F.J.; Reiners, P.W.; Wartho, J.-A.; Hodges, K.V., 2012, Variable shortening rates in the eastern Himalayan thrust belt, Bhutan: Insights from multiple thermochronologic and geochronologic data sets tied to kinematic reconstructions, Tectonics, 31, TC5004, 10.1029/2012TC003155.

Ludwig, K., 2008, unpublished material, User's manual for Isoplot 3.70.

Raczek, I.; Stoll, B.; Hofmann, A.W.; Jochum, K.P., 2001, High-precision trace element data for the USGS reference materials BCR-1, BCR-2, BHVO-1, BHVO-2, AGV-1, AGV-2, DTS-1, DTS-2, GSP-1 and GSP-2 by ID-TIMS and MIC-SSMS, Geostandards Newsletter-the Journal of Geostandards and Geoanalysis, 25, 77-86, 10.1111/j.1751-908X.2001.tb00789.x.

Schwarz, W.H.; Trieloff, M., 2007, Intercalibration of ^{40}Ar-^{39}Ar age standards NL-25, HB3gr hornblende, GA1550, SB-3, HD-B1 biotite and BMus/2 muscovite, Chem. Geol., 242, 218-231.

Stacey, J.S.; Kramers, J.D., 1975, Approximation of terrestrial lead isotope evolution by a two-stage model, Earth and Planetary Science Letters, v. 26, p. 207-221.

Steiger, R.H.; Jäger, E., 1977, Subcommission on geochronology: Convention on the use of decay constants in geo- and cosmochronology, Earth and Planetary Science Letters, 36, 21-23.

Table A1: Trace element analyses from Shyok Volcanics samples

Sample	BCUM12-146c	NBMU10-043	NBNU10-019	NBUM10-016	NBUM10-045	NBUM10-048	NBUM10-054	NBUM10-077	NBUM10-089	NBWA10-096	Blank
U	1.28	1.62	2.18	0.99	1.17	1.52	0.16	1.15	0.54	0.89	0.00
Nb	4.92	2.36	16.95	4.26	2.32	4.45	1.18	4.16	0.78	6.32	0.00
Ta	0.39	0.32	1.13	0.34	0.17	0.36	0.11	0.33	0.06	0.44	0.00
La	14.40	15.08	25.21	13.26	17.21	18.28	3.65	14.13	6.22	14.94	0.00
Ce	29.23	28.45	51.53	26.24	34.41	34.75	9.08	28.14	12.31	29.22	0.00
Pb	7.11	9.73	9.58	2.80	9.78	6.80	1.20	7.34	2.02	5.77	0.01
Pr	3.59	3.13	6.18	3.31	4.05	3.99	1.31	3.57	1.51	3.63	0.00
Sr	163.43	169.22	604.56	417.00	368.87	504.81	58.52	363.84	469.16	530.10	0.01
Nd	13.83	11.59	24.52	12.90	16.30	15.19	6.27	13.75	6.09	14.43	0.00
Sm	2.84	2.38	5.07	2.80	3.75	2.90	1.81	2.89	1.37	3.03	0.00
Zr	119.60	44.41	230.81	33.82	16.83	69.61	42.39	112.45	23.41	66.40	0.01
Eu	0.84	0.84	1.38	0.94	1.10	0.81	0.58	0.71	0.36	0.93	0.00
Gd	2.90	2.51	4.94	3.01	3.87	2.86	2.23	3.00	1.43	3.13	0.00
Tb	0.42	0.36	0.72	0.44	0.56	0.37	0.40	0.42	0.20	0.45	0.00
Dy	2.45	2.25	3.96	2.60	3.41	1.92	2.61	2.47	1.23	2.61	0.00
Y	12.64	12.40	20.14	13.16	18.03	9.14	13.64	11.95	6.70	13.00	0.00
Ho	0.47	0.46	0.76	0.49	0.67	0.35	0.55	0.47	0.24	0.49	0.00
Er	1.37	1.40	2.15	1.41	2.00	0.96	1.64	1.34	0.72	1.39	0.00
Tm	0.20	0.21	0.29	0.20	0.29	0.13	0.24	0.19	0.10	0.19	0.00
Yb	1.27	1.44	1.90	1.26	1.96	0.83	1.58	1.24	0.70	1.23	0.00
Lu	0.20	0.24	0.30	0.20	0.32	0.13	0.26	0.20	0.11	0.19	0.00
Ti	6732	4929	15021	8381	8173	6311	8410	7483	2812	9394	0.01
Co	16.35	15.07	27.07	22.26	30.19	14.52	21.68	22.79	12.64	19.86	0.00
Th	4.75	8.68	7.21	3.90	7.51	5.61	0.58	4.63	3.06	3.11	0.00

[a] Values are in parts per million (ppm).

Table A2: $^{40}Ar/^{39}Ar$ data for sample NBUM10-45

Lab ID# 633-01	Laser Power (W)	$^{40}Ar^*/^{39}Ar$ ± 2σ		$^{40}Ar/^{39}Ar$ ± 2σ		$^{38}Ar/^{39}Ar$ ± 2σ		$^{36}Ar/^{39}Ar$ ± 2σ		Cl/K	Ca/K	^{39}Ar (moles)	$\%^{40}Ar^*$	$\%\ ^{39}Ar$	Age (Ma) ± 2σ		±2σ Age error with error in J
633-01A	4.0	104.05	0.88	130.95	0.88	0.04109	0.00069	0.0930	0.0012	0.004	7.324	2.33E-16	79.25	12.75	106.12	0.87	1.1
633-01B	5.0	125.51	0.78	130.97	0.78	0.04286	0.00050	0.021	0.000	0.007	9.956	4.11E-16	95.49	22.50	127.26	0.77	1.1
633-01C	5.5	130.74	0.88	134.51	0.87	0.04431	0.00053	0.016	0.001	0.007	10.075	2.99E-16	96.85	16.36	132.37	0.86	1.2
633-01D	6.0	128.40	0.89	131.95	0.87	0.0473	0.0013	0.015	0.001	0.008	9.589	2.01E-16	96.98	11.02	130.09	0.87	1.2
633-01E	6.3	120.8	1.3	124.0	1.1	0.0416	0.0011	0.0139	0.0024	0.007	9.952	7.68E-17	97.04	4.20	122.6	1.3	1.5
633-01F	6.5	116.9	1.8	121.2	1.5	0.0400	0.0017	0.0170	0.0034	0.006	9.187	4.84E-17	96.18	2.65	118.8	1.7	1.9
633-01G	7.0	122.4	1.2	126.24	0.99	0.0460	0.0019	0.0161	0.0024	0.007	10.562	8.80E-17	96.59	4.81	124.2	1.2	1.4
633-01H	8.0	134.4	1.1	137.2	1.1	0.0513	0.0018	0.013	0.001	0.008	11.037	1.50E-16	97.57	8.19	135.9	1.1	1.4
633-01I	9.0	129.4	1.4	133.6	1.3	0.0502	0.0024	0.0176	0.0017	0.008	11.669	6.49E-17	96.49	3.55	131.1	1.4	1.6
633-01J	10.0	125.8	2.0	129.0	1.7	0.0430	0.0035	0.0146	0.0032	0.007	12.449	3.17E-17	97.07	1.74	127.6	1.9	2.1
633-01K	11.0	126.4	2.3	129.8	2.0	0.0478	0.0038	0.0142	0.0040	0.008	9.517	2.69E-17	97.09	1.47	128.1	2.2	2.4
633-01L	15.0	129.4	1.3	180.9	1.4	0.07066	0.00085	0.1783	0.0020	0.006	14.108	1.97E-16	71.20	10.77	131.1	1.3	1.5
J value (± 2σ)	5.823E-04	±	3.6E-06														

Table A3: U/Pb data from this study

Analysis	U[a] (ppm)	$^{206}Pb/^{204}Pb$[b]	U/Th[a]	$^{206}Pb^*/^{207}Pb^*$	± (%)	Isotope ratios $^{207}Pb^*/^{235}U^*$	± (%)	$^{206}Pb^*/^{238}U$	± (%)	error corr.	Apparent ages (Ma) $^{206}Pb^*/^{238}U^*$	± (Ma)	$^{207}Pb^*/^{235}U$	± (Ma)	$^{206}Pb^*/^{207}Pb^*$	± (Ma)	Best age[c] (Ma)	± (Ma)
BCUM12-105 batch 1																		
BCUM12-105-11	284	119271	0.9	20.3374	13.0	0.0958	13.8	0.0141	4.7	0.34	90.5	4.2	92.9	12.2	156.0	304.6	90.5	4.2
BCUM12-105-5	112	29738	1.4	20.0556	44.3	0.0982	44.6	0.0143	5.3	0.12	91.4	4.8	95.1	40.5	188.5	1078.9	91.4	4.8
BCUM12-105-6	170	36856	0.8	20.2535	24.5	0.0973	25.1	0.0143	5.3	0.21	91.5	4.8	94.3	22.6	165.6	580.6	91.5	4.8
BCUM12-105-16	174	61475	0.9	25.3195	30.9	0.0781	31.1	0.0143	3.8	0.12	91.8	3.5	76.4	22.9	-383.8	818.1	91.8	3.5
BCUM12-105-12	224	60832	0.8	24.9102	22.8	0.0799	23.5	0.0144	5.9	0.25	92.4	5.4	78.0	17.7	-341.7	593.2	92.4	5.4
BCUM12-105-3	1576	230679	9.6	19.3598	0.9	0.2931	3.5	0.0412	3.4	0.97	260.0	8.8	261.0	8.2	270.1	19.8	260.0	8.8
BCUM12-105-8	457	118139	1.3	17.7381	1.5	0.5428	3.6	0.0698	3.3	0.91	435.1	13.8	440.3	12.8	467.2	32.6	435	14
BCUM12-105-15	253	326773	3.4	16.6678	1.5	0.8088	1.8	0.0978	1.0	0.54	601.3	5.6	601.8	8.3	603.4	33.4	601.3	5.6
BCUM12-105-7	266	233554	0.7	15.5200	0.9	1.0962	3.0	0.1234	2.8	0.96	750.0	20.0	751.5	15.7	755.9	18.0	750	20
BCUM12-105-14	307	496040	10.9	12.7457	0.5	2.0975	2.5	0.1939	2.4	0.98	1142.4	25.6	1148.0	17.2	1158.5	9.9	1158.5	9.9
BCUM12-105 batch 2																		
BCUM12-105-36	34	1428	1.0	21.4064	114.5	0.0870	114.7	0.0135	6.8	0.06	86.5	5.8	84.7	93.5	34.7	1138.8	86.5	5.8
BCUM12-105-48	32	1582	1.0	10.9099	187.3	0.1741	188.0	0.0138	16.2	0.09	88.2	14.2	163.0	290.7	1460.3	486.6	88	14
BCUM12-105-29	64	2427	1.1	22.2839	42.3	0.0861	42.6	0.0139	5.0	0.12	89.1	4.4	83.9	34.3	-62.4	1073.5	89.1	4.4
BCUM12-105-39	554	17885	0.6	21.0137	6.9	0.0914	7.0	0.0139	1.3	0.18	89.2	1.1	88.8	6.0	78.8	164.8	89.2	1.1
BCUM12-105-33	40	1581	0.8	19.8403	121.8	0.0970	122.0	0.0140	7.2	0.06	89.4	6.4	94.0	110.0	213.6	1055.2	89.4	6.4
BCUM12-105-27	96	8088	0.6	23.3228	24.6	0.0830	24.9	0.0140	4.3	0.17	89.9	3.8	81.0	19.4	-174.8	620.6	89.9	3.8
BCUM12-105-21	332	18110	1.1	20.5362	7.2	0.0947	7.4	0.0141	1.8	0.24	90.3	1.6	91.8	6.5	133.1	169.9	90.3	1.6
BCUM12-105-50	606	31691	0.4	21.3004	3.7	0.0914	3.8	0.0141	1.0	0.26	90.4	0.9	88.8	3.3	46.6	88.6	90.37	0.90
BCUM12-105-46	596	32751	0.7	20.1913	4.4	0.0964	4.7	0.0141	1.6	0.34	90.4	1.4	93.5	4.2	172.8	103.0	90.4	1.4
BCUM12-105-1	88	2839	0.9	23.0098	42.4	0.0847	42.7	0.0141	5.1	0.12	90.5	4.5	82.6	33.9	-141.2	1094.9	90.5	4.5
BCUM12-105-41	33	7462	1.0	4.1852	464.6	0.4661	464.7	0.0141	8.6	0.02	90.6	7.7	NA	NA	NA	NA	90.6	7.7
BCUM12-105-2	441	13891	0.7	21.2472	5.8	0.0920	6.7	0.0142	3.3	0.50	90.7	3.0	89.4	5.7	52.5	138.8	90.7	3.0
BCUM12-105-17	53	2554	0.8	14.8069	89.5	0.1325	89.9	0.0142	9.1	0.10	91.1	8.2	126.3	107.2	854.3	329.2	91.1	8.2
BCUM12-105-38	208	13420	3.7	19.3674	8.4	0.1014	9.0	0.0142	3.1	0.35	91.1	2.8	98.0	8.4	269.2	193.1	91.1	2.8
BCUM12-105-35	39	3461	0.9	19.0971	41.8	0.1029	42.7	0.0143	8.8	0.21	91.2	8.0	99.5	40.5	301.4	992.5	91.2	8.0
BCUM12-105-42	215	18168	1.9	19.7389	12.0	0.0997	12.3	0.0143	2.9	0.23	91.3	2.6	96.5	11.3	225.4	277.7	91.3	2.6
BCUM12-105-12	102	3826	1.5	18.0063	15.3	0.1094	15.9	0.0143	4.1	0.26	91.5	3.7	105.4	15.9	433.9	343.5	91.5	3.7
BCUM12-105-24	47	3217	0.8	50.5750	85.7	0.0390	86.6	0.0143	12.2	0.14	91.5	11.1	38.8	33.0	NA	NA	92	11
BCUM12-105-8	52	1518	0.7	13.1688	103.8	0.1499	104.1	0.0143	7.1	0.07	91.6	6.4	141.8	138.6	1093.4	269.1	91.6	6.4
BCUM12-105-11	536	14355	3.8	21.3392	5.7	0.0926	5.8	0.0143	1.3	0.21	91.7	1.1	89.9	5.0	42.2	136.4	91.7	1.1
BCUM12-105-3	366	15919	2.4	20.4774	8.3	0.0966	8.5	0.0144	2.1	0.24	91.9	1.9	93.7	7.6	139.9	195.0	91.9	1.9
BCUM12-105-18	140	9125	1.0	20.3617	16.0	0.0976	16.8	0.0144	5.3	0.31	92.2	4.8	94.5	15.2	153.2	376.5	92.2	4.8
BCUM12-105-30	263	12099	7.8	20.3719	11.2	0.0975	12.0	0.0144	4.4	0.36	92.2	4.0	94.5	10.8	152.0	262.1	92.2	4.0
BCUM12-105-13	321	19652	1.0	21.4498	10.9	0.0927	11.1	0.0144	2.0	0.18	92.3	1.8	90.0	9.6	29.8	262.9	92.3	1.8
BCUM12-105-37	70	5748	0.6	25.1091	51.4	0.0793	51.9	0.0144	7.2	0.14	92.4	6.6	77.5	38.7	-362.2	1413.3	92.4	6.6
BCUM12-105-43	288	7805	0.9	20.8125	4.5	0.0957	4.9	0.0144	2.0	0.41	92.4	1.8	92.8	4.4	101.7	106.6	92.4	1.8
BCUM12-105-47	429	17874	2.2	21.3621	4.6	0.0942	5.1	0.0146	2.0	0.40	93.4	1.9	91.4	4.4	39.7	110.9	93.4	1.9
BCUM12-105-31	41	3004	0.6	5.9952	291.0	0.3361	291.4	0.0146	15.8	0.05	93.5	14.6	294.2	949.8	2525.8	93.6	94	15
BCUM12-105-9	242	15766	4.6	22.4600	8.4	0.0898	8.8	0.0146	2.5	0.28	93.7	2.3	87.4	7.4	-81.6	207.0	93.7	2.3
BCUM12-105-23	349	13641	0.7	20.1447	9.3	0.1012	13.7	0.0148	10.1	0.74	94.6	9.5	97.9	12.8	178.2	216.2	94.6	9.5
BCUM12-105-20	29	1394	1.3	12.3431	131.0	0.1658	131.8	0.0148	14.7	0.11	95.0	13.9	155.7	192.6	1221.8	351.2	95	14
BCUM12-105-15	72	5079	0.7	30.1429	41.3	0.0680	41.8	0.0149	6.6	0.16	95.1	6.2	66.8	27.0	-860.0	1228.6	95.1	6.2
BCUM12-105-19	156	1120	1.0	19.5161	21.4	0.1057	22.1	0.0150	5.2	0.24	95.8	4.9	102.0	21.4	251.7	498.2	95.8	4.9
BCUM12-105-10	192	7439	1.1	17.9887	15.3	0.1149	15.6	0.0150	3.2	0.20	95.9	3.0	110.4	16.4	436.0	342.5	95.9	3.0
BCUM12-105-51	197	13656	0.8	21.1440	19.6	0.1008	21.8	0.0155	9.5	0.44	98.9	9.3	97.6	20.3	64.1	470.7	98.9	9.3
BCUM12-105-34	546	28488	0.6	21.0787	4.7	0.1093	4.9	0.0167	1.3	0.26	106.8	1.4	105.3	4.9	71.5	112.4	106.8	1.4
BCUM12-105-52	429	39119	1.1	21.1319	4.7	0.1157	4.9	0.0177	1.3	0.27	113.3	1.5	111.2	5.2	65.5	112.9	113.3	1.5

Table A3: U/Pb data from this study

Analysis	U[a] (ppm)	$^{206}Pb/^{204}Pb$[b]	U/Th[a]	$^{206}Pb^*/^{207}Pb^*$	± (%)	Isotope ratios $^{207}Pb^*/^{235}U^*$	± (%)	$^{206}Pb^*/^{238}U$	± (%)	error corr.	Apparent ages (Ma) $^{206}Pb^*/^{238}U^*$	± (Ma)	$^{207}Pb^*/^{235}U$	± (Ma)	$^{206}Pb^*/^{207}Pb^*$	± (Ma)	Best age[c] (Ma)	± (Ma)
BCUM12-105-40	653	50759	3.2	21.0176	3.1	0.1281	4.7	0.0195	3.5	0.75	124.7	4.3	122.4	5.4	78.4	74.6	124.7	4.3
BCUM12-105-53	331	2705	0.7	19.3429	6.7	0.1568	10.6	0.0220	8.2	0.77	140.2	11.4	147.9	14.6	272.1	154.1	140	11
BCUM12-105-16	134	10838	0.6	21.2686	11.5	0.1617	11.8	0.0249	2.8	0.24	158.8	4.4	152.2	16.7	50.1	274.5	158.8	4.4
BCUM12-105-54	76	6508	1.1	21.1700	14.4	0.1768	14.7	0.0271	2.9	0.20	172.7	4.9	165.3	22.4	61.2	344.6	172.7	4.9
BCUM12-105-55	75	5896	1.2	21.7276	14.3	0.1741	14.5	0.0274	2.4	0.17	174.4	4.2	162.9	21.8	-1.1	346.1	174.4	4.2
BCUM12-105-45	39	3952	1.0	18.7292	39.0	0.2077	39.5	0.0282	6.0	0.15	179.4	10.7	191.7	69.1	345.5	915.2	179	11
BCUM12-105-56	739	117740	1.4	19.7068	2.4	0.2340	3.2	0.0334	2.1	0.66	212.1	4.4	213.5	6.1	229.2	54.8	212.1	4.4
BCUM12-105-28	367	16649	2.0	19.6624	3.3	0.2428	4.8	0.0346	3.4	0.72	219.5	7.4	220.7	9.4	234.4	75.6	219.5	7.4
BCUM12-105-14	347	56072	3.4	17.0493	0.8	0.6663	1.7	0.0824	1.5	0.87	510.4	7.4	518.4	7.0	554.3	18.5	510.4	7.4
BCUM12-105-4	128	34885	1.0	17.1540	3.2	0.6902	4.6	0.0859	3.3	0.71	531.0	16.6	532.9	19.1	540.9	70.8	531	17
BCUM12-105-57	96	25838	3.1	15.5443	1.0	1.0617	6.0	0.1197	5.9	0.99	728.8	40.8	734.7	31.4	752.6	21.7	729	41
BCUM12-105-14	211	19971	1.3	13.3929	0.8	1.5873	3.1	0.1542	3.0	0.96	924.4	25.7	965.3	19.3	1059.6	17.0	1060	17
BCUM12-105 batch 3																		
BCUM12-105-5	29	1249	0.9	10.6110	249.8	0.1744	250.0	0.0134	9.1	0.04	86.0	7.7	163.2	395.9	1512.9	751.3	86.0	7.7
BCUM12-105-82	39	1098	0.8	10.6484	177.0	0.1751	177.2	0.0135	6.9	0.04	86.6	5.9	163.9	274.6	1506.3	399.3	86.6	5.9
BCUM12-105-68	82	8195	0.7	19.1261	41.3	0.0991	41.7	0.0137	6.1	0.15	88.0	5.3	95.9	38.2	297.9	980.6	88.0	5.3
BCUM12-105-74	362	24705	0.9	19.5319	6.0	0.0971	6.3	0.0138	1.8	0.29	88.1	1.6	94.1	5.6	249.8	138.2	88.1	1.6
BCUM12-105-61	75	3719	0.9	25.4374	39.8	0.0747	40.3	0.0138	6.2	0.15	88.2	5.4	73.1	28.4	-395.9	1073.2	88.2	5.4
BCUM12-105-80	43	2758	1.1	17.9520	103.3	0.1058	103.5	0.0138	6.3	0.06	88.2	5.5	102.1	100.8	440.6	723.0	88.2	5.5
BCUM12-105-69	98	4122	0.8	25.0127	27.8	0.0762	28.1	0.0138	4.3	0.15	88.5	3.8	74.6	20.2	-352.2	729.1	88.5	3.8
BCUM12-105-2	253	12800	1.2	20.8263	10.2	0.0924	10.3	0.0140	1.7	0.17	89.3	1.5	89.7	8.9	100.1	241.3	89.3	1.5
BCUM12-105-8	33	3949	1.0	8.3464	194.9	0.2309	195.1	0.0140	9.2	0.05	89.5	8.2	210.9	389.7	1953.4	155.5	89.5	8.2
BCUM12-105-16	274	19139	0.9	20.2397	12.4	0.0953	12.7	0.0140	2.3	0.19	89.5	2.1	92.4	11.2	167.2	291.4	89.5	2.1
BCUM12-105-55	51	4175	0.7	15.7696	88.7	0.1224	89.1	0.0140	8.8	0.10	89.6	7.9	117.3	99.0	722.1	411.6	89.6	7.9
BCUM12-105-66	54	4491	0.7	24.1601	56.0	0.0800	56.8	0.0140	9.4	0.17	89.8	8.4	78.2	42.7	-263.5	1531.4	89.8	8.4
BCUM12-105-28	44	2381	1.0	26.8877	65.4	0.0721	66.1	0.0141	9.8	0.15	90.0	8.8	70.7	45.2	-542.6	1953.6	90.0	8.8
BCUM12-105-10	54	3096	0.8	26.2075	43.0	0.0740	43.7	0.0141	8.0	0.18	90.0	7.2	72.5	30.6	-474.3	1183.9	90.0	7.2
BCUM12-105-84	37	2539	0.7	0.9404	2781.1	2.0739	2781.2	0.0141	9.0	0.00	90.5	8.1	NA	NA	NA	NA	90.5	8.1
BCUM12-105-98	85	5363	0.5	25.1359	45.1	0.0776	45.2	0.0142	4.0	0.09	90.6	3.6	75.9	33.1	-365.0	1220.7	90.6	3.6
BCUM12-105-72	161	7929	1.0	21.9407	22.2	0.0890	22.5	0.0142	3.6	0.16	90.7	3.2	86.6	18.7	-24.7	544.1	90.7	3.2
BCUM12-105-3	52	863	0.8	17.0377	52.1	0.1156	53.0	0.0143	9.7	0.18	91.4	8.8	111.1	55.8	555.8	1218.8	91.4	8.8
BCUM12-105-38	37	4714	0.8	5.8682	270.5	0.3360	270.7	0.0143	7.9	0.03	91.5	7.2	294.1	843.1	2561.7	1.4	91.5	7.2
BCUM12-105-27	44	2063	0.7	-1.4265	2754.6	-1.3840	2754.6	0.0143	9.5	0.00	91.6	8.6	NA	NA	NA	NA	91.6	8.6
BCUM12-105-23	34	1290	0.7	21.8912	79.6	0.0904	80.0	0.0144	8.4	0.11	91.9	7.7	87.9	67.5	-19.2	2353.9	91.9	7.7
BCUM12-105-65	53	2631	0.8	23.4735	49.1	0.0843	49.9	0.0144	9.1	0.18	91.9	8.3	82.2	39.4	-190.8	1298.5	91.9	8.3
BCUM12-105-101	408	18953	0.5	20.6201	8.2	0.0960	8.2	0.0144	1.1	0.14	91.9	1.0	93.1	7.3	123.5	192.7	91.9	1.0
BCUM12-105-131	498	31418	3.9	21.6110	2.3	0.0916	2.9	0.0144	1.8	0.62	91.9	1.7	89.0	2.5	11.9	55.3	91.9	1.7
BCUM12-105-11	379	12833	3.1	20.1591	6.9	0.0984	7.0	0.0144	1.4	0.19	92.1	1.2	95.3	6.4	176.5	161.4	92.1	1.2
BCUM12-105-119	291	11173	0.8	22.1508	9.5	0.0896	9.8	0.0144	2.2	0.23	92.2	2.0	87.2	8.2	-47.8	231.9	92.2	2.0
BCUM12-105-26	213	7149	1.6	20.7815	11.5	0.0955	12.0	0.0144	3.4	0.28	92.2	3.1	92.7	10.6	105.1	273.1	92.2	3.1
BCUM12-105-134	45	1190	0.7	26.6357	106.6	0.0745	107.1	0.0144	9.6	0.09	92.2	8.8	73.0	75.6	-517.4	1540.6	92.2	8.8
BCUM12-105-6	345	20105	5.3	21.3531	7.2	0.0932	7.6	0.0144	2.4	0.32	92.3	2.2	90.4	6.5	40.7	171.2	92.3	2.2
BCUM12-105-2	969	26548	4.8	20.8903	4.1	0.0952	4.2	0.0144	1.1	0.27	92.4	1.0	92.4	3.7	92.8	96.0	92.4	1.0
BCUM12-105-7	40	2522	0.9	21.9231	50.3	0.0913	50.8	0.0145	6.5	0.13	92.9	6.0	88.7	43.2	-22.7	1294.6	92.9	6.0
BCUM12-105-81	52	2775	0.8	21.7053	31.7	0.0924	32.1	0.0145	5.0	0.16	93.1	4.6	89.8	27.6	1.4	781.6	93.1	4.6
BCUM12-105-132	480	58265	12.8	20.9444	5.7	0.0959	6.1	0.0146	2.2	0.36	93.2	2.0	93.0	5.4	86.7	134.1	93.2	2.0
BCUM12-105-15	348	14543	0.8	21.5419	11.1	0.0933	11.4	0.0146	2.9	0.25	93.3	2.6	90.6	9.9	19.5	266.8	93.3	2.6
BCUM12-105-86	51	2268	0.8	0.3473	16881.2	5.7884	16881.2	0.0146	6.9	0.00	93.3	6.4	NA	NA	NA	NA	93.3	6.4
BCUM12-105-127	886	55653	4.8	20.7985	1.9	0.0968	2.9	0.0146	2.2	0.75	93.5	2.0	93.8	2.6	103.2	46.0	93.5	2.0

Table A3: U/Pb data from this study

Analysis	U[a] (ppm)	$^{206}Pb/^{204}Pb$[b]	U/Th[a]	$^{206}Pb^*/^{207}Pb^*$	± (%)	Isotope ratios $^{207}Pb^*/^{235}U^*$	± (%)	$^{206}Pb^*/^{238}U$	± (%)	error corr.	Apparent ages (Ma) $^{206}Pb^*/^{238}U^*$	± (Ma)	$^{207}Pb^*/^{235}U$	± (Ma)	$^{206}Pb^*/^{207}Pb^*$	± (Ma)	Best age[c] (Ma)	± (Ma)
BCUM12-105-53	88	4633	0.4	22.3226	29.2	0.0904	29.7	0.0146	5.0	0.17	93.7	4.6	87.9	25.0	-66.6	727.2	93.7	4.6
BCUM12-105-100	370	33931	3.8	21.3530	6.7	0.0946	7.1	0.0147	2.6	0.36	93.8	2.4	91.8	6.3	40.7	159.2	93.8	2.4
BCUM12-105-128	175	7521	0.6	22.8486	15.9	0.0885	16.1	0.0147	2.7	0.17	93.9	2.5	86.1	13.3	-123.8	394.3	93.9	2.5
BCUM12-105-77	33	2810	0.8	36.9987	112.2	0.0547	112.5	0.0147	9.3	0.08	94.0	8.7	54.1	59.3	NA	NA	94.0	8.7
BCUM12-105-95	385	14080	4.4	21.4076	5.4	0.0947	5.7	0.0147	1.9	0.33	94.1	1.8	91.9	5.0	34.5	129.1	94.1	1.8
BCUM12-105-129	560	17978	6.1	20.6506	2.5	0.0983	3.0	0.0147	1.8	0.58	94.2	1.7	95.2	2.8	120.1	58.3	94.2	1.7
BCUM12-105-107	503	19423	0.3	20.2728	4.8	0.1003	5.2	0.0147	2.1	0.39	94.3	1.9	97.0	4.9	163.4	112.8	94.3	1.9
BCUM12-105-70	679	11563	0.9	20.4156	6.5	0.0998	6.6	0.0148	1.0	0.15	94.6	0.9	96.6	6.1	147.0	153.1	94.57	0.92
BCUM12-105-92	162	6278	0.5	25.0832	23.7	0.0819	23.9	0.0149	2.7	0.11	95.3	2.6	79.9	18.4	-359.5	621.0	95.3	2.6
BCUM12-105-20	259	10898	0.7	21.2174	10.2	0.0971	10.4	0.0149	2.3	0.22	95.6	2.2	94.1	9.4	55.9	243.6	95.6	2.2
BCUM12-105-45	552	25631	10.1	20.2392	5.9	0.1021	6.3	0.0150	2.2	0.35	95.9	2.1	98.7	6.0	167.3	138.9	95.9	2.1
BCUM12-105-46	437	16288	3.0	21.3594	6.3	0.0968	6.6	0.0150	2.1	0.32	95.9	2.0	93.8	5.9	40.0	150.3	95.9	2.0
BCUM12-105-54	403	14844	6.6	20.1549	5.1	0.1026	5.5	0.0150	2.1	0.38	96.0	2.0	99.2	5.2	177.0	119.5	96.0	2.0
BCUM12-105-120	904	35941	0.6	21.1358	3.8	0.0980	4.1	0.0150	1.5	0.37	96.2	1.4	95.0	3.7	65.0	90.2	96.2	1.4
BCUM12-105-50	526	14304	0.6	21.1477	4.7	0.0981	6.2	0.0150	4.1	0.66	96.2	3.9	95.0	5.7	63.7	112.0	96.2	3.9
BCUM12-105-122	930	35843	4.7	20.8277	1.8	0.0998	2.3	0.0151	1.5	0.65	96.5	1.4	96.6	2.1	99.9	41.5	96.5	1.4
BCUM12-105-19	34	3405	0.8	24.9653	171.4	0.0833	171.7	0.0151	9.7	0.06	96.6	9.3	81.3	134.9	-347.4	0.0	96.6	9.3
BCUM12-105-130	359	13856	4.3	20.6010	7.5	0.1047	8.5	0.0156	3.8	0.45	100.0	3.8	101.1	8.1	125.7	177.9	100.0	3.8
BCUM12-105-34	109	2864	1.0	24.5456	22.3	0.0879	23.6	0.0157	7.7	0.33	100.1	7.7	85.6	19.3	-303.8	575.2	100.1	7.7
BCUM12-105-9	37	2145	0.9	22.9430	63.1	0.0944	63.9	0.0157	9.7	0.15	100.4	9.7	91.6	56.0	-134.0	1729.4	100.4	9.7
BCUM12-105-30	181	10157	0.7	21.2918	5.4	0.1019	6.7	0.0157	3.9	0.59	100.7	3.9	98.5	6.3	47.5	130.0	100.7	3.9
BCUM12-105-33	129	5719	0.7	19.2573	7.4	0.1304	7.8	0.0182	2.3	0.30	116.3	2.6	124.4	9.1	282.3	169.9	116.3	2.6
BCUM12-105-75	635	11786	1.2	19.6861	5.1	0.1279	5.3	0.0183	1.5	0.28	116.7	1.7	122.3	6.1	231.6	117.3	116.7	1.7
BCUM12-105-94	134	1846	0.7	19.2335	13.9	0.1367	14.1	0.0191	2.7	0.19	121.8	3.3	130.1	17.3	285.1	318.9	121.8	3.3
BCUM12-105-85	158	2645	0.8	18.5785	15.5	0.1459	15.7	0.0197	2.7	0.17	125.5	3.3	138.3	20.4	363.7	351.9	125.5	3.3
BCUM12-105-29	142	7565	0.7	21.1367	11.3	0.1301	11.7	0.0199	3.2	0.28	127.3	4.1	124.2	13.7	65.0	269.0	127.3	4.1
BCUM12-105-125	538	57426	1.2	20.7933	3.0	0.1398	3.2	0.0211	1.2	0.36	134.5	1.5	132.9	4.0	103.8	71.2	134.5	1.5
BCUM12-105-25	778	19745	2.0	20.4850	1.8	0.1422	2.8	0.0211	2.2	0.76	134.8	2.9	135.0	3.6	139.0	43.0	134.8	2.9
BCUM12-105-79	209	15394	1.1	19.0829	8.2	0.1574	8.7	0.0218	2.9	0.34	138.9	4.0	148.4	12.0	303.0	186.9	138.9	4.0
BCUM12-105-21	230	17234	2.1	21.0215	6.7	0.1517	8.5	0.0231	5.3	0.62	147.4	7.7	143.4	11.4	77.9	159.5	147.4	7.7
BCUM12-105-112	1168	96173	0.6	20.2914	1.1	0.1689	1.3	0.0249	0.7	0.51	158.3	1.0	158.5	1.9	161.3	26.3	158.3	1.0
BCUM12-105-88	493	18334	0.5	19.0435	5.9	0.1836	6.5	0.0254	2.8	0.43	161.4	4.5	171.2	10.3	307.7	134.3	161.4	4.5
BCUM12-105-126	259	15026	0.7	20.2489	4.4	0.1730	5.9	0.0254	3.9	0.66	161.8	6.2	162.1	8.9	166.1	103.7	161.8	6.2
BCUM12-105-51	187	19085	1.3	19.2529	9.1	0.2148	9.3	0.0300	1.8	0.19	190.5	3.3	197.6	16.7	282.8	209.4	190.5	3.3
BCUM12-105-103	127	27136	1.2	20.1716	8.3	0.2405	8.5	0.0352	2.0	0.23	222.9	4.3	218.8	16.7	175.1	193.3	222.9	4.3
BCUM12-105-115	325	35429	2.3	19.6676	2.5	0.2731	3.5	0.0389	2.5	0.70	246.3	5.9	245.1	7.6	233.8	57.4	246.3	5.9
BCUM12-105-87	84	21058	1.2	19.0224	9.4	0.3454	9.6	0.0476	1.6	0.17	300.1	4.7	301.2	24.9	310.3	214.9	300.1	4.7
BCUM12-105-121	346	26692	1.6	18.5479	1.5	0.3869	3.4	0.0520	3.0	0.90	327.1	9.7	332.1	9.6	367.5	33.3	327.1	9.7
BCUM12-105-104	466	5490	1.3	18.2133	1.3	0.4192	2.4	0.0554	2.1	0.84	347.4	7.0	355.5	7.3	408.3	29.3	347.4	7.0
BCUM12-105-49	219	40055	1.5	16.9539	2.6	0.4821	4.1	0.0593	3.1	0.78	371.2	11.4	399.5	13.4	566.5	55.5	371	11
BCUM12-105-35	145	53429	0.9	18.1336	3.3	0.5319	3.6	0.0699	1.4	0.39	435.8	5.9	433.0	12.7	418.1	74.2	435.8	5.9
BCUM12-105-52	169	42046	1.6	17.7508	2.6	0.5907	4.9	0.0761	4.1	0.85	472.5	18.7	471.3	18.3	465.6	57.1	473	19
BCUM12-105-59	19	9069	0.4	23.0240	19.5	0.5207	20.5	0.0869	6.2	0.30	537.5	32.0	425.6	71.3	-142.7	486.9	537	32
BCUM12-105-37	75	15658	2.0	16.6358	2.5	0.7641	3.2	0.0922	2.1	0.65	568.5	11.6	576.3	14.3	607.6	53.0	568	12
BCUM12-105-36	449	125950	2.0	16.9564	0.7	0.7559	0.9	0.0930	0.6	0.64	573.0	3.2	571.6	3.9	566.2	15.0	573.0	3.2
BCUM12-105-118	271	91515	2.8	17.0802	1.1	0.7759	1.6	0.0961	1.2	0.74	591.6	6.9	583.1	7.3	550.3	24.1	591.6	6.9
BCUM12-105-39	576	74240	4.4	13.1394	0.6	1.9325	2.1	0.1842	2.0	0.96	1089.7	20.1	1092.4	14.0	1097.9	12.4	1098	12
BCUM12-105-48	186	101645	0.7	13.0633	0.6	2.0305	3.0	0.1924	2.9	0.98	1134.2	30.1	1125.8	20.1	1109.5	12.1	1109	12
BCUM12-105-96	73	18001	1.1	13.0364	2.5	1.7916	3.0	0.1694	1.5	0.52	1008.8	14.3	1042.4	19.3	1113.6	50.7	1114	51

Table A3: U/Pb data from this study

Analysis	U[a] (ppm)	$^{206}Pb/^{204}Pb$[b]	U/Th[a]	$^{206}Pb^*/^{207}Pb^*$	± (%)	Isotope ratios $^{207}Pb^*/^{235}U^*$	± (%)	$^{206}Pb^*/^{238}U$	± (%)	error corr.	Apparent ages (Ma) $^{206}Pb^*/^{238}U^*$	± (Ma)	$^{207}Pb^*/^{235}U$	± (Ma)	$^{206}Pb^*/^{207}Pb^*$	± (Ma)	Best age[c] (Ma)	± (Ma)
BCUM12-105-116	346	392106	1.4	12.9017	0.5	2.0483	1.0	0.1917	0.9	0.89	1130.4	9.7	1131.7	7.2	1134.3	9.4	1134.3	9.4
BCUM12-105-123	87	59365	0.6	12.7496	1.2	2.1291	1.5	0.1969	0.8	0.57	1158.5	8.8	1158.3	10.0	1157.9	23.6	1158	24
BCUM12-105-93	133	201602	0.8	12.6135	0.7	2.2428	1.4	0.2052	1.2	0.87	1203.1	13.6	1194.5	10.0	1179.2	13.9	1179	14
BCUM12-105-71	193	181466	0.8	12.6005	0.4	2.1985	2.4	0.2009	2.4	0.99	1180.2	25.5	1180.6	16.7	1181.2	7.9	1181.2	7.9
BCUM12-105-117	192	119208	1.9	11.2066	4.0	2.4618	4.6	0.2001	2.2	0.48	1175.8	23.6	1260.9	33.3	1409.2	77.5	1409	78
BCUM12-105-43	69	50092	0.9	10.6787	0.8	3.4925	1.6	0.2705	1.4	0.86	1543.3	18.9	1525.5	12.7	1500.9	15.7	1501	16
BCUM12-105-17	82	15784	1.1	9.3626	0.8	4.2778	2.2	0.2905	2.0	0.93	1643.9	29.6	1689.1	18.1	1745.6	15.1	1746	15
BCUM12-105-67	93	109166	0.7	9.0878	0.6	4.8864	1.2	0.3221	1.1	0.85	1799.8	16.7	1799.9	10.5	1800.0	11.8	1800	12
BCUM12-105-99	209	88324	1.3	8.9541	0.4	4.8025	2.1	0.3119	2.1	0.98	1749.9	32.3	1785.3	18.0	1826.9	6.8	1826.9	6.8
BCUM12-105-73	63	60895	1.0	8.7962	0.8	5.1757	2.7	0.3302	2.6	0.96	1839.3	41.1	1848.6	22.9	1859.1	14.4	1859	14
BCUM12-105-60	189	26722	3.2	8.7256	0.3	5.0714	2.4	0.3209	2.3	0.99	1794.3	36.5	1831.3	20.0	1873.7	5.7	1873.7	5.7
BCUM12-105-18	279	206542	1.5	8.7002	0.2	5.3178	0.7	0.3356	0.7	0.97	1865.2	11.8	1871.7	6.4	1878.9	3.1	1878.9	3.1
BCUM12-105-108	142	238925	0.9	8.6886	0.3	5.4047	1.6	0.3406	1.6	0.99	1889.5	26.2	1885.6	13.9	1881.3	4.6	1881.3	4.6
BCUM12-105-111	397	215104	5.9	8.6836	0.1	5.5941	2.7	0.3523	2.7	1.00	1945.6	45.8	1915.2	23.5	1882.4	1.9	1882.4	1.9
BCUM12-105-114	37	55401	0.7	8.6207	1.2	5.3325	2.0	0.3334	1.6	0.80	1854.9	26.4	1874.1	17.5	1895.5	22.1	1895	22
BCUM12-105-62	255	188260	2.0	8.3696	0.2	5.6171	1.3	0.3410	1.3	0.99	1891.3	21.2	1918.7	11.3	1948.4	3.9	1948.4	3.9
BCUM12-105-113	225	340283	7.0	8.3004	0.1	5.8614	0.7	0.3529	0.7	0.98	1948.2	11.4	1955.5	6.0	1963.3	2.5	1963.3	2.5
BCUM12-105-32	38	17845	1.0	8.2199	1.2	6.1127	1.4	0.3644	0.8	0.56	2003.1	13.6	1992.1	12.3	1980.6	20.8	1981	21
BCUM12-105-47	441	141953	1.6	6.9258	1.1	6.5156	3.0	0.3273	2.7	0.93	1825.2	43.7	2048.0	26.0	2280.5	18.6	2280	19
BCUM12-105-57	214	413373	1.5	6.9218	0.2	8.1775	1.5	0.4105	1.4	0.99	2217.3	27.1	2250.9	13.2	2281.5	3.8	2281.5	3.8
BCUM12-105-124	72	92746	0.6	6.3798	1.0	9.0489	4.4	0.4187	4.3	0.97	2254.6	81.3	2343.0	40.2	2420.8	17.5	2421	18
BCUM12-105-89	61	126220	1.0	5.5819	0.3	12.7768	0.7	0.5173	0.7	0.93	2687.5	14.5	2663.3	6.7	2645.0	4.4	2645.0	4.4
NBNU10-41																		
NBNU10-41-44R	1286	140179	40.5	19.5312	0.9	0.1965	1.3	0.0278	0.9	0.70	177.0	1.5	182.2	2.1	249.9	20.7	177.0	1.5
NBNU10-41-43R	414	83540	8.1	16.9544	1.2	0.4782	7.2	0.0588	7.1	0.99	368.4	25.3	396.9	23.5	566.4	26.4	368	25
NBNU10-41-63R	125	27179	3.4	17.3078	3.6	0.5833	6.4	0.0732	5.4	0.83	455.5	23.5	466.6	24.0	521.3	78.0	456	24
NBNU10-41-28R	431	43898	0.4	17.1726	1.1	0.6058	2.3	0.0754	2.0	0.87	468.9	9.2	480.9	8.9	538.5	24.9	468.9	9.2
NBNU10-41-30R	988	95541	4.3	17.1387	0.3	0.6254	1.9	0.0777	1.9	0.99	482.6	8.7	493.2	7.4	542.8	7.0	482.6	8.7
NBNU10-41-42R	1871	429960	4.4	17.2238	0.4	0.6366	1.0	0.0795	0.9	0.93	493.3	4.3	500.2	3.8	532.0	7.8	493.3	4.3
NBNU10-41-20R	715	203195	0.3	17.0104	0.7	0.6481	2.2	0.0800	2.1	0.95	495.9	10.2	507.3	9.0	559.3	15.6	496	10
NBNU10-41-21C	157	13444	1.2	17.0738	3.2	0.6516	3.5	0.0807	1.5	0.43	500.3	7.3	509.5	14.1	551.1	69.2	500.3	7.3
NBNU10-41-8C	152	31225	0.4	17.0022	2.6	0.6563	3.1	0.0809	1.8	0.57	501.7	8.6	512.3	12.7	560.3	56.5	501.7	8.6
NBNU10-41-8R	249	53113	1.5	17.3961	1.4	0.6485	1.8	0.0818	1.2	0.67	507.0	5.9	507.6	7.3	510.2	29.8	507.0	5.9
NBNU10-41-42C	509	239782	2.2	17.1756	0.9	0.6576	2.7	0.0819	2.5	0.94	507.6	12.4	513.2	10.9	538.1	20.5	508	12
NBNU10-41-36R	727	142392	23.2	17.1864	0.6	0.6597	1.4	0.0822	1.2	0.88	509.4	5.9	514.4	5.5	536.7	14.1	509.4	5.9
NBNU10-41-64R	56	27208	0.4	17.8623	7.2	0.6360	7.6	0.0824	2.6	0.35	510.4	13.0	499.8	30.1	451.7	159.0	510	13
NBNU10-41-4R	36	25790	0.6	18.9925	8.0	0.6095	8.6	0.0840	3.0	0.35	519.7	14.8	483.3	32.9	313.9	183.0	520	15
NBNU10-41-23R	1165	109735	15.6	16.8587	0.5	0.6965	1.3	0.0852	1.2	0.92	526.9	5.9	536.7	5.3	578.7	10.9	526.9	5.9
NBNU10-41-31R	94	16551	0.7	18.1112	4.0	0.6558	4.5	0.0861	2.0	0.43	532.7	10.0	512.0	18.1	420.9	90.4	533	10
NBNU10-41-31C	81	22407	0.9	17.7769	3.3	0.6682	3.6	0.0862	1.4	0.39	532.7	7.1	519.6	14.5	462.4	73.1	532.7	7.1
NBNU10-41-38R	194	73701	181.0	17.4249	2.2	0.6834	2.5	0.0864	1.2	0.48	534.0	6.3	528.8	10.4	506.5	48.7	534.0	6.3
NBNU10-41-48R	32	18787	0.8	19.4402	19.5	0.6144	19.6	0.0866	2.0	0.10	535.6	10.1	486.3	75.9	260.6	451.6	536	10
NBNU10-41-2R	350	210791	1.3	17.1124	1.0	0.7006	1.4	0.0869	1.0	0.73	537.4	5.4	539.1	6.0	546.2	21.2	537.4	5.4
NBNU10-41-2C	1664	127778	14.2	17.2118	0.4	0.7005	4.8	0.0874	4.8	1.00	540.4	24.6	539.1	20.0	533.5	9.8	540	25
NBNU10-41-9R	423	244273	8.0	16.9803	0.8	0.7196	1.4	0.0886	1.2	0.84	547.4	6.3	550.4	6.1	563.1	17.0	547.4	6.3
NBNU10-41-48C	37	9607	0.5	17.4013	9.9	0.7071	10.4	0.0892	3.4	0.32	551.0	17.8	543.0	43.9	509.5	217.4	551	18
NBNU10-41-12R	639	140121	1.8	17.2612	0.8	0.7230	3.1	0.0905	3.0	0.97	558.6	16.0	552.5	13.2	527.3	16.7	559	16
NBNU10-41-43C	1113	257777	2.0	16.5547	0.4	0.7606	1.1	0.0913	1.1	0.94	563.4	5.8	574.4	5.0	618.1	8.2	563.4	5.8
NBNU10-41-63C	56	7482	0.2	15.8858	8.7	0.7985	9.2	0.0920	3.0	0.33	567.3	16.3	596.0	41.3	706.5	184.6	567	16

Table A3: U/Pb data from this study

Analysis	U[a] (ppm)	$^{206}Pb/^{204}Pb$[b]	U/Th[a]	$^{206}Pb^*/^{207}Pb^*$	± (%)	Isotope ratios $^{207}Pb^*/^{235}U^*$	± (%)	$^{206}Pb^*/^{238}U$	± (%)	error corr.	Apparent ages (Ma) $^{206}Pb^*/^{238}U^*$	± (Ma)	$^{207}Pb^*/^{235}U$	± (Ma)	$^{206}Pb^*/^{207}Pb^*$	± (Ma)	Best age[c] (Ma)	± (Ma)
NBNU10-41-28C	75	21643	1.5	16.5793	3.9	0.7677	4.3	0.0923	1.8	0.41	569.2	9.5	578.4	18.8	614.9	83.9	569.2	9.5
NBNU10-41-37R	43	12670	0.3	18.0190	12.9	0.7113	13.1	0.0930	2.4	0.18	573.0	13.2	545.5	55.6	432.3	289.1	573	13
NBNU10-41-57C	382	48247	11.6	16.4970	0.7	0.7779	3.9	0.0931	3.8	0.98	573.7	21.0	584.3	17.3	625.7	15.1	574	21
NBNU10-41-58R	164	103898	2.1	16.9774	1.8	0.7593	2.3	0.0935	1.4	0.61	576.2	7.7	573.6	10.1	563.5	39.7	576.2	7.7
NBNU10-41-22R	1520	175753	7.2	16.5864	0.3	0.7839	1.4	0.0943	1.4	0.98	580.9	7.7	587.7	6.3	614.0	6.1	580.9	7.7
NBNU10-41-22C	385	154613	4.0	16.6946	0.8	0.7795	2.1	0.0944	2.0	0.93	581.4	11.0	585.2	9.5	599.9	17.0	581	11
NBNU10-41-33R	410	53727	0.7	16.6876	0.6	0.7892	1.4	0.0955	1.2	0.90	588.1	6.9	590.7	6.1	600.8	13.1	588.1	6.9
NBNU10-41-41R	128	179418	1.2	16.4472	3.2	0.8070	7.5	0.0963	6.7	0.90	592.5	38.1	600.8	33.8	632.2	69.4	592	38
NBNU10-41-37C	38	12755	0.5	17.7114	10.3	0.7538	11.5	0.0968	5.0	0.44	595.8	28.5	570.4	50.1	470.6	228.7	596	29
NBNU10-41-40R	526	121322	8.7	16.4752	0.6	0.8208	2.2	0.0981	2.1	0.96	603.2	11.9	608.5	9.9	628.5	13.0	603	12
NBNU10-41-11R	313	138533	11.9	16.2373	1.6	0.8466	2.4	0.0997	1.8	0.73	612.7	10.2	622.8	11.1	659.8	34.7	613	10
NBNU10-41-6R	844	137588	7.5	16.3074	0.5	0.8540	1.6	0.1010	1.5	0.95	620.3	8.8	626.8	7.3	650.5	10.0	620.3	8.8
NBNU10-41-34C	437	137874	8.5	16.2619	0.7	0.8625	1.2	0.1017	1.0	0.84	624.5	6.0	631.5	5.7	656.6	14.1	624.5	6.0
NBNU10-41-53R	227	103229	2.6	16.3916	1.4	0.8635	2.1	0.1027	1.6	0.76	629.9	9.5	632.0	9.8	639.5	29.3	629.9	9.5
NBNU10-41-56C	91	34357	1.5	16.3267	3.7	0.8726	4.4	0.1033	2.5	0.56	633.9	15.1	637.0	21.0	648.0	78.7	634	15
NBNU10-41-6C	185	39540	1.7	16.2999	1.0	0.8794	1.5	0.1040	1.0	0.70	637.6	6.2	640.7	6.9	651.5	22.4	637.6	6.2
NBNU10-41-44C	145	37196	4.1	16.3961	2.6	0.8809	2.9	0.1048	1.2	0.43	642.2	7.6	641.5	13.6	638.9	55.6	642.2	7.6
NBNU10-41-11C	273	159683	2.6	16.2854	0.6	0.9041	1.6	0.1068	1.5	0.92	654.1	9.1	653.9	7.6	653.5	13.1	654.1	9.1
NBNU10-41-57R	269	96304	3.1	16.2992	0.4	0.9166	1.3	0.1084	1.2	0.95	663.2	7.9	660.6	6.4	651.6	8.5	663.2	7.9
NBNU10-41-17R	274	76602	3.0	16.2268	1.5	0.9231	3.8	0.1086	3.5	0.92	664.8	22.1	664.0	18.5	661.2	32.2	665	22
NBNU10-41-35C	59	24067	3.5	16.0490	4.6	0.9528	6.6	0.1109	4.7	0.71	678.0	30.0	679.6	32.5	684.8	98.9	678	30
NBNU10-41-35R	104	48738	3.6	15.9655	1.9	0.9724	3.3	0.1126	2.7	0.81	687.8	17.6	689.7	16.7	695.9	41.6	688	18
NBNU10-41-50C	80	42489	2.7	15.4667	2.9	1.0151	3.4	0.1139	1.8	0.52	695.2	11.8	711.5	17.6	763.1	62.0	695	12
NBNU10-41-3C	364	33220	2.7	15.2784	1.1	1.0286	3.7	0.1140	3.5	0.96	695.8	23.4	718.2	19.1	788.9	22.2	696	23
NBNU10-41-10R	806	501647	5.4	14.6180	0.2	1.1607	1.2	0.1231	1.2	0.98	748.2	8.5	782.3	6.7	881.0	4.4	748.2	8.5
NBNU10-41-7R	100	34526	0.9	15.3088	2.0	1.1497	3.3	0.1276	2.6	0.80	774.4	19.3	777.1	18.0	784.7	41.6	774	19
NBNU10-41-7C	73	56052	0.9	15.3456	4.1	1.1484	4.5	0.1278	1.9	0.41	775.3	13.6	776.5	24.6	779.7	87.0	775	14
NBNU10-41-27R	347	173697	2.0	15.2535	1.1	1.1796	2.6	0.1305	2.4	0.91	790.7	17.8	791.1	14.5	792.3	22.8	791	18
NBNU10-41-4C	484	269118	9.4	14.4932	0.7	1.2584	3.9	0.1323	3.9	0.98	800.8	29.1	827.2	22.2	898.7	15.0	801	29
NBNU10-41-9C	252	4876	1.3	14.1046	1.3	1.3020	4.6	0.1332	4.4	0.96	806.0	33.3	846.6	26.3	954.5	25.9	806	33
NBNU10-41-27C	313	169624	1.1	14.9615	0.6	1.2538	1.5	0.1360	1.4	0.93	822.3	10.7	825.1	8.5	832.7	11.5	822	11
NBNU10-41-3R	707	226831	2.1	15.0048	0.4	1.2555	2.3	0.1366	2.2	0.98	825.6	17.2	825.9	12.7	826.7	8.4	826	17
NBNU10-41-55C	90	37875	1.1	14.8518	1.4	1.2820	2.0	0.1381	1.4	0.70	833.9	11.0	837.8	11.4	848.1	29.6	834	11
NBNU10-41-62C	128	39423	2.1	14.5409	1.6	1.3252	2.4	0.1398	1.7	0.73	843.3	13.6	856.8	13.7	891.9	33.5	843	14
NBNU10-41-24R	173	87911	1.5	14.5355	1.3	1.4086	3.7	0.1485	3.5	0.93	892.5	28.9	892.6	22.0	892.6	27.7	893	29
NBNU10-41-26C	135	79028	1.0	14.4145	0.8	1.4284	2.6	0.1493	2.5	0.95	897.2	20.8	900.9	15.6	909.9	16.2	910	16
NBNU10-41-51R	176	67450	1.9	14.3191	1.3	1.5048	3.5	0.1563	3.3	0.93	936.1	28.5	932.4	21.4	923.6	26.5	924	27
NBNU10-41-14R	384	98259	1.4	13.9209	0.6	1.6448	1.7	0.1661	1.6	0.94	990.4	14.7	987.6	10.7	981.3	11.6	981	12
NBNU10-41-13	94	164875	1.0	13.9154	1.2	1.5894	1.9	0.1604	1.5	0.76	959.0	13.1	966.1	12.0	982.1	25.2	982	25
NBNU10-41-39R	348	100901	2.2	13.8891	0.7	1.6244	1.9	0.1636	1.8	0.92	976.9	15.9	979.7	12.0	985.9	15.2	986	15
NBNU10-41-45R	205	91906	1.9	13.8140	0.8	1.5645	3.2	0.1567	3.1	0.97	938.6	27.0	956.2	19.8	997.0	16.4	997	16
NBNU10-41-10C	222	45172	0.8	13.8097	1.1	1.5520	2.3	0.1554	2.0	0.87	931.4	17.2	951.3	14.1	997.5	22.5	998	22
NBNU10-41-25R	329	346882	2.2	13.7280	0.5	1.6477	3.2	0.1640	3.2	0.99	979.2	28.8	988.7	20.3	1009.6	10.5	1010	10
NBNU10-41-45C	440	237115	1.2	13.5766	0.8	1.6853	1.1	0.1659	0.8	0.69	989.7	7.3	1003.0	7.3	1032.0	16.7	1032	17
NBNU10-41-25C	545	1012262	1.2	13.5201	0.3	1.7534	1.4	0.1719	1.4	0.98	1022.8	13.4	1028.4	9.3	1040.5	5.5	1040.5	5.5
NBNU10-41-60R	346	110173	1.8	13.5070	0.7	1.6421	1.4	0.1609	1.1	0.84	961.6	10.1	986.5	8.5	1042.4	14.9	1042	15
NBNU10-41-51C	308	160004	5.7	13.3912	0.9	1.7351	2.3	0.1685	2.1	0.93	1003.9	19.4	1021.6	14.5	1059.8	17.2	1060	17
NBNU10-41-19R	745	440483	4.7	13.0964	1.1	1.5593	2.6	0.1481	2.4	0.90	890.3	19.8	954.2	16.3	1104.4	22.6	1104	23
NBNU10-41-61C	388	210159	1.2	12.9429	0.5	1.8630	1.9	0.1749	1.8	0.97	1039.0	17.7	1068.1	12.6	1128.0	9.7	1128.0	9.7

Table A3: U/Pb data from this study

Analysis	U[a] (ppm)	$^{206}Pb/^{204}Pb$[b]	U/Th[a]	Isotope ratios						error corr.	Apparent ages (Ma)						Best age[c] (Ma)	± (Ma)
				$^{206}Pb^*/^{207}Pb^*$	± (%)	$^{207}Pb^*/^{235}U^*$	± (%)	$^{206}Pb^*/^{238}U$	± (%)		$^{206}Pb^*/^{238}U^*$	± (Ma)	$^{207}Pb^*/^{235}U$	± (Ma)	$^{206}Pb^*/^{207}Pb^*$	± (Ma)		
NBNU10-41-49C	98	216275	1.7	12.2072	1.4	2.3041	2.6	0.2040	2.2	0.85	1196.7	24.4	1213.5	18.5	1243.6	26.7	1244	27
NBNU10-41-29C	353	541186	1.7	10.8572	0.5	3.0221	2.7	0.2380	2.7	0.98	1376.2	33.1	1413.2	20.7	1469.5	9.8	1469.5	9.8
NBNU10-41-15R	189	151279	1.7	10.5634	0.5	3.1518	3.3	0.2415	3.3	0.99	1394.3	40.9	1445.4	25.5	1521.4	10.0	1521	10
NBNU10-41-15C	176	156905	0.7	10.3801	0.6	3.4827	2.0	0.2622	1.9	0.95	1501.0	25.7	1523.3	15.9	1554.4	12.0	1554	12
NBNU10-41-18C	238	137055	1.5	8.8686	0.4	4.7922	1.2	0.3082	1.2	0.96	1732.0	17.9	1783.5	10.3	1844.3	6.3	1844.3	6.3
NBNU10-41-18R	128	79836	1.0	8.8238	0.4	4.8441	2.1	0.3100	2.0	0.98	1740.7	31.3	1792.6	17.6	1853.5	7.4	1853.5	7.4
NBNU10-41-30C	230	331983	1.2	8.8020	0.2	4.9264	0.9	0.3145	0.8	0.96	1762.8	12.7	1806.8	7.3	1857.9	4.4	1857.9	4.4
NBNU10-41-46C	526	776631	6.0	8.2344	0.6	5.0079	3.7	0.2991	3.7	0.99	1686.7	54.9	1820.7	31.7	1977.5	10.3	1978	10
NBNU10-41-5R	623	532864	1.7	6.1233	1.1	8.4510	4.0	0.3753	3.9	0.96	2054.4	68.1	2280.7	36.4	2490.2	17.8	2490	18
NBNU10-41-32C	64	188358	1.1	6.0756	0.4	10.6098	1.3	0.4675	1.3	0.96	2472.6	26.3	2489.6	12.4	2503.4	6.7	2503.4	6.7
NBNU10-41-1C	395	72049	1.8	5.6815	0.8	11.3015	4.0	0.4657	3.9	0.98	2464.6	79.5	2548.3	37.0	2615.6	13.2	2616	13
NBNU10-41-5C	216	275880	3.0	5.6609	0.2	11.4341	2.9	0.4694	2.9	1.00	2481.1	60.0	2559.2	27.3	2621.6	3.2	2621.6	3.2
NBNU10-41-16C	565	31474	1.9	5.6479	0.3	10.8494	2.2	0.4444	2.2	0.99	2370.4	44.0	2510.3	20.8	2625.5	5.1	2625.5	5.1
NBNU10-41-1C2	364	219630	5.0	5.6452	0.6	11.4308	4.1	0.4680	4.1	0.99	2474.8	83.6	2558.9	38.4	2626.3	9.9	2626.3	9.9
NBWA10-95																		
NBWA10-95-18	125	2641	0.7	28.8616	45.5	0.0298	46.1	0.0062	7.8	0.17	40.0	3.1	29.8	13.5	-736.8	1330.4	40.0	3.1
NBWA10-95-6	106	1774	0.7	5.7428	797.2	0.1497	797.2	0.0062	10.2	0.01	40.1	4.1	NA	NA	NA	NA	40.1	4.1
NBWA10-95-19	126	3792	0.9	16.0650	35.2	0.0546	35.8	0.0064	6.5	0.18	40.9	2.6	54.0	18.8	682.6	773.8	40.9	2.6
NBWA10-95-4	90	1180	0.7	13.9618	108.0	0.0629	108.8	0.0064	13.2	0.12	40.9	5.4	61.9	65.4	975.3	377.0	40.9	5.4
NBWA10-95-13	169	3496	0.6	33.0820	69.1	0.0266	69.6	0.0064	8.3	0.12	41.1	3.4	26.7	18.3	-1135.7	2373.7	41.1	3.4
NBWA10-95-16	76	1075	0.8	-5.6079	763.5	-0.1597	763.6	0.0065	11.6	0.02	41.7	4.8	NA	NA	NA	NA	41.7	4.8
NBWA10-95-11	77	1599	0.9	19.2902	60.5	0.0466	62.2	0.0065	14.5	0.23	41.9	6.1	46.3	28.1	278.4	1526.3	41.9	6.1
NBWA10-95-11	146	3391	0.6	25.3580	65.7	0.0355	66.4	0.0065	10.0	0.15	41.9	4.2	35.4	23.1	-387.8	1906.4	41.9	4.2
NBWA10-95-20	77	1391	0.8	11.8096	202.2	0.0769	202.6	0.0066	13.0	0.06	42.3	5.5	75.2	148.0	1308.1	686.7	42.3	5.5
NBWA10-95-2	123	2106	0.8	16.9020	41.2	0.0539	43.0	0.0066	12.4	0.29	42.4	5.2	53.3	22.3	573.2	934.6	42.4	5.2
NBWA10-95-10	63	1655	0.8	7.5950	122.8	0.1200	123.8	0.0066	15.5	0.13	42.5	6.6	115.0	135.5	2120.3	285.1	42.5	6.6
NBWA10-95-1	215	6407	1.1	32.7410	45.8	0.0282	46.3	0.0067	6.4	0.14	43.1	2.7	28.3	12.9	NA	NA	43.1	2.7
NBWA10-95-5	83	2182	1.2	2.1732	864.0	0.4280	864.2	0.0067	15.4	0.02	43.3	6.6	NA	NA	NA	NA	43.3	6.6
NBWA10-95-5	96	1591	0.8	18.0203	69.4	0.0517	71.7	0.0068	18.2	0.25	43.4	7.9	51.1	35.8	432.1	1780.6	43.4	7.9
NBWA10-95-1	55	1532	0.9	8.4520	120.4	0.1103	121.6	0.0068	16.7	0.14	43.4	7.2	106.3	123.3	1930.9	178.8	43.4	7.2
NBWA10-95-15	76	4402	0.8	2.2542	1091.6	0.4174	1091.7	0.0068	18.1	0.02	43.8	7.9	NA	NA	NA	NA	43.8	7.9
NBWA10-95-12	55	1199	0.8	5.0988	128.0	0.1893	128.8	0.0070	15.1	0.12	45.0	6.7	176.0	211.2	2794.2	669.4	45.0	6.7
NBWA10-95-9	97	3778	1.0	23.2906	64.2	0.0479	65.3	0.0081	11.7	0.18	52.0	6.1	47.6	30.3	-171.3	1780.5	52.0	6.1
BCUM12-135																		
BCUM12-135-19	227	10675	1.8	22.5269	19.1	0.0794	20.1	0.0130	6.2	0.31	83.1	5.1	77.6	15.0	-88.9	471.6	83.1	5.1
BCUM12-135-25	374	18919	3.4	20.6958	12.7	0.0880	12.8	0.0132	1.3	0.10	84.6	1.1	85.6	10.5	114.9	300.4	84.6	1.1
BCUM12-135-17	485	3074	0.5	16.9207	20.5	0.1077	21.1	0.0132	5.1	0.24	84.6	4.3	103.8	20.8	570.8	449.7	84.6	4.3
BCUM12-135-8	562	28208	4.1	21.5531	8.9	0.0848	9.0	0.0133	1.7	0.19	84.9	1.4	82.7	7.2	18.3	213.0	84.9	1.4
BCUM12-135-10	317	16720	1.3	20.5745	13.1	0.0889	13.3	0.0133	1.9	0.14	84.9	1.6	86.5	11.0	128.8	310.0	84.9	1.6
BCUM12-135-15	360	8945	2.8	20.5378	10.9	0.0891	11.2	0.0133	2.5	0.22	85.0	2.1	86.6	9.3	133.0	257.3	85.0	2.1
BCUM12-135-22	576	48877	3.4	21.4059	4.5	0.0856	5.1	0.0133	2.4	0.48	85.1	2.1	83.4	4.1	34.7	107.0	85.1	2.1
BCUM12-135-20	777	69024	3.7	21.1330	2.9	0.0868	3.4	0.0133	1.9	0.55	85.2	1.6	84.5	2.8	65.4	68.4	85.2	1.6
BCUM12-135-12	187	13888	1.6	24.2007	29.6	0.0758	29.8	0.0133	3.5	0.12	85.2	2.9	74.2	21.3	-267.7	766.0	85.2	2.9
BCUM12-135-7	441	14174	3.0	20.8072	11.5	0.0886	11.9	0.0134	3.3	0.28	85.7	2.8	86.2	9.9	102.2	271.7	85.7	2.8
BCUM12-135-13	470	30169	3.8	21.0493	5.9	0.0877	6.0	0.0134	1.1	0.18	85.7	0.9	85.3	4.9	74.8	141.2	85.73	0.94
BCUM12-135-24	709	52471	4.1	20.8917	5.2	0.0888	5.5	0.0135	1.7	0.30	86.2	1.4	86.4	4.5	92.6	123.6	86.2	1.4
BCUM12-135-4	616	45073	4.2	21.0260	7.7	0.0885	7.8	0.0135	0.9	0.11	86.4	0.7	86.1	6.4	77.4	183.7	86.40	0.74
BCUM12-135-27	352	15882	1.6	20.7597	16.9	0.0897	17.1	0.0135	2.9	0.17	86.5	2.5	87.2	14.3	107.7	401.4	86.5	2.5

Table A3: U/Pb data from this study

Analysis	U[a] (ppm)	$^{206}Pb/^{204}Pb$[b]	U/Th[a]	$^{206}Pb^*/^{207}Pb^*$	± (%)	Isotope ratios $^{207}Pb^*/^{235}U^*$	± (%)	$^{206}Pb^*/^{238}U$	± (%)	error corr.	Apparent ages (Ma) $^{206}Pb^*/^{238}U^*$	± (Ma)	$^{207}Pb^*/^{235}U$	± (Ma)	$^{206}Pb^*/^{207}Pb^*$	± (Ma)	Best age[c] (Ma)	± (Ma)
BCUM12-135-2	394	24409	0.7	21.8301	14.2	0.0856	14.3	0.0136	1.9	0.13	86.8	1.6	83.4	11.5	-12.4	344.3	86.8	1.6
BCUM12-135-9	630	28609	3.9	20.7367	5.7	0.0903	5.9	0.0136	1.3	0.23	86.9	1.1	87.8	4.9	110.2	134.7	86.9	1.1
BCUM12-135-5	515	22718	0.5	20.6890	8.0	0.0905	8.4	0.0136	2.7	0.32	87.0	2.3	88.0	7.1	115.7	188.6	87.0	2.3
BCUM12-135-18	360	25019	2.6	21.6822	15.2	0.0866	15.5	0.0136	2.8	0.18	87.2	2.4	84.3	12.5	3.9	368.2	87.2	2.4
BCUM12-135-14	220	10746	2.2	25.2218	22.2	0.0747	22.4	0.0137	2.9	0.13	87.4	2.5	73.1	15.8	-373.8	582.9	87.4	2.5
BCUM12-135-12	140	13155	2.0	19.7828	18.9	0.0955	19.5	0.0137	4.7	0.24	87.7	4.1	92.6	17.3	220.3	441.9	87.7	4.1
BCUM12-135-11	287	30869	3.3	19.6055	9.5	0.0968	10.0	0.0138	3.0	0.31	88.1	2.7	93.8	8.9	241.1	218.9	88.1	2.7
BCUM12-135-28	440	28266	1.3	22.9133	9.9	0.0831	10.1	0.0138	2.4	0.23	88.4	2.1	81.1	7.9	-130.8	244.0	88.4	2.1
BCUM12-135-3	222	10737	2.4	20.4760	14.2	0.0931	14.4	0.0138	2.5	0.17	88.5	2.2	90.4	12.4	140.1	333.9	88.5	2.2
BCUM12-135-1	209	199443	1.6	11.1068	0.6	3.1252	0.9	0.2517	0.7	0.75	1447.5	8.6	1438.9	6.8	1426.3	11.1	1426	11
BCUM12-135-26	61	65785	1.8	11.0406	1.6	3.1791	2.0	0.2546	1.2	0.58	1462.0	15.2	1452.1	15.4	1437.7	31.0	1438	31
BCUM12-135-21	27	20379	0.9	10.9355	5.7	3.1161	6.0	0.2471	1.8	0.30	1423.7	23.1	1436.7	46.3	1455.9	109.2	1460	110
NBUM12-146a																		
NBUM12-146A-1C	110	12177	0.6	42.9027	81.3	0.0413	81.6	0.0128	6.6	0.08	82.3	5.4	41.1	32.8	NA	NA	82.3	5.4
NBUM12-146A-1C	88	6361	0.7	17.0309	18.1	0.1051	19.4	0.0130	7.1	0.37	83.2	5.9	101.5	18.8	556.6	397.1	83.2	5.9
NBUM12-146A-3C	128	4248	0.7	19.1828	28.0	0.0948	28.4	0.0132	5.0	0.18	84.5	4.2	92.0	25.0	291.1	650.1	84.5	4.2
NBUM12-146A-2C	156	5213	0.6	22.4533	27.4	0.0817	27.6	0.0133	3.6	0.13	85.2	3.0	79.8	21.2	-80.9	681.1	85.2	3.0
NBUM12-146A-2R	111	2297	1.5	17.3994	17.6	0.1104	18.3	0.0139	5.1	0.28	89.2	4.5	106.3	18.4	509.7	388.6	89.2	4.5
BCUM12-97																		
BCUM12-97-3	259	7064	1.0	15.4265	24.1	0.1140	24.3	0.0128	3.2	0.13	81.7	2.6	109.6	25.3	768.6	515.0	81.7	2.6
BCUM12-97-1	331	6178	0.5	18.4620	18.8	0.0963	19.0	0.0129	3.3	0.17	82.6	2.7	93.4	17.0	377.9	425.2	82.6	2.7
BCUM12-97-9	361	24414	0.4	21.3859	10.4	0.0836	10.5	0.0130	1.4	0.14	83.0	1.2	81.5	8.2	37.0	248.8	83.0	1.2
BCUM12-97-7	385	32746	0.3	21.9058	10.5	0.0818	10.9	0.0130	2.8	0.26	83.2	2.3	79.8	8.4	-20.8	255.4	83.2	2.3
BCUM12-97-17	467	12646	0.4	20.1328	8.1	0.0895	8.4	0.0131	2.0	0.24	83.7	1.7	87.1	7.0	179.6	190.1	83.7	1.7
BCUM12-97-16	389	11879	0.5	22.1895	6.5	0.0819	6.7	0.0132	2.0	0.29	84.4	1.6	79.9	5.2	-52.0	157.2	84.4	1.6
BCUM12-97-14	378	35925	0.4	20.2286	11.5	0.0900	11.6	0.0132	1.5	0.13	84.6	1.3	87.5	9.7	168.5	269.0	84.6	1.3
BCUM12-97-10	360	7527	0.5	20.6158	6.9	0.0883	7.1	0.0132	1.6	0.23	84.6	1.4	86.0	5.8	124.0	162.8	84.6	1.4
BCUM12-97-8	432	10164	0.4	20.9018	7.2	0.0873	7.4	0.0132	1.7	0.23	84.7	1.4	84.9	6.1	91.5	171.9	84.7	1.4
BCUM12-97-5	383	18786	0.4	20.5510	9.2	0.0888	9.4	0.0132	1.9	0.20	84.7	1.6	86.3	7.8	131.5	217.7	84.7	1.6
BCUM12-97-4	168	8549	0.7	19.5179	15.4	0.0935	15.5	0.0132	1.7	0.11	84.7	1.4	90.7	13.5	251.4	356.5	84.7	1.4
BCUM12-97-22	252	15229	0.6	23.2867	14.2	0.0784	14.6	0.0132	3.1	0.21	84.7	2.6	76.6	10.8	-170.9	356.4	84.7	2.6
BCUM12-97-6	528	21772	0.3	21.5839	7.6	0.0846	8.0	0.0132	2.4	0.30	84.8	2.1	82.5	6.3	14.9	183.2	84.8	2.1
BCUM12-97-20	495	11239	0.4	20.9166	4.6	0.0873	4.8	0.0133	1.5	0.31	84.9	1.3	85.0	4.0	89.8	109.1	84.9	1.3
BCUM12-97-19	475	99542	0.4	20.7720	7.2	0.0880	7.5	0.0133	1.9	0.26	84.9	1.6	85.6	6.1	106.2	170.7	84.9	1.6
BCUM12-97-18	528	20445	0.3	21.9292	7.6	0.0835	7.9	0.0133	1.9	0.24	85.1	1.6	81.5	6.1	-23.4	184.8	85.1	1.6
BCUM12-97-2	387	24819	0.4	19.7964	8.3	0.0927	8.4	0.0133	1.3	0.16	85.2	1.1	90.0	7.2	218.7	191.3	85.2	1.1
BCUM12-97-23	286	13555	0.4	22.8550	15.2	0.0803	15.4	0.0133	2.2	0.15	85.3	1.9	78.4	11.6	-124.5	377.4	85.3	1.9
BCUM12-97-12	329	9375	0.4	22.3646	12.2	0.0821	12.5	0.0133	2.9	0.23	85.3	2.5	80.1	9.6	-71.2	298.0	85.3	2.5
BCUM12-97-21	431	13698	0.4	20.3694	5.3	0.0902	5.6	0.0133	1.9	0.34	85.4	1.6	87.7	4.7	152.3	123.6	85.4	1.6
BCUM12-97-13	243	9652	0.7	24.0789	16.9	0.0778	17.3	0.0136	3.6	0.21	87.0	3.1	76.1	12.7	-254.9	431.1	87.0	3.1
BCUM12-97-15	242	22514	0.5	20.8920	12.0	0.0900	12.3	0.0136	2.6	0.21	87.3	2.3	87.5	10.3	92.6	285.9	87.3	2.3
BCUM12-97-11	221	13638	0.4	21.7406	11.6	0.0866	13.2	0.0136	6.3	0.48	87.4	5.5	84.3	10.7	-2.5	280.2	87.4	5.5
BCUM12-97-24	419	17344	0.4	22.2784	6.9	0.0852	7.1	0.0138	1.7	0.25	88.1	1.5	83.0	5.6	-61.8	167.3	88.1	1.5
BCUM12-FG																		
BCUM12-FG-31	434	40073	1.1	19.7661	4.0	0.1743	4.8	0.0250	2.6	0.54	159.1	4.0	163.1	7.2	222.3	93.1	159.1	4.0
BCUM12-FG-32	887	6481	3.3	19.8376	2.9	0.1757	3.1	0.0253	1.1	0.34	161.0	1.7	164.4	4.7	213.9	68.2	161.0	1.7
BCUM12-FG-40	583	55546	9.1	20.1403	3.2	0.1734	3.4	0.0253	1.1	0.32	161.3	1.8	162.4	5.1	178.7	75.1	161.3	1.8
BCUM12-FG-15	649	50083	8.8	20.6706	2.2	0.1695	2.6	0.0254	1.4	0.55	161.8	2.3	159.0	3.8	117.8	50.7	161.8	2.3

Table A3: U/Pb data from this study

Analysis	U[a] (ppm)	$^{206}Pb/^{204}Pb$[b]	U/Th[a]	$^{206}Pb^*/^{207}Pb^*$	± (%)	Isotope ratios $^{207}Pb^*/^{235}U^*$	± (%)	$^{206}Pb^*/^{238}U$	± (%)	error corr.	Apparent ages (Ma) $^{206}Pb^*/^{238}U^*$	± (Ma)	$^{207}Pb^*/^{235}U$	± (Ma)	$^{206}Pb^*/^{207}Pb^*$	± (Ma)	Best age[c] (Ma)	± (Ma)
BCUM12-FG-24	494	24410	3.8	20.7024	4.6	0.1693	5.0	0.0254	1.9	0.39	161.8	3.1	158.8	7.3	114.2	108.4	161.8	3.1
BCUM12-FG-35	117	10572	69.2	19.6769	13.7	0.1784	14.0	0.0255	3.1	0.22	162.0	5.0	166.7	21.5	232.7	316.7	162.0	5.0
BCUM12-FG-14	557	48715	8.6	20.7728	4.0	0.1690	4.2	0.0255	1.4	0.32	162.1	2.2	158.5	6.2	106.1	94.9	162.1	2.2
BCUM12-FG-19	649	104252	8.8	20.2833	1.9	0.1741	2.5	0.0256	1.6	0.63	163.0	2.5	163.0	3.7	162.2	44.6	163.0	2.5
BCUM12-FG-26	83	8993	17.4	23.3456	22.8	0.1519	23.5	0.0257	5.7	0.24	163.7	9.2	143.6	31.4	-177.2	574.0	163.7	9.2
BCUM12-FG-29	877	44351	7.6	20.2495	1.9	0.1752	2.1	0.0257	0.8	0.40	163.8	1.3	163.9	3.1	166.1	43.9	163.8	1.3
BCUM12-FG-30	859	67456	6.5	20.3825	1.6	0.1744	1.8	0.0258	0.8	0.44	164.1	1.3	163.2	2.7	150.8	38.3	164.1	1.3
BCUM12-FG-34	189	13706	10.6	19.1795	7.6	0.1859	8.0	0.0259	2.4	0.29	164.5	3.8	173.1	12.7	291.5	174.8	164.5	3.8
BCUM12-FG-6	165	19431	104.3	19.3233	7.1	0.1859	7.7	0.0260	3.2	0.41	165.8	5.2	173.1	12.3	274.4	161.9	165.8	5.2
BCUM12-FG-8	159	6758	44.9	20.2547	8.7	0.1789	9.4	0.0263	3.6	0.39	167.2	6.0	167.1	14.5	165.5	203.8	167.2	6.0
BCUM12-FG-39	174	14043	1.7	16.6001	2.7	0.4875	4.3	0.0587	3.3	0.78	367.7	11.9	403.2	14.2	612.2	57.4	367.7	11.9
BCUM12-FG-1	137	32630	3.1	16.2684	4.6	0.5071	10.9	0.0598	9.9	0.91	374.6	35.8	416.5	37.1	655.7	97.7	374.6	35.8
BCUM12-FG-33	61	7747	1.0	15.4643	4.4	0.9565	5.3	0.1073	2.9	0.56	656.9	18.3	681.5	26.2	763.4	92.4	656.9	18.3
BCUM12-FG-20	105	21425	1.3	15.3784	2.5	1.0013	4.9	0.1117	4.2	0.86	682.5	27.5	704.5	25.1	775.2	53.6	682.5	27.5
BCUM12-FG-42	112	30112	0.9	15.5397	1.6	1.0023	3.1	0.1130	2.6	0.86	689.9	17.2	705.0	15.6	753.2	33.1	689.9	17.2
BCUM12-FG-28	177	22560	0.8	15.4087	1.2	1.0422	2.8	0.1165	2.5	0.90	710.2	16.9	725.0	14.6	771.0	26.2	710.2	16.9
BCUM12-FG-9	115	63030	0.7	14.8734	2.4	1.0947	4.4	0.1181	3.7	0.83	719.5	24.9	750.8	23.3	845.0	50.4	719.5	24.9
BCUM12-FG-36	316	87793	1.0	15.0264	1.6	1.1036	3.5	0.1203	3.1	0.89	732.1	21.8	755.1	18.8	823.7	33.5	732.1	21.8
BCUM12-FG-7	144	41972	0.7	14.9284	1.6	1.1313	2.0	0.1225	1.2	0.62	744.8	8.8	768.3	10.8	837.4	32.6	744.8	8.8
BCUM12-FG-25	74	14264	1.1	15.3356	2.7	1.1295	3.1	0.1256	1.6	0.52	762.9	11.6	767.5	16.9	781.0	56.4	762.9	11.6
BCUM12-FG-10	248	37931	0.7	15.0235	1.4	1.1572	1.9	0.1261	1.3	0.68	765.5	9.3	780.6	10.3	824.1	29.0	765.5	9.3
BCUM12-FG-27	59	17906	0.9	15.3964	5.4	1.1481	6.3	0.1282	3.2	0.51	777.6	23.3	776.3	34.0	772.7	113.6	777.6	23.3
BCUM12-FG-11	46	11851	0.8	14.8786	4.8	1.1955	5.8	0.1290	3.3	0.56	782.2	24.1	798.5	32.1	844.3	99.8	782.2	24.1
BCUM12-FG-17	59	23184	0.8	15.1330	3.8	1.2109	4.9	0.1329	3.0	0.62	804.4	23.0	805.6	27.3	808.9	80.4	804.4	23.0
BCUM12-FG-22	199	97761	0.5	14.8591	0.9	1.2424	1.5	0.1339	1.2	0.78	810.0	8.8	820.0	8.4	847.0	19.6	810.0	8.8
BCUM12-FG-2	185	65306	0.5	15.0002	1.2	1.2458	1.6	0.1355	1.0	0.63	819.3	7.7	821.5	8.9	827.3	25.5	819.3	7.7
BCUM12-FG-23	133	46062	0.6	14.9615	1.8	1.2684	2.5	0.1376	1.6	0.67	831.3	12.7	831.7	13.9	832.8	38.2	831.3	12.7
BCUM12-FG-38	157	33999	0.7	14.9797	2.1	1.2790	2.6	0.1390	1.4	0.55	838.8	11.1	836.4	14.7	830.2	44.8	838.8	11.1
BCUM12-FG-4	56	32011	0.8	14.9747	5.6	1.2847	6.6	0.1395	3.4	0.52	842.0	27.0	838.9	37.6	830.9	117.3	842.0	27.0

Note: All uncertainties are reported at the 1σ level, and include only measurement errors. Analyses conducted by LA-MC-ICPMS, as described by Gehrels et al. [2008]. U/Pb and $^{206}Pb/^{207}Pb$ fractionation is calibrated relative to fragments of a large Sri Lanka zircon of 563.5±3.2 Ma (2σ). U decay constants and composition as follows: ^{238}U = 9.8485 x 10-10, ^{235}U = 1.55125 x 10-10, $^{238}U/^{235}U$ = 137.88.

[a] U concentration and U/Th are calibrated relative to Sri Lanka zircon standard and are accurate to ~20%.

[b] Common Pb correction is from measured ^{204}Pb with common Pb composition interpreted from Stacey and Kramers [1975]. Common Pb composition assigned uncertainties of 1.5 for $^{206}Pb/^{204}Pb$, 0.3 for $^{207}Pb/^{204}Pb$, and 2.0 for $^{208}Pb/^{204}Pb$.

[c] Analyses for which for which errors could not be computed analytically are not included. Best age is determined from $^{206}Pb/^{238}U$ age for analyses with $^{206}Pb/^{238}U$ age <900 Ma and from $^{206}Pb/^{207}Pb$ age for analyses with $^{206}Pb/^{238}U$ age >900 Ma.

APPENDIX B

CHAPTER 3 APPENDIX

SAMPLE DESCRIPTIONS

Our studies of New Idria neptuinite and joaquinite were conducted on two specimens from the State Gem Mine. The first was a large single crystal of neptunite (SGM) collected from the mine. The second (DGM) was a specimen that contained both wall rock (primarily glaucophane) and vein material (neptunite, joaquinite, and natrolite). After crushing, five small fragments from the SGM crystal were selected for analysis. I analyzed two additional neptunite crystals as well as five joaquinite crystals broken from the DGM specimen. The joaquinite grains were 0.2-1 mm across, bright yellow, inclusion-free, translucent, and euhdral crystals that exhibited lamellar twinning and occasional intergrowth of crystals. The neptunite crystals (ranging in size from 0.5 to 5 mm) were very deep red-orange to nearly black, and the individual crystals broken from the DGM specimen were euhedral prisms.

INDUCTIVELY COUPLED PLASMA SOURCE MASS SPECTROSCOPY (ICPMS)

All laser ablation ICPMS analyses for mineral chemistry and (U-Th)/Pb dating were conducted using a Photon Machines *Analyte G2* instrument package – featuring an *Atlex 300* ArF excimer ultraviolet (193 nm) laser – for sampling of polished mineral sections and a Thermo Scientific *iCAP Q* quadrupole ICPMS for chemical measurements.

Mineral Chemistry – Methods

For general mineral chemistry analyses, the ablation run for each sample was performed by rastering a 20 µm laser spot across the sample over a distance of ~600 µm. In doing so, I applied a 4 mJ laser energy at 50% output power and a pulse frequency of 4 Hz for a total of ca. 60 s. Ablated material was then transferred into the plasma source of the *iCAP Q* using a mixed He+Ar carrier gas. For most analyses, a plasma RF power of 1400 W was used. Prior to each unknown and standard analysis, a 20 s background run was done, and a 20 s washout followed each analysis. I selected isotopes to measure based on the reported compositions of minerals in the joaquinite and neptunite groups. Measured isotopes were: ^{7}Li, ^{23}Na, ^{24}Mg, ^{27}Al, ^{29}Si, ^{44}Ca, ^{47}Ti, ^{51}V, ^{55}Mn, ^{57}Fe, ^{64}Zn, ^{88}Sr, ^{89}Y, ^{93}Nb, ^{125}Te, ^{129}Xe, ^{134}Ba, ^{139}La, ^{140}Ce, ^{141}Pr, ^{146}Nd, ^{147}Sm, ^{153}Eu, ^{157}Gd, ^{159}Tb, ^{163}Dy, ^{165}Ho, ^{166}Er, ^{169}Tm, ^{172}Yb, ^{175}Lu, ^{232}Th, and ^{238}U for joaquinite and ^{7}Li, ^{23}Na, ^{24}Mg, ^{27}Al, ^{29}Si, ^{39}K, ^{44}Ca, ^{47}Ti, ^{51}V, ^{55}Mn, ^{57}Fe, and ^{64}Zn for neptunite. For all analyses, I used NIST glass SRM 610 (Pearce et al., 1997) as my primary standard, and a standard analysis was run between every 5 unknowns, between measurements on different minerals, and at the beginning and end of every day's analytical session. Data were reduced using the *Iolite* software package (Paton et al., 2011) using its trace element data reduction scheme (Woodhead et al., 2007), which results in an output of semi-quantitative elemental weight percentages for each analysis. These data were then normalized such that all measured elements summed to 100 weight percent. At the 2σ (~ 95%) confidence level, assumed uncertainties for major elements were ~5 % of the reported values, whereas those for trace elements were ~10 %. Table DR1 shows the results of ICPMS analysis of the

mineral chemistry of five joaquinite crystals from specimen DGM, and Table B2 shows the results for the seven analyses of DGM and SGM neptunites (Table B2).

Joaquinite and Neptunite Mineral Characteristics and Chemistry

For this study, I focused on samples collected from the State Gem Mine (also known as the Dallas Gem Mine, 36.33555° N, 120.60694° W, WGS84). Because both joaquinite and neptunite contain significant quantities of trace elements that are difficult to measure using typical electron microprobe techniques, I elected to analyze these minerals instead by laser ablation, inductively coupled, plasma-source mass spectrometry (ICPMS) in the Group 18 Laboratories at Arizona State University. This procedure precluded the evaluation of chemical zoning in individual crystals, but the similarity of measured bulk compositions among different crystals of the same mineral suggest that intracrystalline zoning is relatively minor.

Empirically, joaquinite is variably hydrous, so I normalized the compositional data such that Si + Al =8 for the purposes of calculating a chemical formula for the State Gem Mine joaquinite as:

$(Ba_{1.97}Sr_{0.03})_{\Sigma=2}(Na_{0.74}Ca_{0.28})_{\Sigma=1.02}(REE_{1.44}Sr_{0.56}Th_{0.03}U_{0.01})_{\Sigma=2.04}$

$(Fe_{0.70}Mn_{0.06}Mg_{0.02}Zn_{0.06}Li_{0.14}Ti_{0.19}Nb_{0.01})_{\Sigma=1.18}Ti_2\ (Si_{7.99}Al_{0.01})_{\Sigma=8}O_{26}(OH_{0.50}O_{0.50})_{\Sigma=1}\cdot H_2O,$

where the relative abundances of OH and O are based on total charge balance. For this discussion, sites in joaquinite will be referred to by their dominant cation. While the apparent excess of atoms in the Fe and, to a lesser extent, the Na and REE sites seem to violate stoichiometry, it should be noted that charge excesses created by Ca, Ti, Th, and

U in sites where they are not dominant are balanced out by charge deficiencies caused by Li, Sr, and Al. Furthermore, adding up the species with their typical charges (using Fe^{2+} and Mn^{2+}) requires 26.75 O for charge balance, which is within the acceptable range for joaquinite due to O and OH solid solution. Finally, excess in the Fe and Na sites of joaquinite has been repeatedly documented (Chihara et al., 1974; Laid and Albee, 1972; Matsubara et al, 2001).

Individual neptunites separated from two different samples (DGM and SGM) yielded distinctive chemistries. For the DGM crystals, the average formula was:

$(K_{0.88}Na_{0.06}Li_{0.06})_{\Sigma=1}Na_2Li(Fe_{1.36}Mg_{0.45}Mn_{0.18}\ Zn_{0.01})_{\Sigma=2}Ti_2Si_8O_{24}$.

For the SGM crystals, the average formula was:

$(K_{0.83}Na_{0.11}Li_{0.05}Ca_{0.01})_{\Sigma=1}Na_2Li(Fe_{1.25}Mg_{0.51}Mn_{0.23}\ Zn_{0.01})_{\Sigma=2}Ti_2Si_8O_{24}$.

For both samples, the formulae were calculated assuming 24 oxygens. Both formulae are well within the variation observed for other neptunite analyses (Laird and Albee, 1972; Zadov et al., 2011)

(U-Th)/Pb – Methods and Results

Also using the *Analyte G3* laser, I ablated 50 µm pits with a depth of approximately 50 µm for (U-Th)/Pb geochronology of joaquinite (Figure B2). In doing so, I applied a 5 mJ laser energy at 100% output power and a pulse frequency of 5 Hz for a total of 50 s. Ablated material was then transferred into the plasma source of the *iCAP Q* using a mixed He+Ar carrier gas. For all, a plasma RF power of 1400 W was used. Prior to each unknown and standard analysis, a 20 s background run was done, and a 20 s washout followed each analysis. Measured isotopes were: ^{29}Si, ^{200}Hg, ^{202}Hg, ^{204}Pb, ^{206}Pb,

^{207}Pb, ^{208}Pb, ^{232}Th, and ^{238}U. Given the rarity of joaquinite, there is no available matrix-matched isotopic standard for it. Instead, I turned to BLR-1 titanite (1046 ± 5 Ma; Sun et al., 2012) as my primary standard, and MMT titanite from the McClure Mountain syenite (523.98 ± 0.12 Ma (2σ); Schoene and Bowring, 2006) as a secondary standard. Four primary standard analyses were performed at the beginning and end of the run, and an additional analysis were run after every three unknowns. Two MMT analyses were performed along with every group of BLR-1 analyses.

The resulting data were reduced in *Iolite* using the *VizualAge_UcomPbine* scheme (Chew et al., 2014). Hg was detected at levels well above background throughout all analyses; this is unsurprising given New Idria's origins as a mercury mine. Unfortunately, ^{204}Hg interferes with measurements of ^{204}Pb, precluding the use of a common Pb correction that utilizes ^{204}Pb. As a result, I report my final ages based on the common Pb correction scheme of Andersen (2002) for each analysis, which does not require knowledge of ^{204}Pb. Errors for isotopic measurements and apparent ages are quoted, as noted earlier, at the 2σ confidence level and reflect the propagation of analytical imprecision. Joaquinite (U-Th)/Pb data are reported in Table B3.

$^{40}AR/^{39}AR$ GEOCHRONOLOGY – METHODS AND RESULTS

Neptunite $^{40}Ar/^{39}Ar$ analyses were performed individual ~0.5 mm crystal fragments wrapped in Al foil and packaged in aluminum planchettes for neutron irradiation in the Oregon State University using Cd shielding. The irradiation package also contained standard HD-B1 (24.18 ± 0.18 Ma; Schwarz and Trieloff, 2007) as an irradiation monitor, as well as synthetic Ca and K salts to permit corrections for

interfering isotopic reactions. Gasses were liberated for analysis in an ultra-high vacuum extraction line using a Photon Machines *Fusions CO_2* infrared (10.6 μm) laser operated incrementally at successively higher power levels until the sample was fused. Gasses were purified and analyzed after each heating increment. Purification was accomplished using metal alloy getters to remove reactive gasses. Purified gas was admitted to the mass spectrometer for measurement of argon isotopes. The largest isotope (^{40}Ar) was measured using a $1x10^{11}$ Ohm Faraday detector or an ion counting multiplier, depending on signal size. All other argon isotopes (^{39}Ar, ^{38}Ar, ^{37}Ar, and ^{36}Ar) as well as backgrounds were measured on an ion counting multiplier by peak jumping. Detector intercalibration for samples that required Faraday measurement of ^{40}Ar was performed using multiple air shots. Average background values (as measured by ion counting) were 7431, 573.2, 9.24, 379.7, and 36.80 c.p.s for ^{40}Ar, ^{39}Ar, ^{38}Ar, ^{37}Ar, and ^{36}Ar, respectively. The average mass discrimination factor was 0.99468 ± 0.00034 per amu. The ^{40}Ar/^{39}Ar analytical process in the Group 18 Laboratories is automated by the *Mass Spec* software written by A. Deino. The resulting data were reduced using an off-line version of *Mass Spec* and *Isoplot* software written by K. Ludwig (Ludwig, 2008). Further details of laser step heating ^{40}Ar/^{39}Ar methods used at Arizona State University can be found in Long et al. (2012). All ^{40}Ar/^{39}Ar apparent ages (reported in Table B4) here were calculated using the decay constants, branching ratio, and atmospheric ^{40}Ar/^{36}Ar ratio recommended by Steiger and Jäger (1977).

FIGURE CAPTIONS

Figure B1. Cross-section drawn after that of Tsujimori et al. (2007). Line of section is indicated on Figure 3.1. All contacts shown are faults, with relative sense of motion as indicated. Note that this section shows detail extrapolated from off the line of section (see Tsujimori et al., 2007). Unit shading is the same as Figure 3.1.

Figure B2. Joaquinite crystals analyzed for (U-Th)/Pb geochronology. Circles (50 μm in diameter) indicate the footprints of laser ablation pits, and the numbers designate individual analyses in Table DR3. Other circular features evident in the photomicrographs but not labeled are test ablation pits drilled prior to geochronologic analysis.

Figure B3. $^{40}Ar/^{39}Ar$ laser step heating spectra for neptunite sample SGM-1 through SGM-4 in plots A-D, respectively. For each frame, the top, middle, and bottom panels show the percent radiogenic yield, the Ca/K ratio, and the date (respectively) for each heating step. Errors shown for each step reflect both analytical errors and errors in J, and are reported at. 2σ. Integrated total gas dates are indicated at the bottom of each plot. Plateau segments are marked by the arrows with associated dates labeled.

FIGURE B1

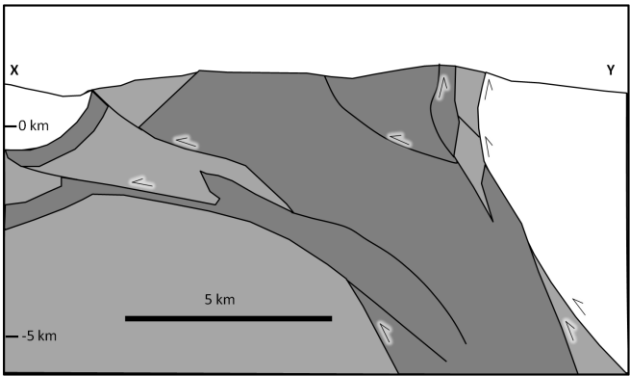

FIGURE B2

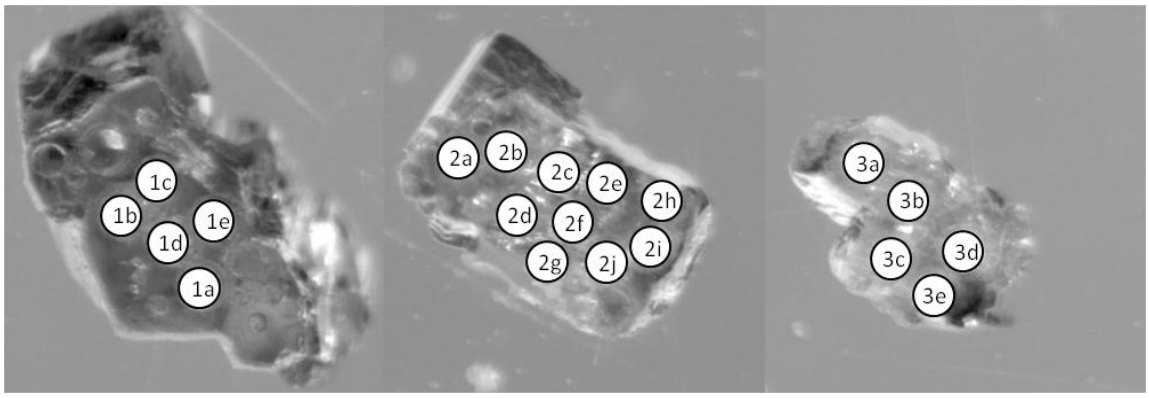

FIGURE B3

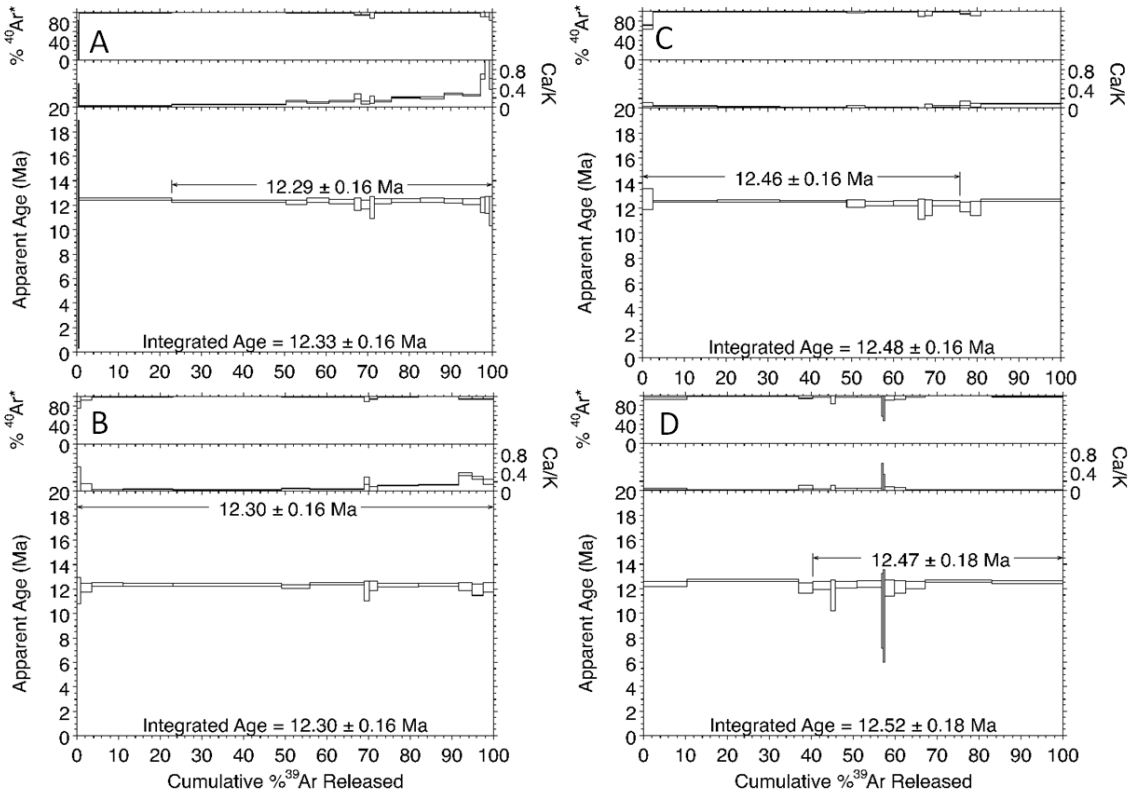
A
B
C
D
% 40Ar*
Ca/K
Apparent Age (Ma)
12.29 ± 0.16 Ma
12.30 ± 0.16 Ma
12.46 ± 0.16 Ma
12.47 ± 0.18 Ma
Integrated Age = 12.33 ± 0.16 Ma
Integrated Age = 12.30 ± 0.16 Ma
Integrated Age = 12.48 ± 0.16 Ma
Integrated Age = 12.52 ± 0.18 Ma
Cumulative %39Ar Released

Table B1: LA-ICPMS analyses of joaquinite

	DGM-1	DGM-2	DGM-3	DGM-4	DGM-5
wt%					
SiO_2	35	36	35	35	35
BaO	22	22	22	22	22
TiO_2	13	13	13	13	13
Ce_2O_3	7.7	7.7	7.7	8.2	8.0
SrO	5.1	4.6	4.6	4.2	4.5
La_2O_3	4.1	3.8	3.7	4.3	3.9
FeO	3.5	3.6	3.7	3.8	3.7
Nd_2O_3	2.7	3.5	3.6	3.5	3.5
Na_2O	1.6	1.7	1.7	1.7	1.7
CaO	1.3	1.2	1.1	1.0	1.1
Pr_2O_3	0.74	0.85	0.86	0.84	0.87
ThO_2	0.72	0.48	0.45	0.57	0.52
ZnO	0.38	0.35	0.36	0.31	0.34
MnO	0.36	0.31	0.26	0.32	0.31
Sm_2O_3	0.31	0.47	0.56	0.49	0.50
UO_3	0.25	0.28	0.32	0.23	0.27
Nb_2O_{10}	0.24	0.15	0.04	0.18	0.11
Li_2O	0.18	0.16	0.15	0.12	0.15
Gd_2O_3	0.15	0.25	0.31	0.29	0.28
Y_2O_3	0.073	0.11	0.16	0.13	0.11
ppm					
Eu	400	620	780	680	690
Dy	220	380	560	460	400
Mg	190	850	180	270	180
Al	130	240	120	180	130
Tb	39	83	41	80	60
Er	29	41	62	54	42
V	25	54	27	51	39
Ho	24	40	60	48	39
Yb	3.3	3.6	4.2	5.3	3.1
Tm	1.4	1.7	2.2	2.3	1.6
Lu	0.32	0.37	0.26	0.53	0.25
a.p.f.u					
Si	8.0	8.0	8.0	8.0	8.0
Ti	2.3	2.2	2.1	2.2	2.2
Nb	0.019	0.012	0.0030	0.014	0.0086
Fe	0.68	0.67	0.70	0.73	0.71
Mg	0.011	0.047	0.010	0.015	0.010
Mn	0.071	0.060	0.051	0.061	0.060
Zn	0.064	0.058	0.060	0.053	0.058
Li	0.16	0.14	0.14	0.11	0.14
Na	0.70	0.74	0.76	0.74	0.74
Ca	0.33	0.29	0.27	0.25	0.27
Sr	0.68	0.60	0.60	0.55	0.59
Ba	2.0	1.9	2.0	2.0	2.0
ΣREE	1.3	1.4	1.4	1.5	1.4
Th	0.038	0.025	0.023	0.030	0.027
U	0.012	0.013	0.015	0.011	0.013

Note: a.p.f.u is atoms per formula unit. Each a.p.f.u analysis normalized to Si+Al=8. All Fe is calculated as Fe^{2+}.

Table B2: LA-ICPMS analyses of neptunite

	DGM-1a	DGM-1b	DGM-1c	DGM-1d	DGM-1e	DGM-2a	DGM-2b	DGM-2c	DGM-2d	DGM-2e	SGM-1a	SGM-1b	SGM-1c	SGM-1d	SGM-1e
wt%															
SiO_2	54	54	54	54	54	54	54	54	54	54	54	54	55	55	54
TiO_2	18	18	18	18	18	18	18	18	18	18	18	17	17	18	18
FeO	11	11	11	11	11	11	11	11	11	11	11	10	9	10	11
Na_2O	7.2	7.2	7.1	7.1	7.2	7.2	7.1	7.2	7.3	7.2	7.4	7.5	7.4	7.4	7.3
K_2O	4.7	4.6	4.6	4.7	4.7	4.6	4.7	4.7	4.6	4.6	4.3	4.4	4.5	4.5	4.5
MgO	2.1	2.1	2.2	2.1	2.1	2.0	2.0	2.0	1.9	2.0	2.1	2.5	2.5	2.5	2.1
Li_2O	1.8	1.8	1.8	1.8	1.8	1.8	1.8	1.8	1.8	1.8	1.8	1.8	1.8	1.8	1.8
MnO	1.4	1.3	1.4	1.4	1.4	1.6	1.4	1.4	1.5	1.5	1.6	2.0	2.0	2.0	1.6
ppm															
Zn	490	520	530	510	510	540	550	540	550	550	310	480	550	520	310
Al	100	98	78	76	64	46	53	47	60	120	120	110	100	110	110
V	74	78	81	61	45	28	52	75	43	42	34	42	39	38	42
Ca	73	110	72	58	7	22	15	57	32	36	450	450	470	360	270
a.p.f.u															
Si	8.0	8.0	8.0	8.0	8.0	8.0	8.0	8.0	8.0	8.0	8.0	8.0	8.1	8.0	8.0
Ti	2.0	2.0	2.0	2.0	2.0	2.0	2.0	2.0	2.0	2.0	2.0	1.9	1.9	1.9	2.0
Fe	1.4	1.4	1.4	1.3	1.4	1.3	1.3	1.4	1.3	1.3	1.3	1.2	1.2	1.2	1.3
Mg	0.47	0.47	0.48	0.47	0.46	0.44	0.45	0.44	0.43	0.44	0.46	0.54	0.55	0.54	0.46
Mn	0.17	0.17	0.17	0.17	0.17	0.20	0.18	0.18	0.19	0.18	0.20	0.25	0.25	0.25	0.20
Li	1.1	1.1	1.1	1.0	1.1	1.1	1.0	1.0	1.1	1.0	1.1	1.1	1.1	1.1	1.1
Na	2.1	2.1	2.0	2.0	2.1	2.1	2.0	2.1	2.1	2.1	2.1	2.1	2.1	2.1	2.1
K	0.90	0.88	0.88	0.88	0.89	0.87	0.88	0.88	0.87	0.87	0.82	0.82	0.85	0.84	0.85

Note: a.p.f.u is atoms per formula unit. Each a.p.f.u analysis normalized to 24 O. All Fe is calculated as Fe2+. Different numbers denote different grains, different letters denote repeat analyses on the same grain crystals for DGM samples and different grain fragments for SGM sample.

Table B3: U, Th, Pb, and date data for joaquinite.

	ppm				Pb_c corrected isotopic ratios									Pb_c corrected dates in Ma					
	Th	Pb	U/Th	Pb*/ Pb_{total}	$^{207}Pb/^{235}U$	% 2σ	$^{206}Pb/^{238}U$	% 2σ	Corr.	$^{208}Pb/^{232}Th$	% 2σ	$^{207}Pb/^{206}Pb$	% 2σ	$^{207}Pb/^{235}U$	2σ	$^{206}Pb/^{238}U$	2σ	$^{208}Pb/^{232}Th$	2σ
1a	4770	69	0.50	0.66	0.0163	43.6	0.00212	10.4	0.77	0.00062	39.0	0.057	33.5689	16.4	7.0	13.6	1.4	12.4	4.8
1b	5910	51	0.69	0.44	0.0132	8.4	0.00207	5.3	1.00	0.00054	22.1	0.0461034	0.0176	13.3	1.1	13.33	0.69	11.0	2.3
1c	7600	96	0.51	0.60	0.0182	39.6	0.00223	7.2	0.76	0.00065	24.7	0.059	42.1585	18.3	7.2	14.4	1.0	13.1	3.2
1d	8850	34	0.37	0.30	0.01320	4.5	0.002077	3.7	1.00	0.000598	13.7	0.0460914	0.0065	13.32	0.59	13.38	0.50	12.1	1.7
1e	6910	33	0.47	0.33	0.01288	5.5	0.002027	4.0	1.00	0.000605	16.0	0.0460921	0.0048	13.00	0.71	13.05	0.53	12.2	2.0
2a	7000	41	0.30	0.50	0.0141	8.5	0.00219	5.0	0.55	0.000603	14.6	0.04636	3.0198	14.2	1.2	14.08	0.74	12.2	1.8
2b	7290	41	0.38	0.44	0.0135	8.1	0.00212	4.7	1.00	0.00057	21.1	0.0461022	0.0119	13.6	1.1	13.67	0.64	11.5	2.3
2c	8730	116	0.53	0.60	0.0201	37.8	0.00230	8.3	0.82	0.00071	33.9	0.061	52.8926	20.1	7.5	14.8	1.2	14.3	4.9
2d	5280	72	0.85	0.53	0.0131	8.4	0.00207	5.8	0.65	0.00055	65.5	0.046131	0.1951	13.2	1.1	13.34	0.76	11.1	7.3
2e	6700	47	0.37	0.53	0.0146	26.7	0.00208	6.7	0.84	0.00057	22.7	0.051	23.7154	14.7	3.9	13.37	0.91	11.6	2.7
2f	8130	34	0.16	0.57	0.0128	15.6	0.00201	9.5	0.71	0.000584	13.2	0.04655	3.0075	12.9	2.0	12.9	1.2	11.8	1.6
2g	5850	75	0.43	0.68	0.0157	42.0	0.00192	9.9	0.89	0.00067	29.9	0.057	41.8848	15.8	6.5	12.4	1.2	13.5	3.9
2h	6960	109	0.51	0.71	0.0150	61.3	0.00189	12.2	0.89	0.00060	47.1	0.052	34.7490	15.0	9.1	12.1	1.5	12.0	5.8
2i	5310	45	0.40	0.57	0.0135	13.4	0.002052	4.8	0.69	0.00060	28.3	0.0474	10.9705	13.6	1.8	13.22	0.63	12.1	3.4
2j	7910	43	0.25	0.53	0.0131	9.2	0.00205	6.3	0.75	0.00064	17.2	0.04638	2.3717	13.2	1.2	13.19	0.81	12.9	2.2
3a	5820	141	1.2	0.61	0.0125	8.8	0.00197	6.1	1.00	0.00065	100.0	0.046126	0.0911	12.6	1.1	12.66	0.75	13	13
3b	6500	85	0.30	0.71	0.026	69.5	0.00251	20.3	0.92	0.00069	55.1	0.074	52.7027	26	18	16.1	3.3	14.0	7.7
3c	8180	59	0.58	0.42	0.0133	8.3	0.00209	5.7	1.00	0.00060	20.0	0.0461006	0.0054	13.4	1.1	13.48	0.74	12.1	2.5
3d	6890	43	0.44	0.44	0.0136	8.1	0.00214	5.1	1.00	0.00058	19.0	0.0461037	0.0119	13.7	1.1	13.77	0.69	11.7	2.1
3e	6990	53	0.44	0.50	0.01359	5.8	0.002138	4.1	1.00	0.00061	27.7	0.0461124	0.0132	13.71	0.79	13.77	0.56	12.4	3.5

Note: Pb_c is common Pb. Pb* is radiogenic Pb. Different sample numbers denote different grains; different letters denote repeat analyses on the same grain Crystal. Corr. is the $^{207}Pb/^{235}U$ - $^{206}Pb/^{238}U$ error correlation coefficient.

Table B4: Ar isotope and date data

Lab ID#	Laser (W)	$^{40}Ar^*/^{39}Ar$ ± 2σ		$^{40}Ar/^{39}Ar$ ± 2σ		$^{38}Ar/^{39}Ar$ ± 2σ		$^{36}Ar/^{39}Ar$ ± 2σ		^{39}Ar (moles)	$\%^{40}Ar^*$	$\%\ ^{39}Ar$	Age (Ma) ± 2σ		± 2σ w/ J error
SGM-1															
866-01A	0.9	17.19	11.93	143.0	3.4	0.0958	0.0043	0.426	0.042	1.5E-17	12	0.10	32	22	22
866-01B	1.0	6.3	1.2	9.120	0.071	0.01392	0.00071	0.0095	0.0040	6.0E-17	69	0.42	11.8	2.2	2.2
866-01C	1.1	5.1	5.0	18.91	0.36	0.0182	0.0017	0.047	0.017	1.9E-17	27	0.14	9.6	9.3	9.3
866-01D	1.3	6.608	0.041	6.689	0.035	0.012137	0.000083	0.000212	0.000075	3.2E-15	99	22	12.445	0.078	0.17
866-01E	1.4	6.522	0.040	6.577	0.035	0.012089	0.000084	0.000128	0.000067	3.9E-15	99	28	12.284	0.075	0.17
866-01F	1.5	6.483	0.088	6.591	0.015	0.01212	0.00019	0.00032	0.00029	7.0E-16	99	4.9	12.21	0.17	0.22
866-01G	1.5	6.589	0.089	6.698	0.025	0.01208	0.00018	0.00032	0.00029	7.8E-16	99	5.5	12.41	0.17	0.23
866-01H	1.6	6.511	0.073	6.599	0.027	0.01207	0.00018	0.00025	0.00023	8.5E-16	99	6.0	12.26	0.14	0.20
866-01I	1.7	6.39	0.26	6.577	0.023	0.01231	0.00030	0.00061	0.00089	2.4E-16	97	1.6	12.03	0.50	0.52
866-01J	1.8	6.37	0.20	6.528	0.032	0.01201	0.00027	0.00050	0.00066	3.1E-16	98	2.1	11.99	0.37	0.40
866-01K	2.0	6.25	0.48	6.575	0.028	0.01202	0.00047	0.0011	0.0016	1.3E-16	95	0.93	11.76	0.90	0.91
866-01L	2.5	6.53	0.11	6.637	0.024	0.01218	0.00019	0.00032	0.00036	6.0E-16	99	4.2	12.30	0.20	0.25
866-01M	3.0	6.561	0.072	6.643	0.022	0.01210	0.00015	0.00024	0.00023	1.0E-15	99	7.0	12.36	0.14	0.20
866-01N	3.5	6.576	0.081	6.677	0.016	0.01213	0.00018	0.00031	0.00027	8.3E-16	99	5.8	12.38	0.15	0.21
866-01O	4.0	6.541	0.090	6.637	0.020	0.01203	0.00020	0.00030	0.00030	6.3E-16	99	4.4	12.32	0.17	0.23
866-01P	5.0	6.51	0.11	6.610	0.027	0.01215	0.00022	0.00029	0.00037	5.9E-16	99	4.1	12.27	0.21	0.26
866-01Q	6.0	6.37	0.32	6.637	0.029	0.01197	0.00043	0.0010	0.0011	1.7E-16	96	1.2	11.99	0.60	0.61
866-01R	8.0	6.366	0.368	6.659	0.028	0.01231	0.00044	0.0011	0.0012	1.5E-16	96	1.1	11.99	0.69	0.71
866-01S	10.0	6.11	0.64	6.648	0.039	0.01294	0.00064	0.0018	0.0021	9.0E-17	92	0.63	11.5	1.2	1.2
SGM-2															
866-02A	1.1	11.59	10.77	125.0	2.0	0.082	0.013	0.384	0.037	2.0E-17	9	0.16	22	20	20
866-02B	1.2	6.27	0.59	7.775	0.074	0.0124	0.0027	0.0050	0.0020	1.1E-16	81	0.84	11.8	1.1	1.1
866-02C	1.2	6.41	0.19	6.724	0.035	0.0114	0.0013	0.00102	0.00063	3.5E-16	96	2.7	12.07	0.36	0.39
866-02D	1.3	6.569	0.073	6.687	0.025	0.01211	0.00022	0.00034	0.00023	9.6E-16	99	7.5	12.37	0.14	0.20
866-02E	1.3	6.536	0.048	6.616	0.014	0.01217	0.00013	0.00021	0.00015	1.5E-15	99	12	12.309	0.090	0.18
866-02F	1.3	6.546	0.044	6.607	0.034	0.01215	0.00010	0.00015	0.00010	3.3E-15	99	26	12.328	0.084	0.17
866-02G	1.4	6.461	0.062	6.545	0.020	0.01204	0.00019	0.00023	0.00020	9.0E-16	99	7.0	12.17	0.12	0.19
866-02H	1.4	6.575	0.061	6.653	0.035	0.01212	0.00016	0.00020	0.00017	1.6E-15	99	13	12.38	0.11	0.19
866-02I	1.4	6.27	0.44	6.530	0.037	0.01205	0.00043	0.0008	0.0015	1.6E-16	96	1.3	11.81	0.83	0.84
866-02J	1.5	6.48	0.21	6.638	0.027	0.01242	0.00034	0.00047	0.00070	2.7E-16	98	2.1	12.21	0.39	0.42
866-02K	2.0	6.523	0.058	6.595	0.014	0.01212	0.00016	0.00019	0.00019	1.2E-15	99	9.7	12.29	0.11	0.19
866-02L	3.0	6.541	0.056	6.611	0.015	0.01227	0.00018	0.00019	0.00018	1.2E-15	99	9.6	12.32	0.11	0.18
866-02M	4.0	6.46	0.16	6.666	0.020	0.01197	0.00029	0.00068	0.00055	4.2E-16	97	3.3	12.17	0.31	0.34
866-02N	6.0	6.32	0.23	6.541	0.034	0.01236	0.00032	0.00071	0.00078	3.6E-16	97	2.8	11.91	0.44	0.46
866-02O	10.0	6.43	0.21	6.589	0.029	0.01233	0.00039	0.00049	0.00070	3.0E-16	98	2.3	12.12	0.39	0.42
SGM-3															
866-03A	1.1	6.73	0.44	10.169	0.033	0.01473	0.00035	0.0116	0.0015	2.6E-16	66	2.6	12.66	0.83	0.85
866-03B	1.2	6.639	0.042	6.727	0.015	0.01231	0.00017	0.00024	0.00013	1.5E-15	99	15	12.502	0.078	0.17
866-03C	1.2	6.634	0.049	6.704	0.014	0.01213	0.00015	0.00017	0.00016	1.5E-15	99	15	12.494	0.091	0.18
866-03D	1.3	6.630	0.042	6.698	0.015	0.01206	0.00014	0.00017	0.00013	1.6E-15	99	16	12.486	0.078	0.17
866-03E	1.3	6.55	0.16	6.681	0.018	0.01252	0.00025	0.00038	0.00054	4.4E-16	98	4.4	12.34	0.30	0.34

866-03F	1.3	6.534	0.090	6.635	0.018	0.01191	0.00021	0.00028	0.00030	6.7E-16	99	6.8	12.31	0.17	0.23
866-03G	1.3	6.56	0.10	6.685	0.019	0.01222	0.00025	0.00035	0.00033	5.9E-16	98	5.9	12.35	0.19	0.24
866-03H	1.4	6.30	0.42	6.646	0.036	0.01251	0.00047	0.0011	0.0014	1.5E-16	95	1.5	11.87	0.79	0.81
866-03I	1.4	6.37	0.31	6.688	0.028	0.01192	0.00048	0.0010	0.0011	1.8E-16	96	1.8	12.00	0.59	0.61
866-03J	1.5	6.57	0.10	6.661	0.019	0.01216	0.00021	0.00026	0.00032	6.6E-16	99	6.6	12.37	0.18	0.24
866-03K	2.0	6.38	0.20	6.639	0.023	0.01223	0.00031	0.00082	0.00067	2.6E-16	96	2.6	12.02	0.37	0.40
866-03L	3.0	6.32	0.29	6.611	0.026	0.01188	0.00043	0.00093	0.00098	2.4E-16	96	2.4	11.90	0.55	0.57
866-03M	10.0	6.689	0.049	6.760	0.034	0.01234	0.00014	0.00019	0.00012	1.9E-15	99	19	12.60	0.09	0.18
SGM-4															
866-04A	1.1	6.57	0.11	6.965	0.017	0.01221	0.00023	0.00127	0.00036	9.0E-16	95	11	12.37	0.20	0.25
866-04B	1.2	6.723	0.048	6.828	0.037	0.01212	0.00013	0.00029	0.00010	2.3E-15	99	27	12.660	0.090	0.18
866-04C	1.2	6.37	0.22	6.560	0.025	0.01208	0.00034	0.00059	0.00075	2.9E-16	97	3.4	12.00	0.42	0.45
866-04D	1.3	6.50	0.17	6.660	0.022	0.01221	0.00029	0.00049	0.00057	3.7E-16	98	4.3	12.23	0.32	0.35
866-04E	1.3	6.07	0.67	6.619	0.043	0.01229	0.00068	0.0018	0.0023	9.1E-17	92	1.1	11.4	1.3	1.3
866-04F	1.3	6.51	0.14	6.655	0.020	0.01193	0.00026	0.00042	0.00046	4.5E-16	98	5.2	12.27	0.26	0.30
866-04G	1.3	6.56	0.13	6.694	0.021	0.01215	0.00028	0.00038	0.00043	4.9E-16	98	5.7	12.36	0.24	0.29
866-04H	1.4	5.4	1.6	6.724	0.089	0.0111	0.0014	0.0045	0.0055	3.3E-17	80	0.39	10.1	3.0	3.0
866-04I	1.4	5.2	2.0	6.69	0.10	0.0110	0.0013	0.0051	0.0068	3.3E-17	78	0.38	9.8	3.8	3.8
866-04J	1.5	6.37	0.34	6.686	0.029	0.01261	0.00041	0.0010	0.0012	1.9E-16	96	2.3	12.00	0.64	0.66
866-04K	2.0	6.42	0.26	6.648	0.025	0.01239	0.00040	0.00071	0.00089	2.3E-16	97	2.7	12.09	0.50	0.52
866-04L	3.0	6.49	0.16	6.661	0.021	0.01228	0.00027	0.00050	0.00053	4.0E-16	98	4.6	12.23	0.30	0.33
866-04M	6.5	6.675	0.049	6.740	0.014	0.01224	0.00014	0.00016	0.00016	1.4E-15	99	16	12.570	0.092	0.18
866-04N	10.0	6.636	0.062	6.858	0.015	0.01227	0.00014	0.00069	0.00020	1.4E-15	97	17	12.50	0.12	0.19

J value	2σ
0.001048	0.000013

REFERENCES

Andersen, T., 2002, Correction of common lead in U-Pb analyses that do not report Pb-204: Chemical Geology, v. 192, no. 1-2, p. 59-79, PII S0009-2541(02)00195-X, 10.1016/S0009-2541(02)00195-X.

Chew, D. M., Petrus, J. A., Kamber, B. S., 2014, U-Pb LA-ICPMS dating using accessory mineral standards with variable common Pb: Chemical Geology, v. 363, p. 185-199, 10.1016/j.chemgeo.2013.11.006.

Chihara, K., Komatsu, M., Mizota, T., 1974, A joaquinite-like mineral from Ohmi, Niigata Prefecture, Central Japan: Mineralogical Journal, v. 7, no. 4, p. 395-399.

Laird, J., Albee, A.L., 1972, Chemical composition and physical, optical, and structural properties of benitoite, neptunite, and joaquinite: American Mineralogist, v. 57, p. 85-102.

Long, S.P., McQuarrie, N., Tobgay, T., Coutand, I., Cooper, F.J., Reiners, P.W., Wartho, J.-A., Hodges, K.V., 2012, Variable shortening rates in the eastern Himalayan thrust belt, Bhutan: Insights from multiple thermochronologic and geochronologic data sets tied to kinematic reconstructions: Tectonics, p. 31, TC5004, 10.1029/2012TC003155.

Ludwig, K.R., 2008, User's manual for Isoplot 3.70: A geochronological toolkit for Microsoft Excel: Berkeley Geochronology Center, Special Publication 4.

Matsubara, S., Mandarino, J.A., Semenov, E.I., 2001, Redefinition of a mineral in the joaquinite group: Orthojoaquinite-(La): Canadian Mineralogist, v. 39, p. 757-760, 10.2113/gscanmin.39.3.757.

Paton, C, Hellstrom, J, Paul, B,Woodhead, J, Hergt, J, 2011, Iolite: freeware for the visualisation and processing of mass spectrometric data: Journal of Analytical Atomic Spectrometry, v. 26, no. 12, p. 2508-2518.

Pearce, N.J.G., Perkins, W.T., Westgate, J.A., Gorton, M.P., Jackson, S.E., Neal, C.R., Chenery, S.P., 1997, A compilation of new and published major and trace element data for NIST SRM 610 and NIST SRM 612 glass reference materials: Geostandards Newsletter-the Journal of Geostandards and Geoanalysis, v. 21, no. 1, p. 115-144, 10.1111/j.1751- 908X.1997.tb00538.x.

Schoene, B., Bowring, S.A., 2006, U-Pb systematics of the McClure Mountain syenite: thermochronological constraints on the age of the Ar-40/Ar-39 standard MMhb: Contributions to Mineralogy and Petrology, v. 151, no. 5, p. 615-630, 10.1007/s00410-006-0077-4.

Schwarz, W.H., Trieloff, M., 2007, Intercalibration of Ar-40-Ar-39 age standards NL-25, HB3gr hornblende, GA1550, SB-3, HD-B1 biotite and BMus/2 muscovite: Chemical Geology, v. 242, no. 1-2, p. 218-231, 10.1016/j.chemgeo.2007.03.016.

Steiger, R.H., Jager, E., 1977, Subcommission on geochronology - convention on use of decay constants in geochronology and cosmochronology: Earth and Planetary Science Letters, v. 36, no. 3, p. 359-362, 10.1016/0012-821X(77)90060-7.

Sun J.F., Yang J.H., Wu F.Y., Xie L.W., Yang Y.H., Liu Z.C., Li X.H., 2012, In situ U-Pb dating of titanite by LA-ICPMS: Chinese Science Bulletin, v. 57, no. 20, p. 2506-2516, 10.1007/s11434-012-5177-0.

Tsujimori, T., Liou, G. J., Coleman, R. G., 2007, Finding of high-grade tectonic blocks from the New Idria serpentinite body, Diablo Range, California: Petrologic constraints on the tectonic evolution of an active serpentinite diapir, *in* Cloos, M., Carlson, W. D., Gilbert, M. C., Liou, J. G. and Sorensen, S. S. (eds.) Convergent Margin Terranes and Associated Regions: A Tribute to W. G. Ernst: Geological Society of America, Special Papers 419, p. 67–80.

Woodhead, J.D., Hellstrom, J., Hergt, J.M., Greig, A., Maas, R., 2007, Isotopic and elemental imaging of geological materials by laser ablation inductively coupled plasma-mass spectrometry: Geostandards and Geoanalytical Research, v. 31, no. 4, p. 331-343.

Zadov, A. E., Gazeev, V. M., Karimova, O. V., Pertsev, N. N., Pekov, I. V., Galuskin, E. V., Galuskina, I. O., Gurbanov, A. G., Belakovsky, D. I., Borisovsky, S. E., Kartashov, P. M., Ivanova, A. G., Yakubovich, O. V., 2011, Magnesioneptunite, KNa2Li(Mg,Fe)(2)Ti2Si8O24, a new mineral species of the neptunite group: Geology of Ore Deposits, v. 53, no. 8, p. 775-782, 10.1134/S1075701511080186.

APPENIX C

CHAPTER 5 APPENDIX

ANALYTICAL METHODS

We employed laser ablation inductively coupled plasma source (ICPMS) methods for (U-Th)/Pb dating of detrital zircons, magmatic zircons, and joaquinite. Laser step heating methods were used for $^{40}Ar/^{39}Ar$ dating of glaucophane and neptunite. All geochronologic and thermochronologic analyses were conducted in the Group 18 Laboratories at Arizona State University.

In situ zircon U/Pb geochronology

Zircons found in a polished thick section of one of the meta-trondhjemite slices found along Fault 3 was dated using a Photon Machines *Analyte G3* instrument package – featuring an *Atlex 300* ArF excimer ultraviolet (193 nm) laser – for sampling and a Thermo Scientific *iCAP Q* quadrupole ICPMS for isotopic measurements. Owing to the small size of these zircons, ablation pits were 20 µm, power output was set to 50%, pulse frequency was 10 Hz, and grains were ablated for 30 s. Ablated material was then transferred into the plasma source of the *iCAP Q* using a mixed He + Ar carrier gas. For all, a plasma radiofrequency power of 1400 W was used. Prior to each unknown and standard analysis, a 20 s background run was done, and a 20 s washout followed each analysis. Measured isotopes were: ^{29}Si, ^{200}Hg, ^{202}Hg, ^{204}Pb, ^{206}Pb, ^{207}Pb, ^{208}Pb, ^{232}Th, and ^{238}U. SL zircon (563.5 ± 3.2 Ma, Gehrels et al., 2008), my primary standard for this work, was run after every three unknowns. The resulting data were reduced in *Iolite* (Paton et al., 2011) using the VizualAge_UcomPbine scheme (Chew et al., 2014) and plotted using Isoplot (Ludwig, 2008). Errors for isotopic measurements and apparent ages are quoted here at the 2σ confidence level and reflect the propagation of analytical imprecision.

Detrital zircon U/Pb geochronology

Detrital zircons – hand picked from heavy mineral separates, mounted in epoxy, and polished – were also dated by laser ablation ICPMS. For these analyses, the *Atlex 300* laser was operated with 5 mJ of laser energy at 100% output power and a pulse frequency of 5 Hz for a total of 40 s. The beam aperture was set such that the resulting ablation pits were roughly 35 µm in diameter. Isotopic analyses were done the same was as for the in situ zircon studies, with Plešovice zircon (337.1 ± 0.2 Ma; Slama et al., 2008) and SL zircon (563.5 ± 3.2 Ma;, Gehrels et al., 2008) were used as primary and secondary standards. Primary standards were run every five unknowns, and secondary standards were run every ten unknowns. Data reduction and presentation procedures for these analyses were the same as for the *in situ* data.

Joaquinite (U-Th)/Pb geochronology

Also using the *Analyte G3* laser, I ablated 50 µm pits for (U-Th)/Pb geochronology of epoxy-mounted joaquinite crystals. This was accomplished by applying 5 mJ laser energy at 100% output power and a pulse frequency of 5 Hz for a total of 50 s. Isotopic measurements of the ablated material followed closely those used for the detrital zircon analyses except that, given the rarity of joaquinite, there is no available matrix-matched isotopic standard for it and I were forced to standardize with another mineral. I elected to use BLR-1 titanite (1046 ± 5 Ma; Sun et al., 2012) as my primary standard, and MMT titanite from the McClure Mountain syenite (523.98 ± 0.12 Ma; Schoene and Bowring, 2006) as my secondary standard. Four primary standard analyses were performed at the beginning and end of the run, and an additional analysis

were run after every three unknowns. Two MMT analyses were performed along with every group of BLR-1 analyses.

$^{40}Ar/^{39}Ar$ geochronology

Argon isotopic studies focused on multigrain aliquots of glaucophane and ca. 0.25-0.5 mm neptunite crystals. These analyses were performed on neutron-irradiated samples using a Nu Instruments *Noblesse* magnetic-sector mass spectrometer. Appropriately cleaned samples were wrapped in Al foil and packaged in Al planchettes for neutron irradiation in the Oregon State University TRIGA reactor using Cd shielding. The irradiation package also contained standard HD-B1 (24.18 ± 0.18 Ma; Schwarz and Trieloff, 2007) as an irradiation monitor, as well as synthetic Ca and K salts to permit corrections for interfering isotopic reactions. Gasses were liberated for analysis in an ultrahigh-vacuum extraction line using a Photon Machines *Fusions* CO_2 infrared (10.6 μm) laser operated incrementally at successively higher power levels until the sample was fused. Gasses were purified after each stepwise heating increment using metal alloy sponges (getters) and admitted to the Noblesse for isotopic measurements. . The largest isotope (^{40}Ar) was measured using a $1x10^{11}$ Ohm Faraday detector or an ion counting multiplier, depending on signal size. All other argon isotopes (^{39}Ar, ^{38}Ar, ^{37}Ar, and ^{36}Ar) as well as backgrounds were measured on an ion-counting multiplier by peak jumping. Detector intercalibration for samples that required Faraday measurement of ^{40}Ar was performed using multiple air shots. Average background values (as measured by ion counting) were 42600, 1873.8, 64.7, 766.1, and 265.6 c.p.s for ^{40}Ar, ^{39}Ar, ^{38}Ar, ^{37}Ar, and ^{36}Ar, respectively. The average mass discrimination factor was 0.99503 ± 0.00023 per amu. The $^{40}Ar/^{39}Ar$ analytical process was

automated and the resulting data reduced using the *Mass Spec* software written by A. Deino and *Isoplot* software written by K. Ludwig (Ludwig, 2008). Further details of the methods used at Arizona State University can be found in Long et al. (2012). All $^{40}Ar/^{39}Ar$ apparent ages reported here were calculated using the decay constant, branching ratio, and atmospheric $^{40}Ar/^{36}Ar$ ratio recommended by Steiger and Jäger (1977).

Table C1: U, Th, Pb, and date data for zircon samples 254 and 234

	ppm			Isotopic ratios							Dates in Ma					
	Th	Pb	U/Th	207Pb/ 235U	2σ	206Pb/ 238U	2σ	Corr.	207Pb/ 206Pb	2σ	207Pb/ 235U	2σ	206Pb/ 238U	2σ	207Pb/ 206Pb	2σ
254-1a	502	63	1.68	0.134	0.019	0.01677	0.00061	0.99	0.0612	0.0091	127	17	107.2	3.9	520	300
254-1b	130	23	2.957	0.17	0.044	0.01743	0.00088	0.37	0.073	0.019	155	37	111.4	5.6	700	510
254-1c	196	26	2.015	0.141	0.029	0.018	0.00081	0.04	0.058	0.012	131	25	115	5.1	290	380
254-2	180	34	2.81	0.124	0.019	0.01754	0.0012	0.34	0.0496	0.006	118	17	112.1	7.4	500	150
254-3	622	103	1.88	0.238	0.03	0.01741	0.00099	0.37	0.098	0.011	211	24	111.2	6.2	1440	180
254-4	2600	147	0.431	0.605	0.053	0.01827	0.0012	0.08	0.242	0.018	476	34	116.7	7.4	3137	92
234-1	99	194	0.01	2.6	0.2	0.2135	0.0039	0.94	0.0859	0.0039	1255	34	1246	21	1267	61
234-2	16	117	0.039	5.692	0.097	0.1508	0.0018	0.46	0.2738	0.0048	1925	15	905	10	3319	28
234-3	222	147	0.011	0.597	0.016	0.07425	0.00092	1.00	0.058	0.0013	473	10	462.4	5.3	509	49
234-4	812	106	0.014	0.1074	0.0076	0.01471	0.00035	0.99	0.0526	0.0028	102.8	6.8	94.1	2.2	270	100
234-5	38	68	0.032	2.35	0.054	0.2136	0.0026	0.99	0.080	0.0017	1222	16	1247	14	1169	43
234-6	234	555	0.029	3.90	0.062	0.2935	0.0034	0.99	0.09607	0.00081	1612	13	1658	17	1545	16
234-7	102	193	0.26	2.814	0.048	0.241	0.0034	0.97	0.08447	0.00095	1359	12	1391	17	1296	22
234-8	334	83	0.2	0.1873	0.0044	0.02508	0.00027	0.91	0.0542	0.0011	174	3.8	159.6	1.7	362	46
234-9	107	191	0.021	2.278	0.035	0.211	0.0023	1.00	0.0785	0.00092	1203	11	1233	12	1152	23
234-10	71	67	0.033	0.86	0.021	0.1041	0.0012	0.90	0.0602	0.0012	627	12	638.2	7.2	584	45
234-11	78	49	0.081	0.5291	0.0096	0.06779	0.0008	0.70	0.05678	0.00092	431.1	6.5	422.8	4.8	475	35
234-12	41	9	0.054	0.18	0.011	0.0259	0.00052	0.43	0.0508	0.0031	166	9.2	164.8	3.3	180	110
234-13	134	54	0.22	0.315	0.015	0.0375	0.0014	0.95	0.0602	0.0013	275	12	236.8	8.4	587	48
234-14	148	214	0.072	1.837	0.03	0.1765	0.0019	0.62	0.07551	0.0009	1057	11	1048	11	1081	25
234-15	324	422	0.014	1.565	0.031	0.1578	0.0023	0.80	0.0725	0.0011	956	12	944	13	990	32
234-16	251	76	0.032	0.2134	0.0052	0.03123	0.00035	0.99	0.0495	0.001	196.5	4.3	198.3	2.2	172	43
234-17	65	221	0.027	8.72	0.18	0.3707	0.007	0.30	0.1706	0.0016	2300	19	2029	33	2560	15
234-18	135	219	0.012	2.101	0.048	0.2029	0.0033	0.35	0.0752	0.0013	1145	16	1190	17	1065	34
234-19	111	333	0.06	6.41	0.058	0.3768	0.0027	0.81	0.12324	0.00059	2032.1	8.2	2061	13	2002.5	8.5
234-20	57	72	0.031	1.542	0.036	0.1555	0.0022	0.98	0.0717	0.0015	944	14	931	12	958	42
234-21	49	47	0.018	1.227	0.049	0.1218	0.0026	0.98	0.0737	0.0028	804	22	740	15	959	77
234-22	96	219	0.038	4.164	0.076	0.2535	0.0028	1.00	0.1188	0.0011	1664	15	1456	15	1933	17
234-23	122	345	0.025	6.058	0.079	0.3564	0.0033	0.98	0.1228	0.00093	1981	12	1966	16	1994	14
234-24	223	36	0.048	0.194	0.011	0.01915	0.00057	0.69	0.0732	0.0034	177.9	9.4	122.2	3.6	902	93
234-25	121	211	0.014	2.235	0.041	0.2033	0.002	0.64	0.0796	0.0012	1188	13	1194	11	1174	29
234-26	219	79	0.057	0.3113	0.0095	0.04103	0.00053	0.96	0.0552	0.0016	274	7.3	259.2	3.3	383	60
234-27	682	193	0.087	0.2735	0.0041	0.0352	0.00041	0.45	0.05664	0.00098	245.3	3.3	223	2.6	459	38
234-28	11	9	4	0.752	0.011	0.09194	0.00071	0.78	0.05933	0.00069	568.5	6.3	566.9	4.2	570	26
234-29	289	1002	0.057	8.99	0.15	0.4432	0.0052	0.13	0.1467	0.001	2337	15	2363	23	2309	12

Table C1: U, Th, Pb, and date data for zircon samples 254 and 234

	ppm			Isotopic ratios							Dates in Ma					
	Th	Pb	U/Th	207Pb/ 235U	2σ	206Pb/ 238U	2σ	Corr.	207Pb/ 206Pb	2σ	207Pb/ 235U	2σ	206Pb/ 238U	2σ	207Pb/ 206Pb	2σ
234-30	109	93	0.0094	1.512	0.087	0.1305	0.0035	0.95	0.0825	0.0036	913	35	789	20	1167	90
234-31	123	341	0.15	5.01	0.15	0.3157	0.003	0.67	0.1142	0.0022	1802	15	1768	15	1842	21
234-32	68	131	0.019	3.89	0.20	0.2047	0.0045	0.99	0.1352	0.0053	1582	39	1198	24	2137	70
234-33	61	45	0.081	0.737	0.054	0.0334	0.001	0.96	0.1561	0.0089	546	31	211.9	6.3	2260	110
234-34	137	301	0.046	4.542	0.086	0.3159	0.0046	0.75	0.1044	0.0011	1735	16	1768	23	1698	19
234-35	587	80	0.017	0.1061	0.0039	0.0155	0.0002	0.98	0.0503	0.0019	102.6	3.7	99.2	1.3	184	73
234-36	227	424	0.025	2.429	0.046	0.205	0.0023	0.97	0.086	0.0011	1248	13	1201	12	1330	23
234-37	339	50	0.031	0.1126	0.0052	0.01527	0.00025	0.99	0.0546	0.0026	107.9	4.7	97.7	1.6	330	94
234-38	40	55	0.038	1.540	0.044	0.1633	0.0025	0.97	0.0684	0.0017	942	17	975	14	840	55
234-39	93	166	0.013	2.314	0.048	0.2102	0.0029	0.98	0.08	0.0012	1215	14	1229	15	1185	29
234-40	176	199	0.18	1.202	0.024	0.1235	0.002	0.96	0.06976	0.00087	800	11	750	11	914	25
234-41	550	169	0.035	0.2492	0.0061	0.03541	0.00049	0.90	0.05136	0.00099	225.4	5	224.6	3	243	40
234-42	231	125	0.01	0.456	0.016	0.05935	0.00074	0.97	0.0549	0.0019	380	11	371.6	4.5	375	72
234-43	187	268	0.11	1.776	0.034	0.1756	0.0024	0.96	0.07336	0.00082	1033	12	1043	13	1019	22
234-44	101	161	0.014	2.187	0.046	0.2008	0.0026	0.98	0.0793	0.0014	1175	15	1181	14	1165	35
234-45	249	371	0.15	1.544	0.022	0.1387	0.0017	0.69	0.07944	0.0009	947.2	9	837.3	9.6	1179	23
234-46	145	27	0.0092	0.1576	0.0086	0.01964	0.0003	0.99	0.0573	0.003	147.4	7.5	125.3	1.9	450	110
234-47	588	1000	0.074	16.84	0.41	0.466	0.012	0.98	0.2616	0.0014	2913	24	2457	53	3255.2	8.6
234-48	279	736	0.023	5.62	0.065	0.3307	0.0025	0.19	0.12278	0.0008	1917	10	1841	12	1996	11
234-49	221	817	0.074	11.6	0.29	0.462	0.01	0.99	0.1809	0.0012	2562	26	2448	44	2659	11
234-50	433	51	0.011	0.0854	0.0033	0.01285	0.00021	0.97	0.0486	0.0019	83	3.1	82.3	1.3	129	75
234-51	79	191	0.015	4.487	0.081	0.3047	0.0044	0.41	0.1065	0.0014	1723	15	1713	22	1732	24
234-52	125	319	0.093	4.97	0.11	0.3337	0.0064	0.91	0.1075	0.0011	1811	20	1853	31	1752	18
234-53	124	431	0.009	9.65	0.17	0.4325	0.006	0.45	0.1609	0.0021	2398	16	2315	27	2457	22
234-54	136	219	0.018	2.092	0.04	0.1916	0.0024	0.44	0.079	0.0012	1144	13	1129	13	1162	31
234-55	69	102	0.083	1.265	0.066	0.1164	0.0015	0.61	0.0775	0.0032	817	27	709.7	8.9	1091	74
234-56	255	391	0.021	1.848	0.039	0.1788	0.0025	0.92	0.07449	0.00071	1059	13	1060	14	1052	20
234-57	776	108	0.043	0.1166	0.005	0.01666	0.00053	0.97	0.0501	0.0013	111.5	4.5	106.5	3.4	192	55
234-58	181	245	0.39	1.609	0.022	0.161	0.0015	0.32	0.07206	0.00062	972.1	8.8	962.4	8.5	987	18
234-59	154	358	0.43	4.926	0.088	0.3233	0.0037	0.98	0.10984	0.00081	1803	15	1805	18	1794	13
234-60	68	116	0.048	2.337	0.067	0.1882	0.0043	0.99	0.09	0.0017	1216	21	1110	23	1415	36
234-61	157	229	0.014	1.84	0.039	0.1689	0.0023	0.98	0.0788	0.0015	1056	14	1006	12	1149	39
234-62	330	45	0.026	0.219	0.012	0.02176	0.0008	0.57	0.0725	0.0026	199	10	138.7	5.1	921	77
234-63	300	267	0.024	0.945	0.016	0.1065	0.0011	0.76	0.06384	0.00097	673.6	8.6	652.4	6.2	725	32
234-64	142	107	0.027	0.783	0.02	0.092	0.0012	0.99	0.0616	0.0016	584	12	567.4	7.3	623	54
234-65	196	305	0.087	4.37	0.1	0.2863	0.0056	0.41	0.1102	0.001	1702	20	1620	28	1799	17

Table C1: U, Th, Pb, and date data for zircon samples 254 and 234

	ppm			Isotopic ratios							Dates in Ma					
	Th	Pb	U/Th	207Pb/ 235U	2σ	206Pb/ 238U	2σ	Corr.	207Pb/ 206Pb	2σ	207Pb/ 235U	2σ	206Pb/ 238U	2σ	207Pb/ 206Pb	2σ
234-66	184	449	0.018	4.404	0.069	0.3004	0.0036	0.95	0.10544	0.00098	1709	13	1692	18	1720	17
234-67	596	421	0.018	0.6165	0.0088	0.0757	0.00074	0.35	0.05893	0.00069	487	5.5	470.3	4.4	559	26
234-68	160	25	0.03	0.1302	0.0068	0.01745	0.00037	0.72	0.0548	0.0029	123.5	6	111.5	2.3	340	100
234-69	315	390	0.03	1.510	0.022	0.15	0.0013	0.61	0.07252	0.00079	933.8	8.9	900.7	7	993	23
234-70	389	850	0.031	4.168	0.056	0.2866	0.0029	0.97	0.10469	0.00092	1665	11	1624	15	1705	16
234-71	701	187	0.03	0.2181	0.0061	0.0319	0.00055	0.66	0.0496	0.0011	199.7	5	202.4	3.5	169	45
234-72	242	213	0.0088	0.912	0.020	0.1039	0.0011	0.97	0.0636	0.0012	657	11	636.8	6.5	715	39
234-73	180	144	0.032	0.746	0.020	0.0927	0.0013	0.92	0.0582	0.0013	564	12	571.5	7.9	509	48
234-74	199	111	0.026	0.518	0.015	0.0677	0.001	0.67	0.0553	0.0014	421.6	9.9	421.9	6.2	397	53
234-75	123	43	0.028	0.2725	0.0091	0.0387	0.00063	0.98	0.0508	0.0015	243.5	7.2	244.7	3.9	226	60
234-76	60	157	0.13	4.865	0.091	0.3237	0.0049	0.26	0.1086	0.0012	1796	15	1808	23	1773	20
234-77	74	126	0.014	2.247	0.074	0.1931	0.003	0.66	0.084	0.0021	1190	23	1137	16	1267	47
234-78	350	42	0.01	0.0945	0.0045	0.01405	0.00028	0.99	0.0495	0.0023	91.3	4.2	90	1.8	157	90
234-79	123	146	0.17	1.114	0.032	0.1207	0.0025	0.96	0.06586	0.00087	755	15	734	14	802	29
234-80	238	104	0.028	0.373	0.015	0.0518	0.0012	0.96	0.0524	0.0018	319	11	325.6	7.2	273	71
234-81	574	423	0.026	0.665	0.014	0.08088	0.00098	0.96	0.05943	0.00082	515.9	8.2	501.2	5.8	571	30
234-82	403	114	0.011	0.2227	0.0051	0.03174	0.0003	0.98	0.051	0.0012	203.8	4.3	201.4	1.9	225	49
234-83	292	189	0.043	0.657	0.018	0.0841	0.0014	0.73	0.0564	0.0012	510	11	520.2	8.2	453	46
234-84	127	160	0.048	1.415	0.025	0.1434	0.0015	0.41	0.07141	0.00095	893	10	863.4	8.3	958	27
234-85	262	641	0.048	6.303	0.099	0.3299	0.0038	0.67	0.1383	0.0011	2016	14	1837	18	2204	13
234-86	141	205	0.018	1.698	0.046	0.1645	0.0024	0.63	0.0749	0.0014	1005	18	983	13	1050	36
234-87	102	64	0.022	0.546	0.017	0.06869	0.00084	0.98	0.0578	0.0017	440	11	428.2	5.1	490	65
234-88	89	133	0.39	1.834	0.035	0.1776	0.0026	0.97	0.07458	0.00065	1056	13	1053	14	1053	18
234-89	73	116	0.016	2.015	0.043	0.1906	0.0023	1.00	0.0765	0.0013	1116	15	1125	12	1099	36
234-90	105	49	0.14	0.364	0.012	0.05069	0.00071	0.89	0.0521	0.0016	314.2	9.2	318.7	4.4	267	64
234-91	345	143	0.04	0.3531	0.0095	0.04831	0.00062	0.96	0.0532	0.0014	306	7	304.1	3.8	312	53
234-92	408	79	0.14	0.1645	0.008	0.02095	0.00021	0.07	0.056	0.0024	153.6	6.8	133.6	1.3	403	85
234-93	183	254	0.042	1.614	0.036	0.1619	0.0022	0.43	0.07254	0.00093	976	14	967	13	991	26
234-94	225	368	0.0089	2.051	0.036	0.1935	0.0023	0.45	0.077	0.0011	1131	12	1140	12	1108	28
234-95	84	101	0.018	1.405	0.055	0.1491	0.0025	0.62	0.0687	0.0024	885	23	895	14	860	74
234-96	752	718	0.048	0.943	0.035	0.1	0.0016	0.38	0.0686	0.0021	662	15	613.9	9.6	824	38
234-97	139	79	0.019	0.48	0.017	0.064	0.001	0.97	0.0545	0.0017	395	11	399.5	6.3	351	67
234-98	129	137	0.044	0.942	0.025	0.1032	0.0015	0.98	0.0661	0.0015	670	13	633.1	9	789	48
234-99	173	25	0.023	0.1105	0.006	0.01652	0.00027	1.00	0.0485	0.0027	105.7	5.5	105.6	1.7	120	100
234-100	262	592	0.0083	3.618	0.053	0.2662	0.0023	0.99	0.0984	0.0012	1553	12	1521	12	1586	22
234-101	216	333	0.0065	1.968	0.034	0.1822	0.0018	0.96	0.0785	0.0013	1102	12	1078	10	1144	31

Table C1: U, Th, Pb, and date data for zircon samples 254 and 234

	ppm			Isotopic ratios							Dates in Ma					
	Th	Pb	U/Th	207Pb/ 235U	2σ	206Pb/ 238U	2σ	Corr.	207Pb/ 206Pb	2σ	207Pb/ 235U	2σ	206Pb/ 238U	2σ	207Pb/ 206Pb	2σ
234-102	276	618	0.013	3.23	0.100	0.247	0.0043	0.17	0.0941	0.0016	1452	23	1421	22	1497	30
234-103	109	194	0.11	1.843	0.044	0.1722	0.0029	0.99	0.0773	0.0011	1055	16	1023	16	1122	28
234-104	133	112	0.11	0.587	0.018	0.0728	0.0014	0.95	0.0585	0.0011	467	12	452.5	8.7	529	42
234-105	160	26	0.025	0.1142	0.0055	0.01657	0.00027	0.46	0.0499	0.0024	109.2	5	105.9	1.7	170	91
234-106	322	737	0.014	3.598	0.058	0.2714	0.0034	0.82	0.0963	0.0007	1547	13	1547	17	1551	14
234-107	27	5	0.064	0.143	0.013	0.01723	0.00053	0.56	0.0619	0.0057	137	12	110.1	3.3	450	170
234-108	1372	296	0.072	0.1791	0.0083	0.02123	0.00035	0.65	0.06	0.0023	166.2	7	135.4	2.2	543	78
234-109	89	236	0.011	4.803	0.091	0.3129	0.0041	0.37	0.1101	0.0016	1783	16	1754	20	1795	28
234-110	149	36	0.039	0.1868	0.009	0.02429	0.00037	0.58	0.0555	0.0025	172.6	7.6	154.7	2.3	359	90
234-111	502	110	0.043	0.338	0.036	0.02182	0.00062	0.05	0.1048	0.0088	289	27	139.1	3.9	1400	150
234-112	65	105	0.27	1.746	0.057	0.1647	0.0037	0.96	0.0766	0.0015	1018	22	981	21	1088	40
234-113	216	336	0.016	2.056	0.041	0.1896	0.0026	0.13	0.0786	0.001	1134	14	1120	14	1152	25
234-114	274	422	0.009	2.07	0.034	0.1934	0.0018	0.99	0.078	0.0012	1136	11	1139.3	9.9	1133	30
234-115	706	234	0.018	0.2643	0.0078	0.0323	0.00035	0.96	0.0584	0.0012	237.3	6.3	204.9	2.2	527	47
234-116	343	72	0.014	0.1613	0.0059	0.02344	0.00034	0.35	0.0495	0.0017	151.2	5.1	149.3	2.1	169	68
234-117	142	18	0.015	0.0925	0.0065	0.01272	0.00025	0.88	0.053	0.0037	89	6	81.5	1.6	230	130
234-118	271	607	0.013	3.589	0.071	0.2614	0.004	0.66	0.0992	0.0012	1542	16	1495	20	1604	23
234-119	304	231	0.016	0.691	0.013	0.08492	0.00085	0.97	0.05917	0.00093	532.3	7.8	525.3	5.1	557	35
234-120	274	33	0.011	0.0866	0.0049	0.01317	0.0002	0.99	0.0474	0.0026	83.9	4.5	84.4	1.3	80	100
234-121	41	199	0.028	27.09	0.41	0.6592	0.0081	0.98	0.2968	0.002	3383	15	3261	32	3452	10
234-122	71	62	0.035	0.812	0.031	0.1002	0.0026	0.98	0.0582	0.0017	599	17	615	15	505	62
234-123	670	207	0.068	0.238	0.0056	0.03222	0.00039	0.02	0.0536	0.0012	216.8	4.7	204.4	2.5	338	48
234-124	67	106	0.0062	1.975	0.058	0.184	0.0028	0.45	0.078	0.0023	1098	20	1088	15	1094	60
234-125	121	604	0.016	24.59	0.48	0.676	0.011	0.88	0.2621	0.0014	3295	20	3323	45	3258	8.7
234-126	298	109	0.056	0.2861	0.0063	0.03871	0.00055	0.84	0.0535	0.001	254.9	5	244.8	3.4	333	42
234-127	175	139	0.0043	0.757	0.035	0.0912	0.0016	0.46	0.0602	0.0026	564	20	563.3	9.7	522	88
234-128	135	171	0.045	1.545	0.044	0.1545	0.0033	0.59	0.0721	0.001	941	18	925	19	981	28
234-129	1457	407	0.012	0.2219	0.004	0.03203	0.00041	0.94	0.05021	0.00062	203.2	3.3	203.2	2.6	202	28
234-130	315	584	0.025	2.953	0.035	0.2351	0.0019	0.60	0.09104	0.00059	1396	8.6	1361	10	1445	12
234-131	188	374	0.077	3.569	0.071	0.2593	0.0028	0.99	0.0988	0.0014	1541	15	1486	14	1604	27
234-132	317	125	0.012	0.401	0.045	0.03551	0.00068	0.94	0.0808	0.0078	327	30	224.9	4.2	930	160
234-133	799	586	0.02	0.693	0.011	0.08681	0.00093	0.68	0.0577	0.00055	533.3	6.9	536.5	5.5	514	21
234-134	72	253	0.069	9.34	0.13	0.4197	0.0043	0.11	0.1612	0.0014	2368	13	2258	19	2465	14
234-135	625	186	0.013	0.316	0.035	0.02226	0.00037	0.97	0.0967	0.0091	264	25	142.2	2.4	1140	160
234-136	206	637	0.007	6.935	0.082	0.3705	0.0031	0.62	0.1347	0.0012	2102	10	2031	14	2156	16
234-137	768	206	0.092	0.2419	0.0046	0.03485	0.00039	0.99	0.05038	0.00069	219.6	3.8	220.8	2.4	206	30

Table C1: U, Th, Pb, and date data for zircon samples 254 and 234

	ppm			Isotopic ratios							Dates in Ma					
	Th	Pb	U/Th	207Pb/ 235U	2σ	206Pb/ 238U	2σ	Corr.	207Pb/ 206Pb	2σ	207Pb/ 235U	2σ	206Pb/ 238U	2σ	207Pb/ 206Pb	2σ
234-138	89	20	0.023	0.1764	0.0083	0.02352	0.00042	0.92	0.0546	0.0027	163.8	7.2	149.9	2.7	330	98
234-139	186	58	0.026	0.324	0.028	0.038	0.0025	0.03	0.0584	0.0027	275	21	240	15	479	93
234-140	57	207	0.023	10.47	0.16	0.4562	0.0049	0.50	0.1662	0.0018	2475	14	2426	23	2515	18
234-141	656	688	0.018	1.06	0.019	0.1195	0.0015	0.96	0.06395	0.00076	733.1	9.3	727.3	8.4	734	26
234-142	92	138	0.014	1.944	0.051	0.1834	0.0024	0.46	0.0775	0.0018	1094	18	1085	13	1106	48
234-143	189	252	0.03	1.505	0.029	0.1566	0.0021	0.98	0.06978	0.00099	929	12	938	12	912	30
234-144	107	760	0.023	7.8	1.2	0.2001	0.0099	0.95	0.228	0.024	1820	130	1167	51	2520	190
234-145	64	9	0.04	0.1035	0.0092	0.01659	0.00036	0.64	0.0466	0.0045	98.5	8.4	106	2.3	-30	150
234-146	157	136	0.012	0.822	0.02	0.1005	0.0015	0.40	0.05948	0.00097	609	11	618.3	8.8	572	35
234-147	114	95	0.019	0.838	0.021	0.1006	0.0014	0.44	0.0608	0.0013	615	12	617.6	8.1	611	47
234-148	663	269	0.021	1.3	0.13	0.067	0.0058	0.96	0.125	0.0042	759	62	413	35	1964	68
234-149	342	52	0.012	0.1206	0.004	0.0171	0.00018	0.26	0.0511	0.0016	115.3	3.6	109.3	1.1	222	63
234-150	10	40	0.27	3.9	0.16	0.1145	0.0025	0.20	0.249	0.01	1586	35	698	15	3114	67
234-151	77	219	0.014	6.00	0.11	0.3534	0.0046	0.99	0.1232	0.0013	1971	16	1949	22	2000	19
234-152	15	11	0.74	0.743	0.015	0.09086	0.00087	0.92	0.0595	0.0012	562.7	8.6	560.5	5.1	567	43
234-153	74	145	0.036	2.895	0.055	0.2394	0.0029	0.98	0.0879	0.0014	1378	14	1383	15	1365	32
234-154	174	43	0.017	0.293	0.033	0.01562	0.00042	0.47	0.126	0.012	247	25	99.9	2.7	1570	190
234-155	676	130	0.014	0.147	0.0034	0.02165	0.00027	1.00	0.04923	0.00094	139.1	3	138.1	1.7	158	40
234-156	141	331	0.073	3.63	0.046	0.2698	0.0029	0.20	0.09764	0.00083	1555	10	1539	15	1578	16
234-157	414	394	0.011	0.937	0.014	0.1076	0.001	0.98	0.06314	0.00066	672.7	7.4	658.9	6	711	22
234-158	57	210	0.25	11.87	0.17	0.4074	0.0054	0.78	0.2115	0.0018	2592	14	2201	25	2915	14
234-159	343	330	0.0053	0.985	0.019	0.1109	0.0011	0.43	0.0644	0.0011	694.1	9.8	677.8	6.3	747	35
234-160	358	45	0.049	0.1061	0.0086	0.01273	0.00021	0.99	0.0598	0.0042	101.1	7.6	81.6	1.4	490	130
234-161	147	273	0.013	2.979	0.066	0.2361	0.0041	1.00	0.0913	0.0014	1396	17	1365	21	1441	29
234-162	156	49	0.025	0.361	0.018	0.0406	0.0012	0.34	0.0646	0.0025	309	13	256.7	7.2	688	85
234-163	226	45	0.035	0.1568	0.0054	0.02245	0.00043	0.99	0.0505	0.0015	147.4	4.7	143.1	2.7	218	64
234-164	190	324	0.028	2.304	0.043	0.2016	0.002	0.58	0.0828	0.001	1210	13	1183	11	1256	24
234-165	280	35	0.015	0.1179	0.0093	0.01413	0.00029	0.05	0.0597	0.004	113	8.4	90.4	1.9	520	130
234-166	165	34	0.014	0.1618	0.0079	0.02318	0.00036	0.99	0.051	0.0026	151.3	6.9	147.7	2.3	200	99
234-167	135	105	0.088	2.134	0.039	0.1882	0.0024	1.00	0.0826	0.0011	1156	13	1111	13	1252	27
234-168	273	31	0.0094	0.0868	0.005	0.01325	0.00023	0.73	0.0482	0.0027	84.6	4.7	84.8	1.5	110	100
234-169	123	108	0.046	0.786	0.016	0.0944	0.001	0.45	0.0605	0.001	586.9	9.3	581.5	6.1	608	37
234-170	149	654	0.04	12.98	0.43	0.474	0.011	0.99	0.2231	0.0034	2654	34	2493	50	2996	25
234-171	173	238	0.01	1.567	0.029	0.1565	0.0016	0.95	0.0725	0.0012	956	11	937.1	9.2	990	36
234-172	125	364	0.9	5.86	0.15	0.3514	0.0066	0.69	0.12045	0.00089	1944	24	1938	32	1962	13
234-173	622	112	0.12	0.1535	0.0053	0.02157	0.00032	0.48	0.0521	0.0016	144.5	4.6	137.6	2	261	62

Table C1: U, Th, Pb, and date data for zircon samples 254 and 234

	ppm			Isotopic ratios							Dates in Ma					
	Th	Pb	U/Th	207Pb/ 235U	2σ	206Pb/ 238U	2σ	Corr.	207Pb/ 206Pb	2σ	207Pb/ 235U	2σ	206Pb/ 238U	2σ	207Pb/ 206Pb	2σ
234-174	321	550	0.017	2.151	0.035	0.1959	0.0023	0.30	0.07967	0.00079	1162	12	1153	12	1183	20
234-175	233	28	0.018	0.0906	0.0049	0.01369	0.00024	0.67	0.0486	0.0026	87.6	4.5	87.6	1.5	105	97
234-176	464	59	0.052	0.1	0.0056	0.01502	0.00032	0.16	0.0479	0.0022	96.2	5	96.1	2	86	83
234-177	1112	324	0.048	0.2309	0.0054	0.03358	0.00044	0.66	0.0499	0.001	210.5	4.5	212.9	2.8	186	43
234-178	160	808	0.053	21.41	0.45	0.6191	0.0083	0.64	0.2504	0.0031	3148	21	3103	34	3181	19
234-179	120	266	0.016	3.6	0.063	0.2686	0.0036	0.99	0.0973	0.0012	1547	14	1533	18	1568	23
234-180	143	497	0.0098	10.69	0.22	0.4304	0.0078	0.70	0.1801	0.0017	2488	20	2303	36	2652	16
234-181	190	229	0.011	1.147	0.022	0.124	0.0013	0.99	0.067	0.001	775	10	753.2	7.4	824	33
234-182	345	557	0.0015	33.2	1.4	0.337	0.011	0.04	0.708	0.011	3548	42	1864	54	4753	26
234-183	221	201	0.01	0.836	0.031	0.102	0.0019	0.46	0.0597	0.0019	610	17	626	11	537	68
234-184	750	256	0.042	0.562	0.048	0.04924	0.00082	0.99	0.0834	0.0061	437	25	309.8	5	1090	110
234-185	505	437	0.063	0.946	0.016	0.1089	0.0012	0.95	0.06309	0.00086	675.7	8.1	665.9	7.2	702	30
234-186	4730	656	0.045	0.1973	0.0083	0.0225	0.00055	0.99	0.0633	0.0028	182.6	7	143.4	3.5	651	78
234-187	268	710	0.036	5.345	0.077	0.3388	0.0038	0.23	0.1141	0.001	1876	12	1880	18	1863	17
234-188	313	676	0.011	3.821	0.084	0.2887	0.0053	0.94	0.0951	0.001	1598	17	1632	27	1526	20
234-189	69	96	0.3	1.792	0.029	0.1724	0.0022	0.66	0.07484	0.00068	1040	11	1025	12	1059	18
234-190	234	361	0.013	2.034	0.032	0.187	0.0021	0.63	0.07885	0.00086	1126	11	1105	11	1164	21
234-191	259	184	0.64	0.715	0.012	0.0873	0.001	0.62	0.05936	0.00057	546.7	7.2	539.2	6.1	574	21
234-192	596	350	0.013	0.5239	0.008	0.06807	0.00057	0.99	0.05566	0.00067	427.1	5.4	424.5	3.4	432	27
234-193	456	98	0.015	0.174	0.013	0.01923	0.00065	0.37	0.0714	0.0039	162	12	122.7	4.1	810	110
234-194	928	271	0.017	0.2434	0.0057	0.033	0.00036	0.04	0.05334	0.00098	220.7	4.7	209.3	2.2	324	40
234-195	692	125	0.028	0.1691	0.0068	0.02017	0.0003	1.00	0.0608	0.0021	157.9	5.8	128.7	1.9	583	74
234-196	124	31	0.031	0.201	0.015	0.02096	0.00036	0.61	0.0692	0.0046	184	12	133.7	2.3	730	130
234-197	222	568	0.012	4.612	0.092	0.3041	0.0046	0.45	0.1097	0.0012	1747	18	1710	23	1788	20
234-198	113	25	0.029	0.1792	0.0094	0.0238	0.00046	0.92	0.0545	0.0028	166.8	8.2	151.6	2.9	330	100

Note: Different numbers denote different grains, different letter note repeat analyses on the same grain.

Table C2: Ar and date data for amphibole and neptunite samples

Lab ID#	Laser (W)	$^{40}Ar^*/^{39}Ar$ ± 2σ		$^{40}Ar/^{39}Ar$ ± 2σ		$^{38}Ar/^{39}Ar$ ± 2σ		$^{36}Ar/^{39}Ar$ ± 2σ		Ca/K	^{39}Ar (moles)	$\%^{40}Ar^*$	$\%\ ^{39}Ar$	Age (Ma) ± 2σ		±2σ w/ error in J
254-01 neptunite																
864-01A	0.60	26.62	0.97	28.75	0.17	0.01245	0.00064	0.0071	0.0032	-0.09	1.4E-16	93	3.62	50.0	1.8	1.9
864-01B	0.65	27.78	0.41	28.58	0.12	0.01238	0.00036	0.0026	0.0013	-0.06	3.7E-16	97	9.41	52.17	0.77	0.90
864-01C	0.70	27.93	0.41	28.38	0.11	0.01237	0.00034	0.0015	0.0013	-0.03	3.8E-16	98	9.54	52.44	0.76	0.90
864-01D	0.75	28.57	0.24	28.82	0.18	0.01228	0.00026	0.0008	0.0005	-0.01	8.6E-16	99	21.61	53.63	0.44	0.65
864-01E	0.80	28.53	0.23	28.90	0.17	0.01230	0.00024	0.0012	0.0006	0.04	8.2E-16	99	20.55	53.55	0.43	0.65
864-01F	0.85	27.62	0.56	28.20	0.13	0.01163	0.00047	0.0019	0.0019	0.13	2.4E-16	98	5.91	51.9	1.0	1.1
864-01G	0.90	26.9	1.8	28.45	0.25	0.01162	0.00094	0.0051	0.0059	0.11	7.8E-17	95	1.96	50.6	3.3	3.3
864-01H	0.95	27.65	0.87	28.62	0.16	0.01229	0.00056	0.0033	0.0029	0.12	1.5E-16	97	3.88	51.9	1.6	1.7
864-01I	1.00	27.94	0.70	28.68	0.14	0.01214	0.00059	0.0024	0.0023	0.11	2.2E-16	98	5.46	52.5	1.3	1.4
864-01J	1.20	27.88	0.75	28.69	0.16	0.01214	0.00057	0.0027	0.0025	0.10	1.9E-16	97	4.86	52.4	1.4	1.5
864-01K	1.50	27.58	0.82	28.34	0.16	0.01248	0.00059	0.0025	0.0027	0.03	1.8E-16	97	4.40	51.8	1.5	1.6
864-01L	2.00	28.09	0.70	28.91	0.23	0.01257	0.00057	0.0027	0.0022	0.14	2.0E-16	97	5.11	52.7	1.3	1.4
864-01M	3.00	27.5	1.2	28.48	0.18	0.01242	0.00063	0.0034	0.0041	0.01	1.3E-16	96	3.20	51.6	2.2	2.3
864-01N	5.00	21.5	6.7	26.77	0.66	0.01225	0.00295	0.0178	0.0227	-0.35	1.9E-17	80	0.48	40	13	13
254-02 neptunite																
864-02A	0.60	27.54	0.26	28.43	0.08	0.01269	0.00027	0.0029	0.0008	0.06	6.3E-16	97	28.54	51.73	0.49	0.68
864-02B	0.65	27.93	0.27	28.26	0.09	0.01223	0.00034	0.0011	0.0009	0.04	6.0E-16	99	27.40	52.45	0.51	0.69
864-02C	0.70	27.17	0.70	27.84	0.23	0.01241	0.00058	0.0022	0.0022	0.05	2.0E-16	98	9.22	51.0	1.3	1.4
864-02D	0.70	26.4	1.8	27.79	0.24	0.01314	0.00115	0.0048	0.0061	0.16	7.4E-17	95	3.36	49.6	3.4	3.4
864-02E	0.75	27.66	0.77	28.35	0.21	0.01227	0.00059	0.0023	0.0025	0.05	1.9E-16	98	8.54	52.0	1.4	1.5
864-02F	0.75	25.6	2.5	27.41	0.30	0.01117	0.00118	0.0062	0.0085	0.09	5.7E-17	93	2.60	48.1	4.7	4.7
864-02G	0.80	25.2	2.1	27.23	0.30	0.01206	0.00125	0.0070	0.0069	0.08	5.9E-17	92	2.67	47.3	3.8	3.9
864-02H	0.80	26.0	1.7	27.60	0.22	0.01176	0.00084	0.0053	0.0058	-0.02	8.0E-17	94	3.64	48.9	3.2	3.2
864-02I	1.00	26.81	0.91	27.68	0.14	0.01212	0.00061	0.0029	0.0031	0.12	1.5E-16	97	6.80	50.4	1.7	1.8
864-02J	1.50	25.1	2.6	27.31	0.33	0.01142	0.00128	0.0075	0.0088	0.11	5.1E-17	92	2.32	47.2	4.9	4.9
864-02K	3.00	26.6	1.5	27.71	0.22	0.01280	0.00081	0.0038	0.0049	-0.08	9.6E-17	96	4.39	49.9	2.7	2.7
864-02L	5.00	19	12	27.39	1.10	0.01155	0.00453	0.0279	0.0403	-1.09	1.1E-17	70	0.52	36	22	22
254-03 neptunite																
864-03A	0.60	28.23	0.26	28.69	0.17	0.01228	0.00022	0.0015	0.0007	0.01	1.1E-15	98	45.99	53.00	0.48	0.68
864-03B	0.65	28.16	0.29	28.50	0.16	0.01203	0.00024	0.0011	0.0008	0.02	1.0E-15	99	40.48	52.87	0.53	0.71
864-03C	0.70	26.4	1.9	28.20	0.18	0.01197	0.00075	0.0062	0.0066	0.14	1.3E-16	94	5.02	49.5	3.6	3.6
864-03D	0.70	23.5	5.1	28.56	0.52	0.01239	0.00225	0.0172	0.0172	0.17	3.7E-17	82	1.47	44.2	9.5	9.5
864-03E	0.75	23.1	5.7	28.23	0.39	0.01159	0.00148	0.0174	0.0191	0.38	4.6E-17	82	1.85	43	11	11
864-03F	0.75	20.4	9.2	28.88	0.58	0.01189	0.00227	0.0286	0.0313	-0.01	2.6E-17	71	1.05	38	17	17
864-03G	0.80	19.4	8.3	28.38	0.57	0.01195	0.00228	0.0303	0.0282	-0.47	2.5E-17	68	0.99	37	16	16
864-03H	1.00	22.9	6.6	28.89	0.59	0.01300	0.00181	0.0203	0.0223	-0.19	3.7E-17	79	1.47	43	12	12
864-03I	3.00	22.7	5.8	27.68	0.39	0.01227	0.00144	0.0168	0.0195	0.50	4.2E-17	82	1.68	43	11	11
WPT03 hornblende																
855-01A	0.85	274	170	2082.66	284.84	1.20999	0.17117	6.1208	1.0069	-0.60	2.9E-18	13	0.02	457	250	250
855-01B	1.00	69	43	445.26	33.80	0.25076	0.02446	1.2766	0.1745	8.17	5.6E-18	15	0.05	126	77	77
855-01C	1.05	29	16	177.68	5.32	0.11380	0.00680	0.5030	0.0566	5.96	1.5E-17	16	0.12	55	30	30

Table C2: Ar and date data for amphibole and neptunite samples

Lab ID#	Laser (W)	$^{40}Ar^*/^{39}Ar$ ± 2σ		$^{40}Ar/^{39}Ar$ ± 2σ		$^{38}Ar/^{39}Ar$ ± 2σ		$^{36}Ar/^{39}Ar$ ± 2σ		Ca/K	^{39}Ar (moles)	$\%^{40}Ar^*$	$\%\ ^{39}Ar$	Age (Ma) ± 2σ		±2σ w/ error in J
855-01D	1.10	5	17	79.66	3.05	0.05536	0.00669	0.2532	0.0578	4.38	1.2E-17	6	0.10	10	32	32
855-01E	1.15	10	16	87.63	2.90	0.05931	0.00531	0.2631	0.0539	3.65	1.4E-17	11	0.12	19	30	30
855-01F	1.20	9	12	52.14	1.39	0.03506	0.00434	0.1474	0.0420	1.83	1.8E-17	17	0.15	16	23	23
855-01G	1.40	16.9	6.3	75.46	3.03	0.04767	0.00270	0.1985	0.0227	3.20	5.6E-17	22	0.47	32	12	12
855-01H	1.80	7.9	2.5	36.58	0.32	0.02506	0.00068	0.0976	0.0084	3.57	3.1E-16	22	2.55	14.9	4.7	4.7
855-01I	2.00	4.8	2.1	30.37	0.25	0.02343	0.00091	0.0872	0.0070	3.87	3.5E-16	16	2.92	9.0	3.9	3.9
855-01J	2.20	5.8	2.7	30.19	0.20	0.02425	0.00064	0.0831	0.0090	4.37	3.9E-16	19	3.23	11.0	5.0	5.0
855-01K	2.40	16.4	3.2	49.40	0.26	0.03264	0.00070	0.1127	0.0107	6.76	3.6E-16	33	2.93	30.9	5.9	5.9
855-01L	2.60	23.3	2.1	41.98	0.30	0.02424	0.00097	0.0645	0.0072	7.69	3.1E-16	55	2.60	43.7	4.0	4.0
855-01M	2.80	23.1	2.4	36.63	0.18	0.02598	0.00058	0.0476	0.0079	11.02	5.3E-16	63	4.34	43.4	4.4	4.4
855-01N	3.00	30.3	2.4	41.05	0.33	0.03249	0.00069	0.0395	0.0081	16.83	6.1E-16	73	5.08	56.6	4.5	4.5
855-01O	3.20	36.9	2.1	45.32	0.42	0.04092	0.00071	0.0332	0.0068	24.14	7.0E-16	81	5.76	68.7	3.8	3.8
855-01P	3.40	44.4	1.9	55.34	0.60	0.05451	0.00081	0.0435	0.0061	31.38	7.8E-16	79	6.43	82.4	3.4	3.5
855-01Q	3.50	42.4	1.2	45.81	0.27	0.04824	0.00077	0.0178	0.0040	30.52	7.7E-16	91	6.33	78.7	2.2	2.3
855-01R	3.60	51.6	1.1	55.07	0.51	0.05766	0.00237	0.0196	0.0031	36.20	5.3E-16	92	4.40	95.3	1.9	2.0
855-01S	3.70	45.6	1.1	49.09	0.39	0.05217	0.00167	0.0189	0.0035	33.89	5.0E-16	92	4.14	84.5	2.1	2.1
855-01T	3.80	47.2	1.3	50.11	0.42	0.05517	0.00146	0.0174	0.0042	35.82	5.0E-16	93	4.09	87.4	2.4	2.5
855-01U	3.90	49.1	1.3	51.81	0.52	0.05768	0.00189	0.0169	0.0038	36.23	5.1E-16	93	4.25	90.9	2.3	2.3
855-01V	4.00	48.8	1.3	51.87	0.53	0.05905	0.00191	0.0182	0.0039	37.45	4.8E-16	93	3.95	90.4	2.3	2.4
855-01W	4.20	52.1	1.5	54.80	0.49	0.06124	0.00127	0.0177	0.0046	40.72	5.1E-16	94	4.18	96.4	2.7	2.7
855-01X	4.40	56.9	1.1	58.63	0.61	0.06627	0.00238	0.0155	0.0029	43.80	5.1E-16	96	4.24	105.0	1.9	2.0
855-01Y	4.60	52.68	0.99	54.72	0.38	0.06212	0.00139	0.0156	0.0030	40.13	6.1E-16	95	5.05	97.4	1.8	1.9
855-01Z	4.80	54.5	1.1	57.00	0.41	0.06477	0.00111	0.0170	0.0034	39.34	6.1E-16	94	5.04	100.7	2.0	2.1
855-01AA	5.00	56.0	1.2	59.11	0.59	0.06885	0.00188	0.0201	0.0034	43.52	4.6E-16	93	3.83	103.3	2.1	2.2
855-01AB	5.20	65.3	2.5	71.85	0.96	0.08232	0.00304	0.0354	0.0077	57.55	2.2E-16	89	1.84	120.0	4.4	4.5
855-01AC	5.40	57.5	2.3	63.69	0.75	0.07383	0.00247	0.0320	0.0074	49.93	1.7E-16	89	1.43	106.0	4.2	4.2
855-01AD	5.80	62.6	2.2	69.02	0.53	0.07733	0.00163	0.0341	0.0069	54.90	1.7E-16	89	1.37	115.2	3.8	3.9
855-01AE	6.20	67.9	1.8	74.59	0.65	0.08211	0.00201	0.0358	0.0057	55.28	2.1E-16	89	1.76	124.5	3.2	3.3
855-01AF	6.60	63.2	1.5	66.98	0.44	0.07682	0.00139	0.0247	0.0049	52.24	2.5E-16	93	2.05	116.2	2.7	2.8
855-01AG	7.00	64.3	2.3	68.57	0.58	0.07938	0.00179	0.0266	0.0074	52.76	1.6E-16	92	1.35	118.2	4.1	4.2
855-01AH	8.00	63.0	1.8	69.26	0.44	0.07853	0.00155	0.0341	0.0059	55.69	2.2E-16	89	1.79	115.8	3.3	3.3
855-01AI	10.00	66.7	2.7	85.29	0.58	0.09129	0.00147	0.0780	0.0088	64.14	2.4E-16	76	2.02	122.4	4.9	4.9
13CG06a hornblende																
854-01A	2.80	58.4	1.3	68.38	0.37	0.06348	0.00092	0.0438	0.0041	44.72	4.1E-16	84	16.68	107.8	2.3	2.7
854-01B	3.20	53.6	1.9	59.33	1.77	0.06170	0.00199	0.0291	0.0032	44.72	5.4E-16	89	21.82	99.2	3.4	3.6
854-01C	3.50	51.3	1.4	57.67	0.41	0.06208	0.00097	0.0310	0.0045	44.07	4.8E-16	88	19.51	95.0	2.5	2.8
854-01D	3.70	52.4	2.0	59.32	0.90	0.06446	0.00161	0.0337	0.0063	47.76	2.8E-16	87	11.46	97.0	3.7	3.9
854-01E	3.90	54.6	2.5	62.56	1.28	0.06758	0.00208	0.0379	0.0076	50.59	2.1E-16	86	8.52	101.0	4.6	4.7
854-01F	4.20	57.9	3.1	65.76	1.23	0.07219	0.00245	0.0394	0.0098	56.78	1.5E-16	86	6.02	106.8	5.6	5.8
854-01G	4.60	57.8	3.4	66.51	0.74	0.07422	0.00224	0.0420	0.0111	55.92	1.2E-16	85	4.84	106.7	6.1	6.3
854-01H	5.00	48.3	5.8	64.51	1.15	0.06749	0.00366	0.0659	0.0191	52.37	5.7E-17	73	2.29	90	11	11
854-01I	6.00	43.7	9.9	61.87	1.41	0.07154	0.00555	0.0729	0.0327	55.57	3.5E-17	69	1.42	81	18	18

Table C2: Ar and date data for amphibole and neptunite samples

Lab ID#	Laser (W)	$^{40}Ar^*/^{39}Ar$ ± 2σ		$^{40}Ar/^{39}Ar$ ± 2σ		$^{38}Ar/^{39}Ar$ ± 2σ		$^{36}Ar/^{39}Ar$ ± 2σ		Ca/K	^{39}Ar (moles)	$\%^{40}Ar^*$	$\%\ ^{39}Ar$	Age (Ma) ± 2σ		±2σ w/ error in J
854-01J	10.00	58.9	2.4	66.77	0.47	0.08079	0.00185	0.0420	0.0079	69.11	1.8E-16	86	7.44	108.8	4.4	4.5
CG04 hornblende																
852-01A	2.70	65.4	7.1	138.17	2.85	0.10956	0.00493	0.2622	0.0236	69.06	6.6E-17	46	4.03	120	13	13
852-01B	2.90	36.3	3.9	56.56	1.19	0.06591	0.00274	0.0775	0.0128	45.28	1.3E-16	63	7.88	67.2	7.1	7.2
852-01C	3.10	41.1	4.4	57.39	1.81	0.08057	0.00375	0.0660	0.0140	54.46	1.1E-16	70	6.46	76.1	7.9	8.0
852-01D	3.30	44.8	5.3	62.18	2.11	0.08297	0.00393	0.0713	0.0169	61.18	9.5E-17	70	5.78	82.8	9.5	9.6
852-01E	3.50	54.7	4.5	65.36	1.73	0.10047	0.00376	0.0518	0.0141	72.22	1.1E-16	81	6.64	100.6	8.1	8.1
852-01F	3.70	62.7	4.1	74.31	2.14	0.11210	0.00419	0.0572	0.0123	78.69	1.2E-16	82	7.01	114.8	7.3	7.5
852-01G	3.90	61.6	3.3	70.88	1.01	0.11079	0.00302	0.0490	0.0105	76.99	1.2E-16	84	7.43	112.7	5.9	6.0
852-01H	4.20	61.9	3.8	72.01	1.65	0.10853	0.00348	0.0506	0.0116	71.76	1.3E-16	84	7.74	113.3	6.7	6.9
852-01I	6.00	58.9	1.9	64.80	0.46	0.10053	0.00148	0.0359	0.0060	71.46	4.7E-16	88	28.33	108.0	3.3	3.6
852-01J	10.00	63.1	2.4	70.57	0.95	0.11257	0.00207	0.0468	0.0074	93.58	3.1E-16	86	18.70	115.5	4.3	4.5
WPT13 hornblende																
850-01A	2.70	36.0	4.0	63.21	1.71	0.04839	0.00253	0.0983	0.0133	31.34	1.3E-16	56	6.49	67.2	7.4	7.4
850-01B	3.00	36.5	2.4	48.79	0.83	0.05298	0.00307	0.0509	0.0077	47.81	2.0E-16	74	9.87	68.3	4.4	4.4
850-01C	3.30	39.4	2.3	47.46	0.77	0.05462	0.00255	0.0391	0.0072	59.99	2.6E-16	81	12.74	73.6	4.1	4.2
850-01D	3.60	46.0	2.0	52.49	0.48	0.06190	0.00134	0.0364	0.0065	69.99	3.0E-16	85	14.94	85.6	3.7	3.8
850-01E	3.90	45.9	2.4	51.34	0.46	0.06651	0.00138	0.0334	0.0079	72.76	3.1E-16	87	15.13	85.5	4.4	4.5
850-01F	4.20	51.3	7.9	56.12	8.00	0.06727	0.00970	0.0338	0.0088	80.96	2.3E-16	89	11.53	95	14	14
850-01G	4.60	46.8	3.2	55.24	0.95	0.06855	0.00282	0.0446	0.0100	77.23	1.7E-16	82	8.49	87.1	5.7	5.8
850-01H	5.00	49.4	2.9	57.20	0.95	0.06741	0.00209	0.0427	0.0091	77.38	1.8E-16	84	8.99	91.8	5.3	5.3
850-01I	6.00	57.1	4.0	61.77	1.41	0.07566	0.00288	0.0365	0.0122	93.12	1.5E-16	89	7.22	105.6	7.1	7.2
850-01J	10.00	52.0	5.6	66.12	2.44	0.08904	0.00465	0.0686	0.0172	97.10	9.3E-17	76	4.61	96	10	10
258 hornblende																
845-01A	2.70	57.2	3.7	80.74	1.27	0.07789	0.00290	0.0887	0.0120	40.25	2.0E-16	70	8.44	104.9	6.6	6.7
845-01B	3.00	60.7	3.5	80.32	0.95	0.07302	0.00149	0.0761	0.0115	42.91	3.1E-16	74	12.94	111.2	6.2	6.4
845-01C	3.30	66.1	3.4	79.08	0.94	0.08464	0.00174	0.0564	0.0109	52.92	3.2E-16	82	13.53	120.7	6.0	6.2
845-01D	3.60	70.9	3.3	88.32	1.06	0.09355	0.00186	0.0709	0.0106	49.75	3.5E-16	79	14.56	129.2	5.8	6.0
845-01E	3.90	71.1	3.3	85.73	1.23	0.09608	0.00235	0.0618	0.0106	50.71	2.5E-16	81	10.30	129.5	5.9	6.1
845-01F	4.20	70.0	3.3	83.77	1.45	0.09877	0.00277	0.0611	0.0100	60.35	1.7E-16	82	7.18	127.6	5.7	5.9
845-01G	4.60	65.1	3.2	76.85	1.05	0.10290	0.00264	0.0535	0.0102	59.37	1.6E-16	83	6.51	119.0	5.7	5.9
845-01H	5.00	67.9	4.6	84.38	2.87	0.10139	0.00427	0.0702	0.0132	61.54	1.4E-16	79	5.73	124.0	8.1	8.2
845-01I	6.00	72.8	3.9	91.23	1.56	0.11003	0.00316	0.0790	0.0121	68.40	1.5E-16	78	6.16	132.6	6.8	7.0
845-01J	10.00	79.0	2.7	96.24	0.59	0.11507	0.00144	0.0888	0.0087	122.05	3.5E-16	78	14.64	143.5	4.8	5.1
HBD hornblende																
847-01A	2.70	73	15	173.24	9.85	0.07555	0.00765	0.3478	0.0516	40.61	3.9E-17	42	0.77	134	26	26
847-01B	3.00	21.3	5.3	54.32	0.98	0.03001	0.00222	0.1137	0.0179	12.11	1.4E-16	39	2.85	40.1	9.8	9.8
847-01C	3.30	23.3	6.2	58.73	1.29	0.03279	0.00200	0.1219	0.0209	10.49	1.6E-16	39	3.11	44	11	11
847-01D	3.60	25.4	5.8	56.11	1.05	0.03032	0.00200	0.1062	0.0195	12.04	1.6E-16	45	3.12	48	11	11
847-01E	4.20	31.2	5.0	57.27	0.71	0.02953	0.00155	0.0920	0.0166	20.73	2.2E-16	54	4.49	58.5	9.1	9.2
847-01F	4.80	38.8	3.9	62.56	0.70	0.02990	0.00122	0.0880	0.0131	37.68	2.8E-16	61	5.62	72.3	7.2	7.2
847-01G	5.40	42.4	4.1	59.85	0.48	0.03347	0.00092	0.0720	0.0134	63.82	4.1E-16	69	8.21	78.9	7.4	7.5

Table C2: Ar and date data for amphibole and neptunite samples

Lab ID#	Laser (W)	$^{40}Ar^*/^{39}Ar$ ± 2σ		$^{40}Ar/^{39}Ar$ ± 2σ		$^{38}Ar/^{39}Ar$ ± 2σ		$^{36}Ar/^{39}Ar$ ± 2σ		Ca/K	^{39}Ar (moles)	$\%^{40}Ar^*$	$\%\ ^{39}Ar$	Age (Ma) ± 2σ		±2σ w/ error in J
847-01H	6.00	51.9	4.2	65.83	1.34	0.04085	0.00114	0.0683	0.0133	98.99	4.8E-16	76	9.53	96.2	7.6	7.7
847-01I	8.00	57.3	3.6	67.87	0.33	0.04385	0.00058	0.0630	0.0115	122.79	9.3E-16	81	18.63	105.9	6.4	6.5
847-01J	8.50	57.5	4.5	73.79	0.73	0.04472	0.00089	0.0795	0.0146	110.07	5.6E-16	75	11.27	106.2	8.1	8.2
847-01K	9.00	52.1	2.8	61.58	0.73	0.03758	0.00085	0.0552	0.0088	107.64	6.5E-16	81	12.93	96.5	5.0	5.1
847-01L	9.50	50.3	3.0	57.31	0.34	0.03903	0.00073	0.0486	0.0098	115.95	6.3E-16	84	12.50	93.2	5.5	5.6
847-01M	10.00	62.9	4.0	74.72	1.88	0.04709	0.00195	0.0741	0.0116	149.20	2.1E-16	79	4.10	115.9	7.1	7.2
847-01N	11.00	61.8	5.5	77.88	2.46	0.04977	0.00313	0.0835	0.0167	128.02	1.0E-16	76	2.00	114	9.9	10.0
847-01O	12.00	53.8	9.6	75.26	2.73	0.04489	0.00557	0.0998	0.0306	125.01	4.4E-17	68	0.88	100	17	17
ISZ hornblende																
859-01A	2.70	42.7	6.3	120.79	5.87	0.06305	0.00590	0.2685	0.0239	21.25	0.0E+00	35	0.00	79	11	11
859-01B	2.80	23.0	4.5	58.63	1.36	0.03907	0.00222	0.1230	0.0154	14.65	1.5E-16	39	9.20	43.0	8.4	8.4
859-01C	3.00	27.3	5.1	53.46	1.52	0.04580	0.00329	0.0926	0.0170	22.64	1.4E-16	51	8.50	50.9	9.3	9.3
859-01D	3.30	35.6	4.7	60.16	1.50	0.06148	0.00283	0.0890	0.0157	29.84	1.3E-16	58	8.46	66.0	8.6	8.6
859-01E	3.60	38.8	4.0	57.89	1.58	0.06440	0.00292	0.0714	0.0132	34.52	1.4E-16	66	8.87	71.9	7.4	7.4
859-01F	3.90	41.9	3.9	58.36	1.70	0.07631	0.00410	0.0646	0.0125	44.40	1.4E-16	71	9.01	77.6	7.1	7.2
859-01G	4.20	42.6	3.7	62.29	1.28	0.06641	0.00238	0.0749	0.0121	40.21	1.5E-16	67	9.57	78.8	6.7	6.8
859-01H	4.60	49.2	3.9	66.85	1.99	0.07912	0.00313	0.0700	0.0123	49.32	1.5E-16	72	9.21	90.8	7.1	7.1
859-01I	5.00	47.6	5.0	67.59	2.40	0.07594	0.00385	0.0794	0.0157	56.04	1.2E-16	69	7.24	87.8	8.9	9.0
859-01J	6.00	57.5	3.6	72.49	2.71	0.08990	0.00373	0.0652	0.0096	64.84	2.4E-16	77	14.89	105.5	6.4	6.5
859-01K	10.00	75.7	6.7	129.83	1.86	0.13836	0.00280	0.2088	0.0217	104.45	2.0E-16	56	12.49	138	12	12
859-01L	12.00	78	13	191.42	4.01	0.16511	0.00717	0.4183	0.0427	140.22	4.1E-17	39	2.56	142	23	23
249 Na-Ca amphibole																
848-01A	2.80	31.26	0.23	32.51	0.06	0.01281	0.00021	0.0045	0.0008	2.10	1.8E-15	96	16.97	58.41	0.42	0.56
848-01B	3.00	31.67	0.29	32.60	0.09	0.01271	0.00029	0.0035	0.0010	2.13	1.5E-15	97	14.11	59.16	0.54	0.66
848-01C	3.20	32.73	0.33	33.46	0.08	0.01244	0.00026	0.0028	0.0011	2.13	1.4E-15	98	12.53	61.11	0.60	0.71
848-01D	3.40	33.04	0.43	33.95	0.11	0.01235	0.00030	0.0035	0.0014	2.37	1.2E-15	97	11.28	61.67	0.78	0.87
848-01E	3.50	32.92	0.55	34.17	0.15	0.01265	0.00035	0.0046	0.0018	2.26	9.2E-16	96	8.46	61.5	1.0	1.1
848-01F	3.60	33.02	0.58	34.24	0.16	0.01298	0.00043	0.0045	0.0019	2.30	7.2E-16	96	6.58	61.6	1.1	1.1
848-01G	3.70	32.00	0.62	33.04	0.30	0.01335	0.00047	0.0039	0.0018	2.40	5.6E-16	97	5.12	59.8	1.1	1.2
848-01H	3.90	32.71	0.59	33.26	0.21	0.01160	0.00057	0.0023	0.0019	2.60	0.0E+00	98	0.00	61.1	1.1	1.2
848-01I	3.90	31.9	1.3	32.93	0.41	0.01260	0.00067	0.0038	0.0041	2.89	3.5E-16	97	3.26	59.7	2.4	2.4
848-01J	4.60	32.68	0.40	33.36	0.11	0.01223	0.00033	0.0028	0.0013	2.71	7.8E-16	98	7.19	61.02	0.74	0.83
848-01K	6.00	32.54	0.59	33.29	0.14	0.01193	0.00038	0.0031	0.0019	3.26	6.2E-16	98	5.73	60.8	1.1	1.2
848-01L	10.00	32.78	0.37	33.62	0.09	0.01256	0.00030	0.0034	0.0012	3.00	9.5E-16	97	8.77	61.19	0.67	0.78
254 Na-Ca amphibole																
843-01A	2.70	33.46	0.26	36.84	0.07	0.01404	0.00021	0.0116	0.0008	1.27	2.8E-15	91	6.20	62.64	0.47	0.74
843-01B	2.90	32.63	0.20	34.85	0.07	0.01328	0.00025	0.0077	0.0006	1.44	3.0E-15	94	6.58	61.12	0.36	0.66
843-01C	3.10	31.74	0.22	33.39	0.07	0.01292	0.00014	0.0058	0.0007	1.46	3.4E-15	95	7.40	59.49	0.40	0.67
843-01D	3.30	31.41	0.22	33.25	0.07	0.01307	0.00015	0.0064	0.0007	1.35	3.5E-15	94	7.58	58.87	0.40	0.66
843-01E	3.50	32.21	0.18	34.42	0.08	0.01339	0.00015	0.0077	0.0005	1.34	3.8E-15	94	8.26	60.35	0.32	0.63
843-01F	3.70	32.63	0.19	34.55	0.06	0.01344	0.00018	0.0067	0.0006	1.38	3.6E-15	94	7.91	61.12	0.35	0.65
843-01G	3.90	32.70	0.19	34.18	0.06	0.01306	0.00018	0.0052	0.0006	1.35	3.5E-15	96	7.66	61.25	0.35	0.65

Table C2: Ar and date data for amphibole and neptunite samples

Lab ID#	Laser (W)	$^{40}Ar^*/^{39}Ar$ ± 2σ		$^{40}Ar/^{39}Ar$ ± 2σ		$^{38}Ar/^{39}Ar$ ± 2σ		$^{36}Ar/^{39}Ar$ ± 2σ		Ca/K	^{39}Ar (moles)	$\%^{40}Ar^*$	$\%\ ^{39}Ar$	Age (Ma) ± 2σ		±2σ w/ error in J
843-01H	6.00	32.49	0.09	33.39	0.04	0.01254	0.00009	0.0033	0.0003	1.52	8.9E-15	97	19.44	60.87	0.17	0.57
843-01I	8.00	32.57	0.08	33.44	0.05	0.01249	0.00009	0.0032	0.0002	1.56	1.1E-14	97	22.90	61.02	0.14	0.57
843-01J	10.00	31.44	0.18	32.27	0.06	0.01263	0.00018	0.0031	0.0006	1.55	2.8E-15	97	6.07	58.92	0.33	0.62
216 Na amphibole																
862-01A	2.70	16.58	0.36	32.46	0.50	0.01834	0.00087	0.0539	0.0011	1.37	6.7E-16	51	7.37	31.14	0.66	0.69
862-01B	2.90	27.79	0.31	44.00	0.36	0.02110	0.00064	0.0549	0.0008	0.77	9.2E-16	63	10.20	51.89	0.58	0.67
862-01C	3.10	26.89	0.31	41.84	0.34	0.02099	0.00051	0.0508	0.0008	1.37	9.2E-16	64	10.16	50.23	0.56	0.65
862-01D	3.30	27.81	0.38	40.61	0.47	0.01950	0.00051	0.0435	0.0008	1.11	1.0E-15	68	11.03	51.94	0.69	0.77
862-01E	3.50	26.47	0.27	39.88	0.28	0.02043	0.00048	0.0455	0.0007	1.19	8.6E-16	66	9.56	49.45	0.50	0.59
862-01F	3.70	24.38	0.39	37.42	0.49	0.01857	0.00061	0.0444	0.0009	1.95	7.8E-16	65	8.67	45.61	0.72	0.77
862-01G	3.90	21.02	0.36	37.42	0.39	0.02153	0.00063	0.0560	0.0011	2.92	6.0E-16	56	6.67	39.38	0.66	0.71
862-01H	5.00	30.59	0.31	48.84	0.39	0.02275	0.00048	0.0623	0.0008	3.38	1.1E-15	63	11.81	57.04	0.57	0.67
862-01I	7.00	34.59	0.23	49.44	0.27	0.02126	0.00033	0.0513	0.0005	6.06	1.8E-15	70	19.78	64.37	0.41	0.58
862-01J	10.00	38.83	0.54	65.70	0.66	0.03148	0.00097	0.0945	0.0015	18.01	4.3E-16	59	4.74	72.09	0.98	1.08
KMBS Na amphibole																
861-01A	2.70	34.84	0.17	35.57	0.07	0.01171	0.00008	0.0024	0.0005	0.18	1.3E-14	98	10.36	64.65	0.31	0.81
861-01B	2.90	34.68	0.16	35.34	0.06	0.01186	0.00008	0.0022	0.0005	0.15	1.6E-14	98	12.62	64.37	0.30	0.80
861-01C	3.10	34.22	0.15	34.83	0.06	0.01193	0.00007	0.0020	0.0005	0.19	1.6E-14	98	12.55	63.53	0.28	0.79
861-01D	3.30	33.51	0.13	34.17	0.06	0.01218	0.00015	0.0022	0.0004	0.34	1.4E-14	98	11.03	62.24	0.24	0.76
861-01E	3.50	33.45	0.19	34.14	0.06	0.01226	0.00009	0.0023	0.0006	0.31	1.0E-14	98	8.16	62.13	0.35	0.80
861-01F	3.70	33.43	0.18	34.06	0.06	0.01223	0.00010	0.0021	0.0006	0.34	9.4E-15	98	7.34	62.09	0.32	0.79
861-01G	4.00	33.57	0.20	34.26	0.06	0.01207	0.00011	0.0024	0.0006	0.41	8.5E-15	98	6.61	62.34	0.36	0.81
861-01H	5.00	33.73	0.17	34.35	0.06	0.01213	0.00008	0.0022	0.0006	0.65	1.3E-14	98	9.86	62.63	0.32	0.79
861-01I	7.00	33.46	0.13	33.96	0.05	0.01228	0.00005	0.0020	0.0004	1.68	1.9E-14	99	14.90	62.14	0.24	0.76
861-01J	10.00	33.91	0.11	34.45	0.06	0.01296	0.00010	0.0026	0.0003	4.11	8.4E-15	98	6.57	62.95	0.21	0.76

J value	2σ
1.053E-03	5.6E-06

Table C3: U, Th, and Pb data for joaquinite from sample 254

	ppm				Isotopic ratios										
sample	Th	Pb	U/Th	Pb_c/ Pbtotal	$^{207}Pb/^{235}U$	2σ	$^{206}Pb/^{238}U$	2σ	Corr.	$^{208}Pb/^{232}Th$	2σ	$^{232}Th/^{204}Pb$	2σ	$^{208}Pb/^{204}Pb$	2σ
254-1	5510	120	0.052	0.066	5.69	0.64	0.06	0.021	0.18	0.00698	0.00019	8375	266	58.46	0.96
254-2	6820	158	0.025	0.012	12.34	0.78	0.1077	0.0024	0.80	0.00778	0.00018	7420	198	57.73	0.76
254-3	8960	229	0.013	0.045	33.4	3.5	0.278	0.024	0.99	0.00861	0.00019	6422	168	55.29	0.78
254-4a	8513	209	0.021	0.030	18.8	1.8	0.16	0.011	0.99	0.008256	0.00018	6784	173	56.01	0.74
254-4b	7760	222	0.046	0.033	9.12	0.56	0.0824	0.0019	0.88	0.009521	0.0002	5527	136	52.62	0.67
254-5a	11330	219	0.110	0.024	2.26	0.18	0.0273	0.001	0.95	0.006491	0.00014	9758	249	63.34	0.86
254-5b	9970	221	0.224	0.0092	1.285	0.081	0.0194	0.00039	0.76	0.007446	0.00017	7961	218	59.28	0.89
254-6a	7670	188	0.024	0.021	15.8	1.5	0.1403	0.0095	0.99	0.00824	0.0002	6750	181	55.62	0.64
254-6b	9410	214	0.010	0.013	33.4	3.2	0.287	0.02	0.99	0.00766	0.00017	7597	198	58.19	0.79
254-7	8750	188	0.023	0.021	11.95	0.93	0.1089	0.0052	0.98	0.0072	0.00015	8308	203	59.82	0.77
254-9a	11930	303	0.015	0.0084	22.91	1.4	0.2049	0.0042	0.85	0.00854	0.00018	6484	149	55.37	0.51
254-9b	7140	162	0.019	0.0092	15.15	1.2	0.1383	0.0069	0.98	0.007613	0.00016	7771	202	59.16	0.90
254-10a	6230	148	0.031	0.023	10.57	0.97	0.1007	0.0063	0.98	0.007947	0.00016	7130	170	56.66	0.73
254-10b	5178	151	0.037	0.020	10.66	0.68	0.1	0.0024	0.87	0.00975	0.00021	5394	139	52.59	0.74
254-10c	6390	157	0.033	0.026	11.23	1.2	0.1032	0.0076	0.99	0.00823	0.00019	6858	180	56.44	0.70
254-11a	7740	214	0.032	0.0088	11.93	0.76	0.1092	0.0026	0.90	0.00919	0.0002	5903	153	54.25	0.77
254-11b	12430	340	0.019	0.0089	20.45	1.3	0.1788	0.0048	0.93	0.009143	0.00019	5858	132	53.56	0.46
254-12	3965	228	0.175	0.033	5.58	0.36	0.055	0.0014	0.91	0.01913	0.00046	2323	61	44.44	0.46
254-13	12760	325	0.031	0.023	13.2	1.3	0.1191	0.0082	0.99	0.00852	0.00022	6417	185	54.67	0.70
254-14a	11370	259	0.013	0.0081	22.85	1.5	0.1995	0.0063	0.95	0.007592	0.00016	7655	179	58.12	0.58
254-14b	6550	171	0.034	0.015	11.03	0.77	0.1012	0.0035	0.96	0.00875	0.00023	6282	186	54.97	0.75
254-15	11420	259	0.016	0.009	18.4	1.2	0.164	0.004	0.88	0.00762	0.00018	7571	204	57.69	0.74
254-16a	8680	221	0.048	0.026	8.08	0.69	0.0765	0.0045	0.99	0.00861	0.0002	6338	176	54.57	0.83
254-16b	7780	183	0.030	0.032	10.08	0.62	0.0931	0.002	0.77	0.00784	0.00016	7434	194	58.28	0.95
254-17	10870	287	0.024	0.0079	15.22	1.1	0.1368	0.0047	0.96	0.00884	0.00019	6117	146	54.07	0.56
254-18a	12150	295	0.017	0.0084	18.27	1.2	0.1635	0.0046	0.94	0.008166	0.00017	6876	161	56.15	0.60
254-18b	7448	180	0.017	0.011	22	2.5	0.195	0.017	0.99	0.00805	0.00021	7118	215	57.30	0.88
254-19	4890	163	0.067	0.028	7.93	0.62	0.0755	0.0035	0.97	0.01123	0.00026	4443	121	49.90	0.72
254-21a	5090	168	0.061	0.026	8.56	0.78	0.0813	0.0054	0.99	0.01124	0.0003	4531	141	50.93	0.82
254-21b	5641	164	0.074	0.013	5.44	0.37	0.0545	0.0019	0.94	0.00971	0.00021	5504	149	53.44	0.87
254-22a	6630	137	0.040	0.019	6.33	0.44	0.0622	0.0023	0.95	0.006972	0.00015	8702	227	60.67	0.89
254-22b	11010	253	0.013	0.0092	23.48	1.6	0.2064	0.0068	0.95	0.007719	0.00016	7450	177	57.51	0.67
254-23a	6150	162	0.036	0.032	9.82	0.68	0.0905	0.0035	0.97	0.00887	0.00028	6153	218	54.58	0.87
254-23b	7670	166	0.029	0.032	9.24	0.56	0.0862	0.0017	0.77	0.007308	0.00016	8155	205	59.60	0.74
254-24	9980	286	0.036	0.021	12.03	0.95	0.1097	0.0053	0.99	0.009622	0.0002	5450	125	52.44	0.50

Table C3: U, Th, and Pb data for joaquinite from sample 254

	ppm				Isotopic ratios										
sample	Th	Pb	U/Th	Pb_c/ Pbtotal	$^{207}Pb/^{235}U$	2σ	$^{206}Pb/^{238}U$	2σ	Corr.	$^{208}Pb/^{232}Th$	2σ	$^{232}Th/^{204}Pb$	2σ	$^{208}Pb/^{204}Pb$	2σ
254-25	8560	211	0.025	0.020	15.8	1.7	0.141	0.011	0.99	0.008239	0.00017	6713	162	55.31	0.70
254-26	6520	176	0.071	0.017	5.88	0.57	0.0581	0.0038	0.99	0.00927	0.00028	5754	188	53.34	0.67
254-27a	10660	277	0.030	0.012	12.31	0.92	0.1126	0.0047	0.98	0.00871	0.00019	6202	152	54.02	0.60
254-27b	6040	156	0.046	0.025	8.3	0.73	0.0785	0.0044	0.98	0.008661	0.00019	6383	159	55.28	0.66
254-28a	5620	154	0.043	0.027	9.2	0.65	0.0866	0.003	0.95	0.00925	0.00023	5737	160	53.07	0.66
254-28b	11300	286	0.021	0.0075	16.36	1.0	0.1474	0.0036	0.92	0.008454	0.00017	6511	152	55.04	0.65
254-28c	8130	200	0.043	0.027	7.61	0.53	0.0729	0.0026	0.96	0.00825	0.00019	6802	183	56.12	0.78
254-29	10460	290	0.029	0.018	14.61	1.2	0.1302	0.007	0.97	0.00929	0.0002	5724	152	53.18	0.82
254-30a	8180	179	0.013	0.013	27.6	2.9	0.237	0.019	0.99	0.00731	0.00017	8085	233	59.1	1.0
254-30b	12570	295	0.015	0.0081	19.93	1.3	0.1721	0.0042	0.91	0.007816	0.00016	7329	181	57.28	0.79
254-31	7740	182	0.024	0.023	14.63	1.3	0.1293	0.0078	0.98	0.007798	0.00017	7284	212	56.8	1.1
254-32	5240	173	0.043	0.021	11.59	0.7	0.1046	0.0022	0.80	0.01109	0.0003	4446	138	49.31	0.75
254-33	12430	316	0.022	0.0083	16.53	1.2	0.1456	0.0064	0.98	0.00849	0.00019	6438	168	54.66	0.74
254-35	5310	186	0.042	0.020	12.61	0.79	0.1131	0.0029	0.92	0.01181	0.00028	4156	115	49.08	0.71
254-36a	6090	129	0.052	0.014	5.2	0.37	0.052	0.0018	0.93	0.00719	0.00017	8512	245	61.2	1.0
254-36b	6640	182	0.035	0.028	12.45	1.2	0.1132	0.0082	0.98	0.00922	0.00024	5791	165	53.39	0.62
254-36c	10260	275	0.032	0.017	12.39	1.1	0.1141	0.0069	0.99	0.00903	0.00021	5965	159	53.86	0.70
254-37	7400	175	0.058	0.021	6.17	0.63	0.0607	0.0043	0.99	0.00794	0.00017	7040	193	55.90	0.96

Note: Different numbers denote different grains, diferent letter note repeat analyses on the same grain.

APPENDIX D

CO-AUTHOR STATEMENT OF PERMISSION

All co-authors of all chapters have granted permission to use these articles in this dissertation.